CZECH TECHNICAL UNIVERSITY IN PRAGUE

Faculty of Civil Engineering
Department of Concrete and Masonry Structures

Performance of Cementitious Composites Subjected to Combined Fire and Blast Loading

Chování cementových kompozitů při kombinovaném zatížení požárem a výbuchem

DOCTORAL THESIS

Ing. Kateřina Horníková

Doctoral study programme: Civil Engineering

Branch of study: Building and Structural Engineering

Doctoral thesis tutor: doc. Ing. Marek Foglar, Ph.D.
Ing. Radek Štefan, Ph.D.

Prague, 2023

DECLARATION

Ph.D. student's name: Ing. Kateřina Horníková

Title of the doctoral thesis: Performance of cementitious composites subjected to combined fire and blast loading

I hereby declare that this doctoral thesis is my own work and effort written under the guidance of the tutor doc. Ing. Marek Foglar, Ph.D. and Ing. Radek Štefan, Ph.D..
All sources and other materials used have been quoted in the list of references.

The doctoral thesis was written in connection with research on the project:
- Grant no. GA17-23067S (co-investigator)
- Grant no. SGS16/040/OHK1/1T/11 (co-investigator)
- Grant no. SGS17/045/OHK1/1T/11 (principal investigator)
- Grant no. SGS18/042/OHK1/1T/11 (co-investigator)
- Grant no. SGS19/035/OHK1/1T/11 (co-investigator)
- Grant no. SGS20/040/OHK1/1T/11 (co-investigator)
- Grant no. SGS21/042/OHK1/1T/11 (co-investigator)

In Prague on ....

....
signature

Abstract

This thesis is focused on the study of influence of the material properties of different types of concrete on the resistance to fire and blast loading. The interaction of fire and blast loading has not yet been quantified so far in any way. The aim of this thesis is to quantify this interaction based on an original experimental program. Mainly focusing on the properties of the materials studied, the original experimental program is divided into three main parts. In the first part, the material properties of five materials are determined as a function of the elevated temperature. The determined properties are: bulk density, porosity, thermal conductivity, specific heat capacity, permeability, and compressive strength. In the second part of the experimental program, specimens of three materials are subjected to fire and subsequent blast loading. The specimens are subjected to an elevated temperature of 400 °C, followed by near blast using 40 g of Semtex at a distance of 30 mm from the specimen. The result of these experiments is the level of damage to the specimens and the velocity of the flying debris (soffit velocity) measured using Photonic Doppler velocimetry. In the last part of the experimental program, a numerical simulation of the experiments is performed. the numerical analysis is performed for only the reference material. Within this part, both the change of the mechanical properties by elevated temperature and the blast is simulated. The result is the velocity of the flying debris (soffit velocity) and a comparison of the shock wave propagation velocity through the specimen. As a result of the undertaken experimental program, a trend of behavior is determined, where the main parameter influencing the behavior of concrete elements subjected to fire and subsequent blast loading seems to be the tensile strength. Tensile strength decreases quickly with increasing temperature and is also a key property for the element's resistance to blast.

Keywords

Material properties, cementitious composites, concrete, high temperature loading, near-field blast loading, combined effect of loading, numerical simulation, FE modelling

Abstrakt

Tato práce je věnována studiu vlivu materiálových vlastností různých druhů betonu na odolnost prvků vůči požáru a výbuchu. Interakce zatížení požárem a výbuchem nebyla dosud jakkoli kvantifikována. Cílem této práce je tuto interakci kvantifikovat na základě původního experimentálního programu. Tento původní experimentální program, který je zaměřen především na vlastnosti zkoumaných materiálů je rozdělen do tři hlavní části. V první části jsou stanoveny materiálové vlastnosti pěti materiálů v závislosti na působící zvýšené teplotě. Stanovované vlastnosti jsou: objemová hmotnost, porosita, tepelná vodivost, měrná tepelná kapacita, permeabilita a tlaková pevnost. Ve druhé části experimentálního programu jsou vzorky tří materiálů vystaveny požáru a následnému výbuchu. Vzorky jsou vystaveny působící teplotě 400 °C a následnému blízkému výbuchu pomocí 40 g Semtexu ve vzdálenosti 30 mm od zkušebního vzorku. Výsledkem těchto experimentů je míra poškození vzorků a rychlost odletujících částic měřená pomocí Photonic Doppler velocimetry. V poslední části experimentálního programu je věnována numerické simulaci proběhlých experimentů. Numerická analýza je provedena pouze pro referenční materiál. V rámci této části je modelována jak změna mechanických vlastností vlivem působení zvýšené teploty, tak samotný výbuch. Výsledkem je rychlost odletujících částic a porovnání rychlosti prostupu rázové vlny vzorkem. Výsledkem provedeného experimentálního programu je stanovení trendu chování, kdy hlavním parametrem, ovlivňujícím chování betonových prvků vystavených požáru a následnému zatížení výbuchem, se jeví jejich tahová pevnost. Pevnost v tahu rychle klesá se zvyšující se teplotou a zároveň je klíčovou vlastností pro odolnost prvku vůči výbuchu.

Klíčová slova

Materiálové vlastnosti, cementové kompozity, beton, zatížení vysokou teplotou, zatížení blízkým výbuchem, kombinovaný účinek zatížení, numerická simulace, MKP modelování

Acknowledgements

First of all, I would like to express my gratitude to my supervisor doc. Ing. Marek Foglar, Ph.D. for his guidance and encouragements. His deep knowledge in the field of concrete structures, organizational skills, professional experience, his enthusiasm, and mainly moral support have been essential for completion of this thesis. His personality was fundamental to the completion of this thesis as well as to my personal growth. My deep gratitude for the opportunity to work with him is impossible to describe.

Ing. Radek Štefan, Ph.D., my co-supervisor, is gratefully acknowledged for providing me with an introduction to the fire resistance of concrete structures, for many useful discussions, and for cooperation in experimental program and preparing the publications presenting the results obtained within the thesis.

Last but not least, Ing. Radek Hájek, Ph.D., my good friend, and co-worker is gratefully acknowledged for providing me with blast resistance of concrete structures and numerical simulation, for many useful discussions, for all cooperation, and for lots of time spent in great company.

I also thank researchers from other institution I have collaborated with during my research, namely Doc. Ing. Jiří Pachman, Ph.D. from Institute of Energetic Materials, Faculty of Chemical Technology, University of Pardubice, Czech Republic, and members of their research teams for the support provided during the experimental part of the research presented in this thesis.

I would also like to extend thanks to other members of my supervisor's research team and his Ph.D. students, as well as all my other co-authors, and researchers from the department of Concrete and Masonry Structures who participated on my research.

Finally, I would also like to thank members of my family, friends, and coworkers for providing the support, encouragement, and patience required to finish this thesis. My motto in life is: "People come and people leave, but the most important ones are staying as long as they can.". I am blessed to surround myself with amazing people whom I can still learn a lot from and who are a great support to me. Doctoral studies were not an easy challenge, and I would never done this thesis without the full support of the people closest to me. Thank you to all of you!

Table of Content

List of Annexes

Annex 1   Experimental investigation of physical, thermal, hygral and mechanical properties of cementitious composites at high temperatures

Annex 2   Thermal, spalling, and mechanical behaviour of various types of cementitious composites exposed to fire: Experimental and numerical analysis

Annex 3   Numerical assessment of the response of a heterogeneous concrete-based composite bridge deck to a near field explosion.

1 Introduction

1.1 Motivation and objectives

The separate effect of fire and blast on structures has been studied and described in many papers. That approach is understandable given the complexity of the phenomena.

However, recent studies start to deal with coupled effect of blast and fire loading. The first example, Kakogiannis et. al. [1] describe an experimental program focused on effects of blast and subsequent fire on prestressed panels. The results were verified by numerical simulation in LS-DYNA. RUAN et. al. [2] presented results of coupled effect on RC column. Results were implemented to numerical model and numerical simulation of the tests was undertaken. Zhai et. al. [3] follows this article with study of RC beams subjected to blast after exposure fire. Choi et. al. [4], as the last one from the series, presented results of blast-inducted fire simulation of prestressed panel.

The effect of fire and blast on cementitious composites was studied previously by Marek Foglar' s team. Results were presented for example at Foglar et. al. [5]. This book presented results of long-time experimental program focused on blast resistance of cement composites. Next to the part focused on blast and small part about fire, all the information about blast and subsequent fire experiment there are presented. This experiment can be pronounced as start experiment of these phenomena at our workplace.

The motivation for choosing this topic of the combined effect of fire and blast was the fact that this phenomenon was not well studied yet. At the same time, these the topic presents quite usual, or common situation. As example, a car catches fire and then its gas tank explodes. This situation can occur in an underground parking garage, on a bridge, near an existing residential building, or in a family house where the whole family lives behind a concrete wall. The design of structures for extreme impacts is also becoming common because of the increased frequency of terrorist attacks. In order to design resilient infrastructure, it is necessary to understand how the loads affect the structures. For this reason, this topic was chosen as the theme of this dissertation.

The first suggestion for understanding this phenomenon is to connect the two phenomena – fire and blast – through one of the material properties. The leading material property of this connection should be the permeability of the material. The permeability of a material is closely related to its

heterogeneity. According to the available literature, material heterogeneity influences the blast resistance of these materials. **The first objective of this thesis is to confirm the effect of permeability on fire and blast resistance of the material. The second objective of this thesis is to determine the effect of mechanical properties on the fire and blast resistance of these materials.** With the knowledge of the effect of the exposure temperature on the mechanical properties of the material, the focus goes on the decreasing compressive and tensile strength of the material, depending on the exposed temperature, which has an important role for its resistance. **The third and main objective of this thesis is to understand and quantify the phenomenon of combined effect and to describe the trend of behavior under combined extreme loading** – high temperature (fire) and blast.

1.2 Methodology

In order to achieve the set objectives of the thesis, it was necessary to identify the individual steps to understand the phenomenon studied. Therefore, an original experimental program was proposed and undertaken. This is composed of real tests but also numerical simulations. The experimental program itself was divided into three main parts. The first part of the experimental program deals with the study of the effect of elevated temperature on the material properties of cementitious composites. This part is focused on understanding the behavior of different types of used cementitious composites exposed to high temperature. Five different cementitious composites were used in this part of the experimental program. Based on the findings, three materials were selected to be used in the second part of the experimental program. These three materials were subjected to high temperature and then blast resistance tests. The results were sufficient to describe the behavior of the materials themselves. For a better understanding of the phenomenon, a numerical simulation of the experiments of one of the materials was accordingly performed. Based on that, it is possible to study other parameters that can only be assumed at in the case of the experiments.

For the first part of the experimental program, the sizes of the test specimens are defined by the method used to test the material characteristics. In the second part of the experiment, it is necessary to choose the size of the test specimens with respect to manufacturing, manipulation, and the possibility of testing. From the point of view of performing blast tests, it is preferable to choose the largest test specimens as possible. In the case of high temperature expose, the size of the test specimens is mainly limited by the

size of the test furnace. The most important criteria for the size of the test specimens used is their manipulation ability. Therefore, a slab size of 300 x 300 x 60 mm is chosen. Another important criterion is the determination of the elevated temperature and its increase over time. The elevated temperature is chosen with respect to the used materials, so the materials are damaged but not completely destroyed. In a case of total destruction, it would not be possible to perform blast tests. Therefore, the maximum elevated temperature of 400 °C was chosen with an increase rate of 10 °C/min. The last chosen parameter is the size of the charge used, and its distance from the test specimen. Due to the varying materials of the test specimens, it is necessary to select a charge that will damage the test specimens with high strength but at the same time does not totally destroy the test specimens with high heterogeneity and minimal strength. Therefore, a cylindrical Semtex charge with a diameter of 37 mm, a weight of 40 g, and 30 mm distance from the specimen surface is chosen. Finally, it is necessary to prepare an idealization for numerical simulation of the performed experiments. Within it, an FE model defined by the material properties (obtained in the first part of the experimental program) is created. The other boundary conditions are the same as in the performed experiments. All these steps lead to the achievement of the defined objectives, to the description, and quantification of the trend of the behavior of the elements loaded with the combined loading.

1.3 Outline of the thesis

This thesis is divided into three main parts. Each part of the thesis consists of a separate chapter.

Chapter 2 presents the experiments performed to determine the material properties as a dependence on elevated temperature. This part of the thesis was published in a scientific journal and is presented by Horníková et al. [6], see Annex 1. For the purpose of the thesis, the paper is modified and extended with all the obtained data.

Chapter 3 presents the undertaken fire and blast resistance experiments. This chapter deals with a major part of the whole experimental program. It describes how the test specimens were subjected to elevated temperature and then the blast test was performed. All these data will be published in a scientific journal.

Chapter 4 deals with the numerical simulation of the performed experiments. It presents the developed FE analysis and its results.

Chapter 5 deals with the conclusion of the performed experimental program, evaluation of the set objectives, and recommendation for further research.

2 Material properties

For the purpose of this thesis, the following chapter 2 is reproduced relevant parts of the paper by Horníková et. al. [6] (reference paper), which the authors jointly prepared. This paper is annex 1 of this thesis.

Structural concrete elements must be designed with the required fire resistance. When performing a conventional structural fire design, the heat load and heat transfer in the analyzed structural element must be taken into account. The way of heating affects its material properties and its fire resistance. The heat transfer is influenced by the physical, and thermal properties of the material. The properties such as porosity, thermal conductivity, specific heat capacity, and permeability change with increasing temperature, and, as a result, they also influence the fire resistance of the structural element.

Usually, the research teams use material properties from standards and/or references and perform numerical simulations. This part of the experimental program aims to compare the findings in the literature and provide experimental data for five different cementitious composited exposed to high temperatures: Reference concrete (further denoted as RC), its derivatives air-entrained concrete (AC), and polypropylene fibre concrete (PC), ultra-high-performance concrete with steel fibres (U), and innovative hybrid concrete with mineral insulation shreds (S).

The reference type is the ordinary structural concrete C30/37 according to EN 1992-1-1, cylindrical compressive strength f_{ck}=30MPa. The reference material is compared to its derivatives: Air-entrained concrete which is often used in structural application for its higher durability under frost exposure, and concrete with polypropylene fibers known for its resistance to high temperatures. The reference material is also compared to two completely different cementitious composites: Ultra-high-performance concrete (UHPFRC) with steel fibres known for its high strength and durability and innovative hybrid concrete with mineral insulation shreds with high energy dissipation capacity.

The main aim of this part of the experimental program is to compare the temperature dependences of the selected material properties and simultaneously to compare the effect of the standardized or referenced testing approach on the resultant values of the tested material property. Therefore, some properties have been measured by several methods and/or using different sample dimensions. All results are presented in summary

graphs and are compared with values from valid standards and/or referenced literature. The tests were performed in three accredited laboratories and one university research department which are further denoted as TZ, KU, BZ, and MA, respectively, according to their name abbreviations.

2.1 State of the art – material properties

The material properties of cementitious composites subjected to elevated temperatures have been studied in many experimental programs. However, in most cases, only measurements of some properties are used for consecutive tests. Alternatively, the whole experimental program is aimed at measuring a single property for different types of materials. This chapter gives a brief summary of ways to measure specific material properties for different types of materials.

A general description of the material properties of concrete is presented in Neville [7]. In this case, a description of the main material properties of concrete at room temperature is provided (dry material and wet material). A description of the material properties of concrete exposed to high temperature is provided by Bažant and Kaplan [8]. This reference describes the material properties, the changes in them, and their course, depending on the boundary conditions. Bažant and Kaplan [8] also define the basic mathematical relations between some properties. By contrast, Kodur [9] is dedicated to the main characteristics and their influence on the fire resistance of concrete. This paper presents data obtained experimentally, and the range of some characteristics in dependence on temperature is defined. In *fib* Bulletin [10], the influence of fire on concrete structures is described. Within this description, the Bulletin also presents a description of the material properties. A summary is provided of how these material properties are influenced, and what it implies for the design of concrete structures. The last example is Guo et al. [11], which is focused on the behavior of concrete elements during exposure to high temperatures, and on calculating this behavior. The material properties are defined by mathematical equations.

2.1.1 Thermal and hygral properties

The thermal properties of concrete are important for determining the heat transfer in a concrete element during an assessment of the fire resistance of a structure. Characteristics depending on temperature can be found in valid standards and literature.

Asadi et al. [12] present widely used methods for measuring the thermal conductivity of concrete. They provide the relation between thermal conductivity and other thermal properties (e.g. density and porosity). Wang [13] presents the results of thermal conductivity measurements for eight materials with different water ratios (there used ACI mix design using water-cement ratios of 0.4 and 0.5. In these two types of mixtures 0%, 0.1%, 0.3%, and 0.5% weight of cement was replaced with nano clay). This is one of the few papers in which the thermal conductivity has been measured up to 1 000 °C. Measurements of thermal conductivity for foamed and polystyrene-foamed concrete are described by Sayadi et al. [14]. Othuman and Wang [15] supplement this data with lightweight foamed concrete with material density about 600 kg/m^3. This paper also describes a method in which heat transport is recorded by thermocouples in the tested samples. It also presents the dependence of thermal conductivity on the porosity of the material.

Specific heat capacity is another important material characteristic of concrete. This characteristic is widely used in various theoretical analyses and calculations. There are many methods how to determine this parameter – conventional calorimetry methods, differential thermal analysis (DTA), and differential scanning calorimetry (DSC) methods. These methods determine Specific heat capacity as a function of temperature. Pomianowski et al. [16] presents some of these methods and describe these techniques. Material for this method must be homogeneous and of a very small size. This is very limiting for heterogeneous materials. Černý and Toman [17] designed a nonadiabatic calorimeter, capable of measuring samples of volume of approximately 2.5 liters in the temperature range from 100 °C to 1 000 °C. And further, Ruuska et al. [18] presented another method using a heat flow meter apparatus to determine thermal conductivity and specific heat capacity of inhomogeneous materials.

Permeability is closely connected to material density and its porosity. In Ruuska et al. [18], permeability is defined as gas permeability. Ahlem Houaria et al. [19] compare the gas permeability and the water permeability of concrete, both of these properties in response to elevated temperatures. A very similar topic is studied by Kameche et al. [20], but only for ordinary concrete. Hoseini et al. [21] summarize the test methods for measuring both the liquid and gas permeability of concrete and describe these methods with respect to the fluid and the load conditions employed in the test. Bošnjak et al. [22] present a permeability test for high-strength concrete with and without polypropylene fibers. Methods are described that use non-

typical specimen shapes (for example, a cylinder with a hole). The maximum temperature used in this test is 300 °C, and the results are supplemented by microscopic slides documenting the structure of the material. Noumowe et al. [23] present the results of permeability measurements for three ultra-high performance concretes up to 600 °C. Gawin et al. [24] describe the relation between each characteristic and the changes in permeability depending on temperature.

2.1.2 Mechanical properties

The compressive strength of concrete is one of the fundamental parameters for the design of concrete structures and for assessing their fire resistance. Recent review of material properties was written by Ma et al [25]. This paper provides an overview of sources which deal with changes in material properties. Not only compressive strength is studied, but also flexural strength and modulus of elasticity. This work includes a comparison of many data obtained from the literature. A similar overview is given by Arioz [26]. Phan and Carino [27] provide a review of the mechanical properties of high-strength concrete (HSC) when compared to normal-strength concrete (NSC) It was found that HSC lost its strength more significantly than NSC when exposed to temperature between 25 °C and approximately 400 °C. At higher temperatures, the strength losses of both concretes were very similar. The residual compressive strength at 800 °C of HSC reached only 30% of its original values. It was also reported that HSC is more prone to explosive spalling when exposed to temperature above 300 °C. Varona et al. [28] present the mechanical properties of hybrid fiber-reinforced concrete. In this paper, experimental results for six specific types of concrete and their mechanical properties (not only compressive strength, but also flexural strength and ductility) are discussed. Authors concluded that the effect of high temperature on the residual mechanical properties of hybrid fiber reinforced concretes was less severe than in steel fiber reinforced concretes. Baradaran-Nasiri and Nematzadeh [29] present the mechanical properties of concrete with fine recycled refractory brick aggregates and aluminate cement.

All of these references, and many others, show that the mechanical properties of concrete at high temperatures are a very important topic of scientific investigation. Information can be found about many types of materials including some materials that are not very common. However, in most cases, the mechanical properties are studied separately from other characteristics, and for this reasons, the compressive strength is also investigated in our experimental program.

2.2 Experimental program

2.2.1 Materials

Within this part of experimental program, the material properties of the following types of cementitious composites were measured:

- Ordinary concrete C30/37 used as a reference material (RC)
- Air-entrained concrete (AC)
- Concrete with polypropylene fibers (PC)
- Ultra-high-performance concrete with steel fibers – UHPFRC (U)
- Light-weight innovative hybrid concrete with mineral insulation shreds (S)

The mixtures of the investigated materials are given in Table 1

Table 1 Materials mixtures

	Mat. RC	Mat. AC	Mat. PC	Mat. U	Mat. S
	Weight [kg/m³]				
Cement	370	370	370	650	875
Water	135	135	135	172	437
aggregates 8-16	755	755	755	300	-
aggregates 4-8	195	195	195	460	285
aggregates 0-4	863	863	863	880	-
Superplasticizer	2.6	2.6	2.6	29	-
Air-entraining agent	-	0.4	-	-	-
Polypropylene fibres	-	-	1.5	-	-
Microsilica	-	-	-	80	-
Steel fibres 13mm	-	-	-	120	-
Mineral wool	-	-	-	-	190

Ordinary concrete C30/37 was chosen as the reference material. The material properties of ordinary concrete have been published in many papers and are described in Eurocode EN 1992-1-2 [30]. The properties of the first three types of composites (RC, AC, PC) studied here are very similar. The fourth and fifth materials (U and S) behave completely differently.

2.2.2 Specimens and measured material properties

The list of measured material properties is given in Table 2. Some of the properties were measured by more than one method at different laboratories. The methods that were used may differ according to the material that was used and the size of the specimens. The particular

specimen sizes according to the measured properties and the testing method is given in this table as well.

In the experimental program, the test specimens were exposed to high temperatures up to 1 000 °C. In a few cases, the test was terminated at a lower temperature because of the damage of a specimen. The detailed description of the heat treatment plan assumed for the tests can be found for each specific test method in the appropriate reference given in Table 2.

Table 2 List of the measured material properties and list of the materials, laboratories, procedures, and specimens used in the experimental program.

Material property	Material	Lab. mark	Test procedure	Specimen's dimensions
Bulk Density at room temperature	All types	MA	Pavlíková et al. [31]	50 x 50 x 100 mm
		TZ	EN ISO 1927-6 [32]	150 x 150 x 150 mm
		BZ	EN ISO 1927-6 [32]	150 x 150 x 150 mm
	All except U	KU	EN ISO 1927-6 [32]	Ø100 mm, height 200 mm
	U	KU	EN ISO 1927-6 [32]	Ø50 mm, height 100 mm
Bulk Density at high temperature	All types	MA	Pavlíková et al. [31]	50 x 50 x 100 mm
		TZ	EN 993-1 [33]	50 x 50 x 50 mm
Porosity	All types	MA	Pavlíková et al. [31]	50 x 50 x 100 mm
		TZ	EN 993-1 [33]	50 x 50 x 50 mm
Thermal conductivity	S	TZ	EN 993-15 [34]	350 x 150 x 150 mm
	All except S	TZ	EN 993-15 [34]	300 x 300 x 120 mm
	All types	MA	Černý and Vejmelková [35]	50 x 50 x 50 mm
Specific heat capacity	All types	MA	Toman and Černý [17]	100 x 100 x 50 mm, up to 500 °C
		MA	Toman and Černý [17]	100 x 50 x 50 mm, above 500 °C
Permeability	All types	TZ	EN 993-4 [36]	Ø50 mm, height 50 mm
Compressive strength at high temperature	All except U	KU	EN 12390-3 [37]	Ø100 mm, height 200 mm
	U	KU	EN 12390-3 [37]	Ø50 mm, height 100 mm

2.2.3 Physical properties

2.2.3.1 Bulk density

The main measured temperature-dependent basic physical characteristic was the bulk density of the material. Bulk density was measured for concrete at room temperature and the change in response to temperature.

Bulk density at room temperature was determined according to EN ISO 1927-6 [32] using specimens that were not dry. The results are shown in Table 3 for four independent measurements (the density was measured at four different laboratories, three of which used the above-mentioned method; these measurements are marked TZ, KU, and BZ). The laboratory TZ performed the test on specimens that were prepared for the thermal conductivity and material density for the high-temperature tests at the KU laboratory; the BZ laboratory performed the tests on specimens which were prepared for a test of compressive strength – all specimens were cubes with dimensions of 150 x 150 x 150 mm.
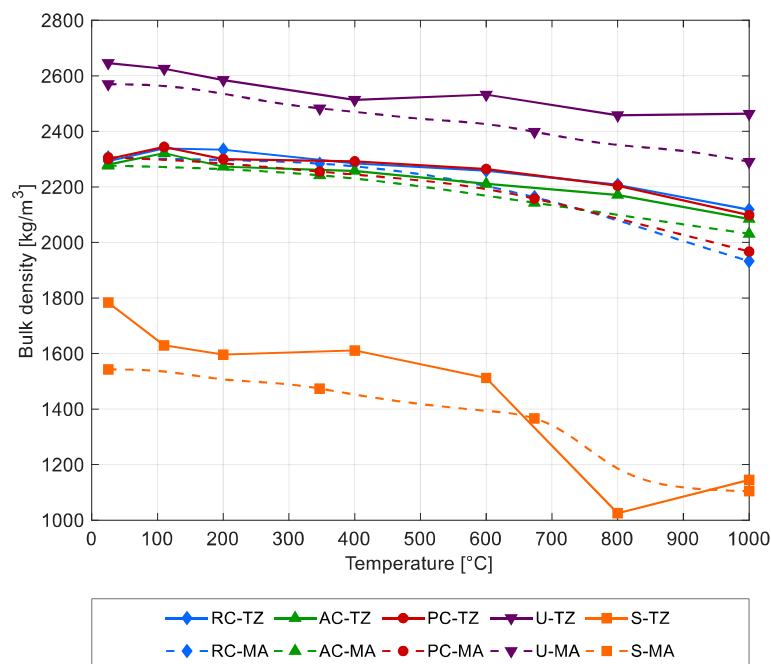
The test performed at the MA laboratory determined the material density at room temperature differently when compared to the method used at laboratories labeled as TZ, KU, and BZ. Bulk density and matrix density were measured by helium pycnometry combined with the gravimetric method by Pavlíková et al. [31]. Helium pycnometry (Pycnomatic ATC device, Thermo Fisher Scientific) provided the matrix density, and the results were supplemented by bulk density measurements, which were calculated from the dimensions of the specimens and its mass in the dry state (dried at 105 °C until constant mass). The specimens were $50 \times 50 \times 100$ mm in size. The whole measurement procedure is given in Horníková et. al. [6]

The results of these two types of measurements are shown in Figure 1.

In Figure 2, selected results (for the reference concrete, its derivatives, and the UHPFRC, i.e. for materials RC, AC, PC, and U, respectively) are compared with the data given in valid standards and literature. Namely, the formula proposed in EN 1992-1-2 [30] is used, with the initial value set to the initial density of material RC or U measured at the TZ laboratory. Moreover, the data given in Kalifa et. al. [38] and Osuji and Ukeme [39] are also used for the comparison. These data refer to normal weight concretes of the compressive strengths of 35 MPa (denoted as M30 in Kalifa et. al. [38]) and 49 MPa (denoted as C40 in Osuji and Ukeme [39]), respectively.

Table 3 Bulk density at room temperature

Laboratory [method reference]	Material density [kg/m³]				
	Material RC	Material AC	Material PC	Material U	Material S
TZ [31]	2 293	2 281	2 301	2 646	1 784
BZ [31]	2 384	2 336	2 333	2 632	1 726
KU [31]	2 360	2 380	2 380	2 620	1 630
MA [30]	2 306	2 277	2 306	2 570	1 541
Mean	2 336	2 319	2 330	2 617	1 670

Figure 1Temperature dependences of the bulk density of the investigated materials

As expected, cementitious composite with mineral insulation shreds (material S) has the lowest bulk density at room temperature. Its average bulk density is 1 670 kg/m³. Ultra-high-performance concrete with steel fibers (material U) has the highest bulk density, with an average value of 2617 kg/m³ caused by high amount of steel fibers and properties of the used aggregates.
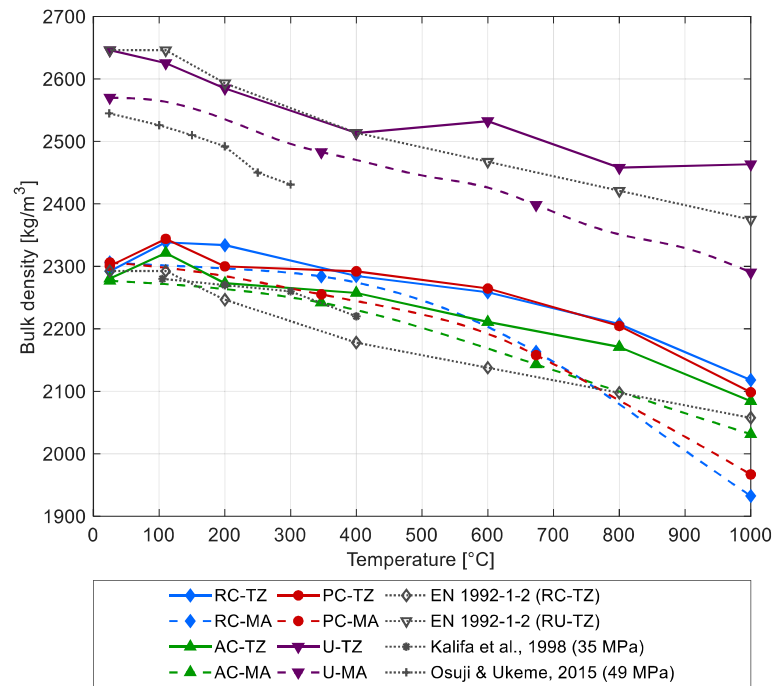
Figure 2Temperature dependences of the bulk density of selected materials (all investigated materials except material S) and their comparison with the data stated in references: EN 1992-1-2 [30], Kalifa et al. [38], and Osuji and Ukeme [39].

Figure 1 shows bulk density slightly decreasing with increasing temperature for all materials, which could be expected as the porosity of the concrete structure increases. A comparison of the two types of measurements shows that the results for materials RC, AC, PC, and U are very similar. Only for material S, the graph of the temperature dependence of the bulk density has a different shape. This may be due to significantly higher porosity results (which will be discussed below), imperfect cohesion of the material, irregular distribution of the mineral insulation shreds, tendency to segregation Bamonte and Gambarova [40], and generally by the fact that this type of light weight porous material is affected more significantly by high temperatures compared to denser types of cementitious composites, see also Štefan et. al. [41].

The results indicate that the two types of test methods are similar and provide comparable results.

2.2.3.2 Porosity

The porosity of concrete was measured by two methods. In the first case (i.e. the test at the TZ laboratory), the porosity was calculated from the weight ratio of the dried specimens and the saturated specimens, with the use of equation (1) according to EN 993-1 [33]:

$$\pi_a = \frac{m_3 - m_1}{m_3 - m_2} \cdot 100 \qquad (1)$$

m_1 weight of a dry specimen [kg],

m_2 weight of the specimen immersed in a liquid [kg],

m_3 weight of a saturated specimen [kg],

π_a apparent porosity [%].

In the second case (at the MA laboratory), the open porosity ψ [%] of the materials was calculated by means of the matrix density and the bulk density Pavlíková et al [31]:

$$\psi = 100 \cdot \left(1 - \frac{\rho_b}{\rho_{mat}}\right) \qquad (2)$$

Where ρ_b is the bulk density [kg/m^3],

ρ_{mat} is the matrix density [kg/m^3].

The whole measurement procedure is given in Horníková et. al. [6]. All results are shown in Figure 3.
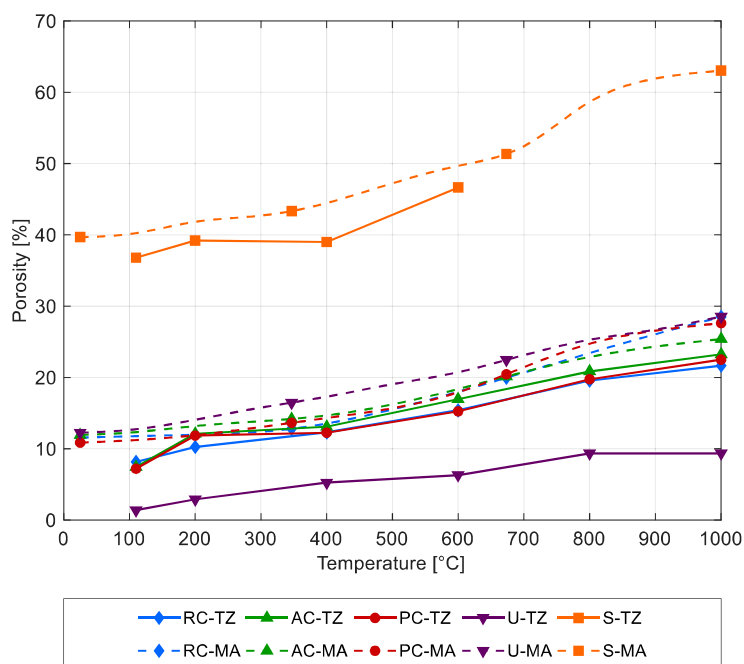

Figure 3Temperature dependences of the porosity of the investigated materials.

The porosity of all materials increases with increasing temperature, as expected. A comparison of the two types of measurements shows that the biggest difference between initial porosity and final porosity is experienced by material U. However, the final porosity results for materials RC, AC, and PC are almost the same for both types of measurements. The final porosity at the highest temperature for materials RC, AC, PC, and U shows an increase of

about 10 %, and for material S, there is an increase in porosity of about 20 %. As already discussed in chapter 2.2.3.1, the lastly mentioned cementitious composite with mineral insulation shreds (material S) exhibited significantly lower bulk density results compared to the other types of studied materials. Based on these results and results of total open porosity, it can be seen that this material was affected more significantly by high temperatures compared to denser types of cementitious composites, see above and Bamonte and Gambarova [40] and Štefan et. al. [41].

2.2.4 Thermal and hygral properties

2.2.4.1 Thermal conductivity

The thermal conductivity of the investigated materials was measured by two different methods. The data obtained by these two methods can be used for different heat transfer modelling approaches – the classical approach using standard thermal conductivity, and the modified approach using so called apparent thermal conductivity, see Černý and Vejmelková [35].

The first method is described in EN 993-15 [34] (used in the TZ laboratory). This method uses a heating wire and a pair of thermocouples. The heating wire and the thermocouples are embedded between two concrete blocks at a known distance. The thermal conductivity is calculated from the thermocouple data (by the change in temperature in a specific area).

The second method (used at the MA laboratory) was used to measure the apparent thermal conductivity. This method is based on an approach that takes into account moisture transport, convective and radiative modes of heat transport, phase-change processes, and chemical reactions, as described in greater detail in Černý and Vejmelková [35]. For the experiments, three specimens with dimensions of 50 × 50 × 50 mm were provided with a set of six temperature sensors (type K thermocouples) installed along their longitudinal axis, 10–15 mm apart and with thermally insulated lateral sides. The specimens were exposed to one-sided heating using a furnace. A constant temperature of 1 000 °C was maintained. The temperature field recorded by a computer was used for the subsequent calculation analysis.

The results from both types of measurements are shown in Figure 4. The measured results are also compared with the data given in valid standards and literature. Namely, the formulas proposed in EN 1992-1-2 [30] are used (upper and lower limit of thermal conductivity of concrete given in EN 1992-1-2 [30]). Moreover, the data given in Kalifa et. al. [38] and Wang [13]

are also used for the comparison. These data refer to normal weight concretes of the compressive strengths of 35 MPa (denoted as M30 in Kalifa et. al. [38]) and 41 MPa (denoted as W4N0 in Wang [13]), respectively.
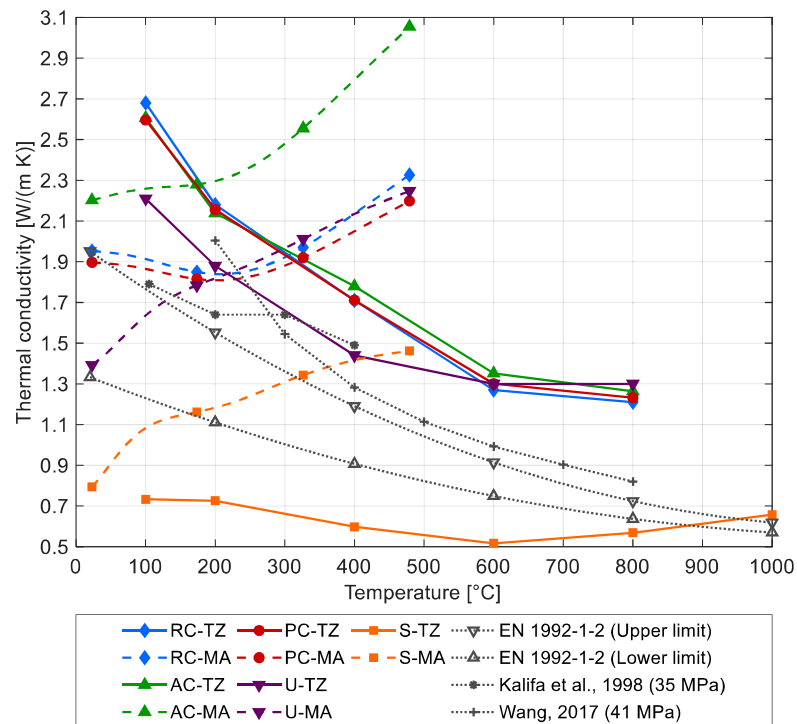

Figure 4Temperature dependences of the thermal conductivity of the investigated materials and their comparison with the data stated in references: EN 1992-1-2 [30], Kalifa et al. [38], and Wang [13].

Figure 4 clearly illustrates that the two types of measurements that were used are not easily comparable. The thermal conductivity for all materials measured at the TZ laboratory decreases with increasing elevated temperature. This trend corresponds with the data given in EN 1992-1-2 [30]. Only material S has a somewhat different course, where the thermal conductivity starts to increase from 600 °C. The results from the MA laboratory are completely different. In most cases, the thermal conductivity always increases with elevated temperatures. Various reasons may have caused the lack of comparability of the methods: one possible explanation is that the results (or the measurements) are affected by some other part of the heat transfer from the measuring device. In general, the results show the lowest thermal conductivity for material S and the highest for concrete AC.

Figure 5 and Figure 6 show the tested specimens at the end of the thermal conductivity measurements at the TZ laboratory. Figure 5 shows the material U specimen with steel fibers. The specimen was not damaged, and the steel fibers are highlighted. However, the material S specimen showed significant

damage. As already discussed in previous chapters, material S exhibited significantly lower bulk density and higher porosity results compared to the other types of studied materials. The damage may also be caused by imperfect cohesion of the material, irregular distribution of the mineral insulation shreds, tendency to segregation Bamonte and Gambarova [40], and generally by the fact that this type of light weight porous material is affected more significantly by high temperatures compared to denser types of cementitious composites Štefan et. al. [41].

Figure 5Tested specimen, material U after thermal conductivity measurements (at the TZ laboratory).

Figure 6Tested specimen, material S after thermal conductivity measurements (at the TZ laboratory).

2.2.4.2 Specific heat capacity

The temperature dependence of the specific heat capacity of the investigated materials was determined using a non-adiabatic method Toman and Černy [17]. The measurement apparatus consisted of a mixing vessel with a volume of 2.5 l that was placed on a compact, flat reciprocal shaker operating at 60 rpm. The apparatus was connected to a monitoring system, which enabled the thermal changes to be observed continuously, see Figure 7. The whole measurement procedure is given in Horníková et. al. [6]
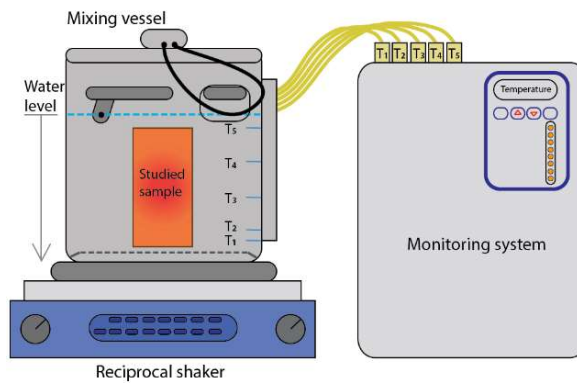
Figure 7The scheme of the non-adiabatic method Horníková et. al. [6]

The measured results are shown in Figure 8. The results are also compared with the data given in valid standards and literature. Namely, there are used the formulas proposed in EN 1992-1-2 [30] for normal weight concrete with the moisture content of 0 % (dry concrete) and 1.5 % of concrete weight, and the data given in Kalifa et. al. [38] for normal weight concrete of the compressive strength of 35 MPa (denoted as M30 in Kalifa et. al. [38]).
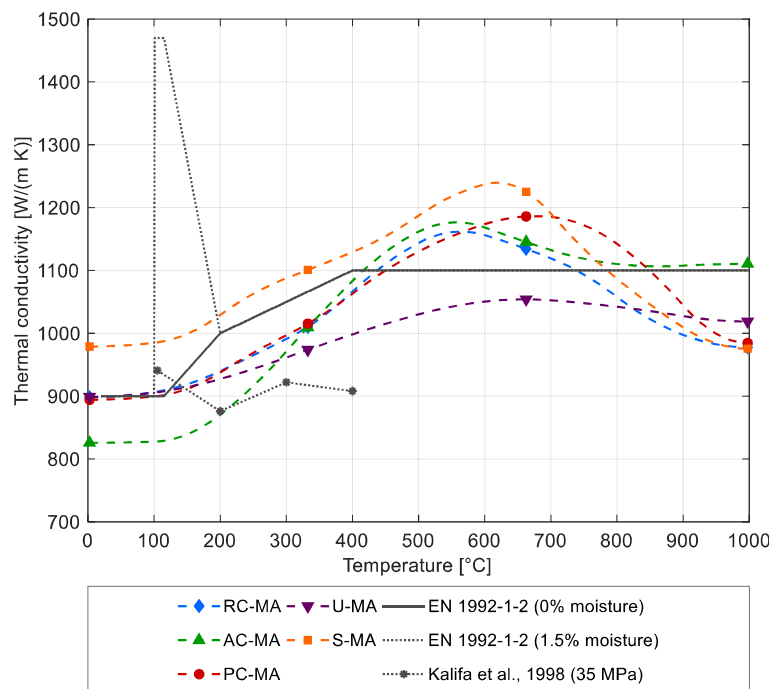
Figure 8Temperature dependences of the specific heat capacity of the investigated materials and their comparison with the data stated in references: EN 1992-1-2 [30] and Kalifa et al. [38].

The results shown in Figure 8 are almost the same as the specific heat capacity defined by standard EN 1992-1-2 [30] for ordinary concrete. The standard course for dry material predicts increasing specific heat capacity up to 400 °C, then continuing with a constant value. The measured

values for all materials increase up to 500 °C − 700 °C and then start decreasing. The final specific heat capacity at 1 000 °C is almost the same as given in EN 1992-1-2 [30].

2.2.4.3 Permeability

The permeability of concrete, as a physical characteristic, can be understood in many ways. In this case, the gas permeability of the material is what is meant. The permeability is measured according to EN 993-4 [36] at three pressure levels. The permeability for material S was measured at 0.6 kPa, 0.8 kPa, and 1 kPa for the high porosity of the material. The permeability of other materials was measured at 5 kPa, 10 kPa, and 15 kPa. During the test, the amount of gas passing through the test specimens is measured by the test device described in EN 993-4 [36]. The results of this test are shown in Figure 9. The results are also compared with the data stated in literature. Namely, there are used the data given in Kalifa et. al. [38] for normal weight concrete of the compressive strength of 35 MPa (denoted as M30 in Kalifa et. al. [38]) and the data given in [42] for normal weight concretes of the compressive strength of 40 MPa and 60 MPa (denoted as B40 and B60, respectively, in Mindeguia [42]).
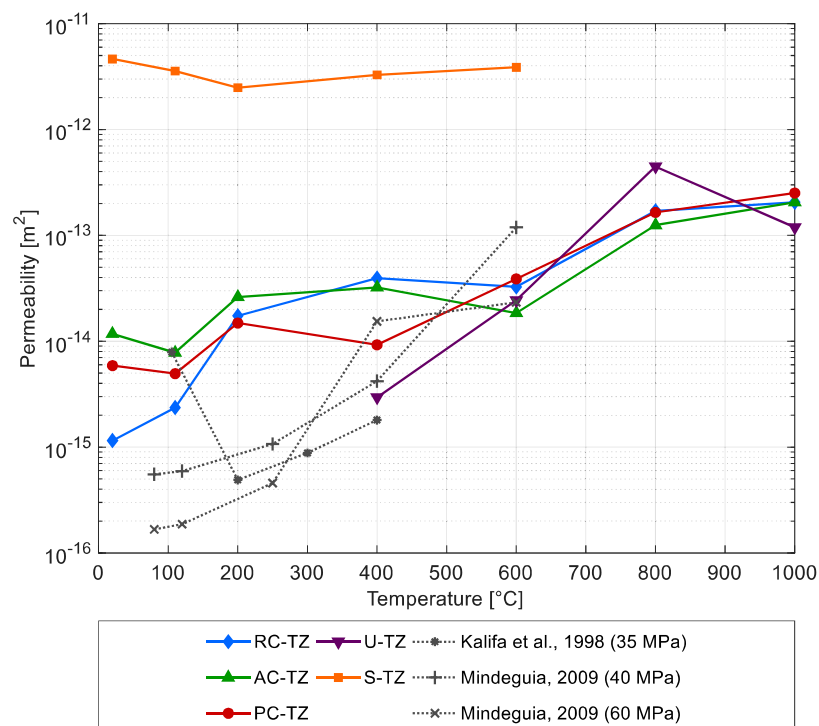

Figure 9Temperature dependences of the permeability of the investigated materials and their comparison with the data stated in references: Kalifa et al. [38] and Mindeguia [42].

The results for materials RC, AC, PC, and U show slowly increasing permeability up to 600 °C. From this temperature on, the permeability increases more rapidly. Material U has the lowest permeability. Up to a temperature of 400 °C for this type of concrete, zero gas permeability was measured. At 800 °C, material U was damaged, and at a temperature of 1 000 °C some aggregates of the material started to change their physical characteristics. The change in the permeability of material S in response to increasing temperature is variable. The main reason for this is probably high porous system of material S, its heterogeneity, and the quantity of mineral insulation shreds (also porous).

Figure 10 shows the tested samples of material U after the permeability measurements. Figure 11 shows the samples of material S after the test. These samples were visibly damaged when exposed to a temperature higher than 800°C.

Figure 10 Tested samples after the permeability test, material U.

Figure 11 Tested samples after permeability test, material S.

2.2.5 Mechanical properties

2.2.5.1 Compressive strength

Several methods can be used for measuring the compressive strength of concrete exposed to high temperatures. The first option is to measure the compressive strength at the high temperature. The second option is to measure the compressive strength after cooling of the sample – when this way is used, the residual strength is measured.

During the experiments, the compressive strength was measured at given temperature (directly on the heated sample, when it is hot). The measurements were made in accordance with RILEM [43], using the hot state testing method. The tested samples are placed in a hydraulic press in an electric furnace. Then heating to the given temperature begins with heating rate is 20 °C per minute. After the desired temperature is reached, the temperature is kept constant for 100 minutes. This ensures equal temperature within the sample. After this time, a conventional test of compressive strength according to EN 12 390-3 [37] is performed made inside the furnace. Then the furnace is opened, cooling begins, so that the next test can be prepared.

Another possibility to determine the compressive strength at a specific temperature is to use ceramic heating pads. Using these, the specimen is heated to the specified temperature and then the compressive strength test is performed. The whole procedure is described in Holan et al. [44] and Muller et al. [45].

The measured compressive strengths are shown in Figure 12. The results for material U are compared with other data, no matter they were measured on the samples of different dimensions. It should be however noted that according to EN 12390-3 [37], the size ratio of the sample plays an important role due to the influence of lateral tension. The measured results are also compared with the data given in literature. Namely, there are used the data given in Wang: [13] for normal weight concrete of the compressive strength of 41 MPa (denoted as W4N0 in Wang [13]), Osuji and Ukeme [39] for normal weight concrete of the compressive strength of 49 MPa (denoted as C40 in Osuji and Ukeme [39]), Pimienta et. al. [46] for UHPFRC concrete of the compressive strength of 165 MPa (denoted as BSI-"fire" in Pimienta et. al. [46]), Pliya et. al. [47] for normal weight concrete without fibres and with steel fibres of the compressive strengths of 46 MPa and 58 MPa (denoted as C2 and CS2-20 in Pliya et. al [47], respectively), and Drzymała et. al. [48] for high performance concrete without fibres and with polypropylene fibres of the

compressive strengths of 73 MPa and 75 MPa (denoted as HPC-reference and HPC-fibre-reinforced in Drzymała et. al. [48], respectively).
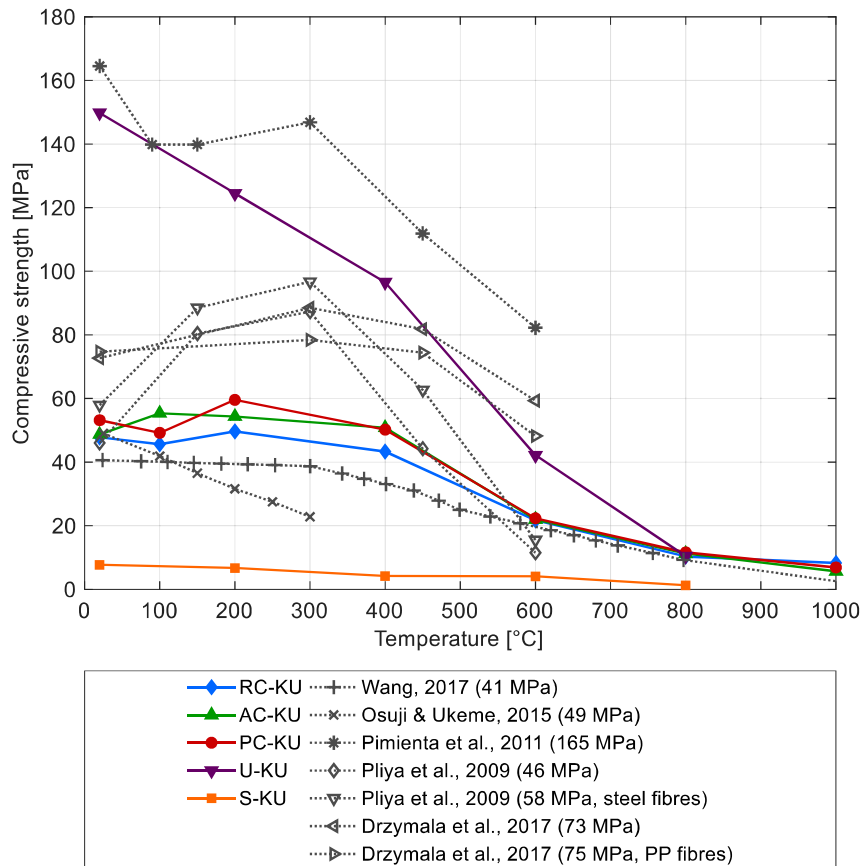

Figure 12 Temperature dependences of the compressive strength of the investigated materials and their comparison with the data stated in references: Wang [13], Osuji and Ukeme [39], Pimienta et al. [46], Pliya et al. [47], Drzymala et al. [48].

In Figure 13, the measured data are presented in the form of relative compressive strength, i.e. the actual strength of a material at a given temperature divided by the initial strength of the material at room temperature. These results are compared with the data for normal weight and normal strength concrete with siliceous aggregates (NSC) and for normal weight and high strength concrete with siliceous aggregates (HSC) given in EN 1992-1-2 [30].
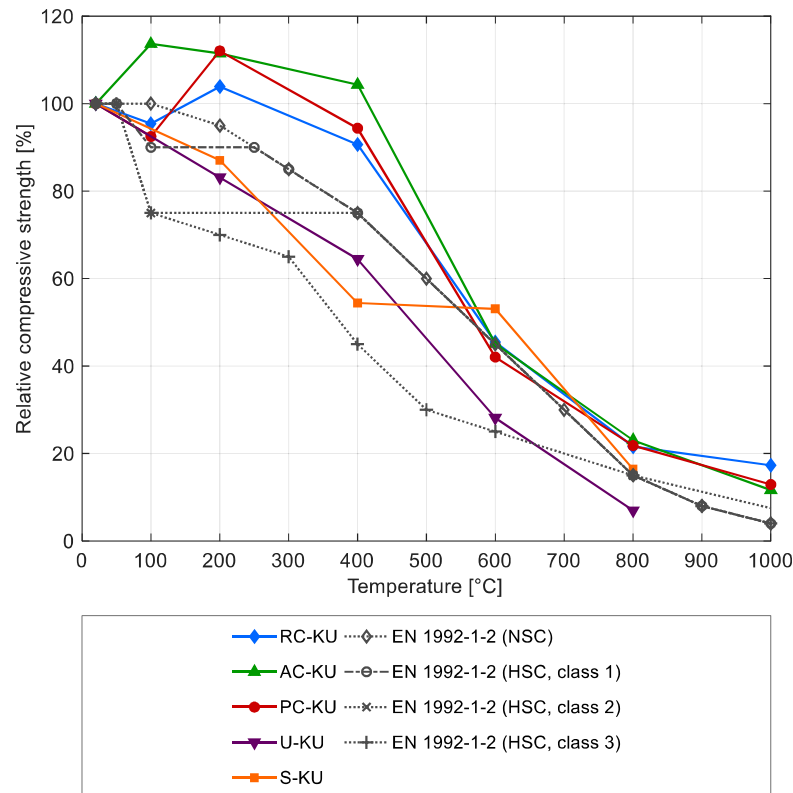
Figure 13 Temperature dependences of the relative compressive strength of the investigated materials and their comparison with the data stated in EN 1992-1-2 [30].

The lowest compressive strength was obtained for cementitious composite with mineral insulation shreds (material S); the maximum value at room temperature was almost 10 MPa due to the high heterogeneity of the material. The maximum value at room temperature was 158 MPa, for UHPFRC (material U). For all materials, the compressive strength decreased with the increasing temperature, except the slight increase at temperatures between 100 − 300 °C for some materials. It should be noted that the increase of the compressive strength after exposure of some samples to temperatures above 100 − 300 °C could be attributed to rehydration of residual and unhydrated cementitious materials activated by higher temperatures Abid et. al. [49] and Peng et. al. [50].

2.3 Summary and discussion

Basic physical, thermal, and mechanical properties of ordinary concrete C30/37 (RC), air-entrained concrete (AC), concrete with polypropylene fibers (PC), ultra-high-performance concrete with steel fibers (U) and concrete with mineral insulation shreds (S) were studied at high temperatures. Ordinary concrete C30/37 (RC) was chosen as a reference material because its

properties are described in the valid standards and in the available literature, and it is widely used for its universal properties. Concrete with mineral insulation shreds (S) was chosen for its heterogeneity. Ultra-high-performance concrete with steel fibers was chosen as an example of a dense impermeable homogeneous cement composite.

The methods that were used and the achieved results have been described and continuously discussed within the part dedicated to the experimental program. As expected, with increasing temperature the material density, the thermal conductivity (for TZ laboratory) and the compressive strength of all materials decreased. The porosity, the specific heat capacity and the gas permeability increased with increasing temperature for all tested materials. These changes are based on the transport and evaporation of water from the material. While the water is evaporating, the amount of open pores increases, and new pores are formed (together with crack propagation). When moisture leaves the material, the material loses weight and loses a part of its thermal conductivity. The formation of new pores generates a place for gases and, therefore, the gas permeability increases.

The compressive strength decreased with increasing temperature for all materials. The compressive strength at the highest temperature was about 20 % of the value at room temperature, and this value was almost the same for all the studied materials. The compressive strength increased slightly at approx. 200 °C. This is usual for many types of concrete, but the design codes and standards neglect this phenomenon.

The most significant differences were found between the results obtained by two methods used for the measurement of thermal conductivity and the available data of thermal conductivity. Using the first test method, described in EN 993-15 [34], the thermal conductivity decreased with increasing temperature. This is comparable with the design codes and with the data from the available literature. Using the second method, the evolution of thermal conductivity has the opposite direction. These two types of tests seem not to be comparable, and further investigation is required.

Table 4 shows a summary of the results of all tests performed on all materials. The tabular summary presents the percentage change in the properties and provides a basis for comparisons, e.g. the thermal conductivity of ordinary concrete at room temperature is 28 % lower for the tests performed at the laboratory MA than for the tests performed at the TZ laboratory.

The development of the thermal and material properties of concrete exposed to high temperatures can be used for an assessment of existing structures, in the design of new structures with a high risk of fire loading, or for numerical simulations of structures subjected to fire loading.

Table 4 Summary of the results

		Laboratory mark [method reference]	Ordinary concrete		Air-entrained concrete		Concrete with polypropylene fibers		UHPFRC		Cementitious composite with mineral insulation shreds	
			Material RC		Material AC		Material PC		Material U		Material S	
			Value at temperature:		Value at temperature:		Value at temperature:		Value at temperature:		Value at temperature:	
Density	[°C]	MA [30]	25 °C	1 000 °C	25 °C	1 000 °C	25 °C	1 000 °C	25 °C	1 000 °C	25 °C	1 000 °C
	[kg/m³]		2 306	1 932	2 277	2 031	2 306	1 967	2 570	2 290	1 543	1 104
	[%]		83.80%		89.22%		85.29%		89.12%		71.57%	
	[°C]	TZ [31], [32]	100 °C	1 000 °C	100 °C	1 000 °C	100 °C	1 000 °C	100 °C	1 000 °C	100 °C	1 000 °C
	[kg/m³]		2 339	2 118	2 322	2 085	2 344	2 099	2 626	2 464	1 630	1 145
	[%]		90.57%		89.79%		89.53%		93.83%		70.27%	
Porosity	[°C]	MA [30]	100 °C	1 000 °C	25 °C	1 000 °C	25 °C	1 000 °C	25 °C	1 000 °C	25 °C	1 000 °C
	[%]		11.57	28.48	11.95	25.39	10.86	27.62	12.25	28.53	39.68	63.03
	[%]		246.25%		212.47%		254.27%		232.90%		158.84%	
	[°C]	TZ [32]	100 °C	1 000 °C	100 °C	1 000 °C	100 °C	1 000 °C	100 °C	1 000 °C	100 °C	600 °C
	[%]		8.15	21.65	7.45	23.25	7.20	22.50	1.40	9.35	36.80	46.65
	[%]		265.64%		312.08%		312.50%		667.86%		126.77%	
Thermal conductivity	[°C]	TZ [33]	100 °C	800 °C	100 °C	800 °C	100 °C	800 °C	100 °C	800 °C	100 °C	1 000 °C
	[W/mK]		2.68	1.21	2.61	1.26	2.60	1.23	2.21	1.30	0.73	0.66
	[%]		45.15%		48.47%		47.46%		58.82%		89.77%	
	[°C]	MA [34]	23 °C	500 °C	23 °C	500 °C	23 °C	500 °C	23 °C	500 °C	23 °C	500 °C
	[W/mK]		1.95	2.33	2.20	3.05	1.90	2.20	1.39	2.25	0.79	1.46
	[%]		119.14%		138.73%		115.90%		161.42%		184.16%	
Specific heat capacity	[°C]	MA [14]	5 °C	1 000 °C	5 °C	1 000 °C	5 °C	1 000 °C	5 °C	1 000 °C	5 °C	1 000 °C
	[J/kgK]		898.27	977.58	825.76	1 110.58	894.27	984.42	901.28	1 049.87	978.92	975.45
	[%]		108.83%		134.49%		110.08%		116.49%		99.65%	
Permeability	[°C]	TZ [35]	20 °C	1 000 °C	20 °C	1 000 °C	20 °C	1 000 °C	400 °C	1 000 °C	20 °C	600 °C
	[m2]		1.15E-15	2.06E-13	1.17E-14	2.05E-13	5.88E-15	2.51E-13	2.95E-15	1.19E-13	4.65E-12	3.87E-12
	[%]		17825.51%		1750.40%		4264.19%		4048.59%		83.28%	
Compressive strength	[°C]	KU [36]	20 °C	1 000 °C	20 °C	1 000 °C	20 °C	1 000 °C	20 °C	800 °C	20 °C	800 °C
	[MPa]		47.79	8.27	48.71	5.66	53.17	6.86	149.80	10.44	7.71	1.27
	[%]		17.30%		11.62%		12.91%		6.97%		16.43%	

3 Fire and Blast

The combined effect of extreme temperature and blast loading represents a real loading scenario. Many fires are followed by blast (e.g. explosion of gas cylinders during a fire in their surroundings) or fires occur immediately after blast when a fireball ignites surrounding objects. Therefore, some authors extend their studies to include the combined effect of other extreme loadings on concrete structures.

This part of thesis presents the results of an experimental focused on the effect of elevated temperature on the blast resistance of the materials. Three materials were analyzed - ordinary concrete (C30/37), ultra-high performance concrete with steel fibers (UHPFRC) and light-weight innovative hybrid concrete with mineral insulation shreds. Specimens of these three materials were subjected to compressive strength test, tensile strength test and blast resistance test. Before that, the specimens were exposed to 400°C for 3 hours, either from one side or uniformly. After cooling, the specimens were subjected to blast resistance test. For reference, the blast testing was also performed on not previously heated specimens. Therefore, in the experiment, the blast resistance of unheated, one-side, and uniformly heated specimens were compared.

The effect of fire and blast on cementitious composites were studied previously by Marek Foglar's team by experimental program. Results were presented at Štefan et. al. [51]. The other part of these experiments was presented at Foglar et. al. [5]. This book presented results of long-time experimental program for study of blast resistance of cement composites. Next to part about blast and small part about fire there are presented all information about blast and subsequent fire experiment. This experiment is possible to know like starts experiment of these phenomena at our workplace.

The results of this part of the experimental program will be presented in a future scientific journal.

3.1 State of the art – fire and blast resistance

Effect of fire and blast on structures has been described in many articles and study at many workplaces. Almost in all cases it is studied just one load type at the time. That approach is understandable given the complexity of the phenomena.

Kakogiannis et al. [1] present the results of an full-scale experimental program on the effect of fire and subsequent blast on the load carrying capacity of reinforced concrete hollow core slabs. The paper also discusses a simplified numerical simulation of this experiment in LS-DYNA software; the most challenging issue seems to be the coupling of a slow phenomenon (fire gradually changes the properties of the element) and an extremely fast phenomenon (blast changes the element and its properties in microseconds). The resulting solution of the issue requires a previous analysis of the change in material properties when exposed to high temperature. In addition to failure and load-bearing capacity, the paper also discusses the effect of high temperatures on the dynamic behavior of the specimens or their natural frequency and dynamic deformation. Zhai et al [3] present the results of full-scale experiment of RC beams subjected to a fire and subsequent blast loading. Compared to the above experiment, the beams were not directly exposed to the fire, but they were heated in a furnace according to ISO834 temperature-time curve for 90 and 120 minutes. The experiment is also supported by numerical verification. Ruan et al. [2] and Fang et al. [52] discuss numerical simulations of the effect of fire and blast on structures. The papers deal with the validation of the experimental data, focusing mainly on the effects of heat transfer through the elements. Štefan et al. [51] present data from an experiment in which reinforced concrete panels were first subjected to a near-field blast and then to a unilateral high temperature exposure for 135 minutes. Štefan et al. [53] follow up the above experiment with a tool for numerical evaluation of the damage to the used elements.

Chen et al. [54], [55], and Guo et al. [56] deal with the effect of fire and blast on RPC-FST columns. They present the progress and results of the experiments performed as well as numerical simulations focused on the load-bearing capacity of columns subjected to fire and subsequent blast.

Choi.et al [4] presented results of blast inducted fire simulation of prestressed panel. Presented experiment is also validated by a numerical model (FE model by LS-DYNA)

The studied phenomenon is very complex mainly due to material heterogeneity of concrete. The issue of heterogeneity is not relevant for steel structures, therefore, for more research was performed on the effects of fire and blast on steel structures.

Liew and Chen [57], Chen and Liew [58], and [59] focus on the durability of steel frame structures. Results of various numerical approaches were presented, motivated by the events of 9/11 and the collapse of the World

Trade Center steel-concrete composite structure. Forni et al. [60] and Vasilchenko et al. [61] deal with the effect of fire and blast on steel columns. Fang et al. [62], [63] deal with numerical simulations of the effect of fire and blast on steel beams and columns.

The study of the combined effect of fire and blast is not possible without understanding these loads separately and thoroughly. The authors of this paper have been studying the effect of near-field blast on cementitious composites for many years. The publications by Foglar and Kovar [64], Foglar et al. [65], Foglar et al. [66], Foglar et al. [67], and Hajek et al. [68] present the results of a long-term full-scale experiments focused on the behavior of various cementitious composites subjected to near-field blast. Several types of specimens including prestressed precast slab were tested. The obtained data were verified by LS-DYNA software numerical simulations focusing on stress changes, shock wave penetration, delamination of the layers, deplanation of the cross section, etc. Stöhr et al. [69] present the results of a scaled-down experiment to simulate the full-scale tests described above. Hajek and Foglar [70], and Hájek et al. [71] deal with experiments and optimization of barriers that aim to deflect or mitigate the effects of a shock wave.

Matsagar [72] compared the performance of composite panels under blast loading. Li et al. [73] investigated the resistance of an ordinary concrete slab and an ultra-high performance concrete slab to contact explosion. Liu et al. [74] deals with increasing the heterogeneity of high-performance concrete material by adding a steel wire mesh reinforcement. Christian and Ong Khim Chye [75] analyze the effect of increasing heterogeneity by adding steel sandwich composite system to the concrete specimens. Other reinforcement methods are presented by Fallon and McShane [76]. They study the response of elastomer-coated concrete subjected to air blast loading. The similar polyuria elastomeric protective coating is studied by Iqbal et al. [77]. Maazoun et al. [78] study RC hollow core slabs retrofitted with a concrete topping combined with CFRP strips.

The same as the blast loading, the effect of high temperature on the structure or the material is subject of many publications. These studies often focus on particular material characteristics. For example, Štefan et al. [79] investigate the change in compressive strength of various cementitious composites subjected to applied high temperature. Bednář et al. [80] present the results of an experiment in which steel fiber reinforced concrete floor slabs were subjected to high temperature with a focus on ductility and tensile strength of the material. Banerji et al. [81] focus on the durability of

UHPFRC beams depending on the amount of wire used. In addition to the change in material properties, many studies also focus on the effect on surface spalling, e.g. Weerasinghe et al. [82] present results on the fire resistance of flat slabs subjected to ISO834 fire conditions and mainly focuses on concrete spalling. The resistance of cementitious composites is evaluated not only for in-situ manufactured elements but also for precast elements. Xu et al. [83] discuss the fire resistance of precast concrete columns.

3.1.1 Near-field blast loading of concrete plates

The overall dynamic response of a concrete panels subjected to near field blast loading is a complex combination of different phenomena. The side facing the explosive charge is loaded by an incident shock wave and impact of high temperature detonation products. The displacement of air that was originally between the charge and the specimen results in additional loading of a significant magnitude. Based on the compressive strength of the material, crater may or may not be formed on the impacted side. In either case, combination of the phenomena results in formation of a strong compressive wave – a shock wave – inside the specimen. The shock wave advancing through the material and compresses it, until it arrives at the other side of the sample where it is reflected as a rarefaction wave. The subsequent expansion may cause spall – a rupture within the specimen - due to stress states in excess of the dynamic tensile strength of the material, see Antoun et al. [84]. The tensile strength of concrete is significantly lower compared to its compressive strength and therefore it is not uncommon to encounter cases where the surface facing the charge is undamaged while the opposite surface shows significant spall damage.

The experimental measurement of the material spall strength is based on the determination of one-dimensional motion of compressible media following the reflection of a shock wave from the free surface of the specimen. Detailed analysis is well described in Antoun et al. [84] or [85]. The methods are well established in the field of shock physics, and applied to rocks especially in plate impact and SHPB experiments but to our best knowledge not so commonly applied to study response of planar concrete samples under explosive near-field blast loading. The free surface velocity history measured in presented experiments provides a lot of information about fracture mechanism, however, only the peak velocity, pull-back signal useful for spall strength comparison for tested samples and terminal velocity of ejected debris are being considered in this contribution.

3.2 Experimental program

3.2.1 Concept of the experiment

The specimens were firstly exposed to an elevated temperature simulating the fire loading. The specimens were placed and heated in two positions. One set was exposed to elevated temperature from one-side only - the specimens were located in the wall of the test furnace. The other set was exposed to elevated temperature from all sides - the specimens were placed inside the test furnace. The reference set was not exposed to elevated temperature. The specimens were subsequently after cooling exposed to near field blast. The blast loading was identical for all the test specimens.

The materials analyzed in this paper were chosen in order to widen the knowledge base. The material properties of these materials were obtained within the previous experimental program, described in Horníková et al. [6] and the previous chapter. The materials were chosen with respect to wide range of their properties.

3.2.2 Materials

Within this part of experimental program, the material properties of the following types of cementitious composites were measured:

- Ordinary concrete C30/37 used as a reference material (RC)
- Ultra-high-performance concrete with steel fibers – UHPFRC (U)
- Light-weight innovative hybrid concrete with mineral insulation shreds (S)

The mixtures of the investigated materials are given in Table 5.

Table 5 Materials mixtures

	Mix RC	Mix U	Mix S
	Weight [kg/m³]		
Cement	370	650	875
Water	135	172	437
aggregate 8-16	755	300	-
aggregate 4-8	195	460	285
aggregate 0-4	863	880	-
Plastificator	2.6	29	-
Microsilica	-	80	-
steel fibers 13mm	-	120	-
mineral wool	-	-	190

Ordinary concrete C30/37 (RC) was chosen as the reference material. UHPFRC (U) was chosen because of its high strength and high blast resistance. Innovative light-weight hybrid concrete with mineral insulation shreds (S) was chosen because of its heterogeneity and high resistance to high temperature.

3.2.3 Specimens

The list of specimens is given in Table 6.

Table 6 List of specimens

Type of test	Material	Sample dimensions
High temperature and blast tests	All types	300 x 300 x 60 mm
Compressive strength changes	All types	150 x 150 x 150 mm
Tensile strength changes	All types	700 x 150 x 150 mm

Concrete slabs 300 x 300 x 60 mm specimens were divided into 3 groups. The first group (3 specimens of each material) was not exposed to elevated temperature. The second group (4 specimens of each material) were subjected to elevated temperatures from both sides i.e. placed in the test furnace. The third group (4 specimens of each material) was subjected to elevated temperature from one side only i.e. placed in the test furnace wall. Thermocouples were cast in one specimen for each material in order to monitor the temperature development during the experiment.

Concrete cubes 150 mm serve the compressive strength investigation. Three specimens were subjected to elevated temperature in order to investigate the residual compressive strength after the experiment.

Concrete beams 700 x 150 x 150 mm serve for the investigation of tension strength under bending (4-point bending arrangement). Three specimens were subjected to elevated temperature in order to compare the residual tensile strength after the experiment.

3.2.4 Exposure to elevated temperature

3.2.4.1 Experiment description

The specimens were subjected to elevated temperatures in a test furnace. The test furnace was heated by 8 gas burners, and the temperature in the furnace was monitored by 12 thermocouples in four vertical levels. The heating rate was 10 °C/min up to temperature of 400 °C. This temperature was held constant for 3 hours. The fire curve is shown in Figure 14. The

maximum temperature and the heating rate were chosen in order to prevent spalling of the specimens.

In total, 4 specimens of 300 x 300 x 60 mm of each material set were placed in the test furnace wall. The wall was built of usual autoclaved aerated concrete bricks and the specimens were fastened using fire resistant foam. In total five thermocouples were placed in one specimen of each set in the position 0, 10, 20, 30, and 50 mm from the heated surface. These thermocouples recorded the temperature development during the test. The wall specimens were insolated by mineral wool from the unheated side.

All remaining specimens were placed directly on the test furnace floor. For the arrangement of the specimens on the test furnace floor, see Figure 15.

A sheath thermocouple was placed in one slab specimen on the test furnace floor of each material and recorded the temperature development while being heated from all sides. The thermocouple was placed in a bored hole and fastened by cement paste.

All specimens were weighted before the experiment. The test furnace was opened at 150 °C inner temperature and cooled for 12 hours. For view of the test furnace after opening, see Figure 16. All specimens were weighted after the experiment and wrapped in a foil in order to prevent the air humidity absorption.
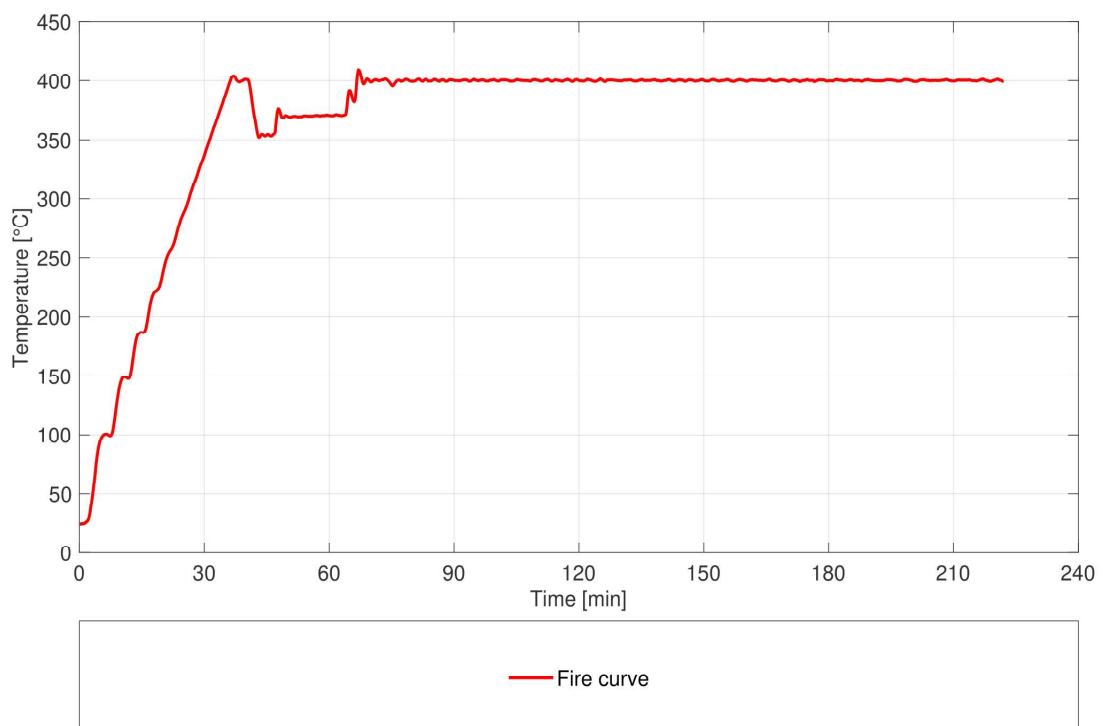
Figure 14 Fire curve during the experiment

Figure 15 Arrangement of the specimens on the test furnace floor (view in the opened furnace)

Figure 16 View into the test furnace after the experiment

Figure 16 documents clearly that some of the specimens were destroyed or severely damaged during the heat treatment. In particular, 3 slabs of the U material, 1 slab and 1 beam of the S material, and 2 slabs of RC material.

The performed measurements provided temperature development in the wall specimens and floor specimens and changes in the weight of the specimens. These results are presented further in the text.

In the following paragraphs, the outcomes of the experiments are presented.

3.2.4.2 Temperature development

During the experiment, the temperature development over the depth of the specimens were measured. Outcomes of the measurements are presented in the following chapter.
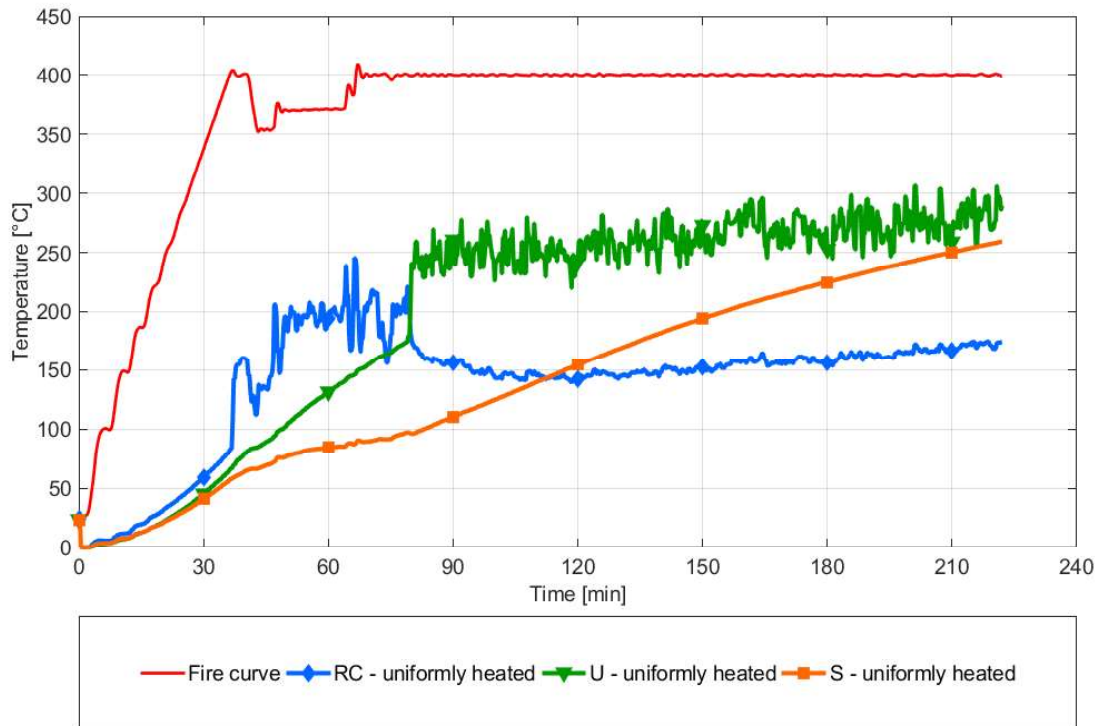
Figure 17 Temperature development in the specimens on the test furnace floor (bored thermocouples)

Figure 17 provides temperature development in specimens located on the floor of the test furnace. At the time of 79.5 minutes, a trend change can be observed and corresponds to explosive collapse of one U-concrete specimen which overturned and damaged the neighboring S and RC specimens. The RC specimen were damaged more severely. Caused by the fall, the thermocouples moved and influenced the further measurement. The temperature development following the explosive collapse is arguable. The maximum specimen temperatures at the time of the explosive collapse are given in Table 7.

Table 7 Maximum specimen temperature at the time of the explosive collapse of one of the U-concrete specimens, t=79.5 min

	RC	U	S
temperature [°C]	202.7	179.7	97.0
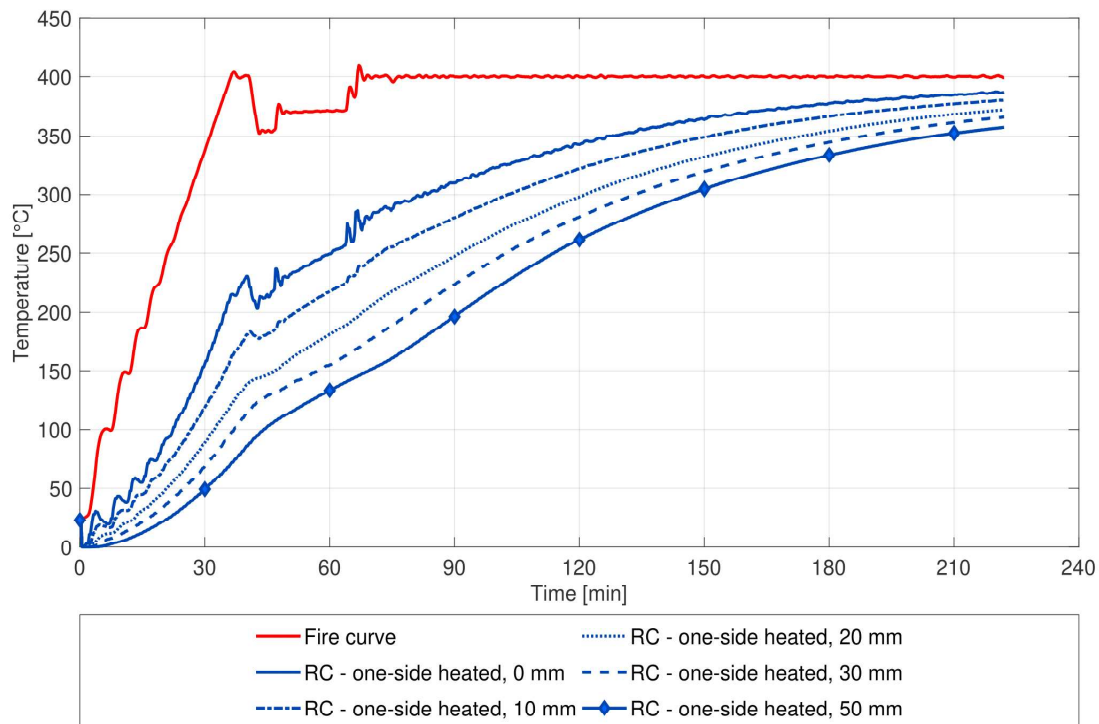
Figure 18 Temperature change in the wall specimen, RC material, data for the varying thermocouple depth (10 stands for 10mm thermocouple depth, etc.)
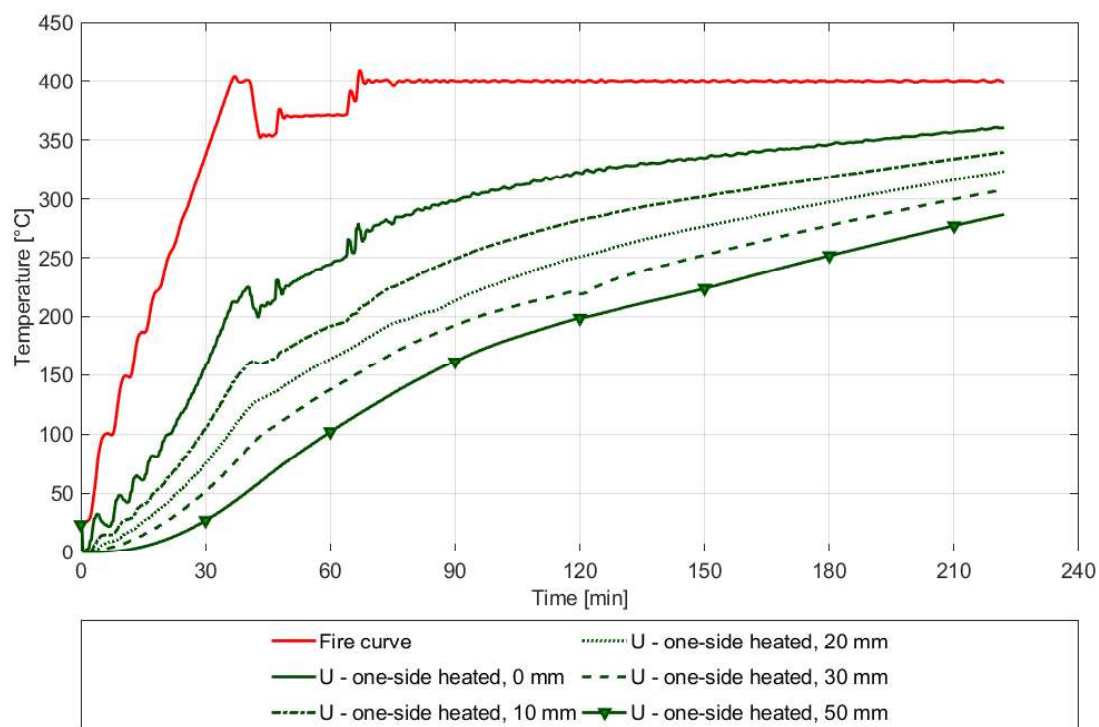

Figure 19 Temperature change in the wall specimen, U material, data for the varying thermocouple depth (10 stands for 10mm thermocouple depth, etc.)
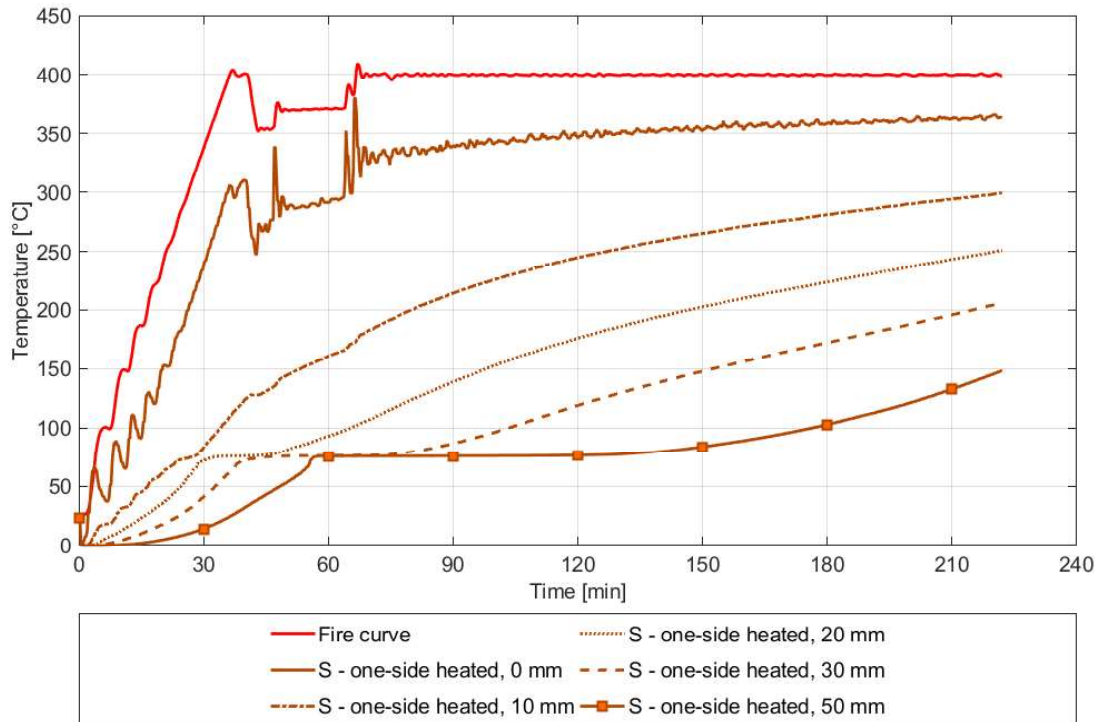
Figure 20 Temperature change in the wall specimen, S material, data for the varying thermocouple depth (10 stands for 10mm thermocouple depth, etc.)

Figure 18 to Figure 20 provide temperature change in wall specimens of the studied materials, the data are provided for various thermocouple depths and compared to the fire curve. Crucial is the maximum reached temperature which affects the changes of material properties in the particular depth.

The maximum reached temperature in the pre-defined depths is provided in Table 8. From all thermocouple positions, the maximum temperature was achieved in material RC. The lowest surface temperature was achieved for material U. In all other thermocouple positions, the lowest temperature was achieved in the S material.

Table 8 Maximum temperature achieved in the defined depths

	0 mm	10 mm	20 mm	30 mm	50 mm
RC	387.4 °C	380.0 °C	371.9 °C	365.4 °C	357.1 °C
U	360.8 °C	339.8 °C	323.5 °C	308.1 °C	286.9 °C
S	379.9 °C	299.2 °C	251.1 °C	206.4 °C	148.5 °C
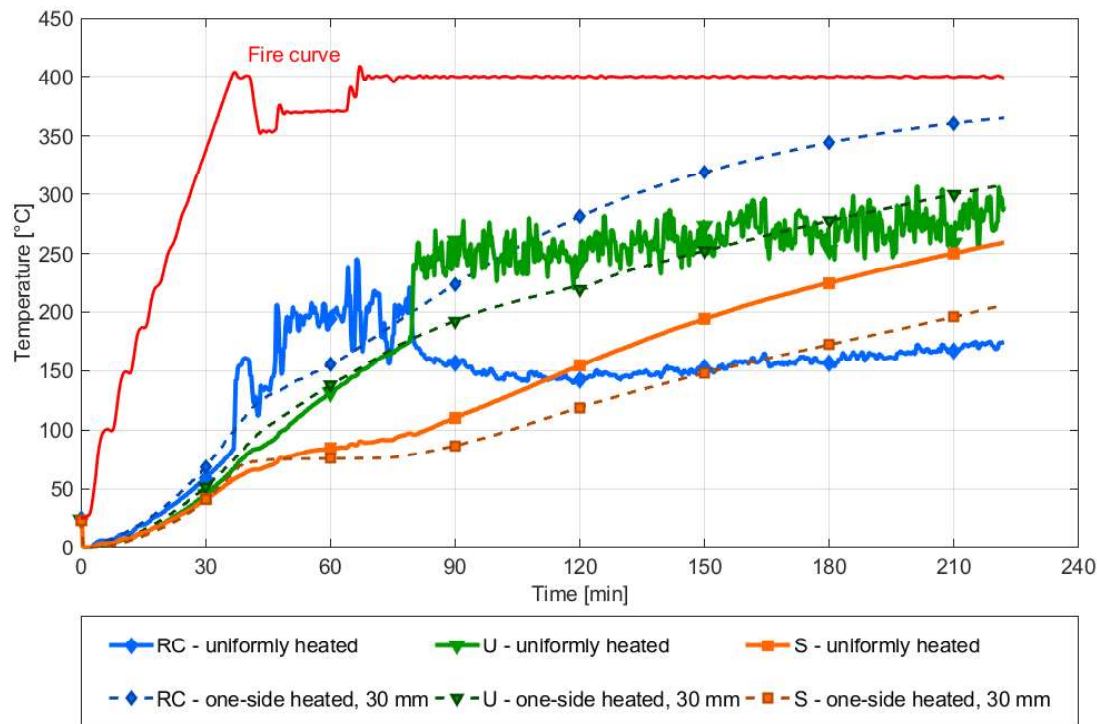
Figure 21 Comparison of temperature development in 30 mm depth of the wall specimen – dashed line, specimens on test furnace floor – solid line

Figure 21 provides a comparison of the temperature development in wall specimens (dashed line) and the specimens located on the floor of the test furnace (solid line). For the comparison, the distance of 30 mm from the heated surface (center of the specimen) was chosen. At the beginning of heating, the temperature rise in all specimens is almost identical. After 37 minutes, the temperature development trend in the RC-specimen placed in the test furnace changes. For the other materials, the temperature development is almost identical up to the time of 79.5 minutes, when one of the U-specimens collapsed. This event damaged the neighboring specimens and influenced the results.

3.2.4.3 Mass change

With temperature rise, free water evaporates and the mass of the specimen changes accordingly. At elevated temperatures, high pore pressures can cause spalling of the material. Within the experiment, the specimens were exposed to temperature of only 400 °C for 3 hours in order to prevent spalling. The weight loss therefore represents the water evaporation from the material.

Table 9 presents the average weight loss of all materials based on the type of specimen. The highest mass decrease experienced by the S material (with high water content), the lowest mass decrease experienced the RC material.

Table 9 Mean mass change due to the heating

	Material RC	Material U	Material S
specimen inside furnace	-3.82%	-6.26%	-15.82%
wall specimen	-3.69%	-5.62%	-13.25%
Cube	-4.14%	-6.24%	-14.58%
Mean	**-3.88%**	**-6.04%**	**-14.55%**

3.2.4.4 Residual compressive strength

Table 10 provides mean residual compressive strength after the exposure to elevated temperature. The lowest relative decrease of material strength experienced the U material (1.8%), the highest relative decrease experienced the S material (22.3%). The decrease of the compressive strength of concrete during exposure to elevated temperature is caused by well-known thermos-hygro-mechanical processes in heated concrete, see e.g. [6] and references therein.

Table 10 Mean residual compressive strength after fire exposure

	Material RC	Material U	Material S
unheated	59.75 MPa	143.39 MPa	26.78 MPa
heated	57.89 MPa	140.81 MPa	20.80 MPa
Δ	**-1.86 MPa**	**-2.58 MPa**	**-5.98 MPa**
	-3.12%	**-1.80%**	**-22.33%**

3.2.4.5 Residual tensile strength

Table 11 provides the mean residual tensile strength after the exposure to elevated temperature. The lowest decrease of the tensile strength was experienced by the U material (3.45%), and the highest decrease experienced the S material (52.27%). The cause of decrease of tensile strength is the same as the one of the compressive strengths.

Table 11 Mean residual tensile strength after elevated temperature exposure

	Material RC	Material U	Material S
unheated	4.04 MPa	8.89 MPa	1.98 MPa
heated	2.60 MPa	8.58 MPa	0.94 MPa
Δ	**-1.44 MPa**	**-0.31 MPa**	**-1.03 MPa**
	-35.65%	**-3.45%**	**-52.27%**

3.2.5 Exposure to near field blast loading

3.2.5.1 Experiment description

The blast experiments were performed at the premises of University of Pardubice, Czech Republic.

The experiments were performed on unheated, one-side heated, and uniformly heated specimens. The summary of the tests can be retrieved from Table 12.

Table 12 Summary of the test samples

	unheated	one-side heated	Uniformly heated	Total
Material RC	3	3	2	8
Material U	3	3	1	7
Material S	3	3	2	8

The blast experiment setup is shown in Figure 22. The test specimen was fastened to a steel supporting structure in order to prevent its movement. The 40 g diameter 37 mm cylindrical Semtex charge was placed at 30 mm distance from the specimen surface. The distance was provided by a paper roll with a thin plastic cap (see Figure 23). This setup was proposed to provide blast loading with energy sufficient for slightly damaging the most blast resistant samples using relatively small amount of explosive. The blast wave focusing induced by the paper tube resulted in more localized loading of the tested concrete samples. The results should not be directly compared to other near field blast experiments where charge is hanged above the tested specimen.

The one-side heated specimens were exposed to blast loading from the heated side in order to imitate blast loading of a concrete wall, ceiling/floor that was already subjected to fire loading. The specimens were weighted before the experiment and after it, in the case when they remained intact. The bottom surface velocity of the specimen right under the charge center was measured during the experiment using Photonic Doppler Velocimetry (further as PDV).

The performed measurements provided specimen soffit/debris velocity, specimen mass, and blast damage assessment.

Two distinct groups of results were obtained from the blast loading experiments for each sample and thermal history. First, a classical post blast observation provided information on the global behavior of the samples. Crater, spall, and breach hole were observed. The amount of material ejected

from both upper and lower surface was determined by simply comparing the weight of the sample before and after the blast.
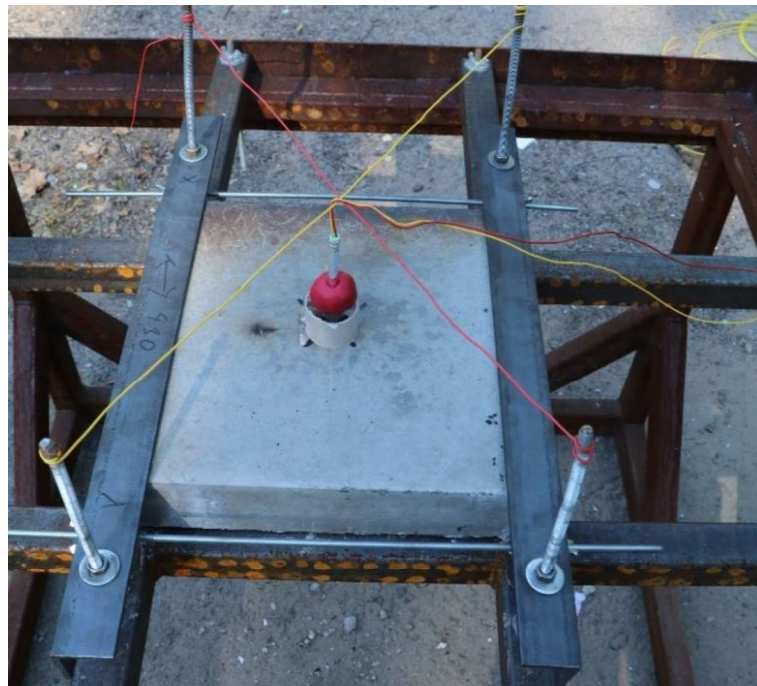

Figure 22 Blast experiment setup

Figure 23 Charge arrangement

On top of the pre- and post- blast sample characterization, measurements capturing the process of the sample response to the near field explosive loading were performed. The motion of the bottom surface of the sample provides wealth of information on the sample failure. Using the same loading scenario for all shots gave a chance to perform a relative comparison of the samples with respect to their type and thermal loading history.

3.2.5.2 Specimen damage

Figure 24 and Figure 25 present both surfaces of specimens after near field blast – material RC. Specimen RC7 (wall specimen) has crater and spall, and all other specimens were breached. Parts of specimens RC6 and RC8 were found deflected towards the charge after the blast.

Unheated specimens	Uniformly heated specimens (furnace floor)	One-side heated specimens (furnace wall)
RC8	RC2	RC5
RC9	RC3	RC6
	Disintegrated during thermal treatment	
RC10	RC4	RC7
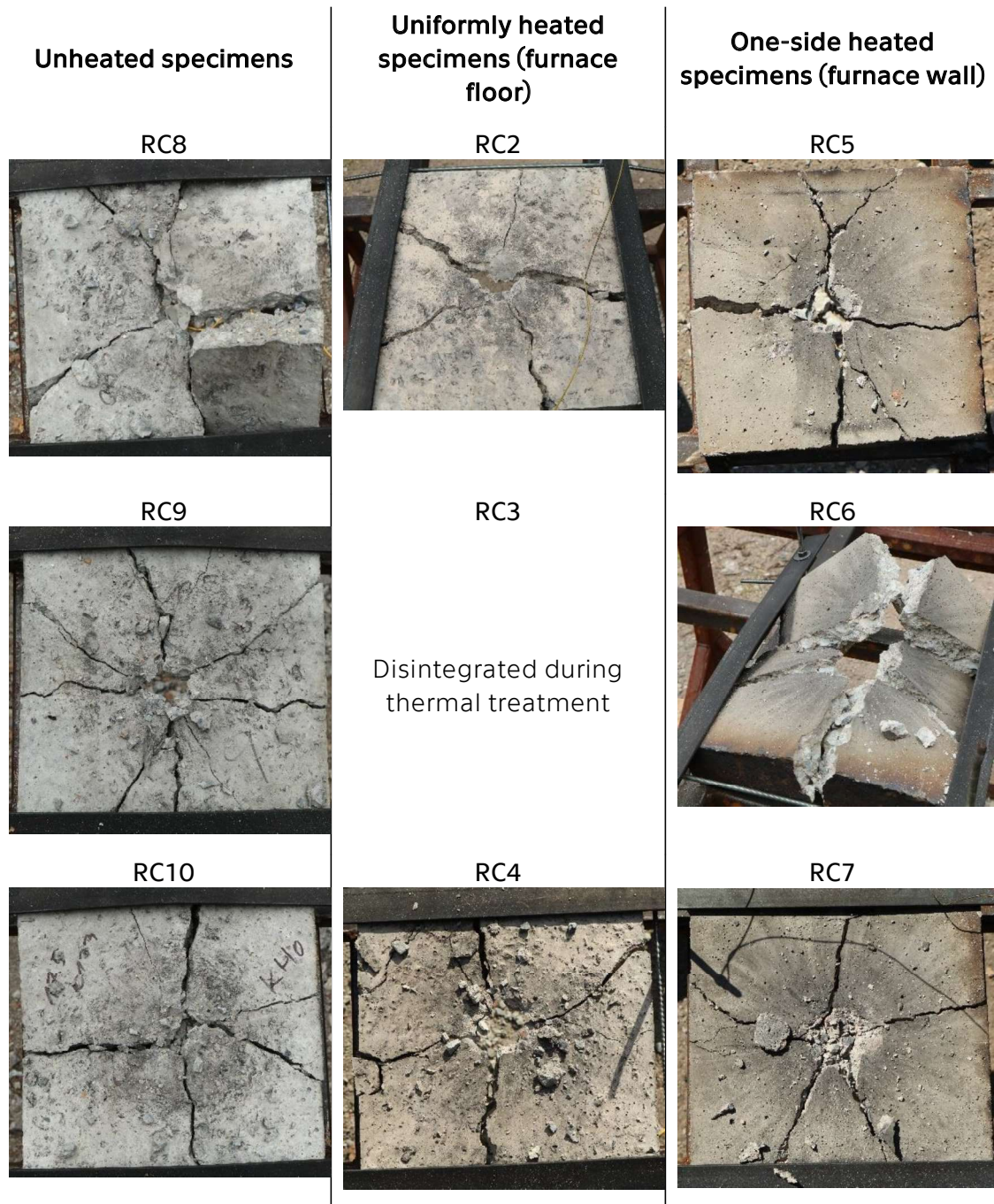
Figure 24 Surface exposed to blast – material RC.

Unheated specimens	Uniformly heated specimens (furnace floor)	One-side heated specimens (furnace wall)
RC8	RC2	RC5
RC9	RC3	RC6
RC10	RC4	RC7

Disintegrated during thermal treatment
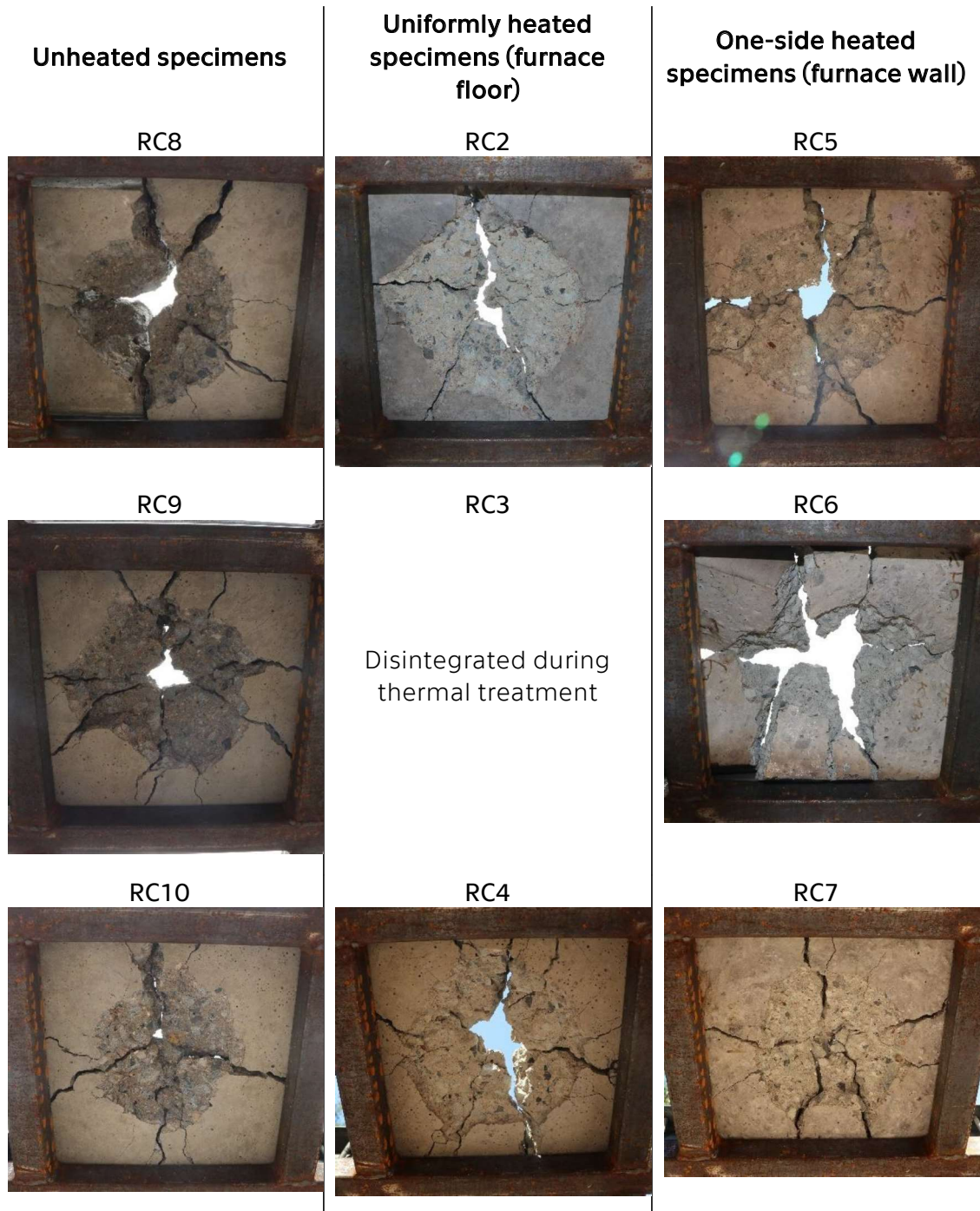
Figure 25 Soffit of the specimen – material RC

Figure 26 and Figure 27 presents both surfaces of specimens after near field blast – material U. None of the specimens were breached. All specimens deflected at the soffit. The focusing effect of the cardboard tube is clearly visible as a light circular area in the center of the specimen.

Unheated specimens	Uniformly heated specimens (furnace floor)	One-side heated specimens (furnace wall)
U2	U4	U5
	Disintegrated during thermal treatment	
U3	U8	U7
U6	U9	U10
	Disintegrated during thermal treatment	
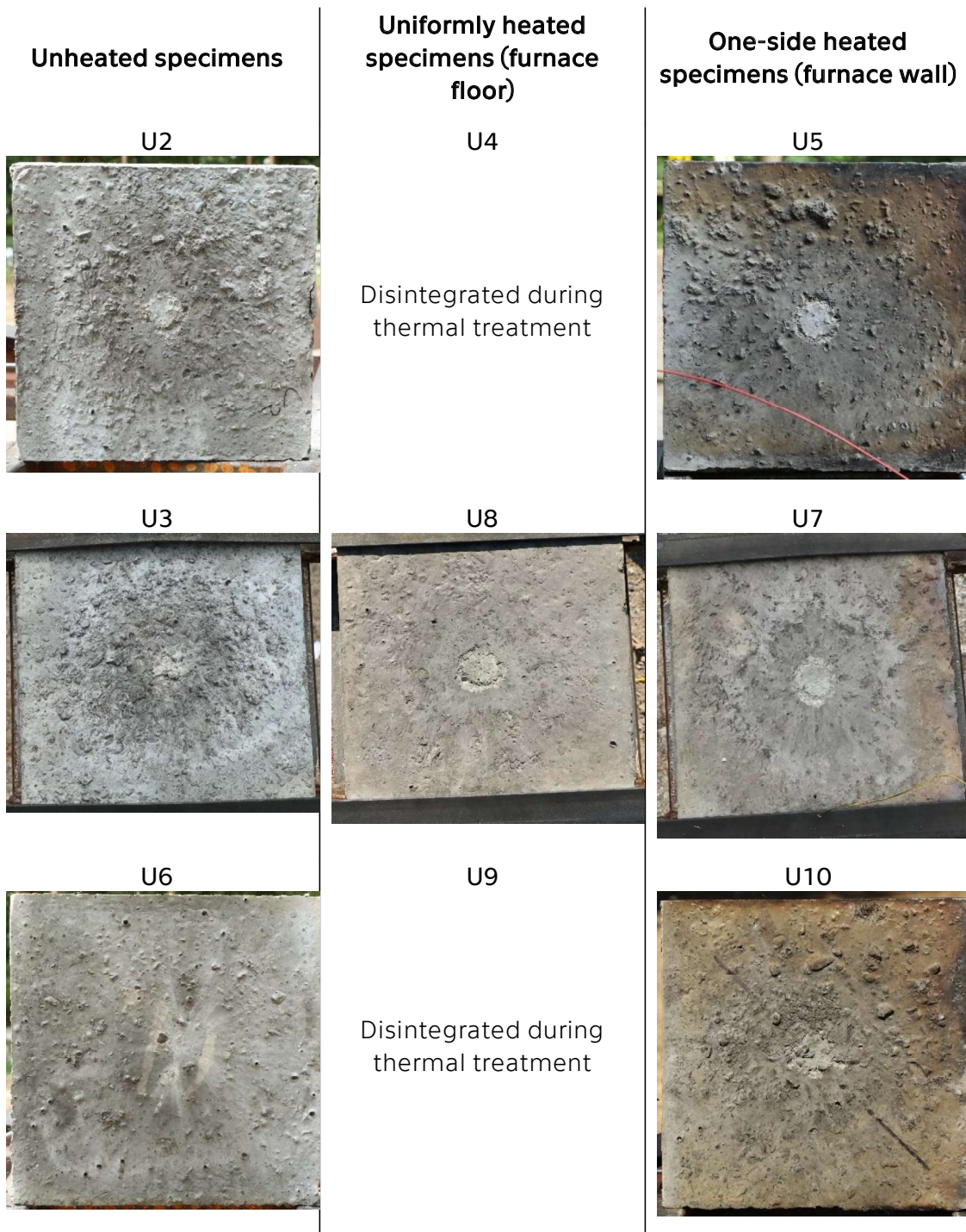
Figure 26 Surface exposed to blast – material U

Unheated specimens	Uniformly heated specimens (furnace floor)	One-side heated specimens (furnace wall)
U2	U4	U5
	Disintegrated during thermal treatment	
U3	U8	U7
U6	U9	U10
	Disintegrated during thermal treatment	
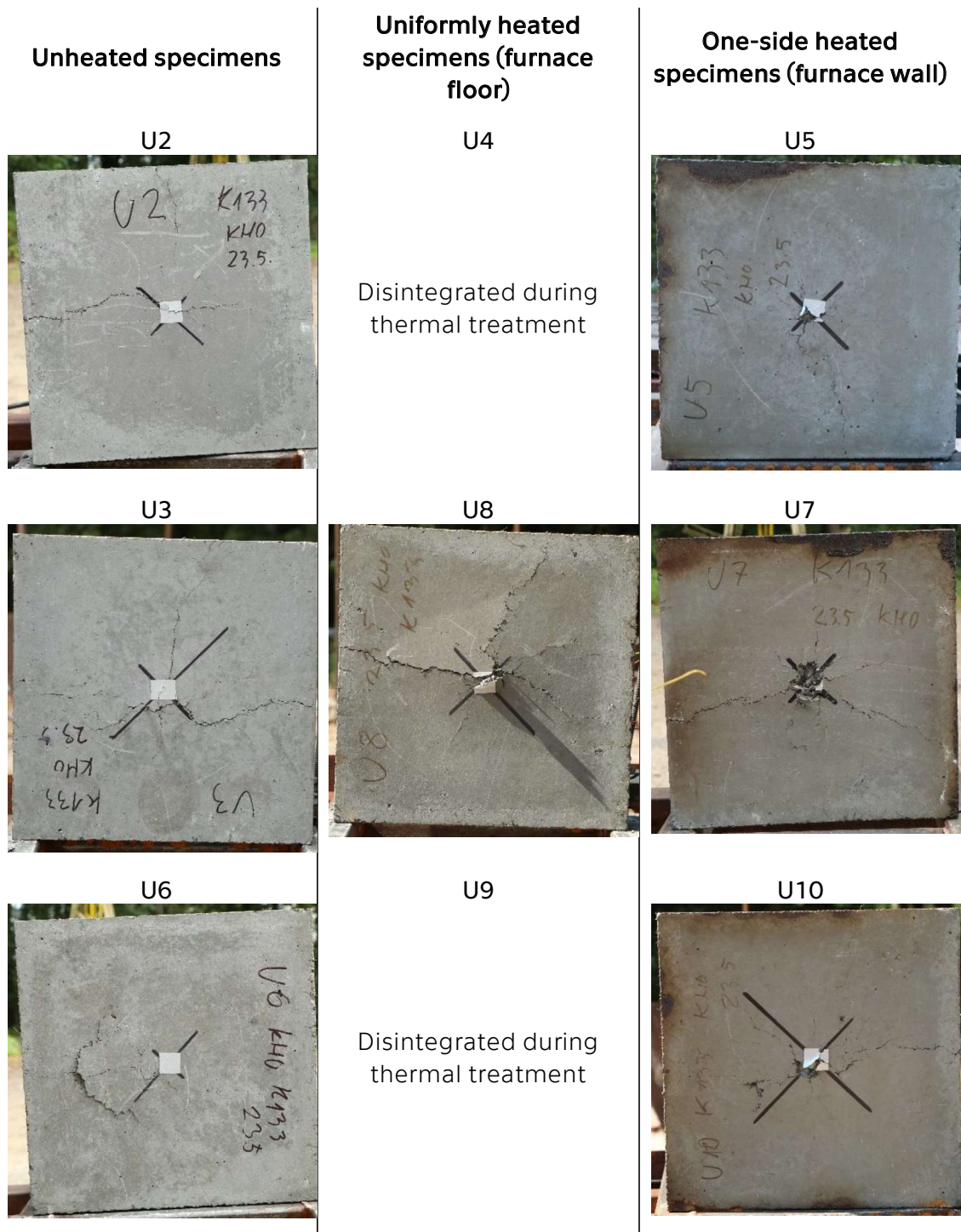
Figure 27 Soffit of the specimen – material U

Figure 28 and Figure 29 present both surfaces of specimens after near field blast – material S. All specimens breached and experienced severe damage. Most of the specimens remained compact only because of their fixation in the metal frame. Due to the level of damage, the specimens were not weighed after the blast.

Unheated specimens	Uniformly heated specimens (furnace floor)	One-side heated specimens (furnace wall)
S8	S2	S5
S9	S3	S6
	Disintegrated during thermal treatment	
S10	S4	S7
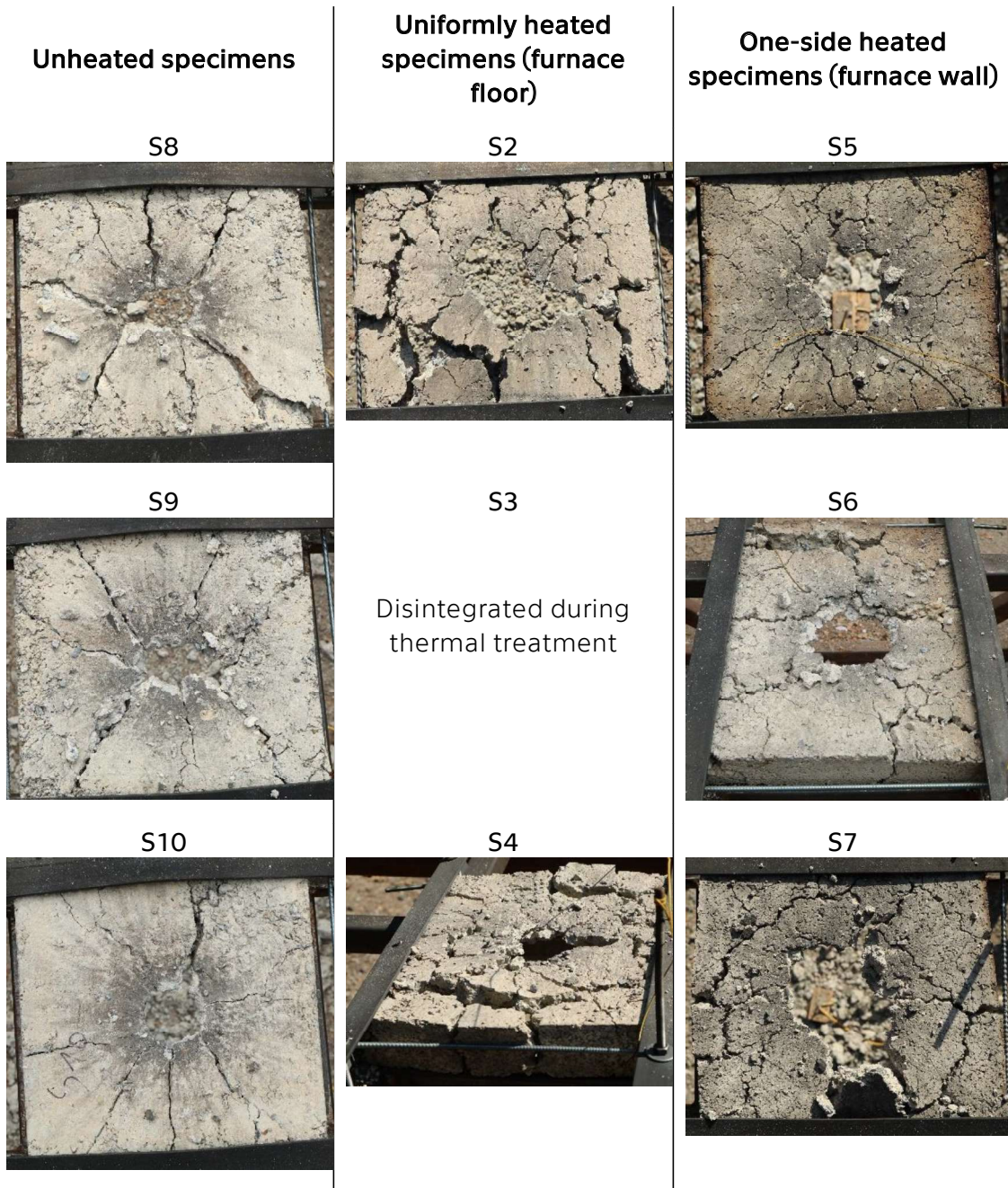
Figure 28 Surface exposed to blast – material S

Unheated specimens	Uniformly heated specimens (furnace floor)	One-side heated specimens (furnace wall)
S8	S2	S5
S9	S3	S6
	Disintegrated during thermal treatment	
S10	S4	S7
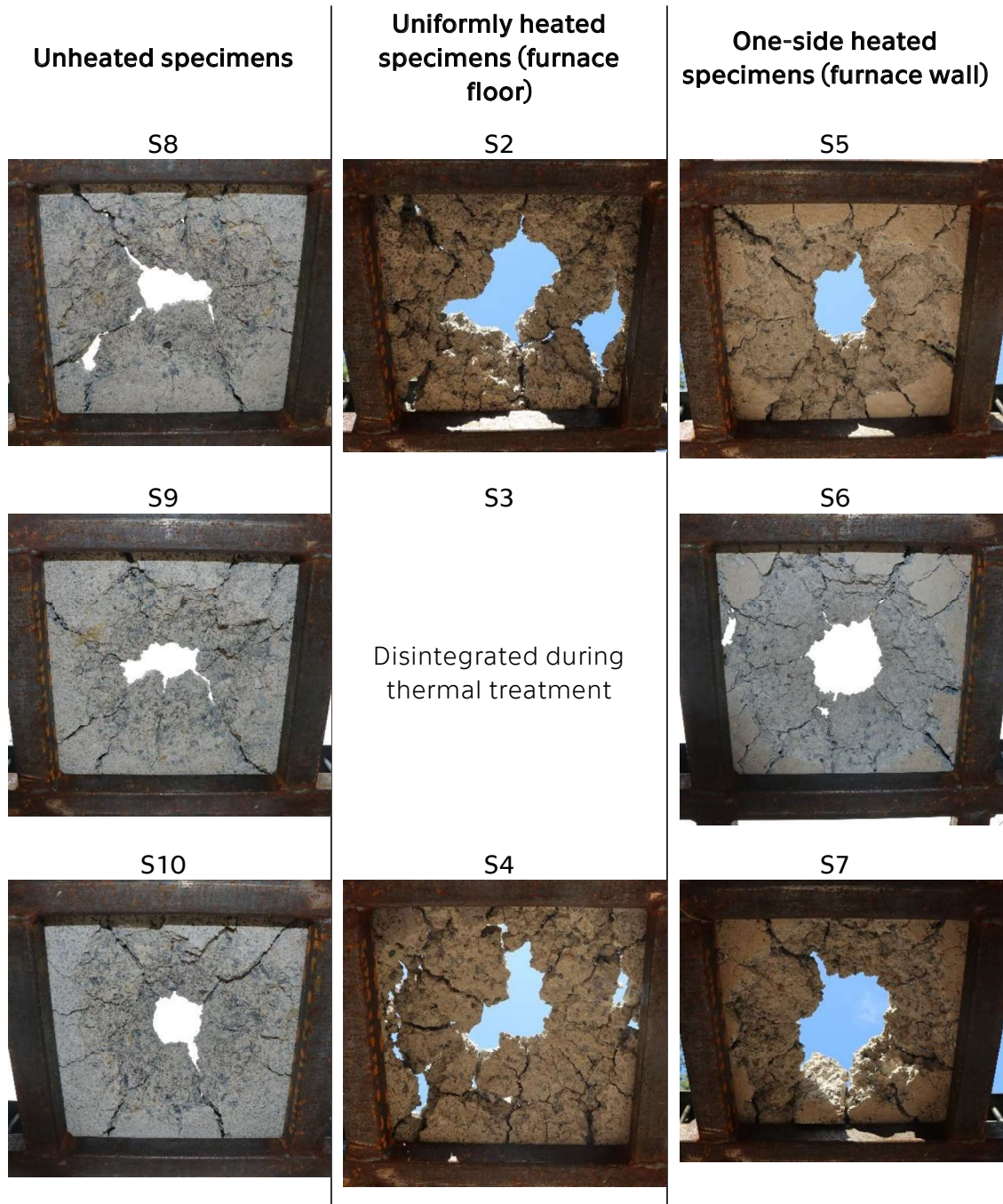
Figure 29 Soffit of specimen – material S

3.2.5.3 Velocity of flying debris

The main output of the PDV measurement is a velocity spectrogram, see a typical PDV velocity spectrogram in Figure 30. The initial velocity jump from zero corresponds to the shock breakout from the sample bottom surface. The following pullback signal and the subsequent ringing is a typical feature of spall layer caused by release of the shock wave at free surface. Depending on the tensile strength of the material, a constant velocity of the scab separated from the bulk of the sample may be observed. For the purpose of this study, the authors have decided to simplify the analysis of the velocity time history to determination of three significant points – maximum, pullback, and terminal velocity. The pullback velocity was used to determine spall strain according to:

$$\sigma_{spall} = \frac{1}{2}\rho_0 C_B \Delta v$$

where σ_{spall} is spall strain [MPa], ρ_0 is bulk density [kg/m³], C_B [m/s] is a sound speed in the material, and Δv [m/s] is a change in velocity from peak to the pullback minimum obtained from spectrogram.

The PDV measurements were performed using a single probe acquiring velocity at a single spot with diameter less than 2 mm. Previous studies have shown that it is not unreasonable to observe large variations in velocity due to large heterogeneity of the concrete samples. The absolute values of the blast induced spall strengths should therefore be used with caution and in this work, there are used only for the purpose of relative comparison of different concrete compositions and effect of the heating.
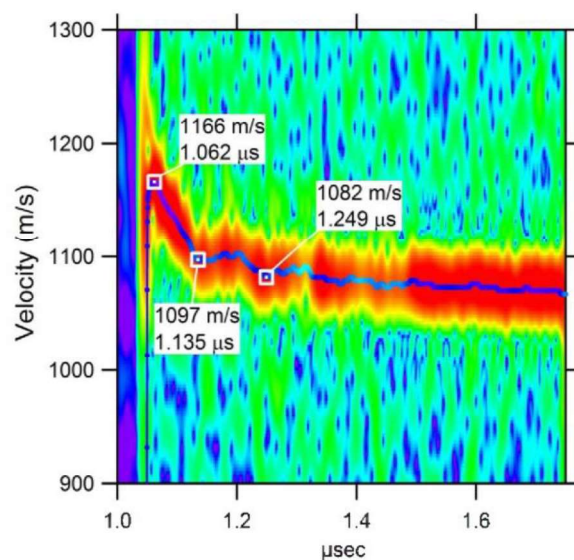
Figure 30 Typical PDV velocity spectrogram
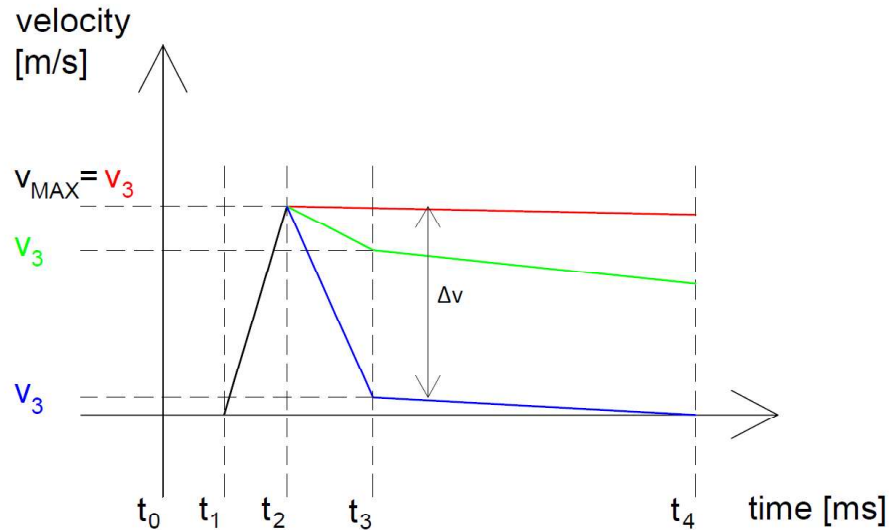
Figure 31 Schematic representation of the simplified velocity history of the bottom surface

3.2.5.3.1 General description of experimental data

During the experiment, the velocity of flying debris of the soffit side was measured using the Photonic Doppler Velocimetry method (further as PDV).

The detonation of any explosive charge induces a time varying shock pulse in the adjacent material. A blast wave profile resulting from interaction of the detonation wave with air should be considered for loading by explosive detonating close, but not in contact with the investigated specimen. The loading pulse can be simplified with a typical triangular shape having instant increase of pressure followed by gradual decay. A shock wave forms at the air-concrete interface and propagates downwards compressing the material. Its reflection from the free surface causes an abrupt velocity jump of the free surface to velocity and formation of tensile wave travelling upwards. The free surface velocity is in first approximation twice the initial particle velocity behind the shock front. The velocity of the bottom surface begins to decay immediately after reaching its maximum. As the rarefaction wave travels back to the compressed specimen, a tensile stress builds up until it exceeds material strength resulting information of a spall plane. Sudden drop of tensile stress to zero results in formation of compression waves travelling back and forth in the spalled layer. In metals, it is manifested by typical reverberations in the velocity time history of the free surface. In concrete, this may not be easily observed due to its inhomogeneity.

The result is a graph of velocity as a function of time, see Figure 31. The graph presents three simplified cases. Time t_0 corresponds to a trigger time

synchronized with the instant of charge detonation. The moment of blast wave impact on the upper surface of the tested specimen and the formation of the shock wave in the material occurs between times t_0 and t_1, and its exact position cannot be determined. At time t_1, the measured surface begins to move as a result of the shock wave reflection from the free surface. Very shortly after that, at time t_2, the measured surface acquires its maximum velocity corresponding to the release from the maximum compressive stress obtained in the sample close to the free surface. The velocity of the bottom surface following the maximum depends on the dynamic tensile strength of the material. Low strength materials rupture practically immediately and fly through the air towards the sensor with more or less constant velocity. This is schematically presented in Figure 31 by the red line. For materials with intermediate tensile strength, the bottom surface velocity record shows drop in the velocity, so called pull-back signal, before reloading or acquiring an almost constant terminal velocity at time t_3. This can be interpreted as deceleration of the free surface due to tensile capacity of the material followed by rupture and constant velocity plateau at t_4. The decrease of the velocity from its peak value to the plateau value corresponds to the energy required for tensile fracture, see the green line. If the pull-back signal goes down all the way to velocity equal to zero, the material does not separate from the bottom surface and stops, see the blue line. This does not mean that it does not spall, just that the spall does not separate from the specimen. The process is schematically illustrated in Figure 32.

The slope of the rising edge corresponds to the attenuation of the shock pulse and is steeper in more homogeneous higher density materials.
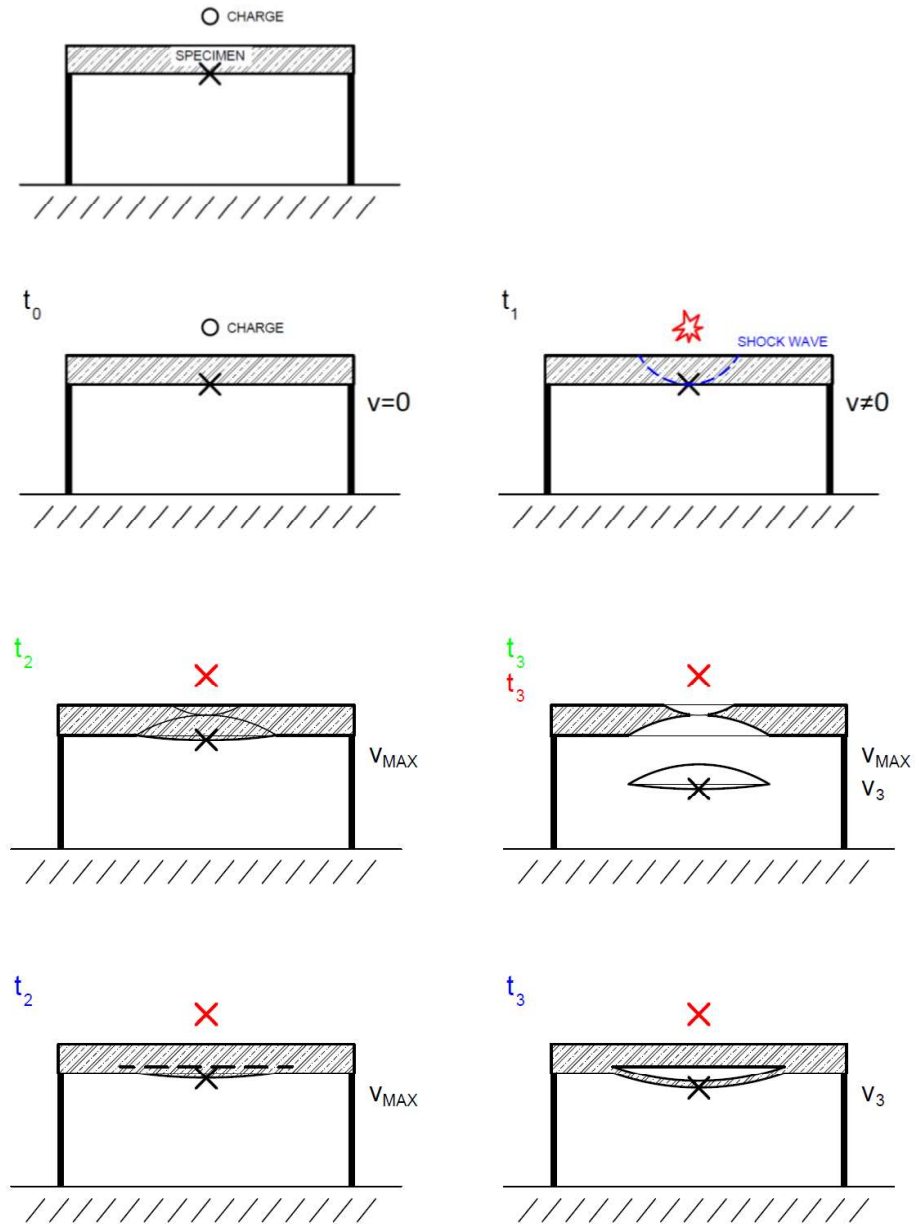
Figure 32 Scheme of the experiment illustrating PDV measurement results

3.2.5.3.2 Velocity spectrograms of all specimens

The following graphs shown in Figure 33 - Figure 35 present all measurement data. These data are compared and evaluated in the following chapters.
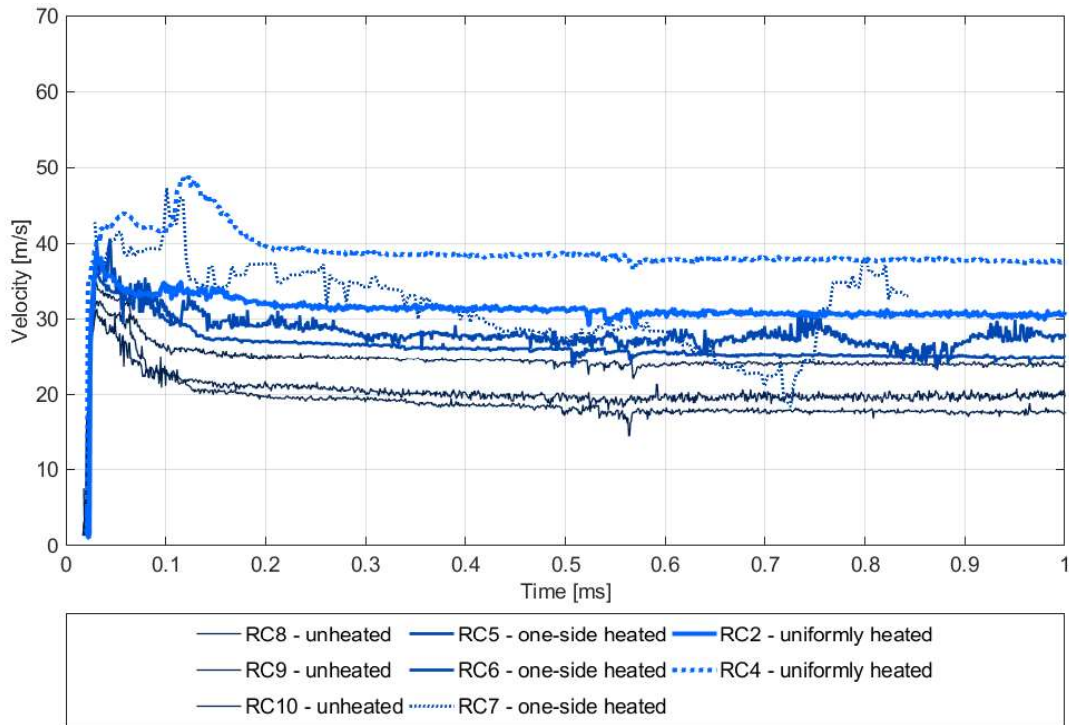
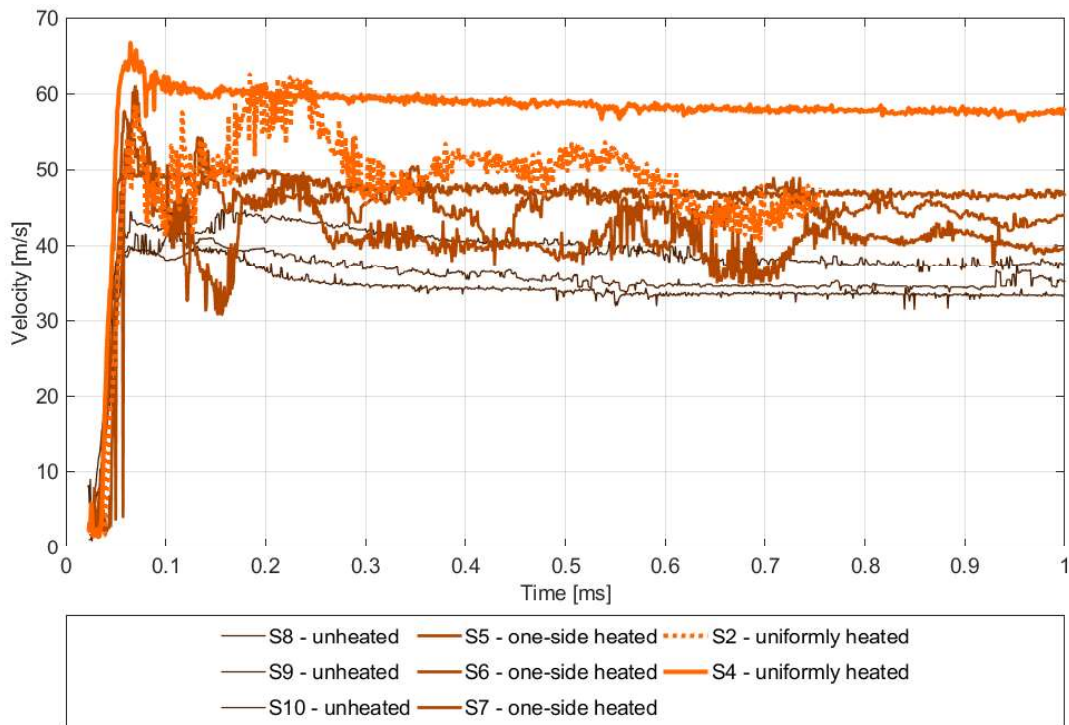**Figure 33 Measurement results for all specimens – material RC**

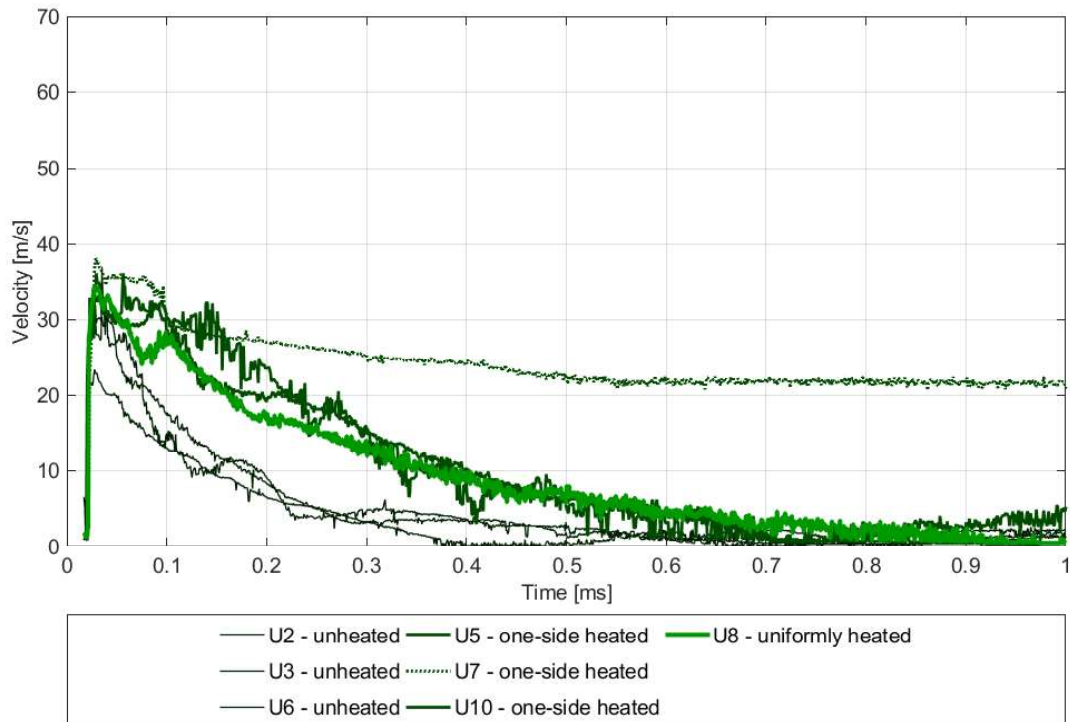**Figure 34 Measurement results for all specimens – material S**

Figure 35 Measurement results for all specimens – material U

3.2.5.3.3 Result interpretation

Because of the complexity of the obtained data (velocity-time dependence graphs), the following method for processing and interpretation was developed.

The values as presented in Figure 33- Figure 35 are idealized with respect to the methodology described in Figure 31 and Figure 32. The values at time t_1 and t_2 are emphasized. The course between points t_2 and t_3 is no longer subjected to investigation. Therefore, the course changes are neglected, the rapid deceleration after reaching the maximum velocity is not taken into account, etc.
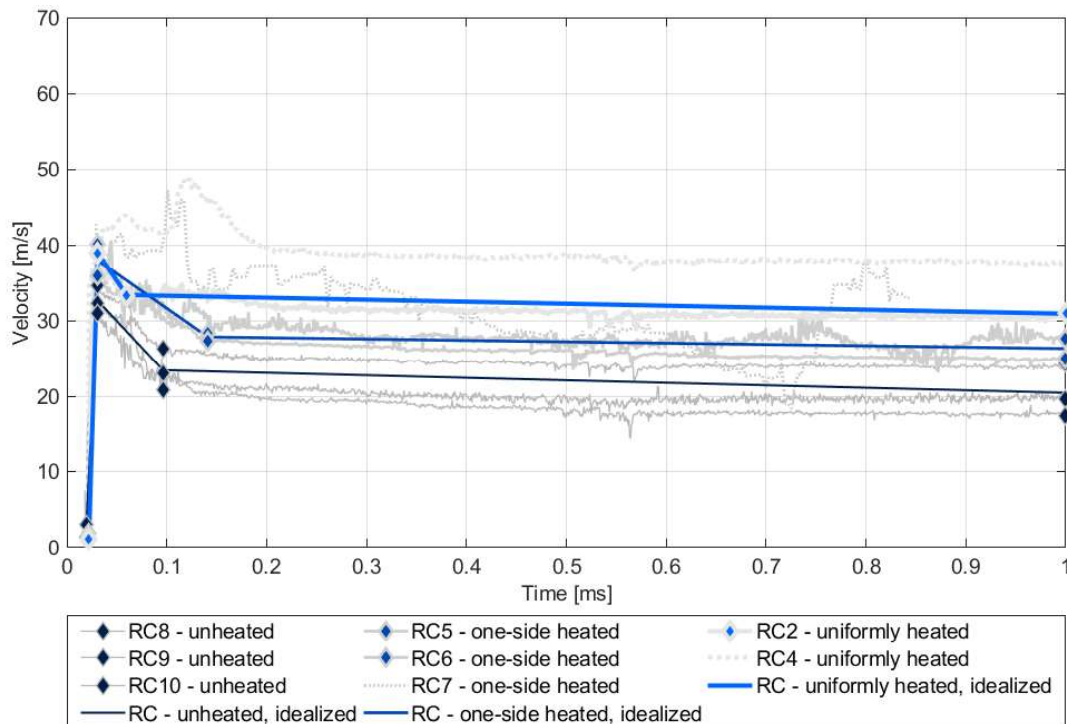
Figure 36 Final graph with idealized trends depending on heated method - material RC

The lines in Figure 36 present idealized trends and the suppressed dotted lines present the real velocity measurements for each specimen. The dotted lines can reproduce the deviation of real values from the idealized value.

The simplified and idealized course can provide all the data needed for the evaluation of the corresponding velocities and times.

3.2.5.4 Experimental findings

3.2.5.4.1 Comparison based on the used material

This chapter presents the idealized curves of the obtained data for each material. The velocity time trends are compared with each other at different phases of heating.

Figure 36 presents results for material RC for the different heat exposure. The measurement of the RC7 specimen (one-side heated) was not considered in the mean values and comparison because of obvious collimator failure which corrupted the results.

The presented results clearly show that the highest debris velocity was achieved at uniformly heated specimens. In opposite, the lowest soffit/debris velocity was achieved at unheated specimens. The maximum achieved velocity is presented in Table 13 together with the occurrence time.

The time difference between the start and end of the steep part of the curve and the slope of this curve is of special importance when evaluating the material properties.

Table 13 Maximum soffit speed - material RC

	time t_1 [ms]	time t_2 [ms]	time t_3 [ms]	velocity v_{max} [m/s]	Velocity v_3 [m/s]	Δv [m/s]
Material RC						
Unheated	0.019	0.031	0.096	32.63	23.40	9.23
One-side heated	0.022	0.031	0.141	38.00	27.82	10.18
Uniformly heated	0.022	0.031	0.060	38.94	33.38	5.56

The steepest (i.e. fastest) velocity increase was measured at one-side heated specimen. The slowest velocity increase was measured for unheated specimens. The t_1 times for all heating types remained almost the same.
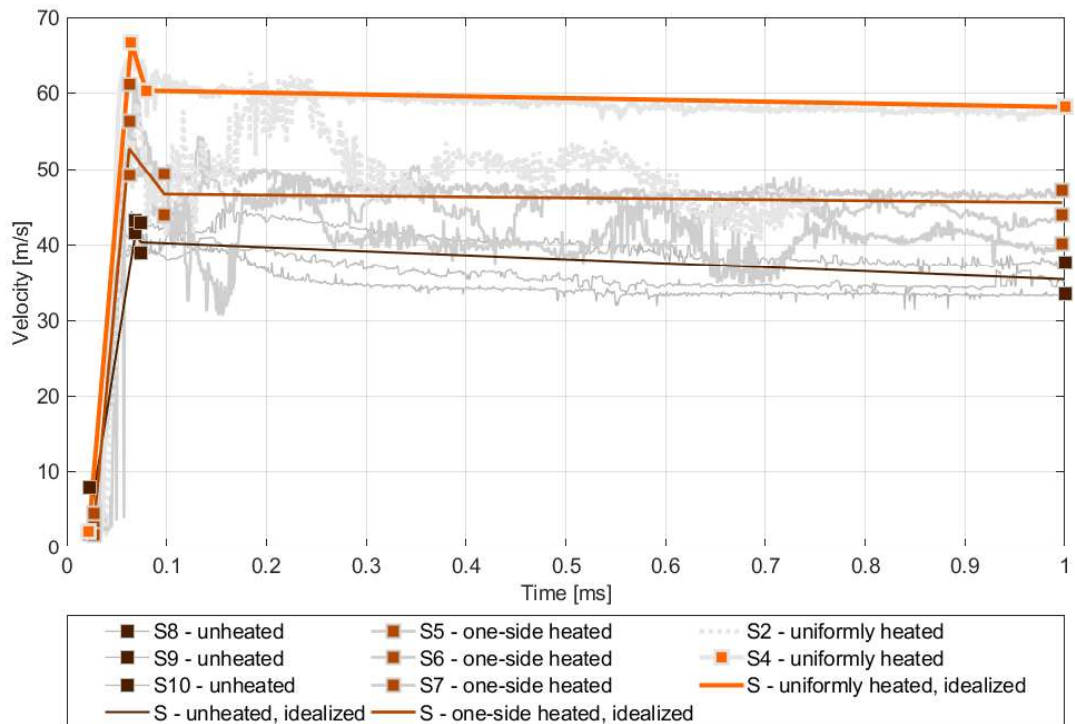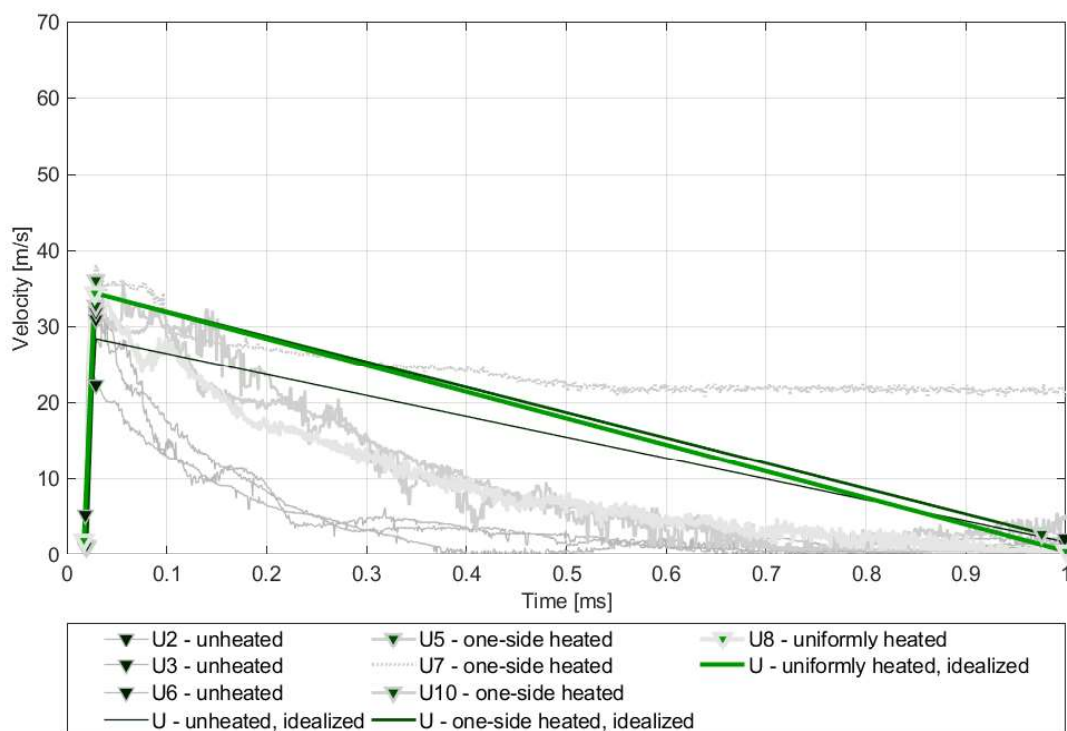

Figure 37 Soffit velocity, S material

Figure 37 presents results of material S for the different heat exposure. The measurement made of the S2 specimen (Uniformly heated) was not considered in the mean values and comparison because of obvious collimator failure which corrupted the results.

The presented results clearly show that the highest debris velocity was achieved at uniformly heated specimens. In opposite, the lowest debris velocity was achieved at unheated specimens. The maximum achieved

velocity is presented in Table 14 together with the occurrence time. The time difference between the start and end of the steep part of the curve and the slope of this curve is of special importance when evaluating the material properties.

Table 14 Maximum soffit speed - material S

	Material S					
	time t_1 [ms]	time t_2 [ms]	time t_3 [ms]	velocity v_{max} [m/s]	Velocity v_3 [m/s]	Δv [m/s]
Unheated	0.023	0.069	0.074	41.39	40.29	1.10
One-side heated	0.030	0.065	0.098	55.48	46.64	8.84
Uniformly heated	0.022	0.065	0.079	66.76	60.25	6.51

The steepest (i.e. fastest) velocity increase was measured at one-side heated specimen. The slowest velocity increase was measured at unheated specimens. The difference in the curve slope for both heating types is negligible. The t_1 times for all heating types remained almost the same, with only minimal differences.

Figure 38 Soffit velocity, U material

Figure 38 presents results for material U with different heat exposure. The measurement of the U7 specimen (one-side heated) was not considered in the mean values and comparison because the reflective foil loosened itself from the specimen without damage of the specimen.

The presented results show clearly that the highest debris velocity was achieved at uniformly heated specimens. In opposite, the lowest debris velocity was achieved at unheated specimens. At specimens without breach/spall, the velocity value decreased again to 0 m/s, the soffit moved in the direction of the blast loading and then returned in the original position without being damaged. The maximum achieved velocity is presented in Table 15 together with the time when it occurred. The time difference between the start and end of the steep part of the curve and the slope of this curve is of special importance when evaluating the material properties.

Table 15   Maximum soffit speed - material U

	Material U					
	time t_1 [ms]	time t_2 [ms]	time t_3 [ms]	velocity v_{max} [m/s]	Velocity v_3 [m/s]	Δv [m/s]
Unheated	0.019	0.029	1.000	28.33	0	28.33
One-side heated	0.020	0.029	1.000	34.33	0	34.33
Uniformly heated	0.017	0.028	1.000	34.33	0	34.33

The steepest (i.e. fastest) velocity increase was measured for one-side heated specimen. The slowest velocity increase was measured for unheated specimens. The t_1 times for all heating types remained almost the same, with only minimal differences.

3.2.5.4.2 Comparison according to heating type

The compared parameters are the same as in the previous chapter: maximum velocity, the times t_1 and t_2 and the slope of the idealized curve. However, what the arrangement varies and allows the comparison of the different materials at the same temperature.

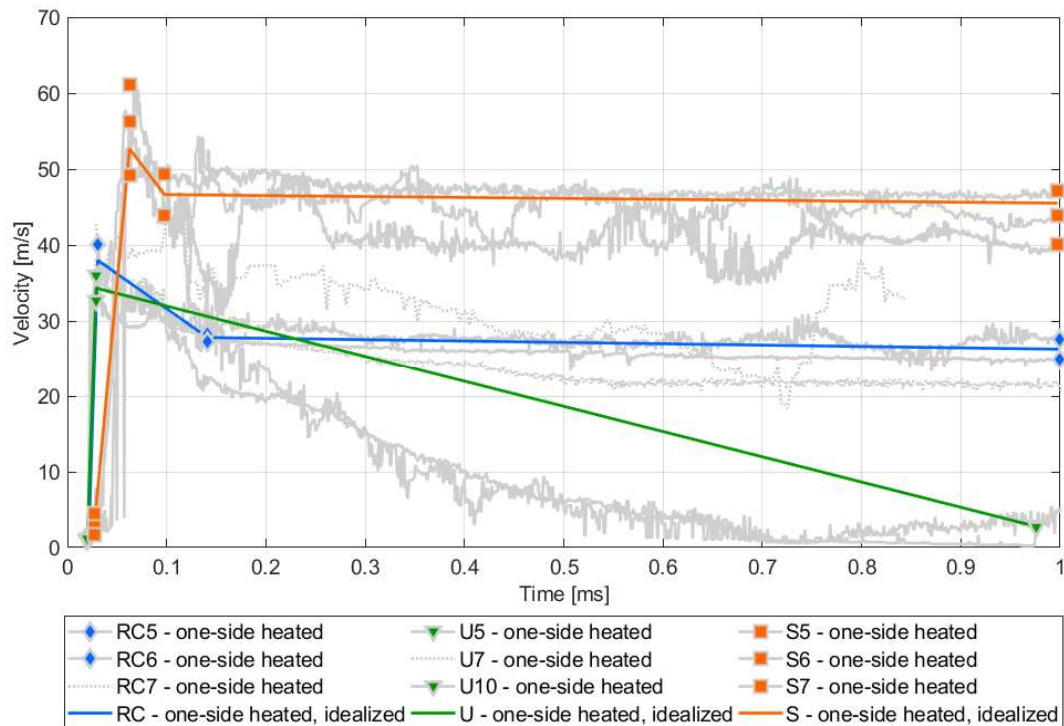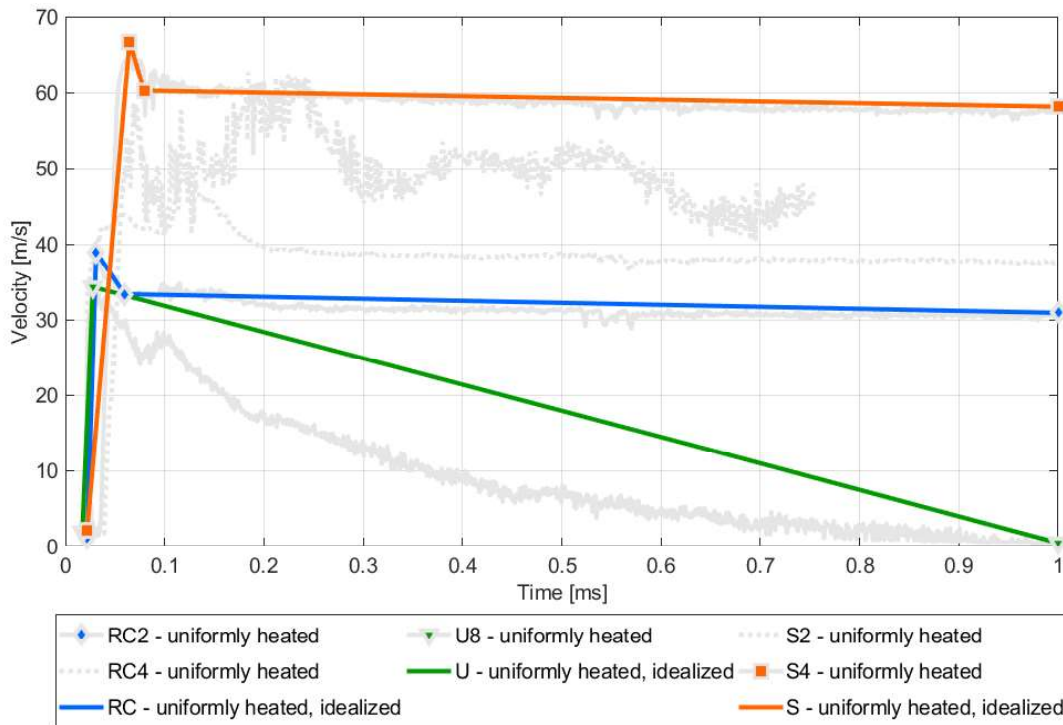Figure 39 presents results for all tested materials on unheated specimens.
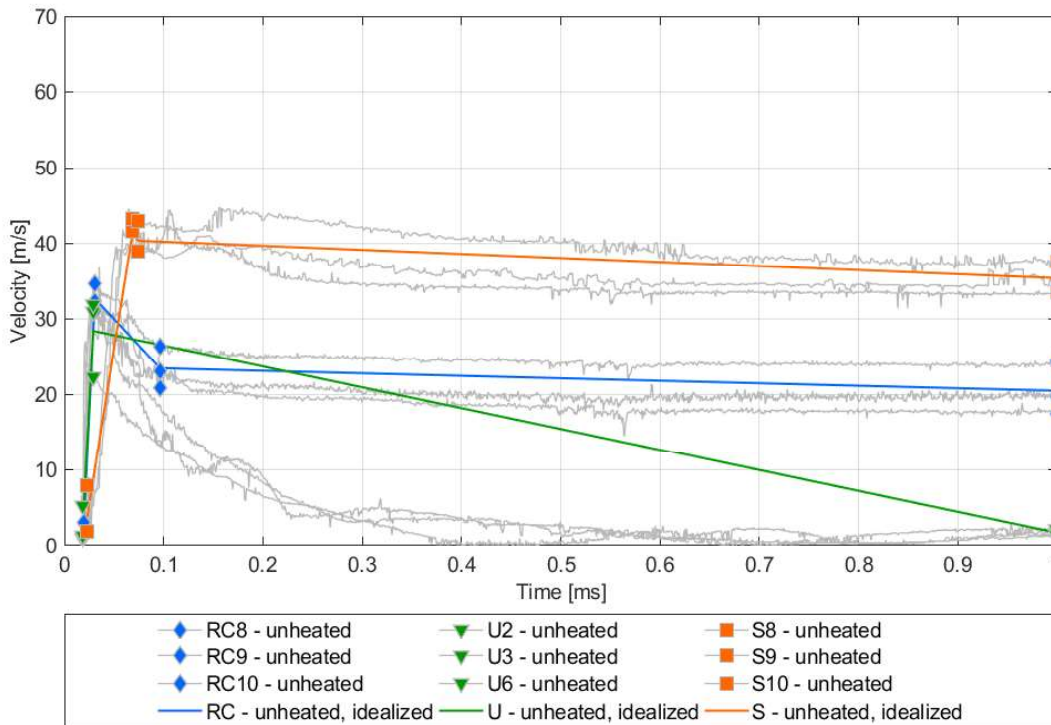
Figure 39 Soffit velocity – unheated specimens

The highest soffit speed was measured for the S material. The lowest soffit speed was measured for U material.

The maximum mean values for all materials are summarized in Table 16. The time difference between the start and end of the steep part of the curve and the slope of this curve is of special importance when evaluating the material properties.

Table 16 Maximum soffit velocities unheated specimens

	Unheated					
	time t_1 [ms]	time t_2 [ms]	time t_3 [ms]	velocity v_{max} [m/s]	Velocity v_3 [m/s]	Δv [m/s]
RC	0.019	0.031	0.096	32.63	23.40	9.23
U	0.019	0.029	1.000	28.33	0	28.33
S	0.023	0.069	0.074	41.39	40.29	1.10

The steepest (i.e. fastest) velocity increase was measured for the U material. The slowest velocity increase was measured for the S material. The difference between RC and U is negligible. There is a difference in time t_1 between material U and S specimens. The lower time t_1 of material U indicates a faster propagation of the shock wave through the specimen compared to S material.

Figure 40 presents results for all tested materials on one-side heated specimens.

Figure 40 Soffit velocity - one-side heated specimens

The highest soffit speed was measured for the S material. The lowest soffit speed was measured for U material.

The maximum mean values for all materials are summarized in Table 17. The time difference between the start and end of the steep part of the curve and the slope of this curve is of special importance when evaluating the material properties.

Table 17   Maximum soffit velocities one-side heated specimens

	One-side heated					
	time t_1 [ms]	time t_2 [ms]	time t_3 [ms]	velocity v_{max} [m/s]	Velocity v_3 [m/s]	Δv [m/s]
RC	0.022	0.031	0.141	38.00	27.81	10.19
U	0.020	0.029	1.000	34.33	0.00	34.33
S	0.030	0.065	0.098	55.48	46.64	8.84

The steepest (i.e. fastest) velocity increase was measured for the RC material. The slowest velocity increase was measured for the S material. The difference between RC and U is negligible There is a difference in time t_1 between material U and S specimens. The lower time t_1 of material U indicates a faster

propagation of the shock wave through the specimen compared to S material.

Figure 41 presents all results for all tested materials on uniformly heated specimens.

Figure 41 Soffit velocity – uniformly heated specimens

The highest soffit speed was measured for the S material. The lowest soffit speed was measured for U material.

The maximum mean values for all materials are summarized in Table 18. The time difference between the start and end of the steep part of the curve and the slope of this curve is of special importance when evaluating the material properties.

Table 18 Maximum soffit velocities uniformly heated specimens

	time t_1 [ms]	time t_2 [ms]	time t_3 [ms]	velocity v_{max} [m/s]	Velocity v_3 [m/s]	Δv [m/s]
RC	0.022	0.031	0.060	38.94	33.38	5.56
U	0.017	0.028	1.000	34.33	0.00	34.33
S	0.022	0.065	0.079	66.76	60.25	6.51

The steepest (i.e. fastest) velocity increase was measured for the U material. The slowest velocity increase was measured for the S material. The difference between RC and U is negligible. There is a difference in time t_1

between material U and S specimens. The lower time t_1 of material U indicates a faster propagation of the shock wave through the specimen compared to material S.

3.2.5.4.3 Spall strength

Based on the measured velocities of a flying debris, the approximate spall strength was calculated by following equations:

$$\sigma_{spall} = \frac{1}{2} \rho_0 C_B \Delta v \tag{1}$$

where σ_{spall} is spall strain [MPa], ρ_0 is bulk density [kg/m³], C_B [m/s] is a sound speed and Δv [m/s] is a change in velocity from peak to the pullback minimum obtained from spectrogram.

Bulk density ρ_0 used in the calculation was determined as part of the experiment. Sound speed C_B used was determined in previous experiments by the authors of this paper. For simplicity, a constant value of the sound speed was assumed regardless of the elevated temperature.

Results of spall strengths are shown in Table 19.

Table 19 Spall strength results

		ρ_0 [kg/m³]	C_B [m/s]	Δv [m/s]	σ_{spall} [MPa]
	Unheated	2 449	4 700	9.2	**52.9**
RC	One-side heated	2 441	4 700	5.6	**32.1**
	Uniformly heated	2 402	4 700	10.2	**57.6**
	Unheated	2 659	5 000	28.3	**188.1**
U	One-side heated	2 478	5 000	34.3	**212.5**
	Uniformly heated	2 560	5 000	34.3	**219.5**
	Unheated	1 705	4 000	1.1	**3.8**
S	One-side heated	1 536	4 000	6.5	**20.0**
	Uniformly heated	1 601	4 000	9.8	**31.4**

This calculation is usually used to calculate the spall strength of homogeneous materials. In this case, it was used to calculate the spall strength of heterogeneous materials (material S is highly heterogeneous). Due to this, the results are very inconsistent and should be regarded as merely indicative.

3.3 Summary and discussion

The presented experimental program was focused on investigation of the difference in blast performance of the unheated, one-side heated, and

uniformly heated specimens for three different types of cementitious composites. The general summary of all results is presented in Table 20. The table is divided into two parts: (i) the results after exposure to elevated temperature and (ii) the blast experiment results.

Ordinary concrete (material RC) experienced the fastest temperature increase. Light-weight hybrid concrete with mineral insulation shreds (material S) experienced the slowest temperature increase. The same material experienced the highest water evaporation and the corresponding highest weight loss. On the contrary, the material RC experienced the lowest water and weight loss. Prediction that the material with the lowest porosity, material U, experiences the least water evaporation during heating proved itself to be false. However, most probably the low porosity of the material and high pore pressures generated during heating of the material probably caused the destruction of one of the specimens placed in the heating furnace. Material U experienced the lowest relative decrease of compressive and tensile strengths, while material S showed the highest relative decrease. The materials U and S experienced approximately twice the decrease in tensile strength compared to compressive strength. Material RC experienced a tenfold decrease in tensile strength compared to its compressive strength. Considering the heating temperatures and the temperatures measured in the specimens, this is principally the effect of evaporation of water from the material.

Table 20 Summary of the results

Type of heating	Material	(i) Elevated temperature				(ii) Blast				
		(1) temperature rise rate	(2) Weight loss	(3) Loss of compressive strength *	(4) Loss of tensile strength **	(5) Damage	(6) Max velocity [m/s]	(7) Speed ratio	(8) Δv	(9) Spall strength [MPa]
Uniformly heated	RC	1	-3.82%	-3.12%	-35.65%	2	38.94	19.35%	10.2	57.6
	U	2	-6.26%	-1.80%	-3.45%	3	34.33	18.85%	34.33	219.5
	S	3	-15.82%	-22.33%	-52.27%	1	66.76	60.83%	9.8	31.4
One-side heated	RC	1	-3.69%	✕	✕	2	38.00	16.45%	5.9	32.1
	U	2	-5.62%	✕	✕	3	34.33	18.85%	34.33	212.5
	S	3	-13.25%	✕	✕	1	55.48	33.65%	6.5	20.0
Unheated	RC	✕	✕	✕	✕	2	32.63	✕	9.2	52.9
	U					3	28.88		28.88	188.1
	S					1	41.51		1.1	3.8

1 – the fastest temperature increase/the biggest damage,3 – the slowest temperature increase/the least damage

* measured by cube specimens, ** measured by beam specimens

The second part (ii) of the table presents the blast experiment results. The material U proved itself to be the most blast resistant (the specimens were intact, with minor damage), while the blast performance of the material S was the worst (the specimens were incoherent after removal from the testing device).

The highest velocity increment during the blast loading was recorded at the S material, the finding corresponds to the earlier presented change of material properties. The low tensile strength of the S material clearly defines the larger blast damage and therefore high velocity speeds of the debris. In opposite, the material U experienced the lowest velocities and lowest tensile/compressive strength decrease. The slabs were not breached and behaved in elastic manner. Column 7 in Table 20 provides percentual change of the velocities between the unheated specimen and the heated specimen.

Column 8 presents a difference is a change in velocity from peak to the pullback minimum obtained from spectrogram, i.e. the difference in the velocity in time t_2 a t_3 used in the spall strength assessment.

Column 9 presents spall strength for the studied material and heat treatment. As stated previously, the formula is usually used to calculate the spall strength of homogeneous materials, in this case, it was used to calculate the spall strength of heterogeneous materials Due to this, the results are very inconsistent and should be regarded as merely indicative.

Assuming the only slope defining parameter is the bulk density, the lowest difference in the slopes of the curves and the lowest value of Δt_1 should experience the material RC (lowest bulk density decrease caused by heating). This assumption did not prove itself to be valid, the lowest slope was measured at material U at the one-side heating as described above. When uniformly heated, this assumption was achieved. This demonstrates that other properties (whether material homogeneity or other mechanical properties) also define the resistance of a material. Therefore, besides bulk density change, the tensile strength plays a role by defining whether the specimen resists the loading, breaches or spalls. The RC material specimens were breached, the U material specimens were not damaged and resisted the loading for a longer time. According to the results above, the material U has a several times higher tensile strength. Therefore, the material with the highest slope change is the S material from which the highest amount of water evaporated. Therefore, the bulk density decrease, and permeability increase is notable. These two material properties cause longer time of blast overpressure propagation through the specimen.

Table 21 shows a comparison of the maximum sofit velocities depending on the type of exposed elevated temperature and the material used. The table shows an increase in maximum soffit velocity for one-sided heated by 16.45% - 27.26%. The smallest increase was observed for specimen material RC, while the highest increase was observed for specimen material S. For uniformly heated specimens, the increase of soffit velocity is 19.35% - 61.3%. The above reasons indicate the trend of the behavior of the element subjected to the combined effect of loading. However, this trend has to be defined for each type of element.

Elements with normal tensile strength (material RC) after subjected to elevated temperature from one side and subsequent blast show a 16.45% increase in soffit velocity and in the case of uniformly heated and subsequent blast, their soffit velocity increases by another 2.49%.

Specimens with very low tensile strength (material S) after one-side heated and subsequent blast show a 27.26% increase in soffit velocity. In the case of uniformly heated and subsequent blast, their soffit velocity then increases by another 26.74% (its overall velocity is several times higher compared to the unheated specimen). The material loses a significant amount of tensile strength which is almost equal to 0 MPa during exposure to the applied temperature.

On the other hand, elements with very high tensile strength (material U) after one side heated and subsequent blast show 21.17% increase in soffit velocity. In the uniformly heated case, the soffit velocity does not change significantly. The loss of tensile strength is the lowest in this case.

Table 21 Maximum velocity depending on elevated temperature and used material of the specimens

		RC	S	U
Unheated	Velocity [m/s]	32.63	41.39	28.33
One-side heated	Velocity [m/s]	38.00	52.68	34.33
	Increase compared to unheated	16.45%	27.26%	21.17%
Uniformly heated	Velocity [m/s]	38.94	66.76	34.33
	Increase compared to unheated	19.35%	61.30%	21.17%
	Increase compared to unheated one-side heated	2.49%	26.74%	0%

Further parameters that influence the velocity of overpressure wave propagation through the material is the material attenuation and its

heterogeneity. Nevertheless, these parameters were not studied in this experiment.

4 Numerical simulation – FE model

For the purpose of this thesis, the following chapter 4 reproduced some relevant parts of the paper by Hájek et. al. [86] (reference paper), which the authors jointly prepared. This paper is annex 3 of this thesis.

The quantification of the effect of elevated-temperature exposure on the subsequent blast resistance presented in the previous chapters is based directly on the measured results, i.e. it is performed by comparing the results measured during the blast experiments (soffit velocity) on the specimens made of different materials and subjected to different types of heating (non-exposed specimens, specimens exposed to elevated temperatures from one side, specimens exposed from all sides).

In order to analyze the problem in more detail, a numerical model was developed. The model was enabled to generalize the findings obtained during the experimental program as it was being used also for the heating regimes different from the elevated temperature exposure applied during the presented fire experiments (target temperature in the furnace of 400 °C).

The experimentally obtained results measured on the specimens exposed to the target temperature of 400 °C were be employed for verification of the model.

4.1 State of the art - concrete-based composites and computer modelling of their blast response

Although the most accurate results are always obtained from experiments (if possible, performed at full scale), many authors use computer modelling to supplement their experimental results and to identify and quantify various physical phenomena that cannot be measured directly during the experiment.

The authors' use of finite element (FE) modelling to study the formation and the behavior of the air shock waves caused by an explosion is presented in Hájek and Foglar [70] and Hájek et al [71]. In both papers, the LS-DYNA commercial hydrocode [87], [88] was used for numerical modelling. The software is based on the finite element method (FEM), either in implicit form or in explicit form. This allows the creation of finite element meshes of elements defined by various mathematical formulations, and their combinations, to create mathematical models for various types of materials and loadings.

The resistance of structures subjected to impact or blast loads is very difficult to determine empirically, so an experiment on a prototype is usually used. A numerical simulation can substitute for many experiments to reduce the costs. Kong et al. [89] studied the resistance of non-composite steel-concrete-steel sandwich panels to high-speed impact. FE modelling in LS-DYNA was included. The FE model was validated against experimental results. Their numerical models were able to predict the initial flexural response of the specimen, followed by the resistance of the tensile membrane at large deformation. However, the authors have pointed out the difficulties of accurate numerical modelling. The strain rate effects of the materials and the choice of the concrete material model has a significant effect on the numerically predicted response.

Hao and Hao [90] conducted a study on the dynamic increase factor (DIF) for concrete. Several empirical DIF relations have been proposed for modelling the concrete material strength increment at high strain rates. A numerical study was conducted using various DIF values, and the results were compared.

Tai et al. [91] studied the dynamic response of a reinforced concrete slab loaded by an air blast. The LS-DYNA numerical model was used in a parametric study on the effect of the reinforcement ratio on the behavior of a reinforced concrete structure.

Matsagar [72] compared the performance of composite and non-composite panels under blast loading. A thorough parametric study was conducted. A finite element model was created in ABAQUS software. Before it was used, the model results were validated against experimental data obtained from the literature. The study included specimens prepared using steel plates, reinforced and non-reinforced concrete slabs, and composite sandwich panels with foam and sand cores. It was possible to perform this kind of extensive parametric study with the use of numerical analysis. It would have been much more expensive and much more time-consuming to have obtained comparable results from an experimental program.

Li et al. [73] investigated the resistance of a normal concrete slab and an ultrahigh-performance concrete slab to contact explosion. A detailed numerical model, including all the essential details of the specimen, was created in LS-DYNA. A thorough study of material models was also presented in the paper. The authors used a novel approach to model the UHPC, based on experimental data. The feasibility and the accuracy of the optimized FE model were discussed in detail.

FE modelling was also used by Stohr et al. [69] to supplement an experimental program to evaluate the use of scaling in blast testing of concrete. The authors created reduced-scale specimens based on the full-scale experimental program presented in Foglar and Kovar [64]. Issues concerning the use of computer modelling on a reduced scale, and on interpreting the results, are also discussed in the paper.

There are various ways to introduce heterogeneity into a structure. Liu et al. [74] increased the heterogeneity of their geopolymer-based high performance concrete material by adding a steel wire mesh reinforcement and an aluminum foam material. Christian and Ong Khim Chye [75] embedded a steel sandwich composite system in their concrete specimens to increase their survivability as blast mitigation panels. Additional steel parts increased the ductility of the specimen as well as the ability to dissipate energy through plastic deformation.

Fallon and McShane [76] studied the response of elastomer-coated concrete subjected to air blast loading. The authors used FE analysis in ABAQUS with a coupled Eulerian-Lagrangian model to accurately portray the air and the structure. This kind of coating is a typical example of a protective measure that can be applied to an existing structure during a retrofit. A similar polyurea elastomeric protective coating was studied by Iqbal et al. [77]. Coatings with suitable material properties can greatly reduce the fragmentation of the tested concrete tiles by dissipating the shock wave energy at the surface of the structure.

A more conventional approach to retrofitting existing structures was studied by Maazoun et al. [78], who tested RC hollow-core slabs retrofitted with a concrete topping combined with CFRP strips. They compared the behavior of the original slabs and the retrofitted slabs based on the experimental results, and also based on explicit FE modelling, using LS-DYNA solver.

4.2 Idealization of the FE model

For the numerical modelling of the experiment presented in chapter 3, it was necessary to idealize the effect of these phenomena. Specifically, the effect of elevated temperature on the specimens. To represent the degradation (or change) in the material, the method of dividing into several layers was chosen. The layer division is shown schematically in Figure 42. Each layer was defined by the material properties at a given temperature. The material properties measured in previous experiments can be used for this definition.
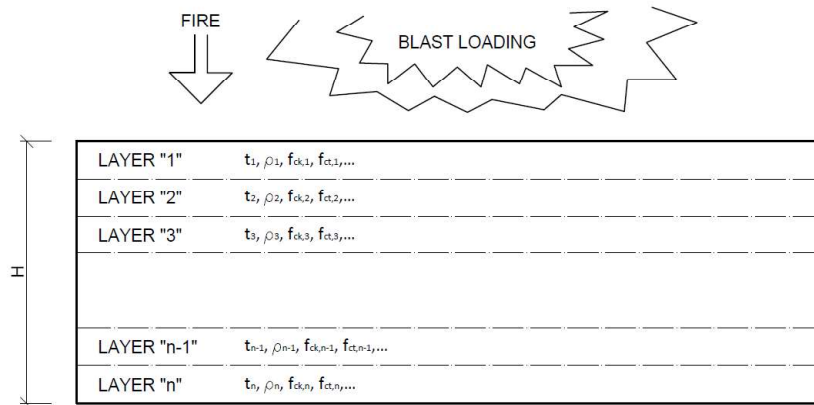
Figure 42 Schematic of the idealization of the FE model - one-side heated specimens

Dividing the model into layers with different properties seems to be a possible solution to include the changes which happen in the specimen due to the effect of high temperature. The specimen changes due to temperature and there are not linear changes in the height of the specimen. This makes it possible to represent this phenomenon in the model and control its effect on the final resistance of the specimen.

4.3 Description of the models

Correct definition of the parameters and boundary conditions of the model determines its functionality and accuracy. If the model is over-simplified and a high mesh step is chosen, the results are not comparable to the real behavior. As the mesh step decreases, the number of nodes increases. Also, the numerical model is more complex to define boundary conditions. In this case, the calculation time is increased. For these reasons, it is necessary to find the optimal settings so that the data obtained from the numerical models are sufficiently exact together with a user-acceptable calculation time.

The following chapters describe the modelling process and the resulting numerical model, including the material models used.

4.3.1 Basic description of the FE models

The final numerical model is shown in Figure 46. Several steps preceded the creation of this numerical model, and these are shown in Figure 43 – Figure 45.

The previous chapter 4.2 describes the idealization of the numerical model. According to this idealization, a numerical model of the specimen was

created. It was divided into 10 layers of equal size. This makes it possible to define properties for each layer separately. The next step was to select the proper step of the mesh. Considering the time required for the analysis and the maximum approximation to the real behavior, it was chosen to be 2 mm in the direction of all axes. After selecting the size of the mesh and splitting the model into layers, a model of the specimen was created.

In the first step, its support (boundary condition) was defined by the support of the individual faces and nodes. This model is shown in Figure 43.
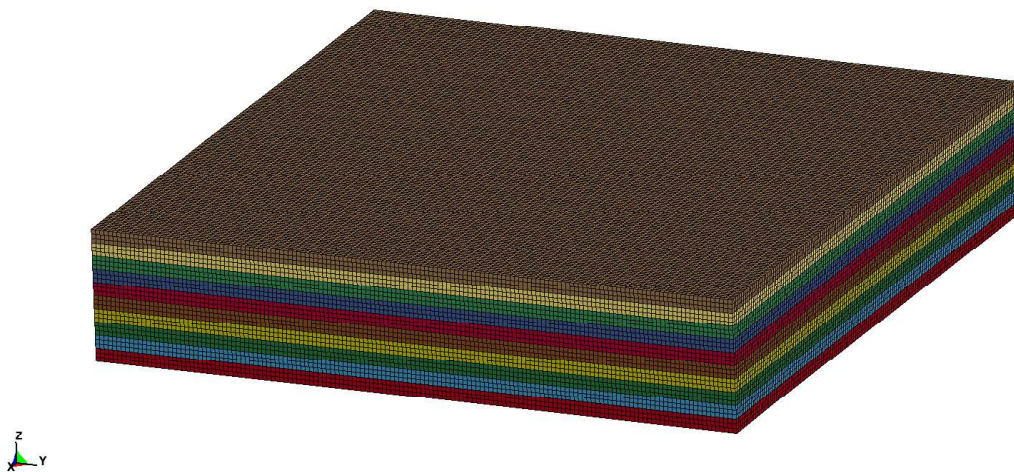
Figure 43 The first version of the FE model

Due to the difficult definition of support (boundary condition), this model was not used. A support was modelled to represent the real support of the model. For this support, a grid step of 5 mm in the direction of all axes was chosen. This model is shown in Figure 44.
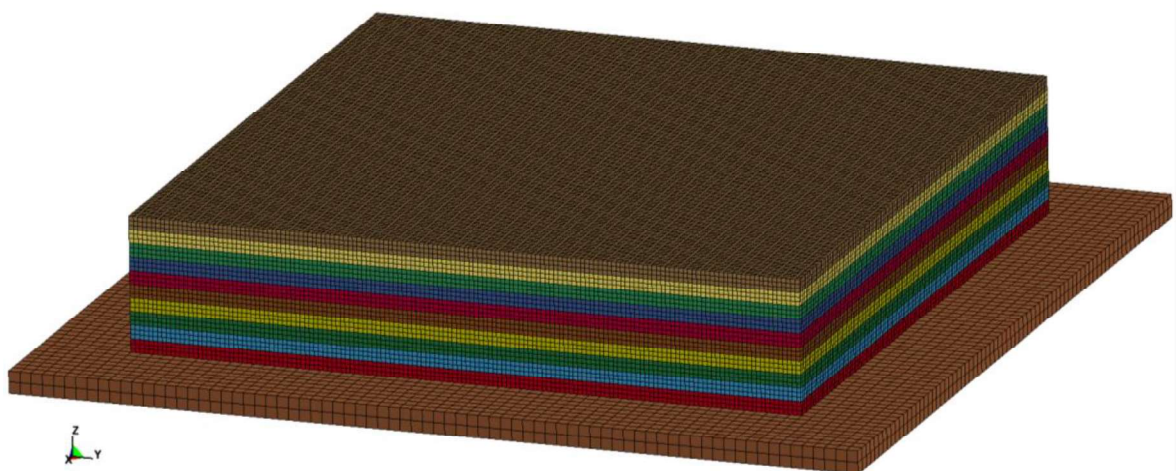
Figure 44 FE model with the first version of the support frame

In the next step, the support was added to the lower support on the upper side of the test specimen. In an effort to simplify, this support was modeled only as a plate. The mesh step is the same as the bottom support, i.e. 5 mm in the direction of all axes. This model is shown in Figure 45.
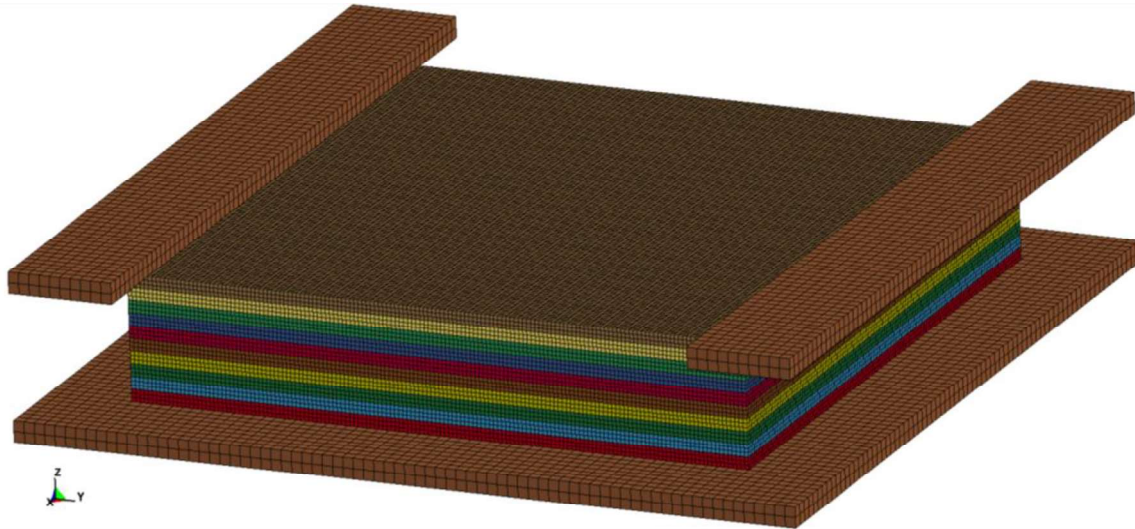
Figure 45 FE model with the second version of the support frame

The final numerical model is shown in Figure 46 final model support corresponds to the experiment performed, i.e., the upper support is the L profile. For comparison with the real support, see Figure 22 and Figure 23. The horizontal connection of the upper supports is neglected since there was no obvious difference in the results from both models. Figure 47 shows the final support of the test specimen.
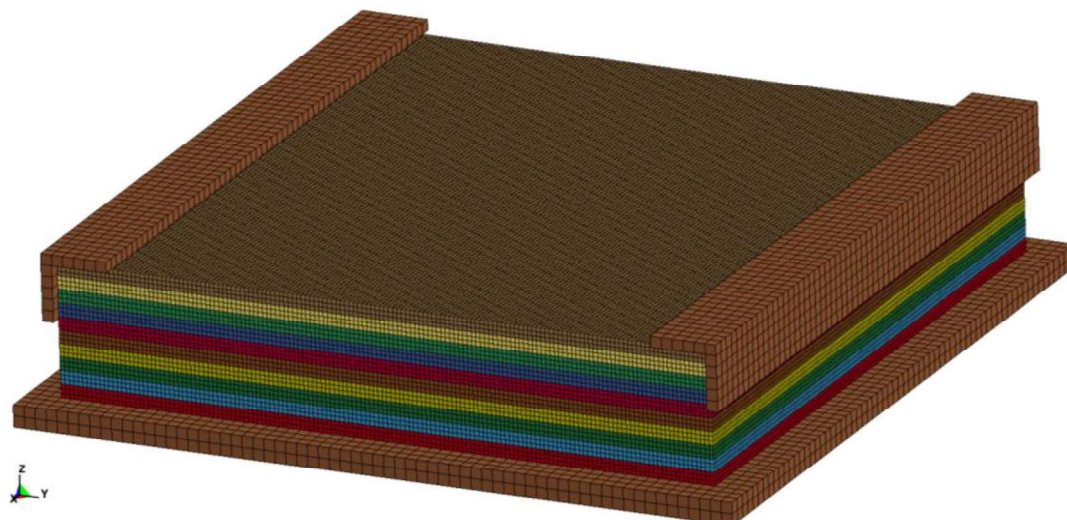
Figure 46 Final FE model
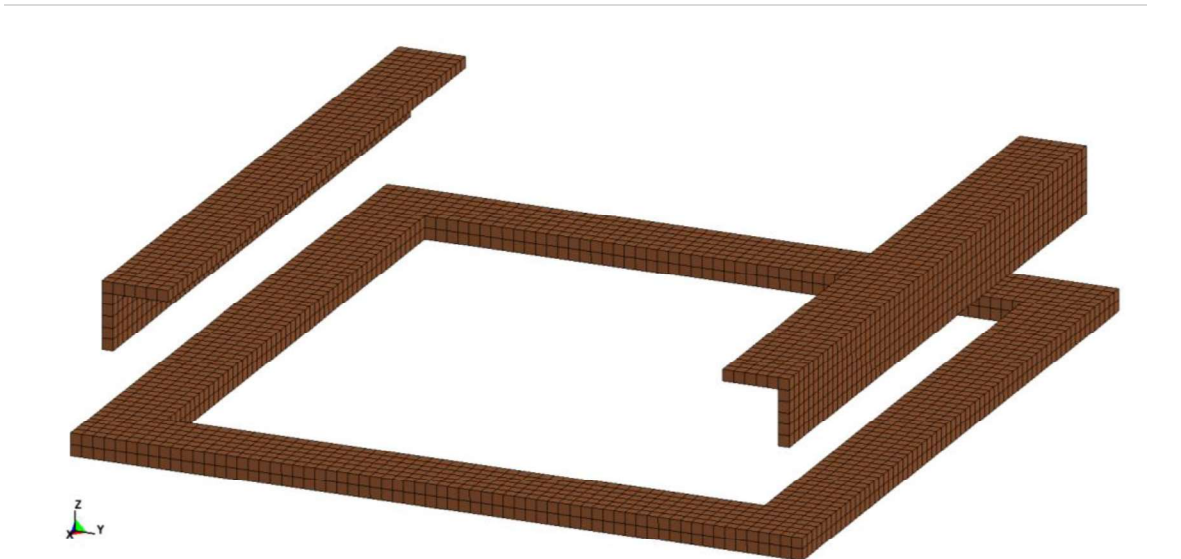
Figure 47 Numerical model of the support frame

4.3.2 Material models

The material models used in the numerical simulation are described below. It is performed for only one tested material - ordinary concrete.

4.3.2.1 Ordinary concrete material model – RC

The numerical model was developed for ordinary concrete with the mixture given in Table 22.

Table 22 Materials mixtures

	Mix RC
	Weight [kg/m³]
Cement	370
Water	135
aggregate 8-16	755
aggregate 4-8	195
aggregate 0-4	863
Plastificator	2.6

The MAT_CSCM (MAT_159) material model of plain concrete (a material model with damage and plasticity) was used.

LS-DYNA manual [92] says: "*This is material type 159. This is a smooth or continuous surface cap model and is available for solid elements in LS-DYNA. The user has the option of inputting his own material properties (option), or requesting default material properties for normal strength concrete (CONCRETE).*"

```
*MAT_CSCM_CONCRETE↓
$#     mid         ro      nplot      incre      irate      erode      recov    itretrc↓
        11 2.3060E-6          3      0.000          1   1.000000      0.000          0↓
$#    pred↓
       0.000↓
$#     fpc       dagg      units↓
   0.059800  16.000000          0↓
```

Figure 48 Print screen of material definition (MAT_159)

Mat_159 is defined by bulk density, compressive strength and maximum aggregate size, see Figure 48. The next values indicate the used units, element erosion, rate effect and other parameters for the calculation. Other possible options for setting the inputs are given in the LS-DYNA manual [92].

4.3.2.2 Supported frame

As presented in chapter 4.3.1 a support frame was also modelled for the specimen. The material model MAT_PLASTIC_KINEMATIC (MAT_003) was used to create this frame. The numerical model of the frame is shown in Figure 47.

LS-DYNA manual [92] says: "*This model is suited for modelling isotropic and kinematic hardening plasticity with the option of including rate effects. It is a very cost-effective model and is available for beam (Hughes-Liu and Truss), shell, and solid elements.*".

```
*MAT_PLASTIC_KINEMATIC↓
$#     mid         ro          e         pr       sigy       etan       beta↓
        21 7.8500E-6 200.00000   0.200000   0.355000      0.000      0.000↓
$#     src        srp         fs        vp↓
       0.000      0.000   1.000000      0.000↓
```

Figure 49 Print screen of material definition (MAT_003)

MAT_003 is defined by bulk density, Young's modulus, Poisson's ratio, and yield stress, see Figure 49. Other parameters like rate effects or effective plastic strain for eroding elements are given in the LS-DYNA manual [92].

4.3.3 Modelling the blast loading

An adjacent detonation of 40 grams with 30 mm standoff above the top surface of the specimen and 37 mm diameter was modeled. In the presented models, the native LS-DYNA function LOAD_BLAST_ENHANCED (LBE) was used instead. This function is derived from U.S. Department of Defense Conventional Weapons Effects Calculation Software (ConWep). The function is set up with the position, and the weight of the charge, and the TNT equivalent of the explosive material. For each selected face, the function calculates the dynamic loading based on the relative standoff distance and

the angle of impact. It should be noted that this approach to modelling of the explosion presumes a spherical explosive charge, and it is calibrated for a limited range of standoff distances and charge weights. Comparison with using fluid dynamics model of air and explosive using arbitrary Lagrangian-Eulerian (ALE) elements is presented in Hájek et al. [86].

The blast loading is defined as shown in Figure 50:

```
*LOAD_BLAST_SEGMENT_SET↓
$#     bid      ssid     alepid      sfnrb      scalep↓
         1         1          0      0.000   1.000000↓
*LOAD_BLAST_ENHANCED↓
$#     bid        m       xbo        ybo         zbo        tbo        unit     blast↓
         1  0.055000    0.000      0.000  37.000000      0.000           5        2↓
$#     cfm       cfl       cft        cfp       nidbo      death     negphs↓
  2.204600  0.003281  1.000000  1.4504E+5               01.0000E+20          0↓
```

Figure 50 Print screen of blast definition

4.3.4 Modelling the effect of elevated temperature

The idealization of the numerical model was split into layers as described above. The test specimen was divided into ten layers of equal size (See Figure 46). During the experiment, five thermocouples were placed in one-side heated specimens. With these, the temperature in the test specimen is known. The maximum temperatures obtained are shown in Table 23. Using the known temperatures, the maximum temperatures reached in all ten layers were determined. These temperatures and other properties of each layer are given in Table 24. Table 25 given properties of unheated specimen.

Table 23 Table of measured temperature by thermocouple

Thermocouple	One-side heated	Uniformly heated
0 mm	387.4 °C	
10 mm	380.0 °C	
20 mm	371.9 °C	400 °C
30 mm	365.4 °C	
50 mm	357.1 °C	

Table 24 Properties of layers for heated specimen

One-side heated specimens					Uniformly heated			
layer	temp.	Compress. Str.	Tensile Str.	Bulk density	temp.	Compress. Str.	Tensile Str.	Bulk density
	[°C]	[MPa]	[MPa]	[kg/m³]	[°C]	[MPa]	[MPa]	[kg/m³]
1	387.4	43.7	1.72	2 285.4				
2	380.0	43.9	1.78	2 286.5				
3	376.0	44.1	1.81	2 287.0				
4	371.9	44.2	1.84	2 287.5				
5	365.4	44.4	1.90	2 288.3	400	43.31	1.62	2 283.4
6	363.3	44.5	1.91	2 288.6				
7	361.3	44.5	1.93	2 288.8				
8	359.2	44.6	1.95	2 289.0				
9	357.1	44.7	1.96	2 289.3				
10	355.0	44.7	1.98	2 289.5				

Table 25 Properties of the unheated specimen (room temperature)

Unheated specimen			
temp.	Compress. Str.	Tensile Str.	Bulk density
[°C]	[MPa]	[MPa]	[kg/m³]
25	59.75	4.04	2 305.9

The maximum temperature reached in the layer defines its material properties. With the knowledge of these temperatures, it was possible to determine the properties. For this purpose, the data obtained from the experimental measurements presented in chapter 2 were used. The values of compressive strength, tensile strength, and bulk density of each layer are given in Table 24 and Table 25. These data were subsequently used to define the numerical material model described in chapter 4.3.2.1. This change in the material properties of the individual layers enabled modelling of the specimen after exposure to elevated temperature.

4.3.4.1 Modelling the effect of other elevated temperature – one-side heated specimen

To verify the trend of the behavior of the specimen in the experiment, an identical calculation was numerically performed as in the experiment but with a different temperature. This temperature influences the material properties of the specimen. Therefore, a heat transfer model was used to determine the maximum temperature reached in the element. The heat transfer model used is presented in Štefan et al. [79].

For the heat transfer model, it is necessary to define the fire curve and the material properties of the specimen - specific heat capacity, thermal conductivity, and bulk density. Thermal conductivity and bulk density were defined using the results presented in chapter 2. Thermal conductivity is shown in Figure 4 (RC - TZ curve). Bulk density is shown in Figure 1 (RC - TZ curve). The specific heat capacity was considered according to the standard with a moisture content of 3% EN 1992-1-2 [30].

As a first step measured data obtained during the experiment (see chapter 3.2.4) was used to validated model The results are shown in Figure 51. Red lines show the measured values during the experiment including the fire curve. Black lines show the result of the heating simulation.
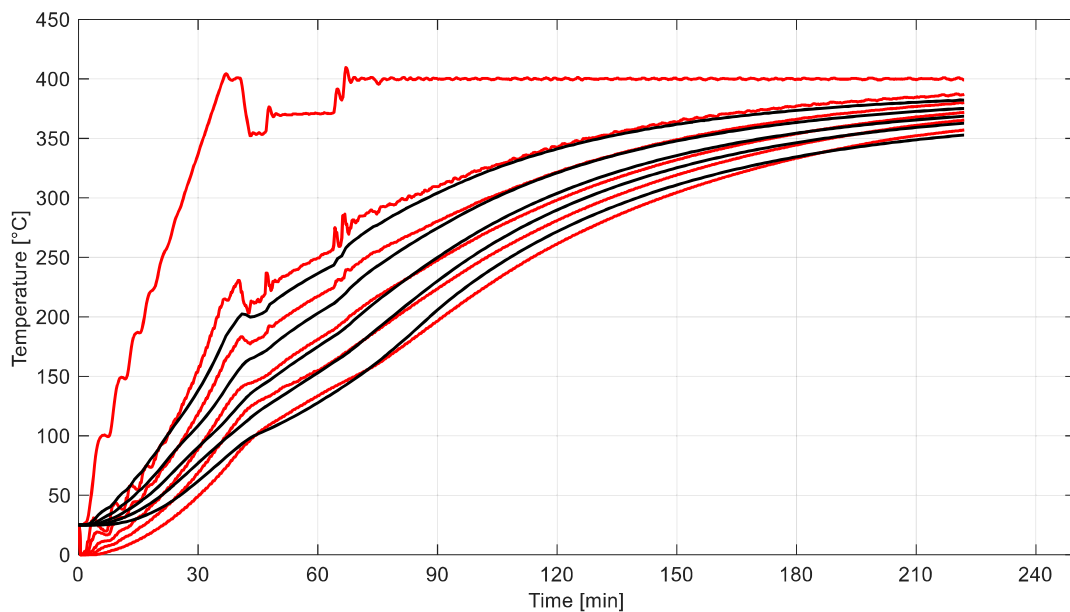
Figure 51 Results of the heating numerical simulation – 400 °C

In the following step, the fire curve was changed. The heating was performed at the same rate as in the previous case (10 °C/min) but up to the temperature of 500 °C. This temperature was held constant for 3 hours. This resulted in the temperature rise in the specimen shown in Figure 52. Red line defines used fire curve. Black lines show the result of the heating simulation.
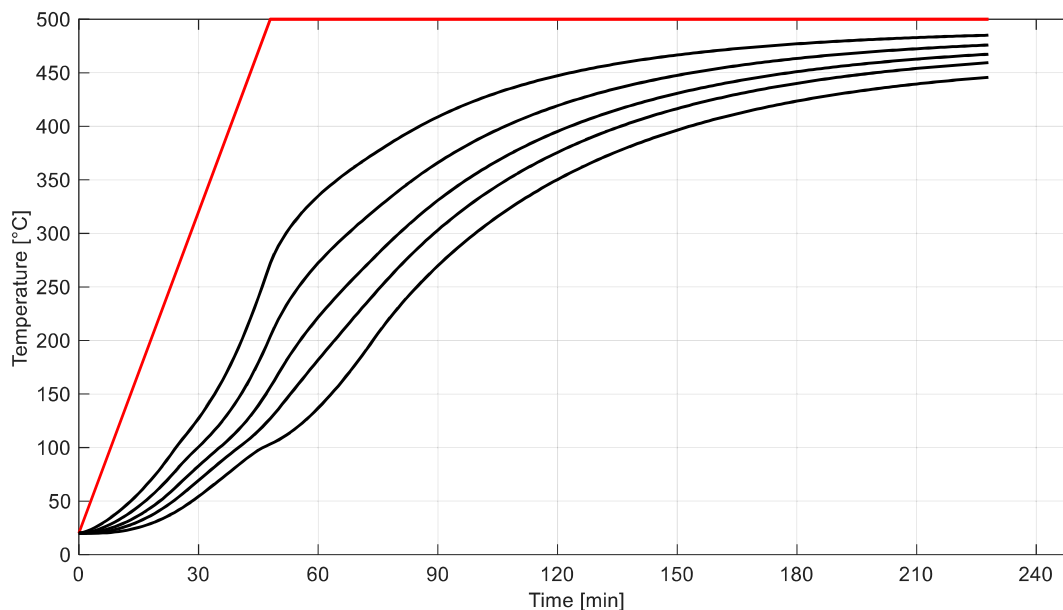
Figure 52 Results of the heating numerical simulation – 500 °C

For use in the FE model, it was necessary to determine temperatures for all ten layers. The procedure was identical to the modelling experiment. The maximum temperatures achieved at the thermocouple level were the input values. The values read from Figure 52 are also shown in Table 26 for simplicity.

Table 26   Temperatures in the specimen

Thermocouple	One-side heat. 400 °C	Uniformly heat. 400 °C	One-side heat. 500 °C	Uniformly heat. 500 °C
		Temperatures		
0 mm	387.4 °C		485.1 °C	
10 mm	380.0 °C		476.0 °C	
20 mm	371.9 °C	400 °C	467.3 °C	500 °C
30 mm	365.4 °C		459.4 °C	
50 mm	357.1 °C		445.8 °C	

4.3.4.2 Modelling of nonlinear changes of tensile and compressive strength

Material property changes at elevated temperatures are discussed in chapter 2. Chapter 2.2.5.1 deals with the loss of compressive strength in dependence on temperature. The decrease in compressive strength is also discussed in chapter 3.2.4.4. Tensile strength changes have not been determined in the study of material properties. However, it was measured in a fire and blast experiment and the results are presented in chapter 3.2.4.5.. The change in these characteristics is described in Eurocode EN 1992-1-2 [30]. The change in both material properties is also shown in Figure 53. EN

1992-1-2 [30] specifies that the value of the compressive or tensile strength at any temperature is the room temperature strength value multiplied by the proper coefficient. These coefficients can also be found in Figure 53.
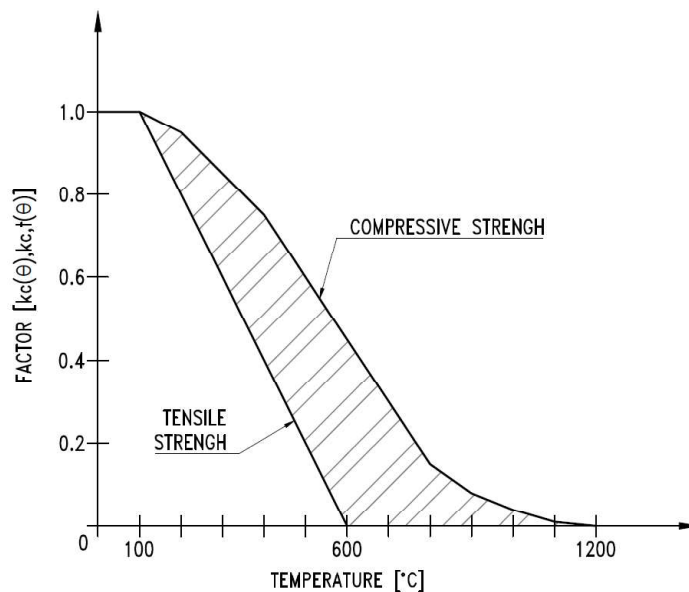
Figure 53 Graph of compressive and tensile strength change according to EN 1992-1-2 [30]

In Figure 53, it can be seen that the tensile strength decreases faster as a function of the effective temperature than the compressive strength. However, this phenomenon is problematic to define in numerical simulation. The material model described in chapter 4.3.2.1 is defined by bulk density, compressive strength and maximum aggregate size. Based on these parameters, it automatically calculates the tensile strength of the material. Due to this, the decrease of tensile strength is not taken into respect while defining the layers, which brings an error into the simulation.

The solution chosen for this problem was to create two numerical models. The models were marked as BC1 (Boundary condition 1) and BC2 (Boundary condition 2). Model BC1 is defined by the real compressive strength. Model BC2 has the compressive strength reduced such that the tensile strength of the material calculated by the material model is equal to the real tensile strength. These two simulations define the range in which the result of the real behavior should be. This range is hatched in the graph in Figure 53.

4.4 Numerical simulation findings

4.4.1 Method of results evaluation

One method of evaluating the results of the numerical simulation is to compare the velocity of the flying debris (soffit velocity). During the fire and

blast experiment, this velocity was measured at the center of the specimen. The evaluation of the velocity in the numerical model was not based on a one value. The velocity of eight elements was determined from the numerical model. The position of the elements is shown in Figure 54 and Figure 55. There are four points in the top view, each 20 mm from the center of the specimen. In the height of the specimens, these are the first and second row points of the mesh. The results in the center of the specimen were not considered in the simulation.
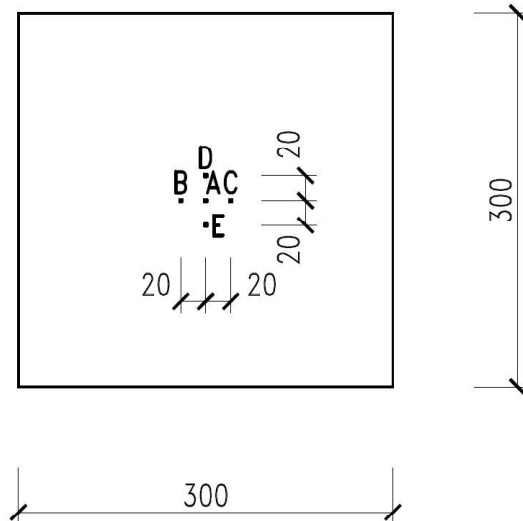
Figure 54 Top view of the measured elements of the specimen
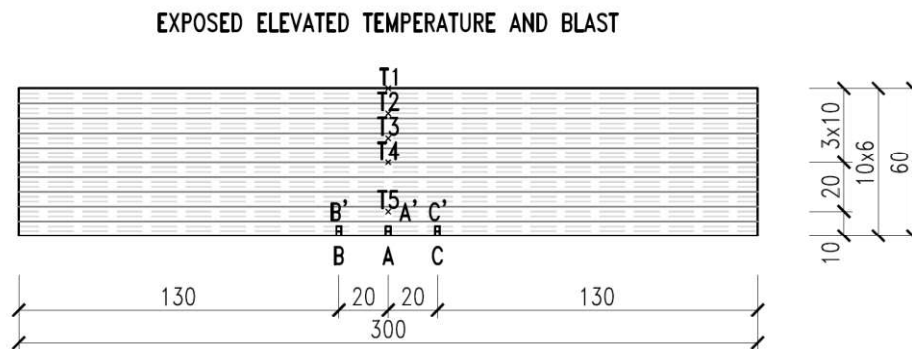
Figure 55 Specimen height distribution of measured elements

The result was the velocity of the single elements depending on time. Graph with this data is shown in Figure 56. The results of the single elements were evaluated the same as in the evaluation of the results from the experiment. This is described in chapter 3.2.5.3. All of the determined velocities were averaged, and an idealized curve was determined, along with the velocities at major points (maximum reached velocity, pull-back velocity, etc.). The final idealized graph is shown in Figure 57.
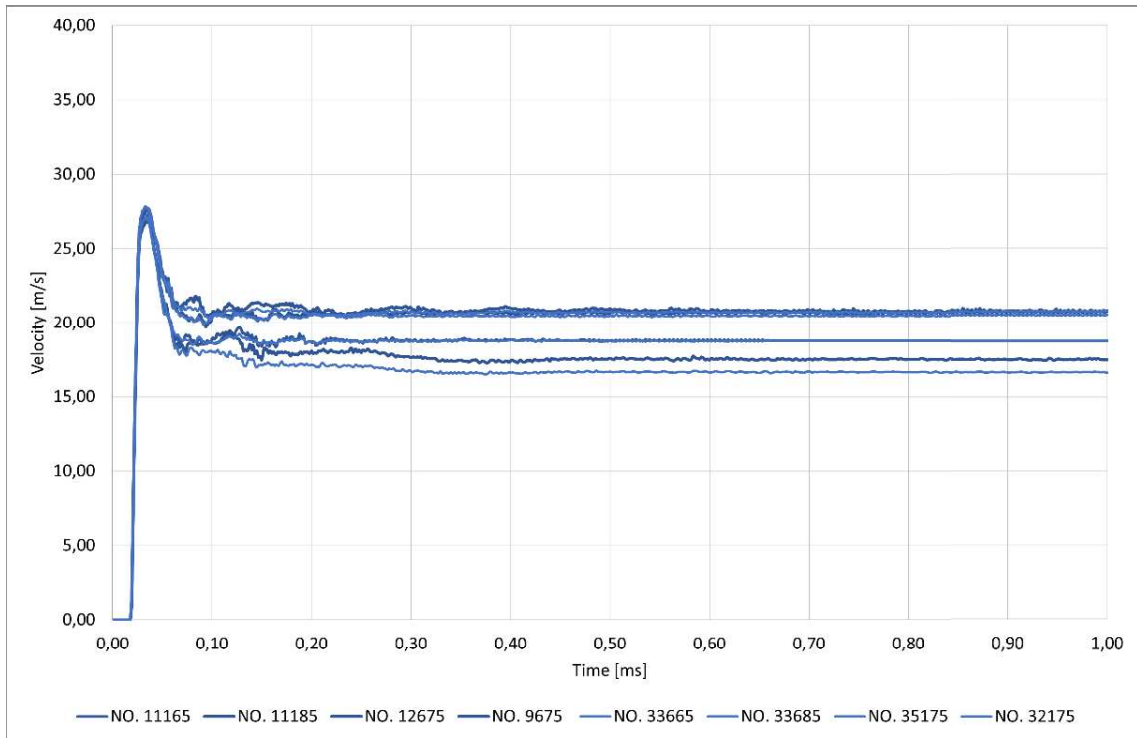
Figure 56 Change soffit velocity depending on time at each element – unheated specimen
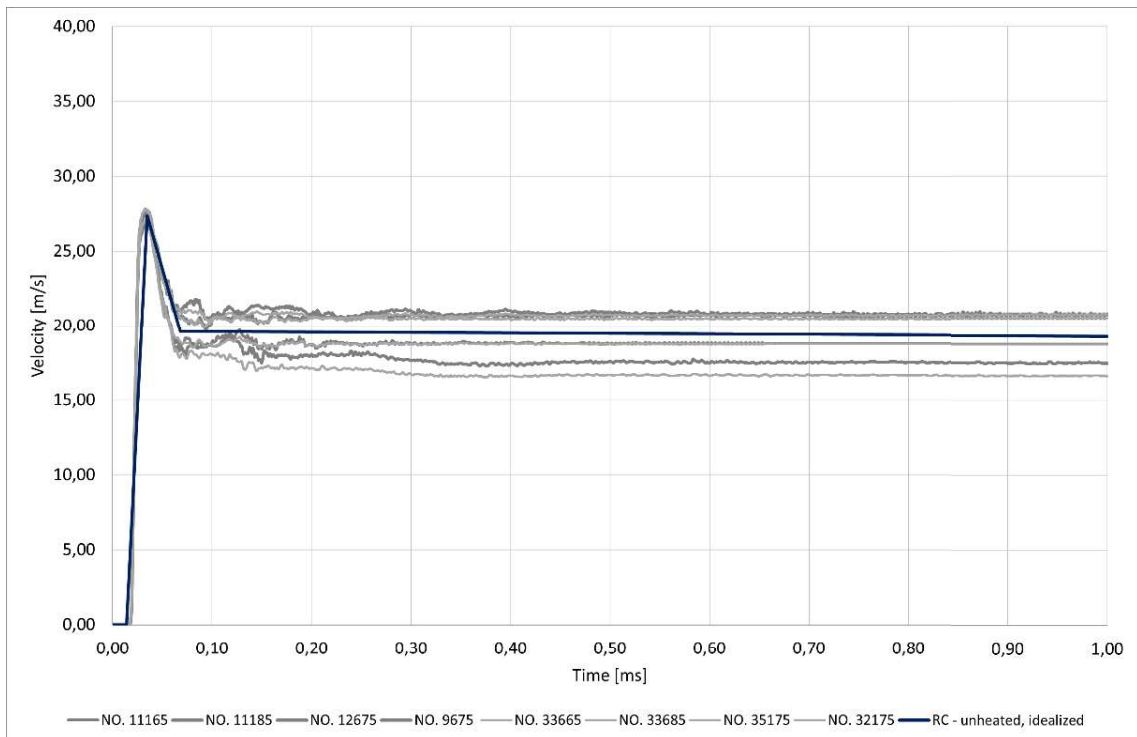
Figure 57 Final graph of results with idealized – unheated specimen

The idealized curves from numerical simulation were then compared with the experimental results. A first comparison is shown in Figure 58.
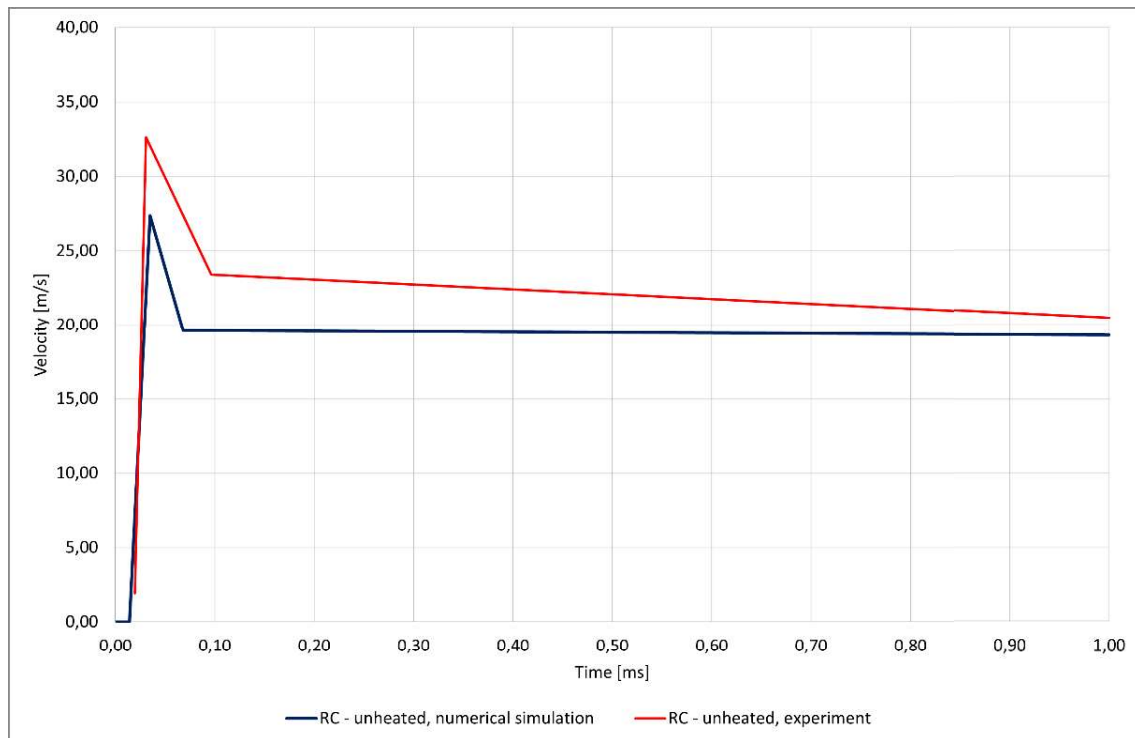
Figure 58 Comparison of experimental and numerical simulation results – unheated specimen

4.4.2 Velocity of flying debris

4.4.2.1 Numerical simulation results

Velocity of the flying debris was determined for all types of test specimens. Figure 57 shows a graph with the results for the unheated sample. The graph also shows the final idealization. The maximum velocity values at a given time are given in Table 27.

Table 27 Maximum soffit velocity in time – unheated specimens

Unheated	t_0	t_1	t_2 (v_{max})	t_3	t_4
Time [ms]	0.0000	0.0139	0.0349	0.0679	1.0000
Velocity [m/s]	0.00	0.00	27.37	19.59	19.30

Calculations and results for other types of elevated temperature exposure are more difficult to interpret. The simulation was done twice as described in chapter 4.3.4.2. The results define the range in which the actual results are located.

The results of the uniformly heated specimen are shown in Figure 59 and Figure 60. The maximum velocities in time are given in Table 28 and Table 29. Figure 59 and Table 28 present the results of the BC1 model. Figure 60 and Table 29 present the results of the BC2 model.
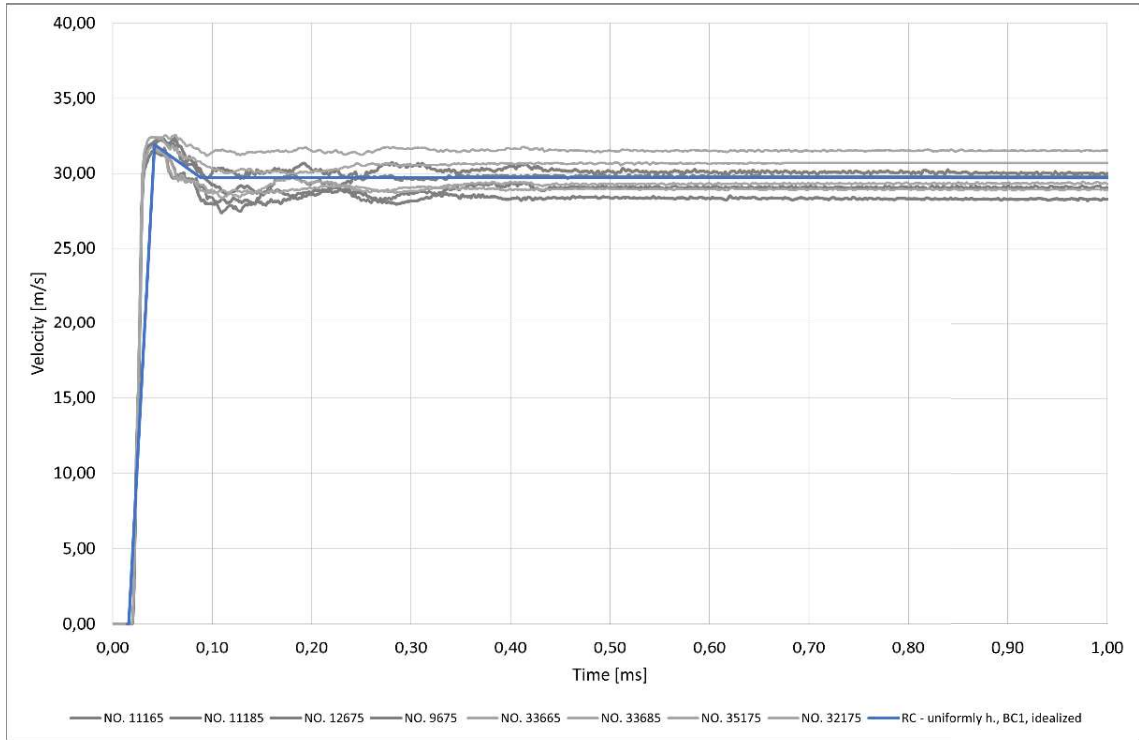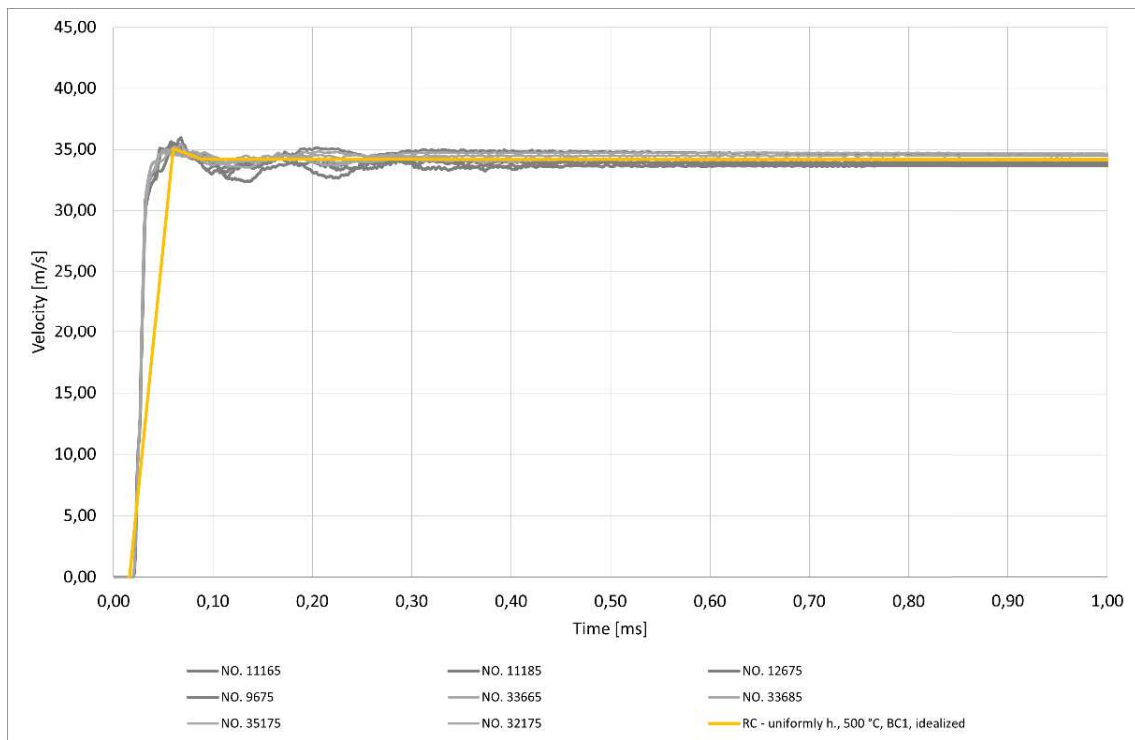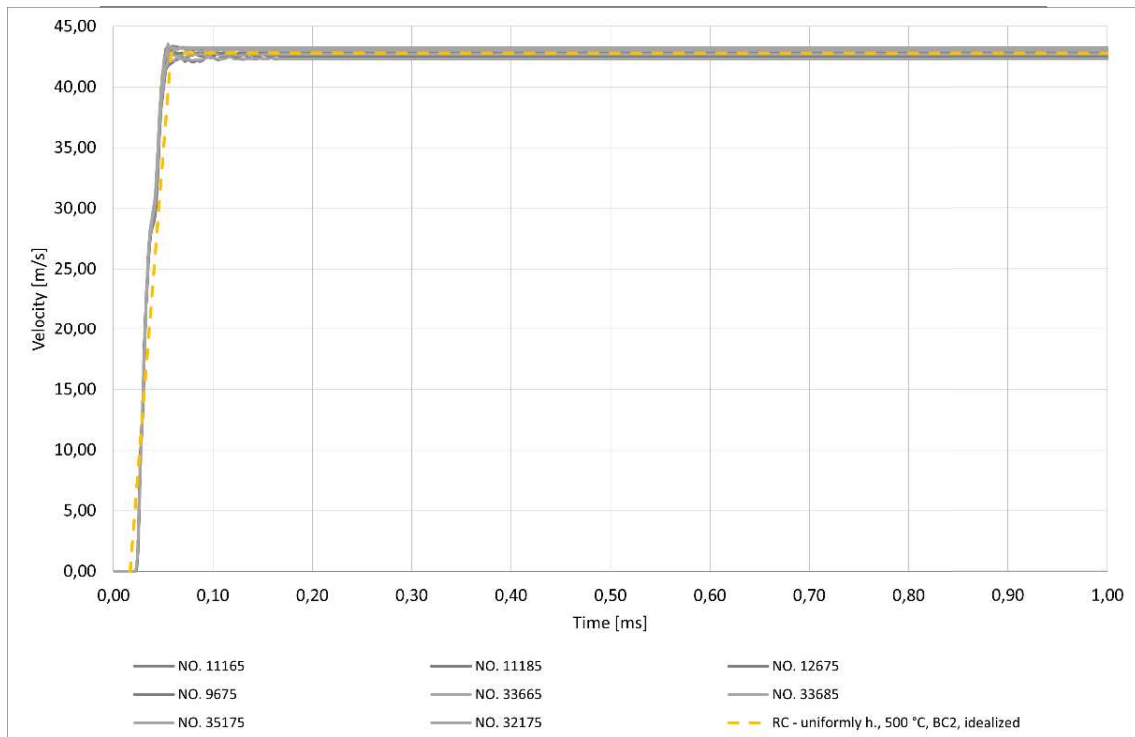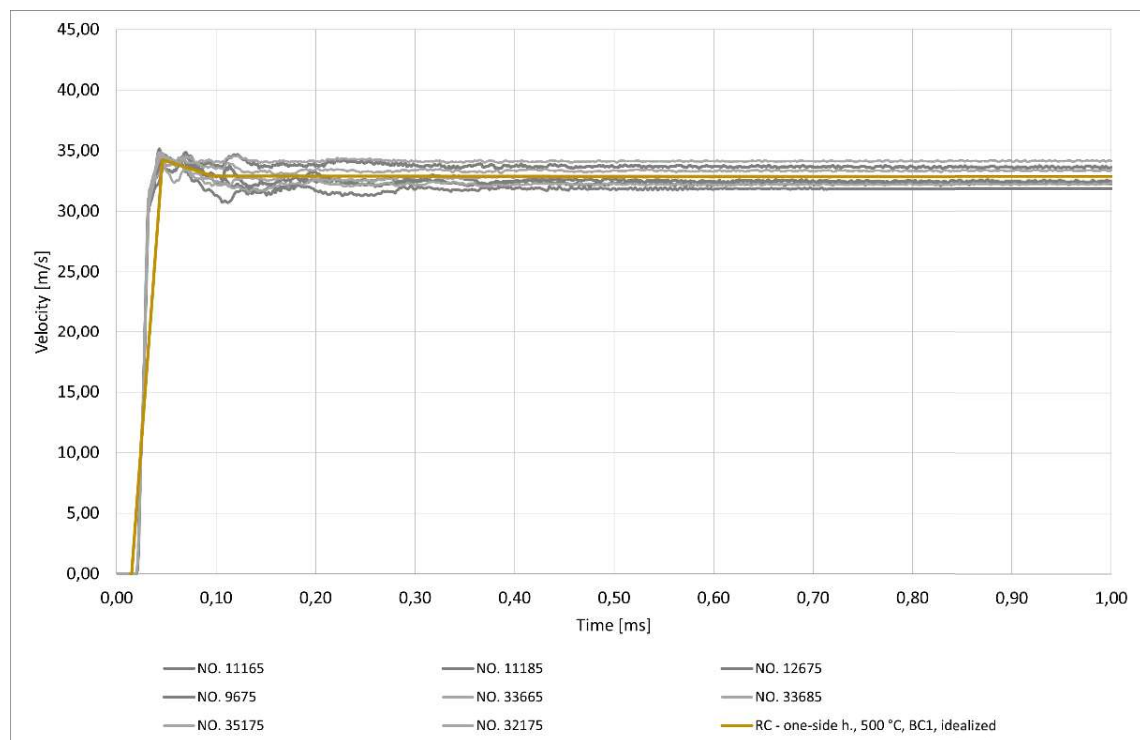
Figure 59 Results of BC1 model – uniformly heated specimen

Table 28   Maximum velocities in time, BC1 model – uniformly heated specimen

Uniformly h.	t_0	t_1	t_2 (v_{max})	t_3	t_4
Time [ms]	0.0000	0.0160	0.0420	0.0887	1.0000
Velocity [m/s]	0.00	0.00	31.92	29.71	29.70
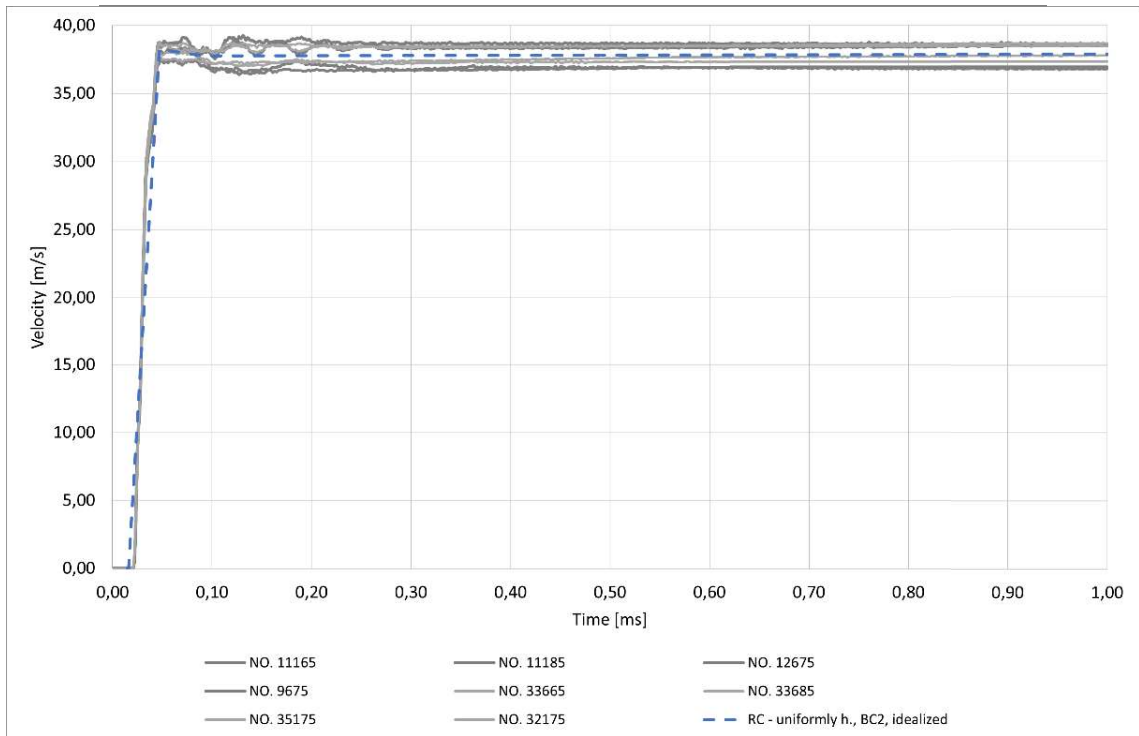
Figure 60 Results of BC2 model – uniformly heated specimen

Table 29 Maximum velocities in time, BC2 model – uniformly heated specimen

Uniformly h. T	t_0	t_1	t_2 (v_{max})	t_3	t_4
Time [ms]	0.0000	0.0159	0.0470	0.0908	1.0000
Velocity [m/s]	0.00	0.00	38.25	37.76	37.89

The results of the one-side heated specimen are shown in Figure 61 and Figure 62. The maximum velocities in time are given in Table 30 and Table 31. Figure 61 and Table 30 present the results of the BC1 model. Figure 62 and Table 31 present the results of the BC2 model.
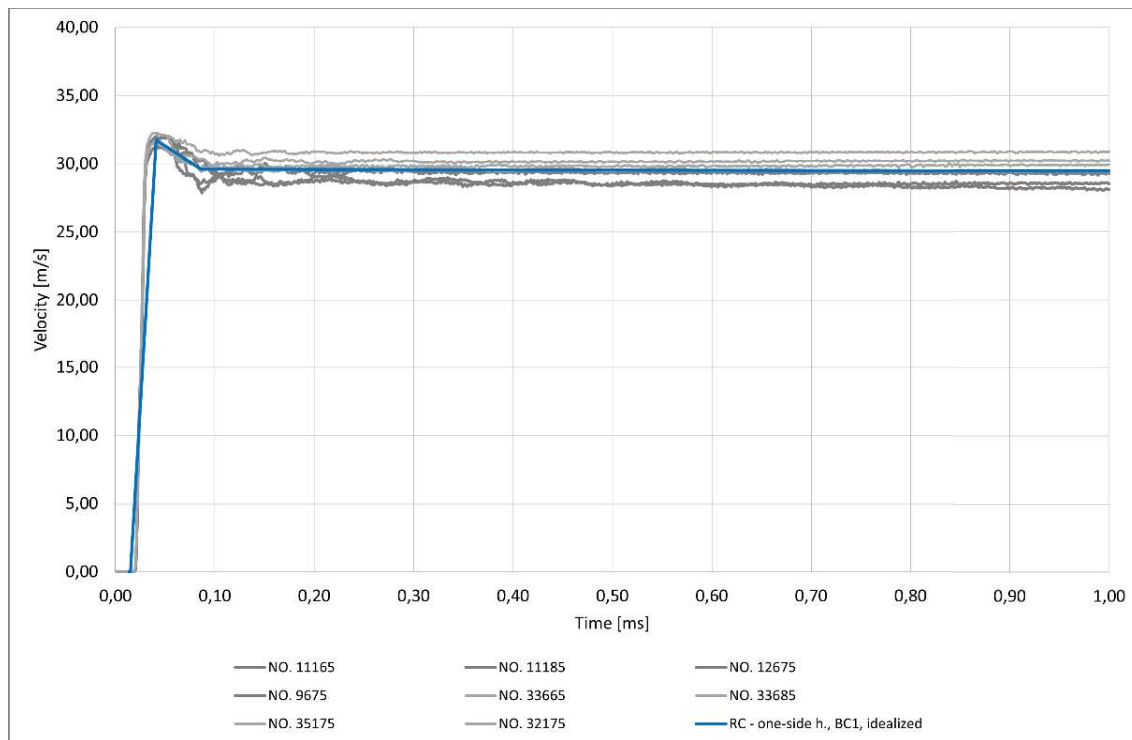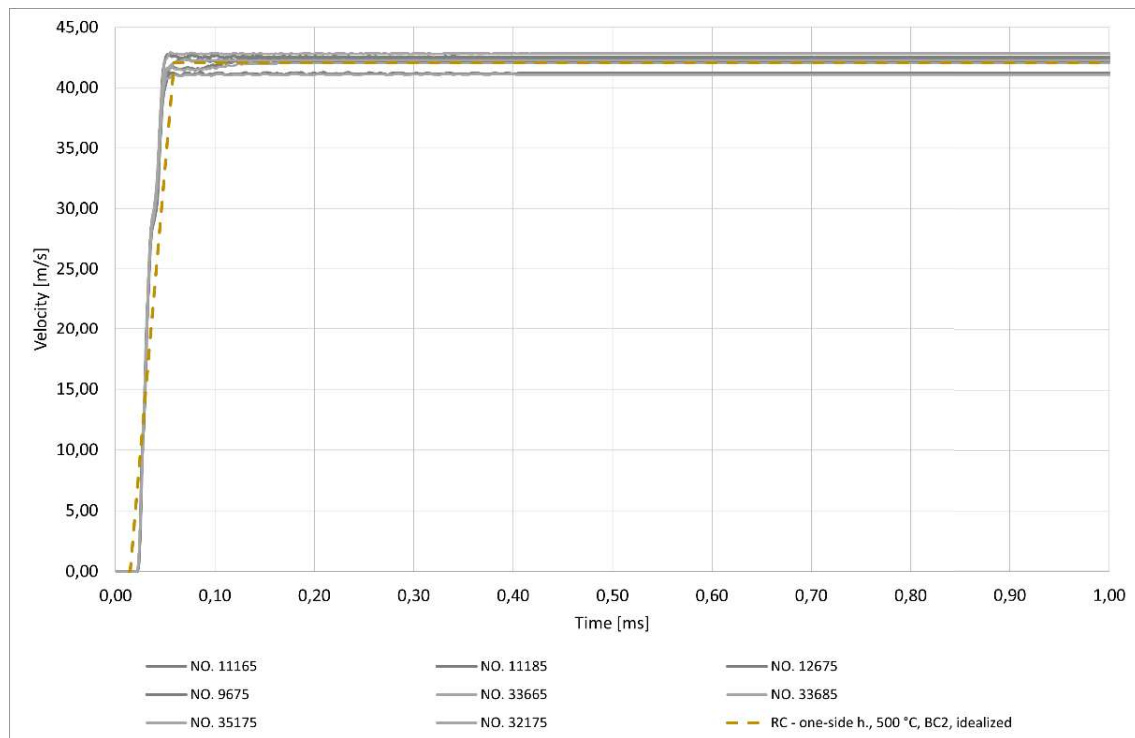

Figure 61 Results of BC1 model – one-side heated specimen

Table 30 Maximum velocities in time, BC1 model – one-side heated specimen

One-side h.	t_0	t_1	t_2 (v_{max})	t_3	t_4
Time [ms]	0.0000	0.0150	0.0409	0.0857	1.0000
Velocity [m/s]	0.00	0.00	31.74	29.62	29.46
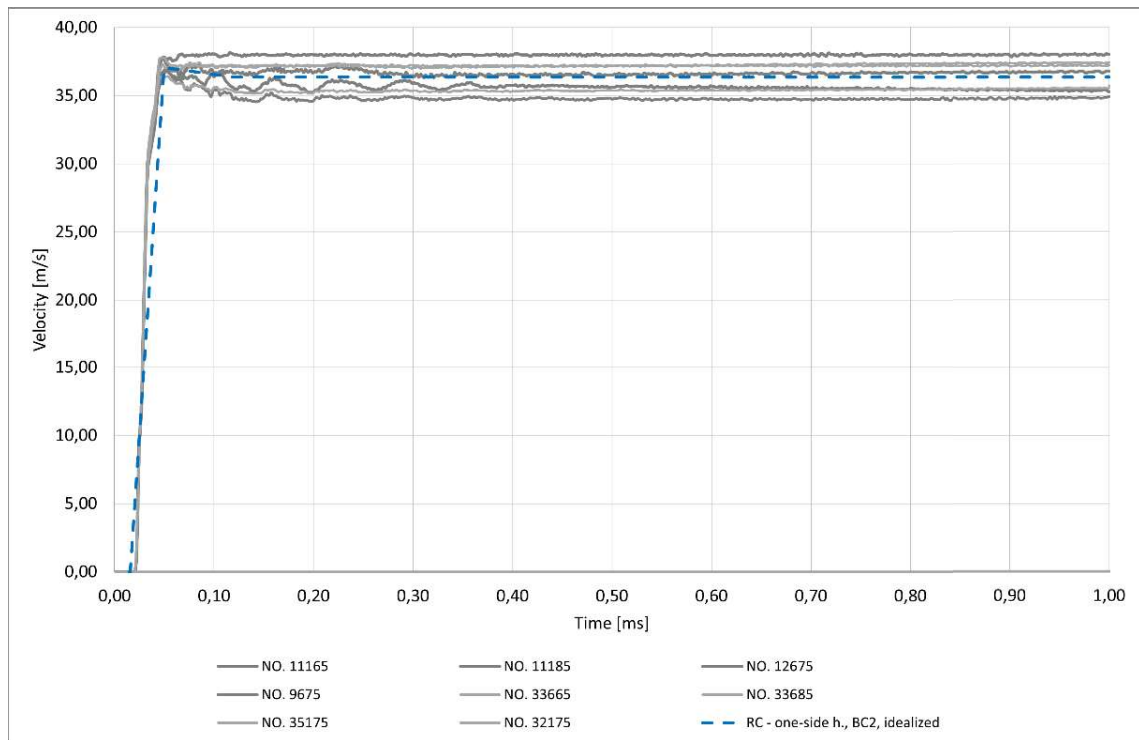
Figure 62 Results of BC2 model – one-side heated specimen

Table 31   Maximum velocities in time, BC2 model – one-side heated specimen

One-side h. T	t_0	t_1	t_2 (v_{max})	t_3	t_4
Time [ms]	0.0000	0.0158	0.0497	0.1177	1.0000
Velocity [m/s]	0.00	0.00	37.07	36.38	36.36

After the numerical simulation of the experimental measurements, a simulation for a different type of heating was simulated. Specimens were exposed to a temperature of 500 °C in theoretical cases. Numerical simulation was performed for both types of elevated temperature exposed - one-side heated and uniformly heated.

The results of this simulation are also divided by the method of exposed temperature. The results of the uniformly heated specimen are shown in Figure 63 and Figure 64. The maximum velocities in time are given in Table 32 and Table 33. Figure 63 and Table 32 present the results of the BC1 model. Figure 64 and Table 32 present the results of the BC2 model.

Figure 63 Results of BC1 model, 500 °C – uniformly heated specimen

Table 32   Maximum velocities in time, BC1 model, 500 °C – uniformly heated specimen

Uniformly h.	t_0	t_1	t_2 (v_{max})	t_3	t_4
Time [ms]	0.0000	0.0160	0.0599	0.0889	1.0000
Velocity [m/s]	0.00	0.00	35.09	34.21	34.18

Figure 64 Results of BC2 model, 500 °C – uniformly heated specimen

Table 33 Maximum velocities in time, BC2 model, 500 °C – uniformly heated specimen

Uniformly h. T	t_0	t_1	$t_2 (v_{max})$	t_3	t_4
Time [ms]	0.0000	0.0168	0.0579	0.0579	1.0000
Velocity [m/s]	0.00	0.00	42.82	42.82	42.76

The results of the one-side heated specimen are shown in Figure 65 and Figure 66. The maximum velocities in time are given in Table 34 and Table 35. Figure 65 and Table 34 present the results of the BC1 model. Figure 66. and Table 35 present the results of the BC2 model.

Figure 65 Results of BC1 model, 500 °C – one-side heated specimen

Table 34 Maximum velocities in time, BC1 model, 500 °C – one-side heated specimen

One-side h.	t_0	t_1	$t_2 (v_{max})$	t_3	t_4
Time [ms]	0.0000	0.0149	0.0459	0.0970	0.0000
Velocity [m/s]	0.00	0.00	34.27	32.90	32.85

Figure 66 Results of BC1 model, 500 °C – one-side heated specimen

Table 35   Maximum velocities in time, BC2 model, 500 °C – one-side heated specimen

One-side h. T	t_0	t_1	t_2 (v_{max})	t_3	t_4
Time [ms]	0.0000	0.0147	0.0589	0.0589	1.0000
Velocity [m/s]	0.00	0.00	42.10	42.10	42.08

4.4.2.2 Comparison of numerical simulation results and their comparison with experiment results

In the following chapter, the results are compared. First, the results are validated, i.e. compared with the results from experimental measurements. The result of this comparison are graphs for each heating type of exposure. In the next part, the results from the numerical simulation are compared with each other based on the temperature exposure again. In the last part, the data from the numerical models are compared after the temperature was exposed to 400 °C and 500 °C.

The heated specimen results are given by the range defined by the two limit state values. The methodology for this calculation is described above.

Velocity change Δv is also given for comparison. This indicates the difference between maximum velocity and pull-back velocity.

4.4.2.2.1 Validation of the results = numerical simulation and experimental comparison

Figure 67 shows the comparison of the experimental measurement results with the numerical simulation for the unheated specimen. Maximum velocity values in times are given in Table 36. Velocity change Δv = 9.23 m/s in the case of the experimental measurement, Δv = 7.78 m/s in the numerical simulation.
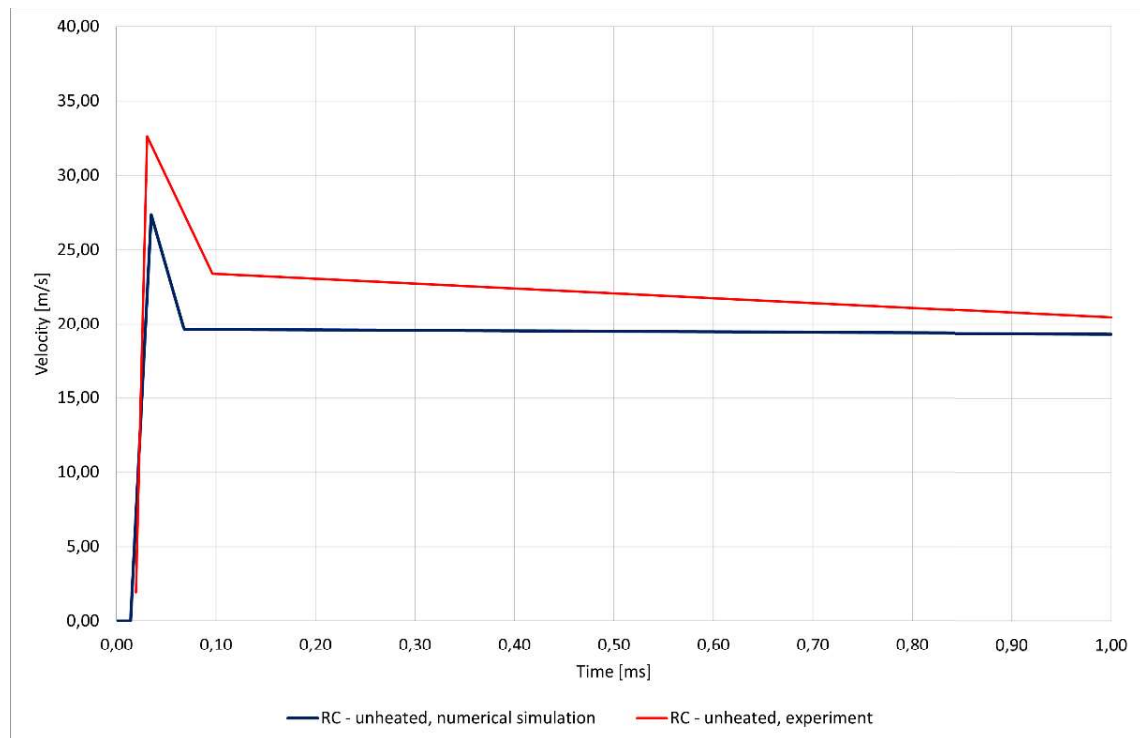
Figure 67 Comparison of experimental and numerical simulation results – unheated specimen

Table 36 Maximum velocities and its comparison – unheated specimen

	Unheated	t_1	t_2 (v_{max})	t_3	t_4	Δv [m/s]
PDV	Time [ms]	0.0193	0.0307	0.0963	1.0000	
	Velocity [m/s]	1.93	32.63	23.40	20.44	9.23
FEM	Time [ms]	0.0139	0.0349	0.0679	1.0000	
	Velocity [m/s]	0.00	27.37	19.59	19.30	7.78

Figure 68 shows the comparison of the experimental results with the numerical simulation for uniformly heated specimens. This comparison is more complex due to the two simulations (BC1 and BC2 models). The values of the maximum velocities in times are given in Table 37. Change in velocity Δv = 5.56 m/s in the case of the experimental measurement, in the numerical simulation Δv = 2.21 m/s. respectively Δv = 0.49 m/s.
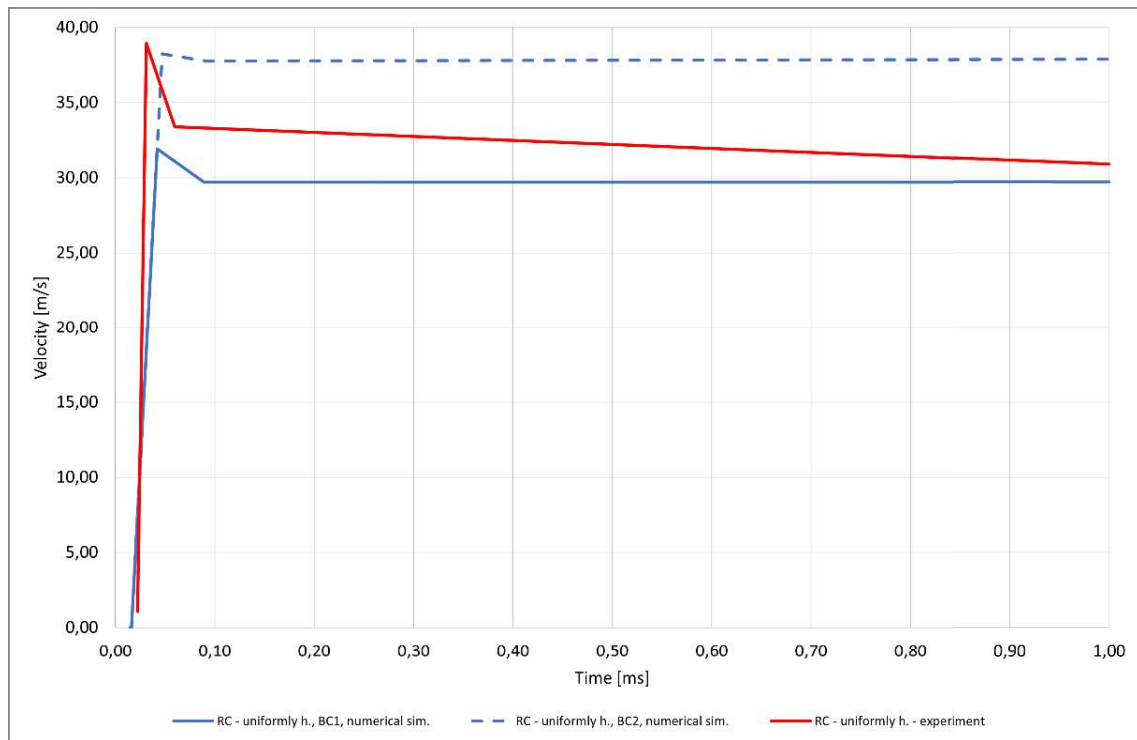
Figure 68 Comparison of experimental and numerical simulation (BC1 and BC2 models) results – uniformly heated specimen

Table 37 Maximum velocities and its comparison – uniformly heated specimen

	Uniformly h.	t_1	t_2 (v_{max})	t_3	t_4	Δv [m/s]
PDV	Time [ms]	0.0220	0.0310	0.0597	1.0000	
	Velocity [m/s]	1.07	38.94	33.38	30.90	5.56
BC1	Time [ms]	0.0160	0.0420	0.0887	1.0000	
	Velocity [m/s]	0.00	31.92	29.71	29.70	2.21
BC2	Time [ms]	0.0159	0.0470	0.0908	1.0000	
	Velocity [m/s]	0.00	38.25	37.76	37.89	0.49

Figure 68 shows the comparison of the experimental results with the numerical simulation for one-side heated specimens. BC1 and BC2 models were also created. The values of the maximum velocities in times are given in Table 37. Change in velocity Δv = 10.18 m/s in the case of the experimental measurement, in the numerical simulation Δv = 2.13 m/s. respectively Δv = 0.70 m/s.
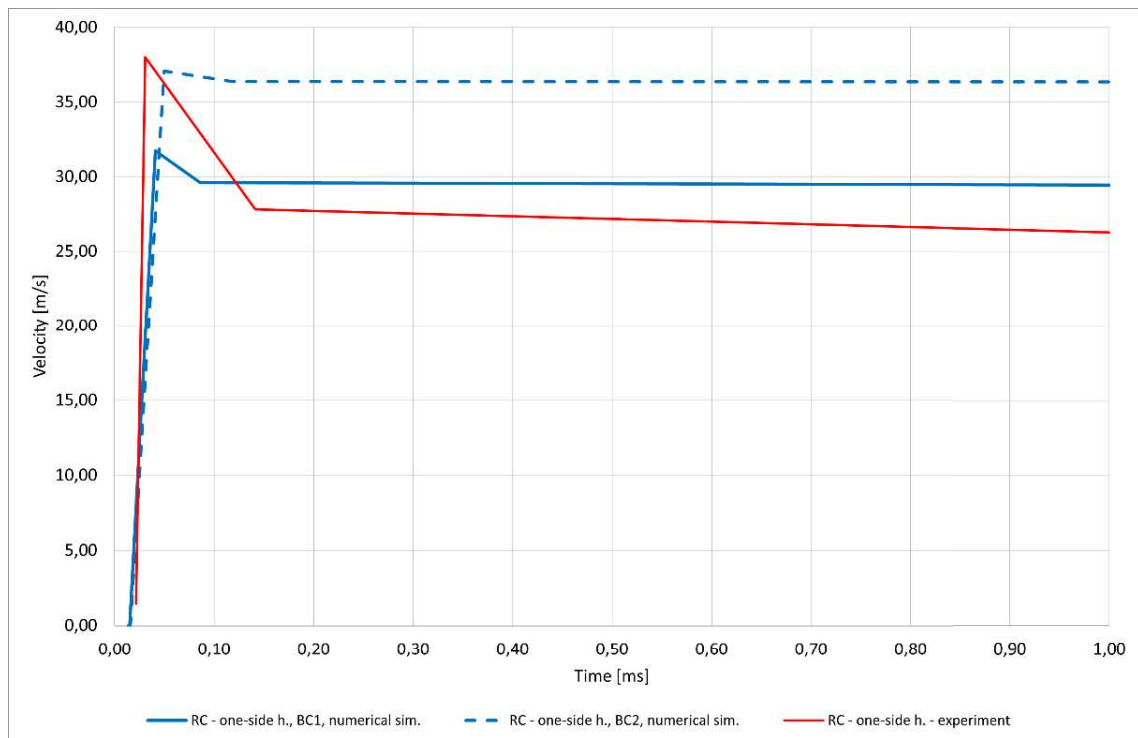
Figure 69 Comparison of experimental and numerical simulation (BC1 and BC2 models) results – one-side heated specimen

Table 38   Maximum velocities and its comparison – one-side heated specimen

	One-side h.	t_1	t_2 (v_{max})	t_3	t_4	Δv [m/s]
PDV	Time [ms]	0.0216	0.0306	0.1412	1.0000	
	Velocity [m/s]	1.48	38.00	27.82	26.28	10.18
BC1	Time [ms]	0.0150	0.0409	0.0857	1.0000	
	Velocity [m/s]	0.00	31.74	29.62	29.46	2.13
BC2	Time [ms]	0.0158	0.0497	0.1177	1.0000	
	Velocity [m/s]	0.00	37.07	36.38	36.36	0.70

4.4.2.2.2 Comparison of numerical simulation results

Comparison of the numerical simulation results with the experiment makes an important part of the validation of the numerical model itself. Comparison of the results according to the heating method is a way to understand the behavior of the specimens.

Comparison of the results of the experiment is presented in chapter 3 in Figure 36. Comparison of the results of the numerical simulation is shown in Figure 70. Maximum velocities in times are given in Table 39. This table also gives a percentage comparison of the maximum velocities with reference to unheated specimens (plus symbol indicates an increase in velocity, minus symbol indicates a decrease in velocity).

The results show that the maximum soffit velocity increased by 15.98% to 35.46% when one-side heated compared to the unheated specimen. Soffit velocity of uniformly heated specimens increased by 16.63% to 39.74% compared to the unheated specimen. From this take, it can be seen that when uniformly heated specimen, soffit velocity is 0.65% to 4.28% higher than one-side heated specimen.
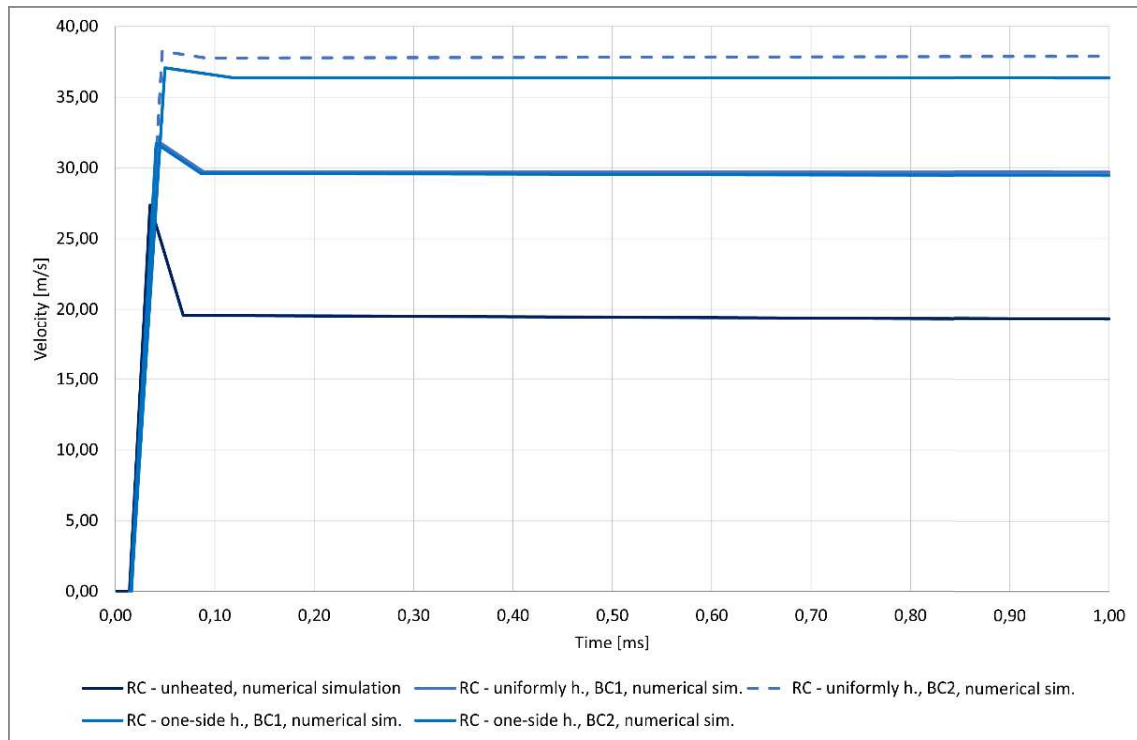
Figure 70 Comparison of numerical simulation results depending on type of heating

Table 39 Maximum velocities in time, BC1 and BC2 models – all types of specimens

		t_1	t_2 (v_{max})	t_3	t_4	Δv [m/s]
Unheated	Time [ms]	0.0139	0.0349	0.0679	1.0000	
	Velocity [m/s]	0.00	27.37	19.59	19.30	7.78
One-side h. BC1	Time [ms]	0.0150	0.0409	0.0857	1.0000	
	Velocity [m/s]	0.00	31.74	29.62	29.46	2.13
	Difference to unheated s.		**15.98%**	**51.15%**	**52.64%**	**-72.63%**
One-side h. BC2	Time [ms]	0.0158	0.0497	0.1177	1.0000	
	Velocity [m/s]	0.00	37.07	36.38	36.36	0.70
	Difference to unheated s.		**35.46%**	**85.64%**	**88.40%**	**-91.00%**
Uniformly h. BC1	Time [ms]	0.0160	0.0420	0.0887	1.0000	
	Velocity [m/s]	0.00	31.92	29.71	29.70	2.21
	Difference to unheated s.		**16.63%**	**51.64%**	**53.91%**	**-71.58%**

Uniformly h. BC2	Time [ms]	0.0159	0.0470	0.0908	1.0000	
	Velocity [m/s]	0.00	38.25	37.76	37.89	0.49
	Difference to unheated s.		**39.74%**	**92.72%**	**96.32%**	**-93.75%**

The results of the numerical simulation correspond with the results from the experiment. As shown in Figure 36 and in Table 40 the unheated specimen has the lowest soffit velocity (velocity of flying debris). The maximum velocity for the one-side heated specimen is 16.45% higher than the unheated specimen. The maximum velocity of the uniformly heated specimen is 19.35% higher than unheated specimen. Changing the exposure to elevated temperature from one-side heated to uniformly heated increases soffit velocity by 2.9%.

Table 40 Maximum velocities in time, experiment results – all types of specimens

		t_1	t_2 (v_{max})	t_3	t_4	Δv [m/s]
Unheated	Time [ms]	0.0193	0.0307	0.0963	1.0000	
	Velocity [m/s]	1.93	32.63	23.40	20.44	9.23
One-side h.	Time [ms]	0.0216	0.0306	0.1412	1.0000	
	Velocity [m/s]	1.48	38.00	27.82	26.28	10.18
	Difference to unheated s.		16.45%	18.89%	28.57%	10.25%
Uniformly h.	Time [ms]	0.0220	0.0310	0.0597	1.0000	
	Velocity [m/s]	1.07	38.94	33.38	30.90	5.56
	Difference to unheated s.		19.35%	42.67%	51.16%	-39.75%

Table 41 shows a comparison of the maximum measured soffit velocity from the experiment and numerical simulation. From the table it can be seen that increase in velocity for the one-side heated specimen is higher than for the uniformly heated specimen and this is valid in both the cases of experimental measurement and numerical simulation. This can also be seen as a validation of the numerical simulation.

Table 41 Comparison of maximum velocities – experiment and numerical simulation

		Numerical simulation	Experiment - PDV
Unheated	Velocity [m/s]	27.37	32.63
One-side heated	Velocity [m/s]	31.74 – 37.07	38.00
	Difference to unheated	**15.98% – 35.46%**	**16.45%**
Uniformly heated	Velocity [m/s]	31.92 – 38.25	38.94
	Difference to unheated	**16.63% – 39.74%**	**19.35%**

4.4.2.2.3 Comparison with simulation for elevated temperature 500 °C

As described above, a simulation for a higher elevated temperature was performed to confirm the behavior.

Figure 71 shows a comparison of the results for uniformly heated specimens at two different temperatures. The resulting values in times are shown in Table 42. The percentage increase in velocities is also given in this table. In the graph it is possible to find the increase in velocities but also the change in the slope of the final curve. The maximum velocity increased by 9.93% - 34.13% when exposed to elevated temperature of 100 °C higher.
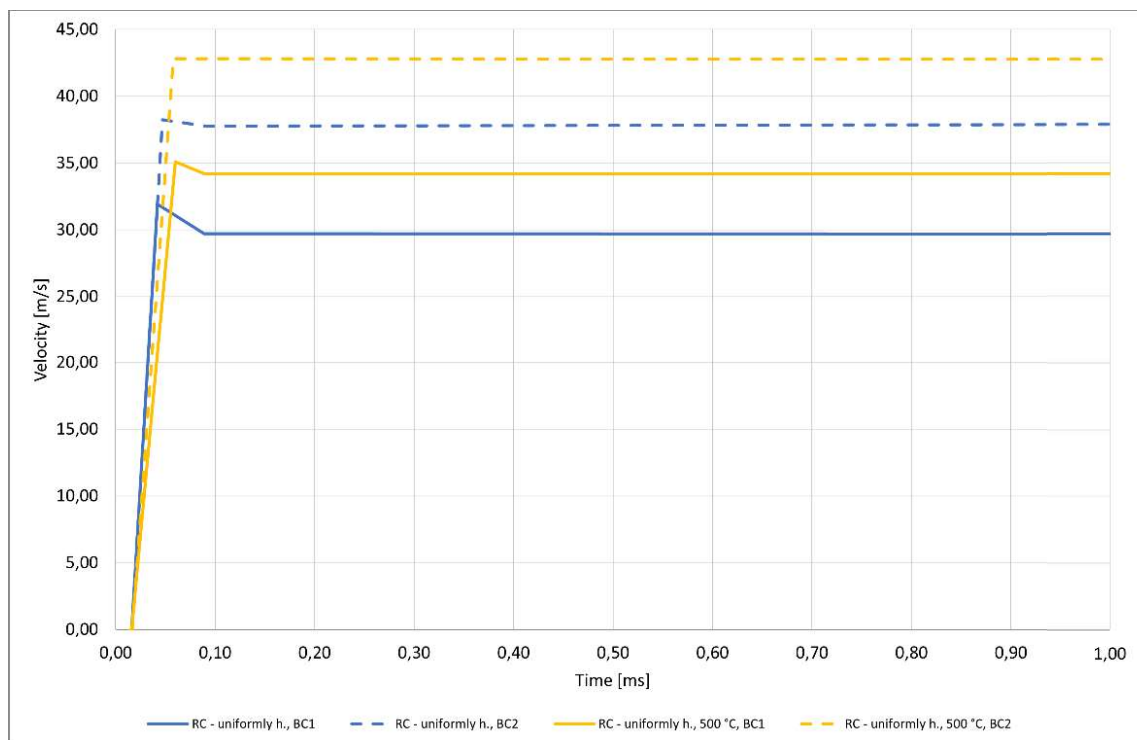
Figure 71 Comparison of results for uniformly heated specimens – 400 °C and 500 °C

Table 42   Maximum velocities in time for uniformly heated specimens – 400 °C and 500 °C

		t_1	t_2 (v_{max})	t_3	t_4	Δv [m/s]
Uniformly 400 °C BC1	Time [ms]	0.0160	0.0420	0.0887	1.0000	
	Velocity [m/s]	0.00	31.92	29.71	29.70	2.21
Uniformly 400 °C BC2	Time [ms]	0.0159	0.0470	0.0908	1.0000	
	Velocity [m/s]	0.00	38.25	37.76	37.89	0.49
Uniformly 500 °C BC1	Time [ms]	0.0160	0.0599	0.0889	1.0000	
	Velocity [m/s]	0.00	35.09	34.21	34.18	0.88
	Difference 400 °C and 500 °C		9.93%	15.14%	15.09%	-60.23%

Uniformly 500 °C BC2	Time [ms]	0.0168	0.0579	0.0579	1.0000	
	Velocity [m/s]	0.00	42.82	42.82	42.76	0.00
	Difference 400 °C and 500 °C		34.13%	44.11%	43.95%	

Comparison for one-side heated specimens is shown in Figure 72. Table 43. shows the maximum velocities in times. It can be seen again that the higher temperatures increased the soffit velocity as well as the slope of the final curve. The maximum velocity increased by 7.95% - 32.63%.
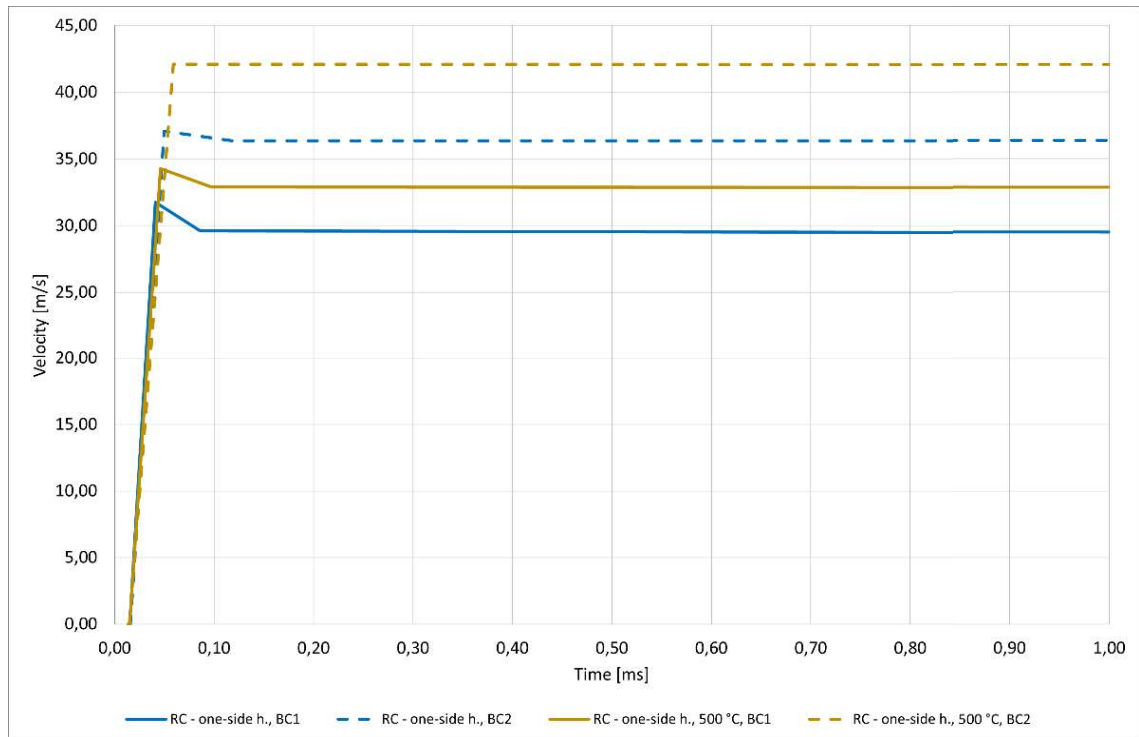
Figure 72 Comparison of results for one-side heated specimens – 400 °C and 500 °C

Table 43   Maximum velocities in time for one-side heated specimens – 400 °C and 500 °C

		t_1	t_2 (v_{max})	t_3	t_4	Δv [m/s]
One-side 400 °C BC1	Time [ms]	0.0150	0.0409	0.0857	1.0000	
	Velocity [m/s]	0.00	31.74	29.62	29.46	2.13
One-side 400 °C BC2	Time [ms]	0.0158	0.0497	0.1177	1.0000	
	Velocity [m/s]	0.00	37.07	36.38	36.36	0.70
One-side 500 °C BC1	Time [ms]	0.0149	0.0459	0.0970	0.0000	
	Velocity [m/s]	0.00	34.27	32.90	32.85	1.37
	Difference 400 °C and 500 °C		7.95%	11.09%	11.53%	-35.82%

One-side 500 °C BC2	Time [ms]	0.0147	0.0589	0.0589	1.0000	
	Velocity [m/s]	0.00	42.10	42.10	42.08	0.00
	Difference 400 °C and 500 °C		**32.63%**	**42.16%**	**42.85%**	

Table 44 shows a comparison of the maximum velocities. It is again true that the increase in velocity is higher for uniformly heated than for one-side heated.

Table 44 Comparison of maximum velocity depending on elevated temperature and type of heating

		One-side heated	Uniformly heated
400 °C	Velocity [m/s]	31.74 − 37.01	31.92 − 38.25
500 °C	Velocity [m/s]	34.27 − 42.10	35.09 − 42.82
	Difference	7.95% − 32.63	9.93% − 34.13%

4.4.3 Fringe of z-velocity comparison

Numerical simulation has the advantage over experiment of being able to study, besides other things, the propagation of the shock wave in the specimens. Several ways can be used for this observation. One of them is to study the change of behavior on a selected cross section. In this case, the cross-sectional area centered on the specimen was chosen. The cut area is also indicated in Figure 73. In this cut, a fringe od z-velocity was chosen. The individual results are shown in Figure 74 − Figure 77. The values were plotted at different times.
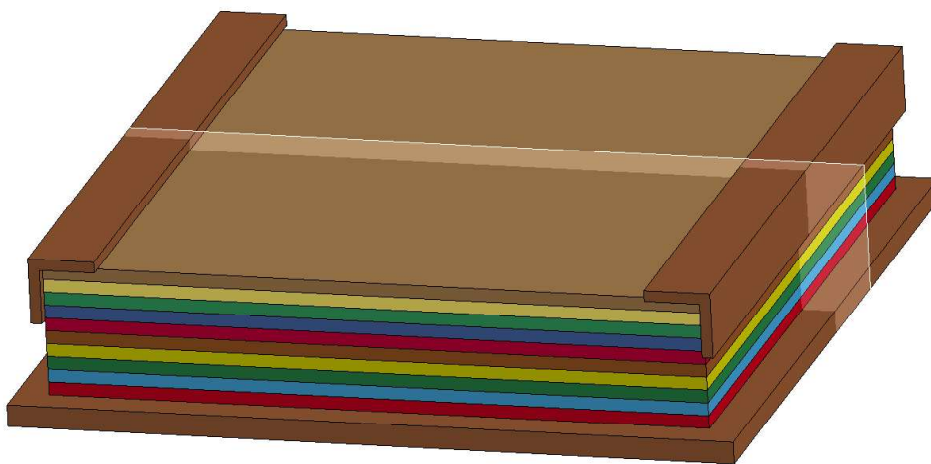
Figure 73 Selected cross section of the specimen

Table 45 gives the times at which the fringes are plotted in Figure 74. For comparison, results for: unheated specimen, one-side heated specimen (BC2 model) and uniformly heated specimen (BC2 model) were chosen.

The selected times represent the times that can be read from the plots presented above. Time t_1 represents the initiation of the surface into motion, time t_2 represents time at which the maximum velocity has been reached, at time t_3 the velocity has decreased (pullback velocity) and t_3 is the final time of the calculation.

Table 45   Times for fringe of z-velocity comparison

	Unheated s.	One-side heated s. BC2	Uniformly heated s. BC2
t_0	0 ms	0 ms	0 ms
t_1	0.0148 ms	0.0158 ms	0.0159 ms
t_2 (v_{max})	0.0349 ms	0.0497 ms	0.0470 ms
t_3	0.0679 ms	0.1177 ms	0.0908 ms
t_4	1 ms	1 ms	1 ms

In Figure 74 it is possible to compare the damage of the elements. The comparison of other parameters is only indicative due to the fact that values at different times after the explosion are plotted. From the point of view of the damage, the one-side heated specimen seems to be the most damaged when the maximum velocity is reached, as well as at time t_3 when the velocity decreases. However, when comparing at the end of the simulation (i.e. at time 1 ms), the uniformly heated specimen is clearly seen to be most damaged.
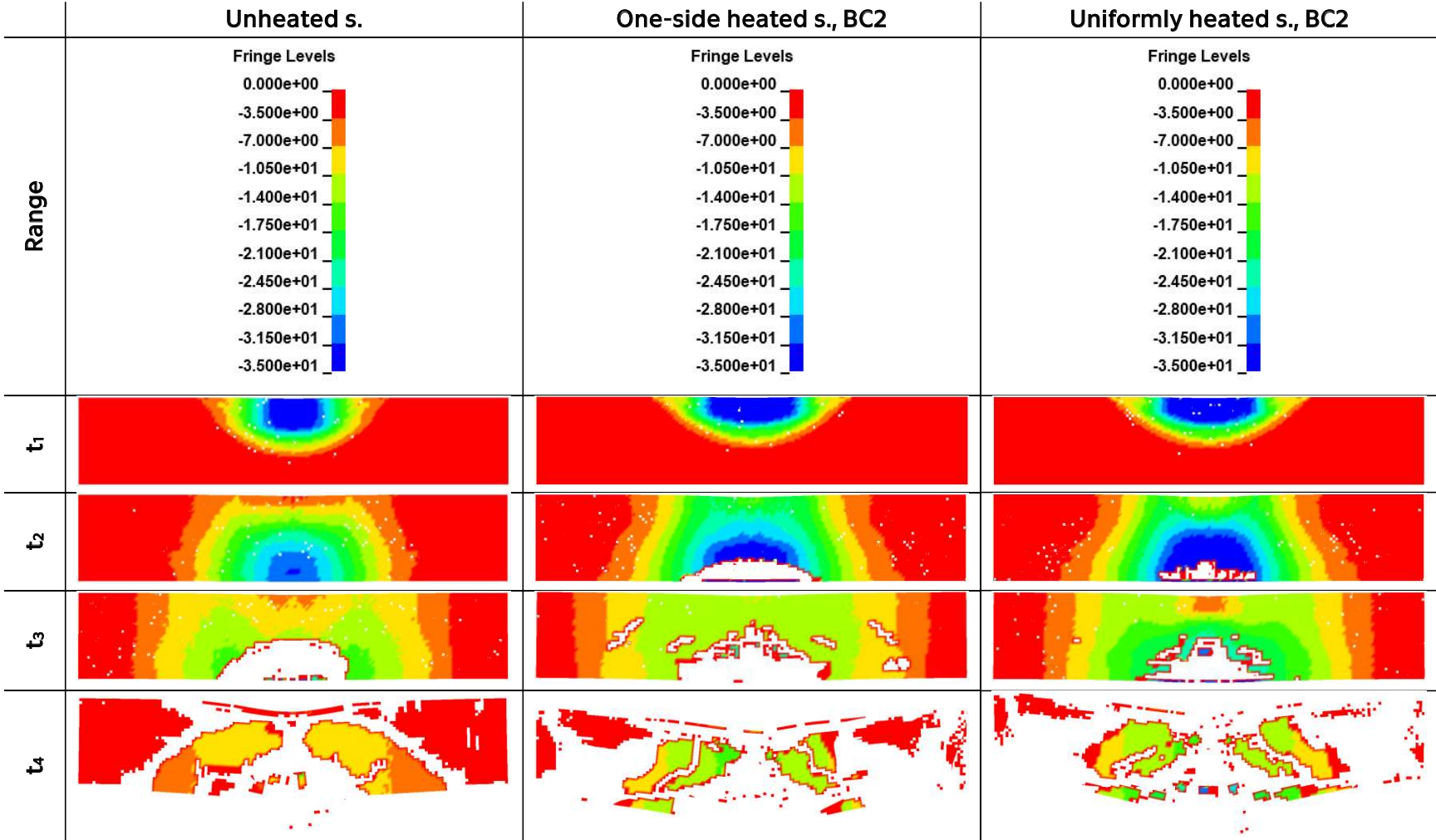
Figure 74 Fringe of z-velocity at various times after detonation

To compare the shock wave propagation or velocity change in the test specimen, it is necessary to plot the fringe of z-velocity at the same time. This plot is shown in Figure 75. The times shown in Table 46 were chosen for comparison. These are the times that were determined when simulation of the unheated specimen was made.

Table 46   Times for fringe of z-velocity comparison

	Unheated s.	One-side heated s. BC2	Uniformly heated s. BC2
t_0	0 ms	0 ms	0 ms
t_1	0.0148 ms	0.0147 ms	0.0149 ms
t_2 (v_{max})	0.0349 ms	0.0347 ms	0.0349 ms
t_3	0.0679 ms	0.0678 ms	0.0678 ms
t_4	1 ms	1 ms	1 ms

As part of the comparison, it is necessary to evaluate all times separately. At time t_1 when the bottom surface starts to move, the velocity propagation in the specimens exposed to the elevated temperature is almost the same. In the unheated specimen, the blast exposure has a more local behavior. At time t_2, i.e. at the time when the maximum soffit velocity has been reached in the unheated specimen, it can be seen that the top surface of the specimen has slowed down significantly, however, the uniformly heated specimen has a high velocity also at the top surface. At time t_3, the uniformly heated specimen is already slowing down at the top surface. The unheated specimen is the most damaged and the propagation of the shock wave through the specimen is completely stopped. At the end of the simulation at time t_4, only the damage level can be compared, which is the highest for the uniformly heated specimen. The unheated element is already slowed down and the heated elements are slowing down.
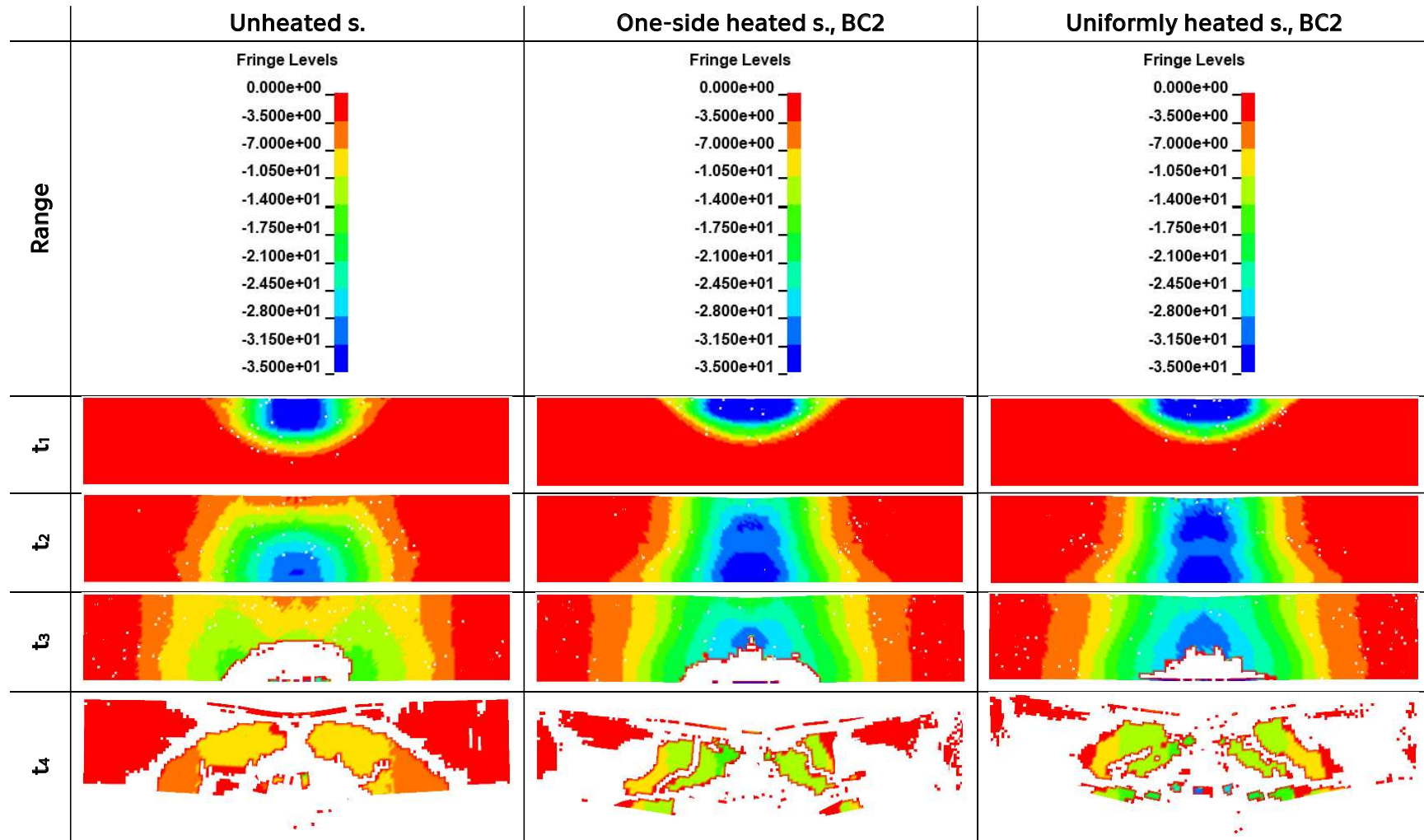
Figure 75 Fringe of z-velocity at various times after detonation

The next comparison is for a simulation with a higher temperature of 500 °C. Figure 76 shows the fringes of z-velocity at the times presented in the resulting graphs. These times are also given in Table 47. This comparison can again be used to compare the damage level of the element when the maximum velocity is reached (at time t_2). The unheated specimens look without any signs of damage while the heated specimens are damaged at both the lower and upper surfaces. While the damage of uniformly heated specimens is much more extensive on both surfaces. The final damage of the specimen is again the largest for the uniformly heated specimen.

Table 47 Times for fringe of z-velocity comparison, temperature 500 °C

	Unheated s.	One-side heated s. 500 °C, BC2	Uniformly heated s. 500 °C, BC2
t_0	0 ms	0 ms	0 ms
t_1	0.0148 ms	0.0147 ms	0.0168 ms
t_2 (v_{max})	0.0349 ms	0.0589 ms	0.0579 ms
t_3	0.0679 ms	---	0.0679 ms
t_4	1 ms	1 ms	1 ms
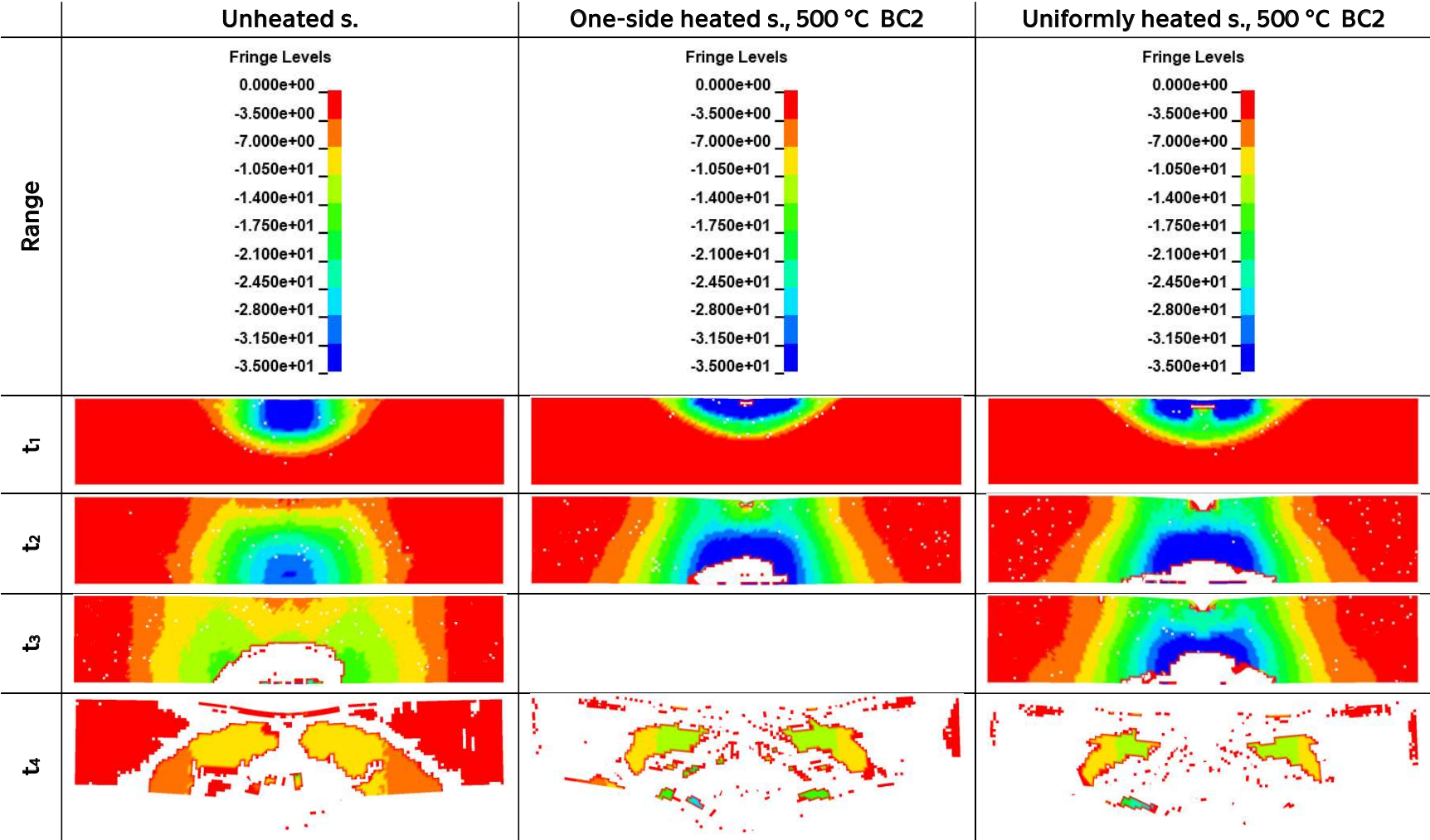
Figure 76 Fringe of z-velocity at various times after detonation, temperature 500 °C

Figure 77 presents a comparison of the fringe of z-velocity in the times of reaching each velocity of the unheated specimen. These times are listed in Table 48.

Table 48 Times for fringe of z-velocity comparison, temperature 500 °C

	Unheated	One-side heated s. 500 °C, BC2	Uniformly heated s. 500 °C, BC2
t_0	0 ms	0 ms	0 ms
t_1	0.0148 ms	0.0147 ms	0.0149 ms
t_2 (v_{max})	0.0349 ms	0.0349 ms	0.0348 ms
t_3	0.0679 ms	0.0678 ms	0.0679 ms
t_4	1 ms	1 ms	1 ms

At time t_1 the first deformation and damage of the heated specimen can be seen. At time t_2, when the maximum velocity of the unheated specimen is reached, the heated specimen is still being accelerated at the bottom surface, and at the same time the top surface is breaking. At time t_3 it is possible to compare the bottom surface damage when damage of similar size appears. In the case of the unheated specimen, the entire specimen slows down slowly, but the heated specimen continues to develop high velocities. At time t_4 the final damage is shown which is highest for the uniformly heated specimen.
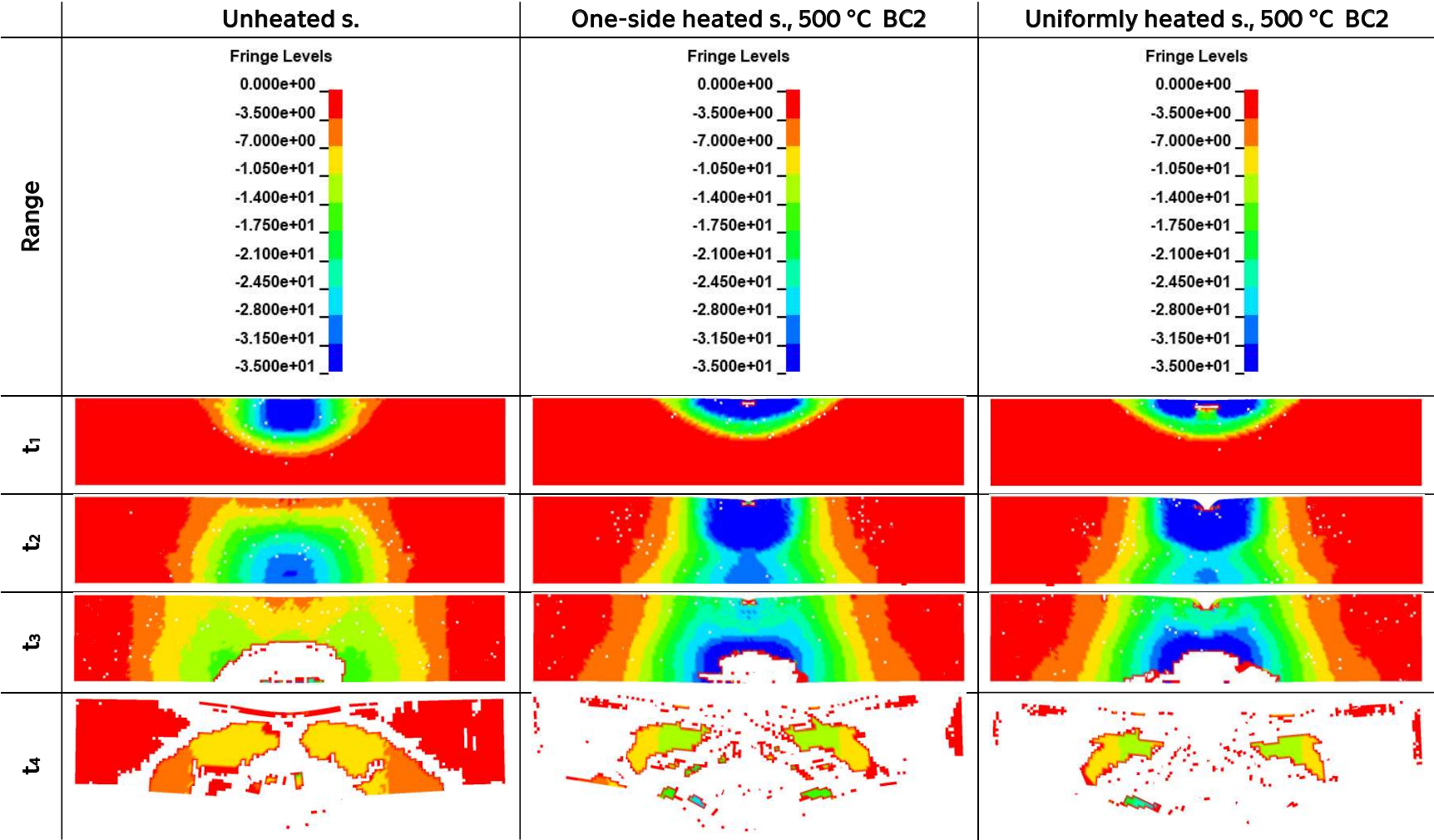
Figure 77 Fringe of z-velocity at various times after detonation, temperature 500 °C

4.5 Summary and discussion

This chapter presented a numerical simulation of the above described experiment. A numerical simulation was performed only for ordinary concrete (RC material). FE model was created in the LS Dyna program. A model of the specimen including its support was created to properly define the boundary conditions. Idealization was performed to model the effect of elevated temperature. In the idealization the specimen is divided into several layers. In each layer, the maximum reached temperature was determined based on its determined material properties.

An issue in this approach represents the compressive and tensile strength of the material. When exposed to elevated temperature, the tensile strength decreases faster than the compressive strength. However, this is not reflected in the material model approach. Therefore, the elements subjected to the elevated temperature were modelled in two limit states (BC1 and BC2 models), or in other words, boundary states. In the first limit state (BC1 model), the compressive strength was determined based on the elevated temperature. Using this approach, the value of the tensile strength in the model is higher than in reality. In the second limit state (BC2 model), the compressive strength value was lowered to correspond to the tensile strength according to the elevated temperature. In this case, the compressive strength of concrete is very conservative. With this approach, a range of the real results was determined.

Numerical simulations were performed for exposure to the elevated temperature of 400 °C, as in the experiment. Alternatively, the effect of exposure to higher temperature of 500 °C was calculated. Based on these temperatures, the material properties at the given points were determined and a simulation of the experiment was performed in the same form as for 400 °C. This extrapolated comparison is used to determine the impact of higher temperatures without the need of further experimental measurement.

The result of the numerical simulation is the determined value of the velocity of the soffit of the specimen. Soffit velocities were determined by averaging the velocity values of eight FE-elements. Based on these values, an idealized velocity-time graph was created. The idealized graph is similar to the resulting idealized graph from the experiment. The values of the maximum velocities achieved are shown in Table 49. The specimens exposed to elevated temperature from only one-side show maximum soffit velocities 15.98% - 35.46% higher than the unheated specimen. Uniformly heated

specimens show maximum soffit velocities 16.63% - 39.74% higher than the unheated specimen. Therefore, when uniformly heated specimen, the soffit velocity is 0.56% - 3.16% higher than one-side heated specimen.

Table 49 Maximum velocities depending on the type of heated

		t_2 (v_{max})	Δv [m/s]
Unheated	Velocity [m/s]	27.37	7.78
One-side h.	Velocity [m/s]	31.74 − 37.07	2.13 − 0.70
	Difference to unheated s.	15.98% - 35.46%	-72.63% - -91.00%
Uniformly h.	Velocity [m/s]	31.92 − 38.25	2.21 − 0.49
	Difference to unheated s.	16.63% - 39.74%	-71.58% - - 93.75%
	Difference to one-side heated s.	0.56% - 3.16%	3.84% - -30.57%

Table 50 shows the maximum soffit velocities in all simulated cases. It the table can be seen that when the elevated temperature is increased up to 500 °C, there is an increase in soffit velocity compared to the unheated specimen by 25.2% - 53.83% in the case of one-side heated specimens. In case of uniformly heated specimens, there is an increase in soffit velocity by 28.21% - 56.44%. Compared to the applied temperature of 400 °C, there is an increase of soffit velocity by 7.95% - 13.56% in the case of one-side heated specimens. In the case of uniformly heated specimens, there is an increase in soffit velocity of 9.93% - 11.95%. In the case of comparison of soffit velocity between one-side heated and uniformly heated when subjected to temperature of 500 °C is lower and ranges between 1.7% - 2.4%.

Table 50 Maximum velocities depending on elevated temperature

		t_2 (v_{max})	Δv [m/s]
Unheated	Velocity [m/s]	27.37	7.78
One-side h. s. 400 °C	Velocity [m/s]	31.74 − 37.07	2.13 − 0.70
	Difference to unheated s.	15.98% - 35.46%	-72.63% - -91.00%
One-side h. s. 500 °C	Velocity [m/s]	34.27 − 42.10	1.37 − 0.00
	Difference to unheated s.	25.20% - 53.83%	-82.43% - -100%
	Difference to 400 °C	7.95% - 13.56%	
Uniformly h. s. 400 °C	Velocity [m/s]	31.92 − 38.25	2.21 − 0.49
	Difference to unheated s.	16.63% - 39.74%	-71.58% - -93.75%
	Difference to one-side h. s. 400 °C	0.56% - 3.16%	

	Velocity [m/s]	35.09 − 42.82	0.88 − 0.00
Uniformly h. s. 500 °C	Difference to unheated s.	28.21% - 56.44%	-88.70% - -100%
	Difference to 400 °C	9.93% - 11.95%	
	Difference to one-side h. s. 500 °C	1.70% - 2.40 %	

The fringes of the z-velocity are the next presented result. The cross-section through the center of the specimen was chosen for the evaluation. This made it possible to see the behavior of various values along its height. At the same time, this makes it possible to study the shock wave propagation and damage in the element that is not visible in a normal experiment. In this observation, it was found that the damage of the unheated specimen is more local than that of the heated specimen. At the same time, the heated specimens start to breach later but the final damage is bigger than the damage of the heated specimens.

From the above, it can be concluded that when exposed to high temperature of 400 °C for 3 hours, there is an increase in soffit velocity of specimens by 15.98% - 39.74% depending on the type of high temperature exposure. When the applied temperature is increased by 100°C, the soffit velocity of specimens is then 7.95% - 13.56% higher.

Interpretation of the numerical simulation results is difficult due to the different types of heating and the method of numerical modelling (BC1 and BC2). Therefore, the graphs shown in Figure 78 and Figure 79 were created. These graphs show the maximum soffit velocity as a function of the temperature. The graphs are separated into one-side heated and uniformly heated specimen of RC material. Both graphs show curves that provide the predicted curves for the computations of the two boundary conditions BC1 and BC2. They define the range of soffit velocities in which the maximum soffit velocities will be as a function of the effective temperature. At the theoretical maximum temperatures of normal fire loading, the maximum soffit velocities are multiply higher than in experimental measurements.
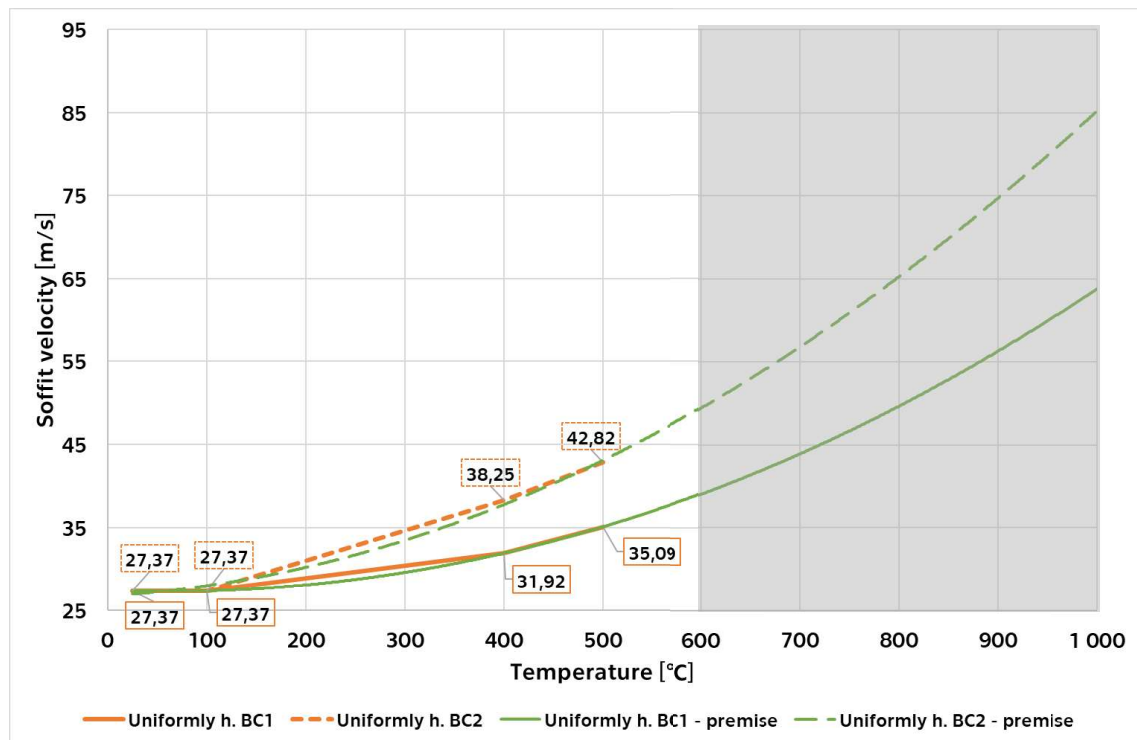
Figure 78   Final graph of maximum soffit velocity depending on elevated temperature – uniformly heated specimen, RC material
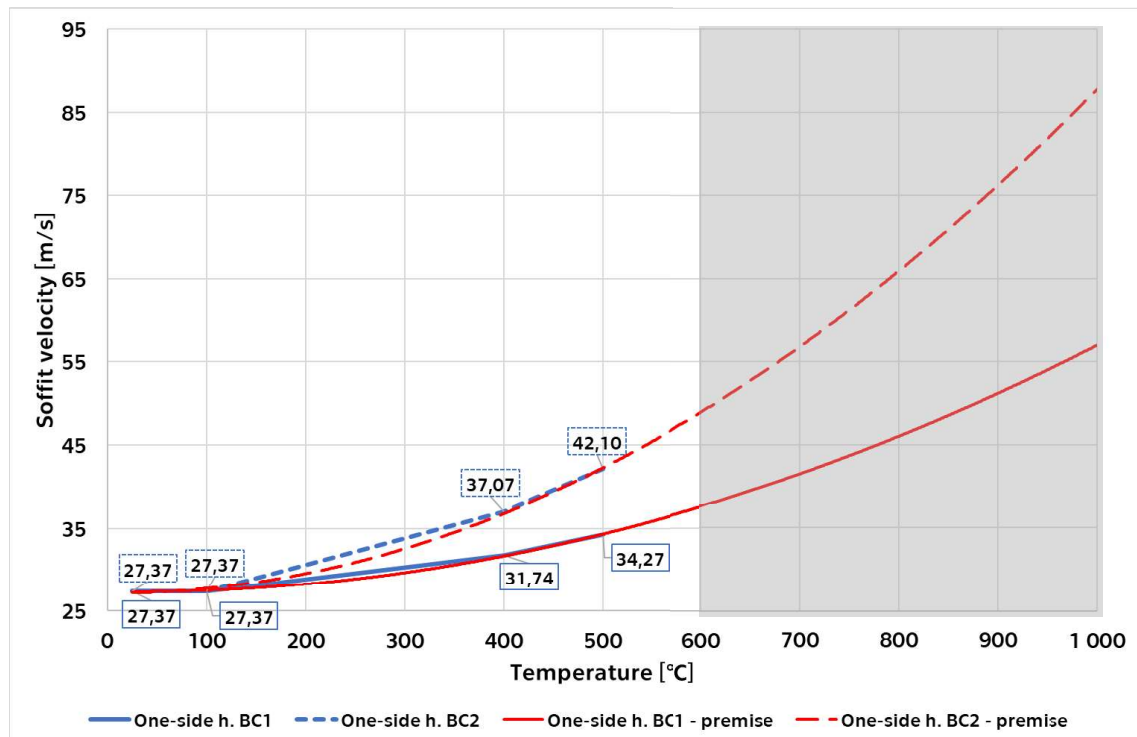
Figure 79   Final graph of maximum soffit velocity depending on elevated temperature – one-side heated specimen, RC material

For temperatures above 600 °C (gray area), the curves are only speculative, and the waveforms are probably to become more steep and the soffit

velocity (velocity of flying debris) to increase much faster. This is because the tensile strength of the material is hypothetically almost zero.

5 Conclusion

The motivation of this thesis was to qualify the combined effect of fire and blast loading because this phenomenon was not well studied yet. At the same time, these the topic presents quite usual, or common situation. The design of structures for extreme impacts is also becoming common and it is necessary to understand how the loads affect the structures.

The foundation of this thesis is a complex original experimental program divided into several parts. These parts correlate with the main objectives of the thesis.

Three main objectives were set for this thesis. The first objective was to confirm the effect of permeability on the fire and blast resistance of the material. In the described experimental program, this prediction did not appear to be a critical parameter. The changing permeability of a material is closely related to other material properties. Its effects on the resistance of the elements to combined loads have not been demonstrated.

The second objective of this thesis was to determine the effect of mechanical properties on the fire and blast resistance of these materials. This objective was achieved. The presented experiments show a major influence of the material tensile strength on its blast resistance. This effect is confirmed by many studies dealing with the effect of blast on cement composites. The elevated temperature influences the tensile strength of the concrete element, which then shows a lower resistance to the exposed blast loading. The tensile strength seems to be the most important parameter of the studied problem.

The third and main objective of this thesis was to understand and quantify the phenomenon of combined effect and to describe the trend of behavior under combined extreme loading - high temperature (fire) and blast. The last objective showed itself to be the most complex one. The achievement was significantly assisted by numerical simulation experiments, also extrapolations of the experimentally obtained data. Throughout the experimental program, attention was focused on the mechanical properties of the materials used. With these in mind, the materials for the second part of the experimental program were selected. The properties of the materials influenced the maximum elevated temperature but also the blast experiment arrangement (distance and size of the charge). All presented results show a prevailing influence of the tensile strength of the materials. A

complex understanding and quantification of the phenomenon is presented throughout the thesis.

5.1 Recommendations for further research

With respect to a better understanding of the described phenomenon, it is appropriate to continue the experiments for further study. Further experiments should be devoted to changes in the elevated temperature. Increasing temperature to values close to the real temperature during a fire. When the temperature of the structure exceeds 600 °C, the tensile strength of the material will be theoretically lost and the changes in the behavior of the structure after reaching this temperature will not be negligible. If the experiments were carried out at lower temperatures, it would be possible to describe the phenomenon also for structures that are not directly exposed to the fire but are far away from the fire and only slightly increase their temperature.

Furthermore, it is necessary to complete the numerical simulation. In the first step, the experiments performed with other materials need to be simulated. Subsequently, it would be advisable to choose a different material model. This should take into respect the influence of the elevated temperature on the material. Then it will be possible to simulate most of the experiments. Ideally, this would simplify the whole experimental program. The whole process could be performed ideally in the following steps: selection of the material to be studied, experimental determination of the basic material properties, numerical simulation of the exposure to elevated temperature, and numerical simulation of the exposure to blast loading. This procedure seems to be ideal and opens many possibilities for further work.

Obviously the most ideal outcome would be to find a relation between the increased temperature and the velocity of flying debris (soffit velocity), as illustrated in the final graphs at the end of chapter 4. If curves of the dependence of soffit velocity on the applied temperature could be determined for a group of materials with similar material properties, this would simplify the whole process of designing and evaluating structures for the combined effect of fire and blast loading.

List of Figures

List of Tables

References

[1] Kakogiannis, D., Pascualena, F., Reymen, B., Pyl, L., Ndambi, J. M., Segers, E., Lecompte, D., Vantomme, J., Krauthammer, T. (2013). Blast performance of reinforced concrete hollow core slabs in combination with fire: Numerical and experimental assessment. *Fire Safety Journal*, *57*, 69-82. DOI: 10.1016/j.firesaf.2012.10.027

[2] Ruan, Z., Chen, L., Fang, Q. (2015). Numerical investigation into dynamic responses of RC columns subjected for fire and blast. *Journal of Loss Prevention In The Process Industries*, *34*, 10-21. DOI: 10.1016/j.jlp.2015.01.009

[3] Zhai, C., Chen, L., Xiang, H., Fang, Q. (2016). Experimental and numerical investigation into RC beams subjected to blast after exposure to fire. *International Journal of Impact Engineering*, *97*, 29-45. DOI: 10.1016/j.ijimpeng.2016.06.004

[4] Choi, S. -J., Lee, S. -W., and Kim, J. -H. J. (2017). Impact or blast induced fire simulation of bi-directional PSC panel considering concrete confinement and spalling effect. Engineering Structures, 149, 113-130. DOI: 10.1016/j.engstruct.2016.12.056

[5] Foglar, M., Hájek, R., Štefan, R., and Stöhr, J. (2016). Vyšetřování vlastností cementových kompozitů vystavených působení extrémních zatížení: experimenty, modelování, technologie. České vysoké učení technické.

[6] Horníková, K., Scheinherrová, L., Štefan, R., Foglar, M. (2020). Experimental investigation of physical, thermal, hygral and mechanical properties of cementitious composites at high temperatures. *Construction and Building Materials*, *255*. DOI: 10.1016/j.conbuildmat.2020.119244

[7] Neville, A.M. (1995) Proparties Of Concrete. 4th and final ed. Harlow: Longman Group. ISBN 0-582-23070-5.

[8] Bažant, Z. and Kaplan, M.F. (1996) Concrete At High Temperatures: Material Properties And Mathematical Models. Concrete Design And Series Construction. Harlow: Longman. ISBN 0-582-08626-4.

[9] Kodur, V. (2014) Properties Of Concrete At Elevated Temperatures. Online. ISRN Civil Engineering 2014: 1-15. doi:10.1155/2014/468510.

[10] Fire Design Of Concrete Structures: Materials, Structures And Modelling: State-Of-Art Report. (2007) Bulletin. Lausanne: International Federation for Structural Concrete. ISBN 978-2-88394-078-9.

[11] Guo, Z. and Shi, X. (2011) Experiment and Calculation of Reinforced Concrete At Elevated Temperatures. Waltham, MA: Butterworth-Heinemann. ISBN 978-0-12-386962-3.

[12] Asadi, I., Shafigh, P., Abu Hassan, Z.F.B. and Mahyuddin, N.B. (2018) Thermal Conductivity of Concrete – A Review. Online. Journal Of Building Engineering 20: 81-93. doi:10.1016/j.jobe.2018.07.002.

[13] Wang, W.-C. (2017) Compressive Strength and Thermal Conductivity Of Concrete With Nanoclay Under Various High-Temperatures. Online. Construction and Building Materials 147: 305-311. doi:10.1016/j.conbuildmat.2017.04.141.

[14] Sayadi, A.A., Tapia, J.V., Neitzert, T.R. and Clifton, G.C. (2016) Effects of Expanded Polystyrene (Eps) Particles on Fire Resistance, Thermal Conductivity and Compressive Strength of Foamed Concrete. Online. Construction and Building Materials 112: 716-724. doi:10.1016/j.conbuildmat.2016.02.218.

[15] Othuman, M. A. and Wang, Y.C. (2011) Elevated-Temperature Thermal Properties Of Lightweight Foamed Concrete. Online. Construction and Building Materials 25 (2): 705-716. doi:10.1016/j.conbuildmat.2010.07.016.

[16] Pomianowski, M., Heiselberg, P., Jensen, R. L., Cheng, R., and Zhang, Y. (2014). A new experimental method to determine specific heat capacity of inhomogeneous concrete material with incorporated microencapsulated-PCM. Cement And Concrete Research, 55, 22-34. doi.org/10.1016/j.cemconres.2013.09.012

[17] Toman, J. and Černy, R. (1995) Calorimetry of Building Materials. Online. Journal Of Thermal Analysis 43 (2): 489-496. doi:10.1007/BF02546837.

[18] Ruuska, T., Vinha, J. and Kivioja, H. (2017) Measuring Thermal Conductivity and Specific Heat Capacity Values Of Inhomogeneous Materials With A Heat Flow Meter Apparatus. Online. Journal of Building Engineering 9: 135-141. doi:10.1016/j.jobe.2016.11.011.

[19] Ahlem Houaria, M.B., Abdelkader, M., Marta, C. and Abdelhafid, K. (2017) Comparison Between the Permeability Water and Gas Permeability Of The Concretes Under The Effect Of Temperature. Online. Energy Procedia 139: 725-730. doi:10.1016/j.egypro.2017.11.278.

[20] Kameche, Z.A., Ghomari, F., Choinska, M. and Khelidj, A. (2014) Assessment of Liquid Water and Gas Permeabilities Of Partially

Saturated Ordinary Concrete. Online. Construction And Building Materials 65: 551-565. doi:10.1016/j.conbuildmat.2014.04.137.

[21] Hoseini, M., Bindiganavile, V. and Banthia, N. (2009) The Effect of Mechanical Stress on Permeability of Concrete: A Review. Online. Cement and Concrete Composites 31 (4): 213-220. doi:10.1016/j.cemconcomp.2009.02.003.

[22] Bošnjak, J., Ožbolt, J. and Hahn, R. (2013) Permeability Measurement on High Strength Concrete Without and With Polypropylene Fibers at Elevated Temperatures Using a New Test Setup. Online. Cement And Concrete Research 53: 104-111. doi:10.1016/j.cemconres.2013.06.005.

[23] Noumowe, A.N., Siddique, R. and Debicki, G. (2009) Permeability of High-Performance Concrete Subjected To Elevated Temperature (600°C). Construction And Building Materials 23 (5): 1855-1861. doi:10.1016/j.conbuildmat.2008.09.023.

[24] Gawin, D., Majorana, C.E. and Schrefler, B.A. (1999) Numerical analysis of hygro-thermal behaviour and damage of concrete at high temperature. Mech. Cohes.-Frict. Mater., 4: 37-74. doi:10.1002/(SICI)1099-1484(199901)4:1<37::AID-CFM58>3.0.CO;2-S

[25] Ma, Q., Guo, R., Zhao, Z., Lin, Z. and He, K. (2015) Mechanical Properties of Concrete At High Temperature—A Review. Online. Construction and Building Materials 93: 371-383. doi:10.1016/j.conbuildmat.2015.05.131.

[26] Arioz, O. (2007) Effects of Elevated Temperatures on Properties of Concrete. Online. Fire Safety Journal 42 (8): 516-522. doi:10.1016/j.firesaf.2007.01.003.

[27] Phan, L.T. and Carino, N.J. (1998) Review of Mechanical Properties of HSC At Elevated Temperature. Journal Of Materials In Civil Engineering 10 (1): 58-65. doi:10.1061/(ASCE)0899-1561(1998)10:1(58).

[28] Varona, F.B., Baeza, F.J., Bru, D. and Ivorra, S. (2018) Influence Of High Temperature On The Mechanical Properties Of Hybrid Fibre Reinforced Normal And High Strength Concrete. Construction and Building Materials 159: 73-82. doi:10.1016/j.conbuildmat.2017.10.129.

[29] Baradaran-Nasiri, A. and Nematzadeh, M. (2017) The Effect Of Elevated Temperatures On The Mechanical Properties Of Concrete With Fine Recycled Refractory Brick Aggregate And Aluminate Cement. Construction and Building Materials 147: 865-875. doi:10.1016/j.conbuildmat.2017.04.138.

[30] EN 1992-1-2 (2006): Eurocode 2: Design of concrete structures Part 1-2. General rules – Structural fire design

[31] Pavlíková, M., Pavlík, Z., Keppert, M., and Černý, R. (2011). Salt transport and storage parameters of renovation plasters and their possible effects on restored buildings' walls. Construction And Building Materials, 25(3), 1205-1212. doi.org/10.1016/j.conbuildmat.2010.09.034

[32] EN ISO 1927-6: Monolithic (unshaped) refractory products – Part 6: Measurement of physical properties.

[33] EN 993-1: Methods of test for dense shaped refractory products – Part 1: Determination of bulk density, apparent porosity and true porosity

[34] EN 993-15: (2005): Methods of test for dense shaped refractory products – Part 15: Determination of thermal conductivity by the hot-wire (Parallel) method

[35] Černý, R. and Vejmelková, E. (2011) Apparent Thermal Conductivity Approach at High-Temperature Measurements of Porous Materials. Measurement 44 (7): 1220-1228. doi:10.1016/j.measurement.2011.04.002.

[36] EN 993-4: (1996): Methods of test for dense shaped refractory products – Part 4: Determination of permeability gases.

[37] EN 12390-3: Testing hardened concrete – Part 3: Compressive strength of test specimens

[38] Kalifa, P., Tsimbrovska, M. and Baroghel-Bouny, V. (1998) High-performance concrete at elevated temperatures - an extensive experimental investigation of thermal and hygral properties and microstructure. International symposium on high-performance and reactive powder concretes. Université de Sherbrooke, Sherbrooke, Canada, 259-279.

[39] Osuji, S.O. and Ukeme, U. (2015) Effects of Elevated Temperature On Compressive Strength Of Concrete: A Case Study Of Grade 40 Concrete. Nigerian Journal of Technology 34 (3): 472-477. doi:10.4314/njt.v34i3.7.

[40] Bamonte, P., and Gambarova, P. (2014). Properties of Concrete Subjected to Extreme Thermal Conditions. Journal Of Structural Fire Engineering, 5(1), 47-62. doi.org/10.1260/2040-2317.5.1.47

[41] R. Štefan, M. Foglar, J. Fládr, Experimental investigation of behaviour of various types of cementitious composites exposed to fire, Beton TKS 15 (6) (2015) 56-61, [in Czech].

References

[42] Mindeguia, J.-C. (2009) Contribution expérimentale à la compréhension des risques d'instabilité thermique des bétons, PhD thesis, UPPA.

[43] Compressive Strength for Service and Accident Conditions. (1995) Online. Materials and Structures 28 (7): 410-414. doi:10.1007/BF02473077.

[44] Holan, J., Novák, J., Müller, P., and Štefan, R. (2020). Experimental investigation of the compressive strength of normal-strength air-entrained concrete at high temperatures. Construction and Building Materials, 248. doi:10.1016/j.conbuildmat.2020.118662

[45] Müller, P., Novák, J., and Holan, J. (2019). Destructive and non-destructive experimental investigation of polypropylene fibre reinforced concrete subjected to high temperature. Journal of Building Engineering, 26. Doi: 10.1016/j.jobe.2019.100906

[46] Pimienta, P., Mindeguia, J.-C., Simon, A. and Behloul, M. (2011) Behavior Of Uhpfrc At High Temperatures. In Designing and Building With UHPFRC, 579-600. Hoboken, NJ USA: John Wiley. doi:10.1002/9781118557839.ch40.

[47] Pliya, P., Beaucour, A.-L. and Noumowé, A. (2009) Strength and porosity of concrete incorporating polypropylene and steel fibres subjected to high temperature. Smirt 20 - Espoo (Helsinki), Finland., 10.

[48] Drzymała, T., Jackiewicz-Rek, W., Tomaszewski, M., Kuś, A., Gałaj, J. and Šukys, R. (2017) Effects of High Temperature on the Properties of High Performance Concrete (Hpc). Procedia Engineering 172: 256-263. doi:10.1016/j.proeng.2017.02.108.

[49] Abid, M., Hou, X., Zheng, W. and Hussain, R.R. (2017) High Temperature and Residual Properties of Reactive Powder Concrete – A Review. Construction and Building Materials 147: 339-351. doi:10.1016/j.conbuildmat.2017.04.083.

[50] Peng, G.F., Chan, S.Y.N. and Anson, M. (2001) Chemical Kinetics Of C-S-H Decomposition In Hardened Cement Paste Subjected to Elevated Temperatures Up To 800°C. Advances in Cement Research 13 (2): 47-52. doi:10.1680/adcr.13.2.47.39294.

[51] Štefan, R. - Foglar, M. - Hájek, R. - Fládr, J. (2016) EXPERIMENTAL ANALYSIS OF FLOOR PANELS MADE OF VARIOUS TYPES OF CONCRETE EXPOSED TO BLAST AND SUBSEQUENT FIRE. Beton TKS 16(1), 42-48.

[52] Fang Q., Zhao J., Chen L., Li D. (2015) Numerical prediction of fire resistance of RC beam subjected to blast and fire - J Tianjin Univ , pp. 873-880

[53] Štefan, R., Foglar, M. (2019). Visualization and analysis of concrete specimens damage after fire and blast experiments. *Iop Conference Series: Materials Science and Engineering*, *596*. DOI: 10.1088/1757-899X/596/1/012040

[54] Chen, W., Pan, J., Guo, Z., Zou, H. (2019). Damage evaluations of fire-damaged RPC-FST columns under blast loading. *Thin-Walled Structures*, *134*, 319-332. DOI: 10.1016/j.tws.2018.10.031

[55] Chen, W., Zhou, Z., Zou, H., Guo, Z. (2018). Predictions of residual carrying-capacities for fire and near-field blast-damaged reactive powder concrete-filled steel tube columns. *International Journal of Protective Structures*, *9*(4), 525-553. DOI: 10.1177/2041419618784738

[56] Guo, Z., Chen, W., Zhang, Y., Zou, H. (2017). Post fire blast-resistances of RPC-FST columns using improved Grigorian model. *International Journal of Impact Engineering*, *107*, 80-95. DOI: 10.1016/j.ijimpeng.2017.05.005

[57] Liew, J. Y. R., Chen, H. (2004). Explosion and Fire Analysis of Steel Frames Using Fiber Element Approach. *Journal Of Structural Engineering*, *130*(7), 991-1000. DOI: 10.1061/(ASCE)0733-9445(2004)130:7(991)

[58] Chen, H., Liew, J. Y. (2005). Explosion and Fire Analysis of Steel Frames Using Mixed Element Approach. *Journal Of Engineering Mechanics*, *131*(6), 606-616. DOI: 10.1061/(ASCE)0733-9399(2005)131:6(606)

[59] Liew, J. Y. R. (2008). Survivability of steel frame structures subject to blast and fire. *Journal Of Constructional Steel Research*, *64*(7-8), 854-866. DOI: 10.1016/j.jcsr.2007.12.013

[60] Forni, D., Chiaia, B., and Cadoni, E. (2017). Blast effects on steel columns under fire conditions. *Journal Of Constructional Steel Research*, *136*, 1-10. DOI: 10.1016/j.jcsr.2017.04.012

[61] Vasilchenko, A., Doronin, E., Ivanov, B., Konoval, V. (2019). Effect of Residual Deformation of a Steel Column on its Fire Resistance under Combined Exposure "Explosion-Fire." *Materials Science Forum*, *968*, 288-293. DOI: 10.4028/www.scientific.net/MSF.968.288

[62] Fang Q., Zhao J., Chen L. (2010) Numerical simulation of fire resistance of steel beams subjected blast and fire - China Civil Eng J, 43, pp. 62-68

[63] Fang Q., Zhao J., Chen L., Li D. (2013) Numerical simulation of deformation and failure of steel columns subjected to blast and fire - J PLA Univ Sci Technol, 14 (4), pp. 398-403

[64] Foglar, M., Kovar, M. Conclusions from experimental testing of blast resistance of FRC and RC bridge decks (2013), International Journal of Impact Engineering, 59, pp. 18-28. DOI: 10.1016/j.ijimpeng.2013.03.008

[65] Foglar, M., Pachman, J., Pelikan, V., Hájek, R., Künzel, M., Kovar, M. (2014). The structural response of a reinforced concrete specimen subjected to adjacent blast loading. In (pp. 171-179). DOI: 10.2495/SUSI140151

[66] Foglar, M., Hajek, R., Kovar, M., Štoller, J. Blast performance of RC panels with waste steel fibers (2015) *Construction and Building Materials*, 94, art. no. 6897, pp. 536-546. DOI: 10.1016/j.conbuildmat.2015.07.082

[67] Foglar, M., Hajek, R., Fladr, J., Pachman, J., Stoller, J. Full-scale experimental testing of the blast resistance of HPFRC and UHPFRC bridge decks (2017). Construction and Building Materials, 145, pp. 588-601. DOI: 10.1016/j.conbuildmat.2017.04.054

[68] Hajek, R., Fladr, J., Pachman, J., Stoller, J., Foglar, M. An experimental evaluation of the blast resistance of heterogeneous concrete-based composite bridge decks (2019). Engineering Structures, 179, pp. 204-210. DOI: 10.1016/j.engstruct.2018.10.070.

[69] Stöhr, J., Hájek, R., Foglar, M. Blast performance of reduced scale reinforced concrete specimens (2015). Proceedings of the Fifteenth International Conference on Civil, Structural and Environmental Engineering Computing. Stirling: Civil-Comp Press Ltd, 2015. ISSN 1759-3433. ISBN 978-1-905088-63-8.

[70] Hajek, R. and Foglar, M. (2015). "Numerical and Experimental Analysis of the Effect of Rigid Barriers on Blast Wave Propagation." ASCE Journal of Structural Engineering, DOI: 10.1061/(ASCE)ST.1943-541X.0001308, 04015061.

[71] Hájek, R., Foglar, M., Fládr, J. Influence of Barrier Material and Barrier Shape on Blast Wave Mitigation (2016). Construction and Building Materials, vol. 120, pp. 54 - 64, 2016. ISSN 0950-0618. DOI: 10.1016/j.conbuildmat.2016.05.078

[72] Matsagar, V.A. Comparative performance of composite sandwich panels and non-composite panels under blast loading (2016). Materials and Structures, 49, pp. 611-629. DOI: 10.1617/s11527-015-0523-8

[73] Li, J., Wu, C., Hao, H., Wang, Z., Su, Y. Experimental investigation of ultra-high performance concrete slabs under contact explosions (2016). International Journal of Impact Engineering, 93, pp. 62-75. DOI: 10.1016/j.ijimpeng.2016.02.007

[74] Liu, J., Wu, C., Li, C., Dong, W., Su, Y., Li, J., Cui, N., Zeng, F., Dai, L., Meng, Q., Pang, J. Blast testing of high performance geopolymer composite walls reinforced with steel wire mesh and aluminium foam (2019). Construction and Building Materials, 197, pp. 533-547. DOI: 10.1016/j.conbuildmat.2018.11.207

[75] Christian, A., Ong Khim Chye, G. Performance of Fiber Reinforced High-strength Concrete with Steel Sandwich Composite System as Blast Mitigation Panel (2014). Procedia Engineering, 95, pp. 150-157. DOI: 10.1016/j.proeng.2014.12.174

[76] Fallon, C., McShane, G.J. Fluid-structure interactions for the air blast loading of elastomer-coated concrete (2019). International Journal of Solids and Structures, 168, pp. 138-152. DOI: 10.1016/j.ijsolstr.2019.03.017

[77] Iqbal, N., Sharma, P.K., Kumar, D., Roy, P.K. Protective polyurea coatings for enhanced blast survivability of concrete (2018). Construction and Building Materials, 175, pp. 682-690. DOI: 10.1016/j.conbuildmat.2018.04.204

[78] Maazoun, A., Matthys, S., Belkassem, B., Lecompte, D., Vantomme, J. Blast response of retrofitted reinforced concrete hollow core slabs under a close distance explosion (2019). Engineering Structures, 191, pp. 447-459. DOI: 10.1016/j.engstruct.2019.04.068

[79] Štefan, R., Foglar, M., Fládr, J., Horníková, K., Holan, J. (2020). Thermal, spalling, and mechanical behaviour of various types of cementitious composites exposed to fire: Experimental and numerical analysis. *Construction and Building Materials*, *262*. DOI: 10.1016/j.conbuildmat.2020.119676

[80] Bednář, J., Wald, F., Vodička, J., Kohoutková, A. (2013). Experiments on membrane action of composite floors with steel fibre reinforced concrete slab exposed to fire. *Fire Safety Journal*, *59*, 111-121. DOI: 10.1016/j.firesaf.2013.04.008

[81] Banerji, S., Kodur, V., Solhmirzaei, R. (2020). Experimental behavior of ultra-high performance fiber reinforced concrete beams under fire

conditions. *Engineering Structures*, *208*. DOI: 10.1016/j.engstruct.2020.110316

[82] Weerasinghe, P., Nguyen, K., Mendis, P., Guerrieri, M. (2020). Large-scale experiment on the behavior of concrete flat slabs subjected to standard fire. *Journal of Building Engineering*, *30*. DOI: 10.1016/j.jobe.2020.101255

[83] Xu, H., Yu, M., Xue, C., Xu, L., Ye, J. (2020). Experimental study on fire resistance of precast concrete columns with efficient reinforcement. *Engineering Structures*, *204*. DOI: 10.1016/j.engstruct.2019.109947

[84] Antoun, T., Seaman, L., Curran, D. R., Kanel, G. I., Razorenov, S. V., Utkin, A. V. (2003). *Spall fracture*. Springer Science and Business Media.

[85] Forbes, J. W. (2012). Shock wave compression of condensed matter: a primer. New York: Springer.

[86] Hájek, R., Horníková, K., and Foglar, M. (2020). Numerical assessment of the response of a heterogeneous concrete-based composite bridge deck to a near field explosion. Engineering Structures, 225.Doi: 10.1016/j.engstruct.2020.111206

[87] LS-DYNA (2006). Theory Manual. Livermore Software Technology Corp. (LSTC).

[88] LS-DYNA (2007). Keyword User's Manual, Version 971. LSTC.

[89] Kong, S. Y., Remennikov, A. M., Uy, B. (2012). Numerical simulation of the response of non-composite steel-concrete-steel sandwich panels to impact loading. *Australian Journal of Structural Engineering*, 12(3). DOI: 10.7158/S11-098.2012.12.3

[90] Hao, Y., Hao, H. (2014). Influence of the concrete DIF model on the numerical predictions of RC wall responses to blast loadings. *Engineering Structures*, 73, 24-38. DOI: 10.1016/j.engstruct.2014.04.042

[91] Tai, Y.S., Chu, T.L., Hu, H.T., Wu, J.Y. (2011) Dynamic response of a reinforced concrete slab subjected to air blast load. *Theoretical and Applied Fracture Mechanics*, 56(3), pp. 140-147. DOI: 10.1016/j.tafmec.2011.11.002

[92] LS-DYNA (2014). Keyword User's Manual Volume II Material Models, Revision 5442. LSTC

List of author's publications

(generated from https://v3s.cvut.cz in reversed chronological order)

(indexed papers are printed in red)

HORNÍKOVÁ, K. Rychlost úlomků cementových kompozitů vystavených výbuchu. In: HORÁKOVÁ, A. and M. PETŘÍK, eds. Proceedings of PhD Workshop, Department of Concrete and Masonry Structures 2022. 11th PhD Workshop of the Department of Concrete and Masonry Structures 2022, Praha, 2022-05-27. Praha: CTU FCE. Department of Concrete and Masonry Structures, 2022. p. 144-149. ISBN 978-80-01-06989-9.

FOGLAR, M., et al. Zodolnění Terminálu T1. [Research Report] 2020.

HORNÍKOVÁ, K. Vyhodnocení měření rychlosti úlomků cementových kompozitů vystavených výbuchu. In: HORÁKOVÁ, A. and M. PETŘÍK, eds. Proceedings of PhD Workshop, Department of Concrete and Masonry Structures 2021. 10th PhD Workshop of the Department of Concrete and Masonry Structures 2021, Praha, 2021-05-21. Praha: CTU FCE. Department of Concrete and Masonry Structures, 2021. ISBN 978-80-01-06842-7.

HORNÍKOVÁ, K. Vliv kombinovaného účinku působení vysoké teploty a výbuchu na betonové prvky. In: HORÁKOVÁ, A. a M. PETŘÍK, eds. Proceedings of PhD Workshop, Department of Concrete and Masonry Structures 2020. 9th PhD Workshop of the Department of Concrete and Masonry Structures 2020, Praha, 2020-11-13. Praha: CTU FCE. Department of Concrete and Masonry Structures, 2020. ISBN 978-80-01-06774-1.

HÁJEK, R., K. HORNÍKOVÁ a M. FOGLAR. Numerical assessment of the response of a heterogeneous concrete-based composite bridge deck to a near field explosion. Engineering Structures. 2020, 225 ISSN 1873-7323. DOI 10.1016/j.engstruct.2020.111206

ŠTEFAN, R. et al. Thermal, spalling, and mechanical behaviour of various types of cementitious composites exposed to fire: Experimental and numerical analysis. Construction and Building Materials. 2020, 262 ISSN 0950-0618. DOI 10.1016/j.conbuildmat.2020.119676

HORNÍKOVÁ, K. et al. Experimental investigation of physical, thermal, hygral and mechanical properties of cementitious composites at high temperatures. Construction and Building Materials. 2020, 255 ISSN 0950-0618. DOI 10.1016/j.conbuildmat.2020.119244

HORNÍKOVÁ, K. a M. FOGLAR. Compressive strength of various types of concrete exposed to elevated temperature. In: Solid State Phenomena Vol. 309. 26. Betonářské dny 2019, Hradec Králové, 2019-11-20/2019-11-21. Zurich: TRANS TECH PUBLICATIONS LTD, 2020. s. 62-67. ISSN 1662-9779. DOI 10.4028/www.scientific.net/SSP.309.62

HORNÍKOVÁ, K. a M. FOGLAR. Tlaková pevnost různých typů betonu vystavených vysoké teplotě. In: 26. Betonářské dny 2019. Hradec Králové, 2019-11-20/2019-11-21. Praha: Česká betonářská společnost ČSSI, 2019. 1.. ISBN 978-80-907611-2-4.

HORNÍKOVÁ, K. a M. FOGLAR. Material Properties of Various Types of Fibre Reinforced Concrete Exposed to Elevated Temperature. In: BÍLÝ, P. et al., eds. Fibre Concrete 2019. Praha, 2019-09-17/2019-09-20. Bristol: IOP Publishing Ltd, 2019. IOP Conference Series: Materials Science and Engineering. sv. 596. ISSN 1757- 899X. DOI 10.1088/1757-899X/596/1/012019

HORNÍKOVÁ, K. Vlastnosti betonu v závislosti na teplotě a jejich vliv na odolnost vůči požáru a výbuchu. In: PETŘÍK, M. a A. HORÁKOVÁ, eds. Proceedings of the 8th PhD Workshop of the Department of Concrete and Masonry Structures. 8th PhD Workshop of the Department of Concrete and Masonry Structures 2019, Praha, 2019-05-31. Praha: CTU FCE. Department of Concrete and Masonry Structures, 2019. ISBN 978-80-01-06574-7.

HORNÍKOVÁ, K. Vlastnosti betonu a jejich vliv na odolnost betonových prvků vůči požáru a výbuchu. In: DVORSKÝ, T. a M. PETŘÍK, eds. PhD Workshop 2018 - CD. PhD Workshop 2018, Praha, 2018-05-25. Praha: CTU FCE. Department of Concrete and Masonry Structures, 2018. ISBN 978-80-01-06417-7.

HORNÍKOVÁ, K. Numerical Simulation of Multi-Layer Cement Composite Loaded by Near Explosion. In: DVORSKÝ, T. a M. PETŘÍK, eds. PhD Workshop 2017 . Collection of Abstracts. PhD Workshop 2017, Praha, 2017-05-26. Praha: CTU FCE. Department of Concrete and Masonry Structures, 2017. s. 18-19. ISBN 978-80-01- 06132-9.

Annex 1

Reprint of the Paper

HORNÍKOVÁ, K. et al. Experimental investigation of physical, thermal, hygral and mechanical properties of cementitious composites at high temperatures. Construction and Building Materials. 2020, 255 ISSN 0950-0618. DOI 10.1016/j.conbuildmat.2020.119244

Contribution of the author of this thesis of the paper

The author of this thesis is the main author of the paper (that was written under the supervision of both authors supervisors). Experiments were designed and evaluated by all authors.

Kateřina Horníková: Conceptualization, Formal analysis, Investigation, Writing – original draft, Writing – review & editing, Visualization.

Lenka Scheinherrová: Formal analysis, Investigation, Writing – original draft, Writing – review & editing.

Radek Štefan: Supervision, Formal analysis, Writing – review & editing, Methodology, Visualization.

Marek Foglar: Supervision, Writing – review & editing, Methodology, Funding acquisition

Experimental investigation of physical, thermal, hygral and mechanical properties of cementitious composites at high temperatures

Kateřina Horníková [a], Lenka Scheinherrová [b], Radek Štefan [a], Marek Foglar [a,*]

[a] *Department of Concrete and Masonry Structures, Faculty of Civil Engineering, Czech Technical University in Prague, Thákurova 7, 166 29 Prague 6, Czech Republic*
[b] *Department of Materials Enginerring and Chemistry, Faculty of Civil Engineering, Czech Technical University in Prague, Thákurova 7, 166 29 Prague 6, Czech Republic*

HIGHLIGHTS

- Study on basic physical, thermal, hygral and mechanical properties of cementitious composites at high temperatures.
- Five types of cementitious composites are studied.
- Several testing methods are compared for each material characteristic.
- The relative decrease in compressive strength is very similar for all types of composites.
- Exposure to high temperatures increases the gas permeability of all types of composites.

ARTICLE INFO

ABSTRACT

This paper presents the results of an experimental program that compares the material properties of various types of cementitious composites subjected to high temperatures. Within this experimental program, measurements of bulk density, porosity, thermal conductivity, specific heat capacity, permeability and compressive strength of the materials were made. All these properties were measured on test samples exposed to high temperatures up to 1000 °C. The results of this experimental investigation are the temperature dependences of the material properties and the relative changes of the properties at high temperatures in relation to their values at room temperature. The paper also presents and compares different methods for measuring the selected properties studied here, and the effect of the measurement methods on the obtained results. All results are compared with values from the valid standards and referenced literature.

© 2020 Elsevier Ltd. All rights reserved.

1. Introduction

Structural concrete elements must be designed with the required fire resistance. When performing a conventional structural fire design, the heat load and heat transfer in the analyzed structural element must be taken into account. The way of heating affects its material properties and its fire resistance. At first, both, physically and chemically bound water evaporate, which consequently leads to thermal decomposition of C-S-H gels and ettringite [1]. In temperature interval between 400 and 500 °C decomposition of portlandite $Ca(OH)_2$ takes place [1,2]. When con-

crete contains quartz aggregates, the α to β transformation of quartz occurs at 573 °C [3]. It is accompanied by non-negligible volume changes, which could lead to severe cracking not only on surface of concrete. At higher temperatures, the decomposition of calcite and/or its modifications (vaterite, aragonite) takes place [1,2].

The heat transfer is influenced by the physical and thermal properties of the material. The properties such as porosity, thermal conductivity, specific heat capacity and permeability change with increasing temperature, and, as a result, they also influence the fire resistance of the structural element.

Usually, the research teams use material properties from standards and/or references and perform numerical simulations. This paper aims to compare the findings in the literature and provide

---

* Corresponding author.
E-mail address: marek.foglar@fsv.cvut.cz (M. Foglar).

experimental data for five different cementitious composited exposed to high temperatures: Reference concrete (further denoted as RC), its derivatives air-entrained concrete (AC) and polypropylene fibre concrete (PC), ultra-high-performance concrete with steel fibres (U) and innovative hybrid concrete with mineral insulation shreds (S).

The reference type is the ordinary structural concrete C30/37 according to EN 1992-1-1, cylindrical compressive strength f_{ck} = 30 MPa.

The reference material is compared to its derivatives: Air-entrained concrete which is often used in structural application for its higher durability under frost exposure, and concrete with polypropylene fibers known for its resistance to high temperatures.

The reference material is also compared to two completely different cementitious composites: Ultra-high-performance concrete (UHPFRC) with steel fibres known for its high strength and durability and innovative hybrid concrete with mineral insulation shreds with high energy dissipation capacity.

The main aim of the paper is to compare the temperature dependences of the selected material properties and simultaneously to compare the effect of the standardized or referenced testing approach on the resultant values of the tested material property. Therefore, some properties have been measured by several methods and/or using different sample dimensions. All results are presented in summary graphs and are compared with values from valid standards and/or referenced literature. The tests were performed in three accredited laboratories and one university research department which are further denoted as TZ, KU, BZ and MA, respectively, according to their name abbreviations.

The paper aims to provide a comprehensive overview both of the original findings and of the referenced results.

2. Literature review

The material properties of cementitious composites subjected to elevated temperatures have been studied in many experimental programs. However, in most cases, only measurements of some properties are used for consecutive tests. Alternatively, the whole experimental program is aimed at measuring a single property for different types of materials. This section gives a brief summary of ways to measure specific material properties for different types of materials.

A general description of the material properties of concrete is presented in Neville [4]. In this case, a description of the main material properties of concrete at room temperature is provided (dry material and wet material). A description of the material properties of concrete exposed to high temperature is provided by Bažant and Kaplan [5]. This reference describes the material properties, the changes in them and their course, depending on the boundary conditions. Bažant and Kaplan [5] also define the basic mathematical relations between some properties. By contrast, Kodur [6] is dedicated to the main characteristics and their influence on the fire resistance of concrete. This paper presents data obtained experimentally, and the range of some characteristics in dependence on temperature is defined. In *fib* Bulletin [7], the influence of fire on concrete structures is described. The Bulletin also presents a description of the material properties. A summary is provided of how these material properties are influenced, and what it implies for the design of concrete structures. The last example is the work by Guo et al. [8], which is focused on the behavior of concrete elements during exposure to high temperatures, and on calculating this behavior. The material properties are defined by mathematical equations.

2.1. Thermal and hygral properties

The thermal properties of concrete are important for determining the heat transfer in a concrete element during an assessment of the fire resistance of a structure. Characteristics depending on temperature can be found in valid standards and literature.

Asadi et al. [9] present widely-used methods for measuring the thermal conductivity of concrete. They provide the relation between thermal conductivity and other thermal properties (e.g. density and porosity). Wang [10] presents the results of thermal conductivity measurements for eight materials with different water ratios (there used ACI mix design using water-cement ratios of 0.4 and 0.5. In these two types of mixtures 0%, 0.1%, 0.3% and 0.5% weight of cement was replaced with nano clay). This is one of the few papers in which the thermal conductivity was measured up to 1000 °C. Measurements of thermal conductivity for foamed and polystyrene-foamed concrete are described by Sayadi et al. [11]. Othuman and Wang [12] supplement this data with light-weight foamed concrete with material density about 600 kg/m^3. This paper also describes a method in which heat transport is recorded by thermocouples in the tested samples. It also presents the dependence of thermal conductivity on the porosity of the material.

Specific heat capacity is another important material characteristic of concrete, which has been widely used in various theoretical analyses and calculations. There are many methods how to determine this parameter as a function of temperature, such as conventional calorimetry methods, differential thermal analysis (DTA) and differential scanning calorimetry (DSC) methods. These techniques are well-developed, nevertheless, the tested materials must be homogeneous and of a very small size [13], which is very limiting for heterogeneous material such as concrete containing coarse aggregates and fibers. For example, Černý and Toman [14] designed a nonadiabatic calorimeter, capable of measuring samples of volume of approximately 2.5 L in the temperature range from 100 °C to 1000 °C. More recently, Ruuska et al. [15] presented another method using a heat flow meter apparatus to determine thermal conductivity and specific heat capacity of inhomogeneous materials.

Permeability is closely connected to material density and its porosity. In [15], permeability is defined as gas permeability. Ahlem Houaria et al. [16] compare the gas permeability and the water permeability of concrete, both of these properties in response to elevated temperatures. A very similar topic is studied by Kameche et al. [17], but only for ordinary concrete. Hoseini et al. [18] summarize the test methods for measuring both the liquid and gas permeability of concrete and describe these methods with respect to the fluid and the load conditions employed in the test. Bošnjak et al. [19] present a permeability test for high-strength concrete with and without polypropylene fibers. Methods are described that use non-typical specimen shapes (for example, a cylinder with a hole). The maximum temperature used in this test is 300 °C, and the results are supplemented by microscopic slides documenting the structure of the material. Noumowe et al. [20] present the results of permeability measurements for three ultra-high performance concretes up to 600 °C. Gawin et al. [21] describe the relation between each characteristic and the changes in permeability depending on temperature.

2.2. Mechanical properties

The compressive strength of concrete is one of the fundamental parameters for the design of concrete structures and for assessing their fire resistance. A recent review of material properties was written by Ma et al [22]. This paper provides an overview of sources which deal with changes in material properties. Not only

compressive strength is studied, but also flexural strength and modulus of elasticity. This work includes a comparison of many data obtained from the literature. A similar overview is given by Arioz [23]. Phan and Carino [24] provide a review of the mechanical properties of high-strength concrete (HSC) when compared to normal-strength concrete (NSC) It was found that HSC lost its strength more significantly than NSC when exposed to temperature between 25 °C and approximately 400 °C. At higher temperatures, the strength losses of both concretes were very similar. The residual compressive strength at 800 °C of HSC reached only 30% of its original values. It was also reported that HSC is more prone to explosive spalling when exposed to temperature above 300 °C. Varona et al. [25] present the mechanical properties of hybrid fiber-reinforced concrete. In this paper, experimental results for six specific types of concrete and their mechanical properties (not only compressive strength, but also flexural strength and ductility) are discussed. Authors concluded that the effect of high temperature on the residual mechanical properties of hybrid fiber reinforced concretes was less severe than in steel fiber reinforced concretes. Baradaran-Nasiri and Nematzadeh [26] present the mechanical properties of concrete with fine recycled refractory brick aggregates and aluminate cement. Vejmelková et al. [27] recently studied high temperature durability of fiber reinforced high alumina cement composites. Several different fiber-reinforced composite mixes based on high alumina cement were designed and their properties were determined as functions of previous thermal load up to 1000 °C. It was found that the application of basalt aggregates and basalt fibers improved significantly the high temperature durability of calcium aluminate cement-based materials. In the most successful mixture the residual values of compressive strength were 50% after exposure to 1000 °C.

All of these references, and many others, show that the mechanical properties of concrete at high temperatures are a very important topic of scientific investigation. Information can be found about many types of materials including some materials that are not very common. However, in most cases the mechanical properties are studied separately from other characteristics, and for this reason the compressive strength is also investigated in our experimental program.

3. Experimental program

3.1. Materials

Within this experimental program, the material properties of the following types of cementitious composites were measured:

- Ordinary concrete C30/37 used as a reference material (RC)
- Air-entrained concrete (AC)

- Concrete with polypropylene fibers (marked PC)
- Ultra-high-performance concrete with steel fibers – UHPFRC (U)
- Light-weight innovative hybrid concrete with mineral insulation shreds (marked S)

Ordinary concrete C30/37 was chosen as the reference material. The label C30/37 refers to values of the compressive strength determined after 28 days of age on samples of defined shapes and dimensions according to [28]. The material properties of ordinary concrete have been published in many papers and are described in Eurocode EN 1992-1-2 [29]. The properties of the first three types of composites (RC, AC, PC) studied here are very similar. The fourth and fifth materials (U and S) behave completely differently as it is obvious from the motivation of the paper.

The mixtures of the investigated materials used in the experimental program are given in Table 1.

3.2. Measured material properties

The list of measured material properties is given in Table 2. Some of the properties were measured by more than one method at different laboratories. The methods that were used may differ according to the material that was used and the size of the specimens. The particular specimen sizes according to the measured properties and the testing method are given in this table as well.

In the experimental program, the test specimens were exposed to high temperatures up to 1000 °C. In a few cases, the test was terminated at a lower temperature because of the damage of a specimen. The detailed description of the heat treatment plan assumed for the tests can be found for each specific test method in the appropriate reference given in Table 2.

3.3. Physical properties

3.3.1. Bulk density

The main measured temperature-dependent basic physical characteristic was the bulk density of the material. Bulk density was measured for concrete at room temperature and the change in response to temperature.

Bulk density at room temperature was determined according to EN ISO 1927-6 [31] using specimens that were not dry. The results are shown in Table 3 for four independent measurements (the density was measured at four different laboratories, three of which used the above-mentioned method; these measurements are marked TZ, KU and BZ). The laboratory TZ performed the test on specimens that were prepared for the thermal conductivity and material density for the high-temperature tests at the KU laboratory; the BZ laboratory performed the tests on specimens which

Table 1
Cementitious composite mixtures used in the experimental program.

	Mat. RC	Mat. AC	Mat. PC	Mat. U	Mat. S
	Weight [kg/m³]				
Cement	370	370	370	650	875
Water	135	135	135	172	437
Siliceous aggregates 8–16	755	755	755	300	–
Siliceous aggregates 4–8	195	195	195	460	285
Siliceous aggregates 0–4	863	863	863	880	–
Superplasticizer	2.6	2.6	2.6	29	–
Air-entraining agent	–	0.4	–	–	–
Polypropylene fibres	–	–	1.5	–	–
Microsilica	–	–	–	80	–
Steel fibres 13 mm	–	–	–	120	–
Mineral wool	–	–	–	–	190

Table 2
List of the measured material properties along with the materials, laboratories, test methods and samples used in the experimental program.

Material property	Material	Lab. mark	Test method	Sample dimensions
Bulk density at room temperature	All types	MA	Pavlíková et al. [30]	$50 \times 50 \times 100$ mm
		TZ	EN ISO 1927-6 [31]	$150 \times 150 \times 150$ mm
		BZ	EN ISO 1927-6 [31]	$150 \times 150 \times 150$ mm
	All except U	KU	EN ISO 1927-6 [31]	Ø100 mm, height 200 mm
	U	KU	EN ISO 1927-6 [31]	Ø50 mm, height 100 mm
Bulk density at high temperature	All types	MA	Pavlíková et al. [30]	$50 \times 50 \times 100$ mm
		TZ	EN 993-1 [32]	$50 \times 50 \times 50$ mm
Porosity	All types	MA	Pavlíková et al. [30]	$50 \times 50 \times 100$ mm
		TZ	EN 993-1 [32]	$50 \times 50 \times 50$ mm
Thermal conductivity	S	TZ	EN 993-15 [33]	$350 \times 150 \times 150$ mm
	All except S	TZ	EN 993-15 [33]	$300 \times 300 \times 120$ mm
	All types	MA	Černý and Vejmelková [34]	$50 \times 50 \times 50$ mm
Specific heat capacity	All types	MA	Toman and Černý [14]	$100 \times 100 \times 50$ mm, up to 500 °C
		MA	Toman and Černý [14]	$100 \times 50 \times 50$ mm, above 500 °C
Permeability	All types	TZ	EN 993-4 [35]	Ø50 mm, height 50 mm
Compressive strength at high temperature	All except U	KU	EN 12390-3 [36]	Ø100 mm, height 200 mm
	U	KU	EN 12390-3 [36]	Ø50 mm, height 100 mm

Table 3
Bulk density at room temperature.

Bulk density [kg/m^3]					
Laboratory [method reference]	Material RC	Material AC	Material PC	Material U	Material S
TZ [31]	2 293	2 281	2 301	2 646	1 784
BZ [31]	2 384	2 336	2 333	2 632	1 726
KU [31]	2 360	2 380	2 380	2 620	1 630
MA [30]	2 306	2 277	2 306	2 570	1 541
Mean	2 336	2 319	2 330	2 617	1 670

were prepared for a test of compressive strength – all samples were cubes with dimensions of $150 \times 150 \times 150$ mm.

The test performed at the MA laboratory determined the material density at room temperature differently when compared to the method used at laboratories labeled as TZ, KU and BZ. Bulk density and matrix density were measured by helium pycnometry combined with the gravimetric method [30]. Helium pycnometry (Pycnomatic ATC device, Thermo Fisher Scientific) provided the matrix density, and the results were supplemented by bulk density measurements, which were calculated from the dimensions of the sample and its mass in the dry state (dried at 105 °C until constant mass). The samples were $50 \times 50 \times 100$ mm in size.

The change in material density depending on temperature was measured by two methods. First the hydrostatic method according to EN 993-1 [32] was used. For these measurements, cubes with dimensions of $50 \times 50 \times 50$ mm were used. The second type of measurements (at the MA laboratory) used a more complicated method. Similarly, to when the basic physical properties were determined at room temperature, the matrix density and the bulk density were measured by helium pycnometry (Pycnomatic ATC device) combined with the gravimetric method. For the measurements, samples with dimensions of $50 \times 50 \times 100$ mm and $100 \times 100 \times 50$ mm were used. First, the samples were dried at 105 °C until constant mass, and then they were heated from room temperature up 200 °C, 300 °C, 400 °C, 500 °C, 600 °C, 700 °C, 800 °C, 900 °C and 1000 °C with a slow heating rate of 1 °C/min. The maximum temperature was maintained for 4–6 h. The time needed was computed based on the basic relationship between the mass of the sample, its specific heat capacity at room temperature, the maximal desired temperature and power of the oven. For further details please see [34]. The samples were cooled naturally in the oven until room temperature was reached. The analyses

were then performed, and therefore, the obtained results obtained by MA laboratory refer to residual properties of the studied materials.

The results of these two types of measurements are shown in Fig. 1.

In Fig. 2, selected results (for the reference concrete, its derivatives, and the UHPFRC, i.e. for materials RC, AC, PC, and U, respectively) are compared with the data given in valid standards and literature. Namely, the formula proposed in EN 1992-1-2 [29] is
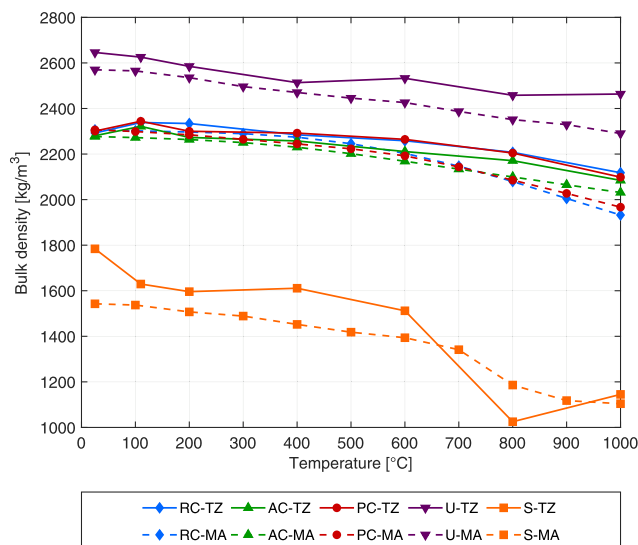
Fig. 1. Temperature dependences of the bulk density of the investigated materials.
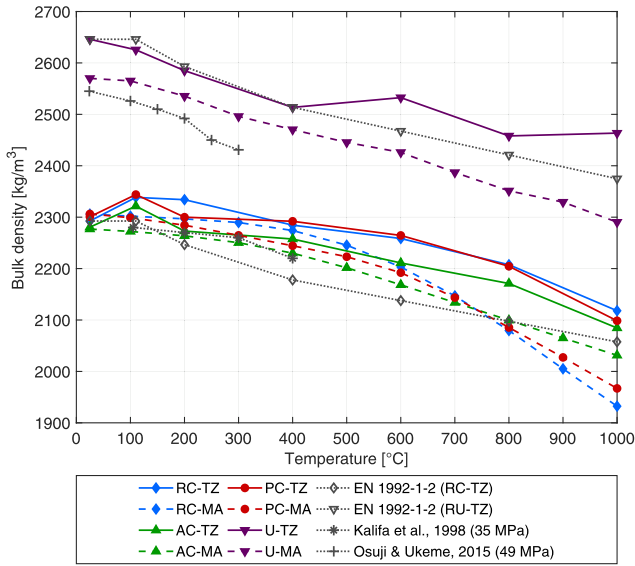
Fig. 2. Temperature dependences of the bulk density of selected materials (all investigated materials except material S) and their comparison with the data stated in references: EN 1992-1-2 [29], Kalifa et al., 1998 [37], and Osuji & Ukeme, 2015 [38].

used, with the initial value set to the initial density of material RC or U measured at the TZ laboratory. Moreover, the data given in references [37,38] are also used for the comparison. These data refer to normal weight concretes of the compressive strengths of 35 MPa (denoted as M30 in [37]) and 49 MPa (denoted as C40 in [38]), respectively.

As expected, cementitious composite with mineral insulation shreds (material S) has the lowest bulk density at room temperature. Its average bulk density is 1670 kg/m³. Ultra-high-performance concrete with steel fibers (material U) has the highest bulk density, with an average value of 2617 kg/m³ caused by high amount of steel fibers and properties of the used aggregates.

Fig. 1 shows bulk density slightly decreasing with increasing temperature for all materials, which could be expected as the porosity of the concrete structure increases. A comparison of the two types of measurements shows that the results for materials RC, AC, PC, and U are very similar. Only for material S, the graph of the temperature dependence of the bulk density has a different shape. This may be due to significantly higher porosity results (will be discussed below), imperfect cohesion of the material, irregular distribution of the mineral insulation shreds, tendency to segregation [39], and generally due to the fact that this type of light weight porous material is affected more significantly by high temperatures compared to denser types of cementitious composites, see also [41].

The results indicate that the two types of applied test methods are similar and provide comparable results.

3.3.2. Porosity

The porosity of concrete was measured by two methods. In the first case (i.e. the test at the TZ laboratory), the porosity was calculated from the weight ratio of the dried samples and the saturated samples, with the use of equation (1) according to EN 993-1 [32]:

$$\pi_a = \frac{m_3 - m_1}{m_3 - m_2} \cdot 100 \tag{1}$$

whete m_1 is the weight of a dry specimen [kg], m_2 is the weight of the specimen immersed in a liquid [kg], m_3 is the weight of a saturated specimen [kg], π_a is the apparent porosity [%].

In the second case (at the MA laboratory), the open porosity ψ [%] of the materials was calculated by means of the matrix density and the bulk density [30]:

$$\psi = \left(1 - \frac{\rho_b}{\rho_{mat}}\right) \cdot 100 \tag{3}$$

where ρ_b is the bulk density [kg/m³], ρ_{mat} is the matrix density [kg/m³].

The accuracy of the gas volume measurements using Pycnomatic ATC device is ± 0.01% of the measured value, whereas the accuracy of the analytical balances is ± 0.0001 g. The expanded combined uncertainty of the bulk density was 2.4%, and the value for total open porosity was 3% [42].

All results are shown in Fig. 3.

The porosity of all materials increases with increasing temperature, as expected. The reason for this phenomenon is the evaporation of free and chemically bound water from the material and thermal decomposition of concrete causing severe cracking in the structure of studied materials, especially at temperatures above 500 °C (decomposition of of main hydration products along with the the α to β transformation of quartz at 573 °C [3,43,44]). Especially the lastly mentioned transformation of quartz can lead to cracking, as it is accompanied by a volume increase of about 2–4% [45]. A comparison of the two types of measurements shows that the biggest difference between initial porosity and final porosity is experienced by material U. However, the final porosity results for materials RC, AC, and PC are almost the same for both types of measurements. The final porosity at the highest temperature for materials RC, AC, PC, and U shows an increase of about 10%, and for material S, there is an increase in porosity of about 20%. As already discussed in Section 3.3.1, the lastly mentioned cementitious composite with mineral insulation shreds (material S) exhibited significantly lower bulk density results compared to the other types of studied materials. Based on these results and results of total open porosity, it can be seen that this material was affected more significantly by high temperatures compared to denser types of cementitious composites, see above and references [39] and [41].
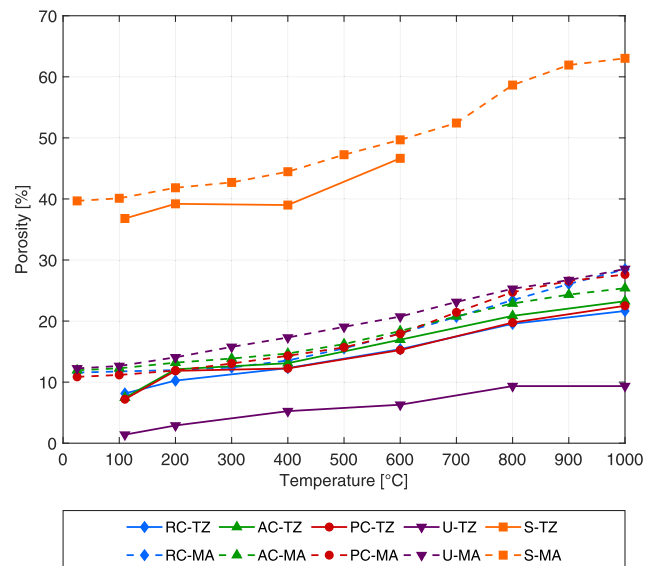

Fig. 3. Temperature dependences of the porosity of the investigated materials.

3.4. Thermal and hygral properties

3.4.1. Thermal conductivity

The thermal conductivity of the investigated materials was measured by two different methods. The data obtained by these two methods can be used for different heat transfer modelling approaches – the classical approach using standard thermal conductivity, and the modified approach using so called "apparent" thermal conductivity, see [34].

The first method is described in EN 993-15 [33] (used in the TZ laboratory). This method uses a heating wire and a pair of thermocouples. The heating wire and the thermocouples are embedded between two concrete blocks at a known distance. The thermal conductivity is calculated from the thermocouple data (by the - change in temperature in a specific area).

The second method (used at the MA laboratory) was used to measure the apparent thermal conductivity. This method is based on an approach that takes into account moisture transport, convective and radiative modes of heat transport, phase-change processes and chemical reactions, as described in greater detail in [34]. For the experiments, three specimens with dimensions of $50 \times 50 \times 50$ mm were provided with a set of six temperature sensors (type K thermocouples) installed along their longitudinal axis, 10–15 mm apart and with thermally insulated lateral sides. The specimens were exposed to one-sided heating using a furnace. A constant temperature of 1000 °C was maintained. The temperature field recorded by a computer was used for the subsequent computational analysis.

The results from both types of measurements are shown in Fig. 4. The measured results are also compared with the data given in valid standards and literature. Namely, the formulas proposed in EN 1992-1-2 [29] are used (upper and lower limit of thermal conductivity of concrete given in [29]). Moreover, the data given in references [37,10] are also used for the comparison. These data refer to normal weight concretes of the compressive strengths of 35 MPa (denoted as M30 in [37]) and 41 MPa (denoted as W4N0 in [10]), respectively.

Fig. 4 clearly illustrates that the two types of measurements that were used are not easily comparable. The thermal conductiv-
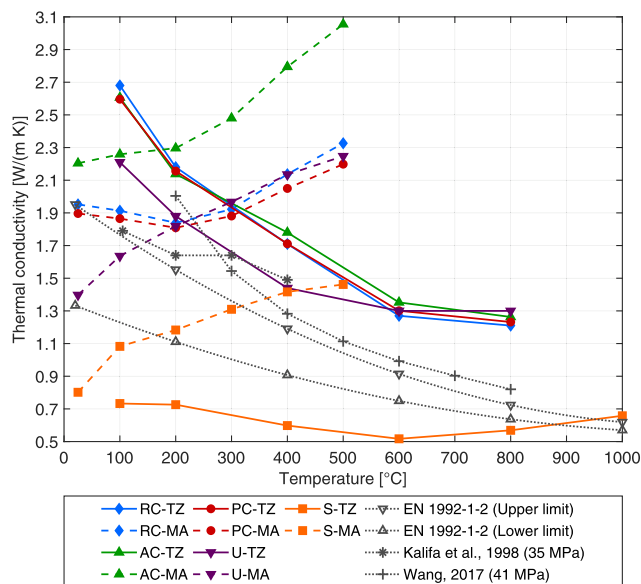
ity for all materials measured at the TZ laboratory decreases with increasing elevated temperature. This trend corresponds with the - data given in EN 1992-1-2 [29]. Only material S has a somewhat different course, where the thermal conductivity starts to increase from 600 °C. The results from the MA laboratory are completely different. In most cases, the thermal conductivity always increases with elevated temperatures. Various reasons may have caused the lack of comparability of the methods: one possible explanation is that the results (or the measurements) are affected by some other part of the heat transfer from the measuring device. In general, the results show the lowest thermal conductivity for material S and the highest for concrete AC.

Fig. 5 and Fig. 6 show the tested samples at the end of the thermal conductivity measurements at the TZ laboratory. Fig. 5 shows the material U sample with steel fibers. The sample was not damaged, and the steel fibers are highlighted. However, the material S sample showed significant damage. As already discussed in previous sections, material S exhibited significantly lower bulk density and higher porosity results compared to the other types of studied materials. The damage may also be caused by imperfect cohesion of the material, irregular distribution of the mineral insulation shreds, tendency to segregation [39], and generally by the fact that this type of light weight porous material is affected more significantly by high temperatures compared to denser types of cementitious composites [41].

3.4.2. Specific heat capacity

The temperature dependence of the specific heat capacity of the investigated materials was determined using a non-adiabatic method [14]. The measurement apparatus consisted of a mixing vessel with a volume of 2.5 l that was placed on a compact, flat reciprocal shaker operating at 60 rpm. The apparatus was connected to a monitoring system, which enabled the thermal changes to be observed continuously, see Fig. 7.

Before the analysis, the samples were dried at 105 °C to a constant mass. After that, the dry samples with dimensions of $100 \times 100 \times 50$ mm were exposed to high temperatures and were

Fig. 4. Tem perature dependences of the thermal conductivity of the investigated materials and their comparison with the data stated in references: EN 1992-1-2 [29], Kalifa et al., 1998 [37], and Wang, 2017 [10].

Fig. 5. Tested sample, material U after thermal conductivity measurements (at the TZ laboratory).

Fig. 6. Tested sample, material S after thermal conductivity measurements (at the TZ laboratory).
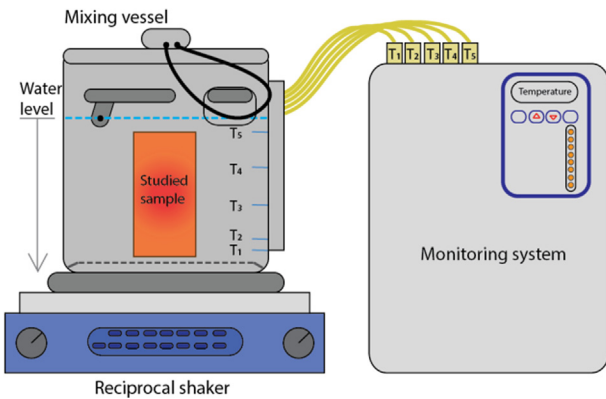

Fig. 7. The scheme of the non-adiabatic method.

heated up to 200, 300, 400 and 500 °C. Samples with dimensions of 50 × 50 × 100 mm were heated up to 600 °C, 700 °C, 800 °C, 900 °C and 1000 °C. The heating rate was 1 °C/min, and the maximum desired temperature was maintained for several hours. Two samples were prepared for each chosen temperature. After heating, one sample was removed from the oven and was quickly placed into the mixing vessel with water that was continuously stirred. The changes in water temperature were measured using a system of five thermocouples in different positions, with relative accuracy of 0.02 °C. The water was stirred until the temperatures of the measured specimen and the calorimeter were equal. Since the mixing vessel was not isolated, the amount of heat loss was determined with the use of calibration. The heat loss calibration curve was used to calculate the theoretical equilibrated temperature of the "sample-calorimeter" system. The whole method and the subsequent calculations are presented in greater detail in [14].

The measured results are shown in Fig. 8. The results are also compared with the data given in valid standards and literature. Namely, there are used the formulas proposed in EN 1992-1-2 [29] for normal weight concrete with the moisture content of 0% (dry concrete) and 1.5% of concrete weight, and the data given in

Fig. 8. Temperature dependences of the specific heat capacity of the investigated materials and their comparison with the data stated in references: EN 1992-1-2 [29] and Kalifa et al., 1998 [37].

reference [37] for normal weight concrete of the compressive strength of 35 MPa (denoted as M30 in [37]).

The results shown in Fig. 8 are almost the same as the specific heat capacity defined by standard EN 1992-1-2 [29] for ordinary concrete. The standard course for dry material predicts increasing specific heat capacity up to 400 °C, then continuing with a constant value. The measured values for all materials increase up to 500 °C – 700 °C and then start decreasing. The final specific heat capacity at 1000 °C is almost the same as the given in EN 1992-1-2 [29].

3.4.3. Permeability

The permeability of concrete, as a physical characteristic, can be understood in many ways. In this case, the gas permeability of
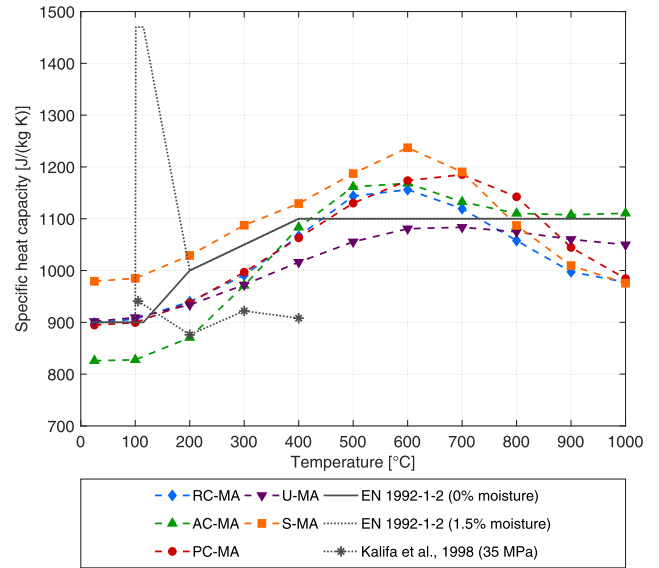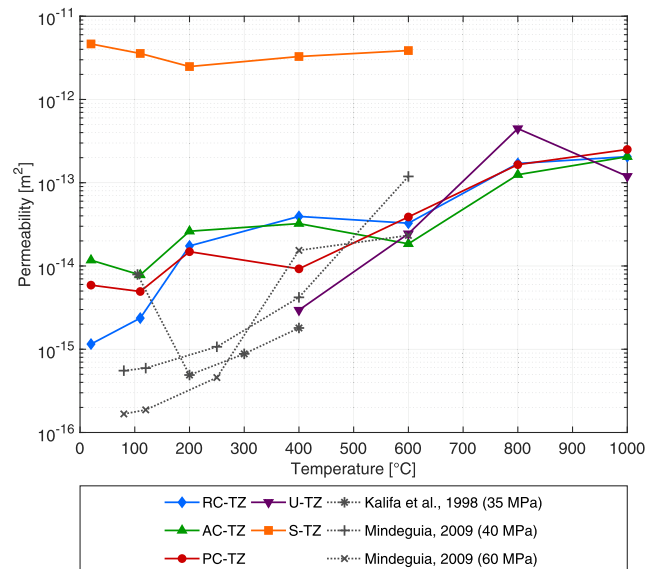

Fig. 9. Temperature dependences of the permeability of the investigated materials and their comparison with the data stated in references: Kalifa et al., 1998 [37] and Mindeguia, 2009 [46].

Fig. 10. Tested samples after the permeability test, material U.

the material is what is meant. The permeability is measured according to EN 993-4 [35] at three pressure levels. The permeability for material S was measured at 0.6 kPa, 0.8 kPa and 1 kPa for high porosity of the material. The permeability of other materials was measured at 5 kPa, 10 kPa and 15 kPa. During the test, the amount of gas passing through the test samples is measured by the test device described in EN 993-4 [35]. The results of this test are shown in Fig. 9 and Fig. 10. The results are also compared with the data stated in literature. Namely, there are used the data given in reference [37] for normal weight concrete of the compressive strength of 35 MPa (denoted as M30 in [37]) and the data given in [46] for normal weight concretes of the compressive strength of 40 MPa and 60 MPa (denoted as B40 and B60, respectively, in [46]).

The results for materials RC, AC, PC, and U show slowly increasing permeability up to 600 °C. From this temperature on, the permeability increases more rapidly. Material U has the lowest permeability. Up to a temperature of 400 °C for this type of concrete, zero gas permeability was measured. At 800 °C, material U was damaged, and at a temperature of 1000 °C some aggregates of the material started to change their physical characteristics. The change in the permeability of material S in response to increasing temperature is variable. The main reason for this is probably high porous system of material S, its heterogeneity and the quantity of mineral insulation shreds (also porous).

Fig. 10 shows the tested samples of material U after the permeability measurements. Fig. 11 shows the samples of material S after the test. These samples were visibly damaged when exposed to a temperature higher than 800 °C.

3.5. Mechanical properties

3.5.1. Compressive strength

Several methods can be used for measuring the compressive strength of concrete exposed to high temperatures. The first option is to measure the compressive strength at the high temperature. The second option is to measure the compressive strength after cooling of the sample – when this way is used, the residual strength is measured.

During the experiments presented in this paper, the compressive strength was measured at given temperature (directly on the heated sample, when it is hot). The measurements were made in accordance with RILEM [48], using the hot state testing method. The tested samples are placed in a hydraulic press in an electric furnace Then heating to the given temperature begins with heating rate is 20 °C per minute. After the desired temperature is reached, the temperature is kept constant for 100 min. This ensures equal

Fig. 11. Tested samples after permeability test, material S.
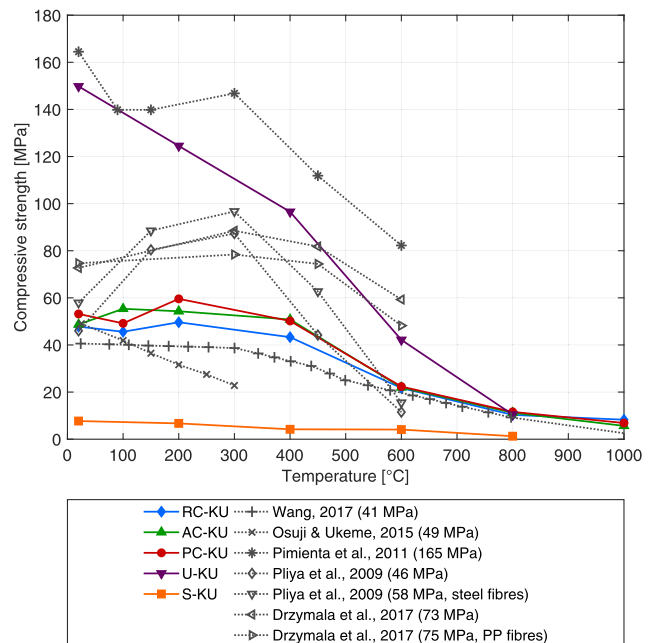

Fig. 12. Temperature dependences of the compressive strength of the investigated materials and their comparison with the data stated in references: Wang, 2017 [10], Osuji & Ukeme, 2015 [38], Pimienta et al., 2011 [49], Pliya et al., 2009 [50], Drzymala et al., 2017 [51].

temperature within the sample. After this time, a conventional test of compressive strength according to EN 12390–3 [36] is performed made inside the furnace. Then the furnace is opened, cooling begins, so that the next test can be prepared.

The measured compressive strengths are shown in Fig. 12. The results for material U are compared with other data, no matter they were measured on the samples of different dimensions. It should be however noted that according to EN 12390–3 [36], the -size ratio of the sample plays an important role due to the influence of lateral tension. The measured results are also compared with the data given in literature. Namely, there are used the data given in references: [10] for normal weight concrete of the compressive strength of 41 MPa (denoted as W4N0 in [10]), [38] for normal weight concrete of the compressive strength of 49 MPa (denoted as C40 in [38]), [49] for UHPFRC concrete of the compressive strength of 165 MPa (denoted as BSI-"fire" in [49]), [50] for normal weight concrete without fibres and with steel fibres of the compressive strengths of 46 MPa and 58 MPa (denoted as C2 and CS2-20 in [50], respectively), and [51] for high performance concrete without fibres and with polypropylene fibres of the compressive strengths of 73 MPa and 75 MPa (denoted as HPC-reference and HPC-fibre-reinforced in [51], respectively).

In Fig. 13, the measured data are presented in the form of relative compressive strength, i.e. the actual strength of a material at a given temperature divided by the initial strength of the material at room temperature. These results are compared with the data for normal weight and normal strength concrete with siliceous aggregates (NSC) and for normal weight and high strength concrete with siliceous aggregates (HSC) given in EN 1992-1-2 [29].

The lowest compressive strength was obtained for cementitious composite with mineral insulation shreds (material S); the maximum value at room temperature was almost 10 MPa due to the high heterogeneity of the material. The maximum value at room temperature was 158 MPa, for UHPFRC (material U). For all materials, the compressive strength decreased with
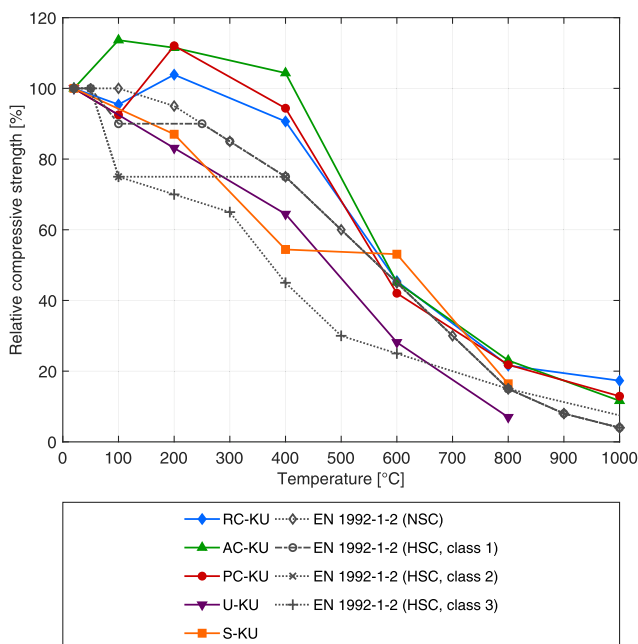
the increasing temperature, except the slight increase at temperatures between 100 and 300 °C for some materials. It should be noted that the increase of the compressive strength after exposure of some samples to temperatures above 100 – 300 °C could be attributed to rehydration of residual and unhydrated cementitious materials activated by higher temperatures [43,52,53].

4. Discussion

Basic physical, thermal and mechanical properties of ordinary concrete C30/37 (RC), air-entrained concrete (AC), concrete with polypropylene fibers (PC), ultra-high performance concrete with steel fibers (U) and concrete with mineral insulation shreds (S) were studied at high temperatures. Ordinary concrete C30/37 (RC) was chosen as a reference material, because its properties are described in the valid standards and in the available literature and it is widely used for its universal properties. Concrete with mineral insulation shreds (S) was chosen for its heterogeneity. Ultra-high-performance concrete with steel fibers was chosen as an example of a dense impermeable homogeneous cement composite.

The methods that were used and the achieved results have been described and continuously discussed within the part dedicated to the experimental program. As expected, with increasing temperature the material density, the thermal conductivity (for TZ laboratory) and the compressive strength of all materials decreased. The porosity, the specific heat capacity and the gas permeability increased with increasing temperature for all tested materials. These changes are based on the transport and evaporation of water from the material. While the water is evaporating, the amount of open pores increases and new pores are formed (together with crack propagation). When moisture leaves the material, the material loses weight and loses a part of its thermal conductivity. The formation of new pores generates a place for gases and, therefore, the gas permeability increases.

The compressive strength decreased with increasing temperature for all materials. The compressive strength at the highest temperature was about 20% of the value at room temperature, and this value was almost the same for all the studied materials. The compressive strength increased slightly at approx. 200 °C. This is usual for many types of concrete, but the design codes and standards neglect this phenomenon.

The most significant differences were found between the results obtained by two methods used for the measurement of thermal conductivity and the available data of thermal conductivity. Using the first test method, described in EN 993-15 [33], the thermal conductivity decreased with increasing temperature. This is comparable with the design codes and with the data from the available literature. Using the second method, the evolution of thermal conductivity has the opposite direction. These two types of tests seem not to be comparable, and further investigation is required.

Table 4 shows a summary the results of all tests performed on all materials. The tabular summary presents the percentage change in the properties and provides a basis for comparisons, e.g. the thermal conductivity of ordinary concrete at room temperature is 28% lower for the tests performed at the laboratory MA than for the tests performed at the TZ laboratory.

The development of the thermal and material properties of concrete exposed to high temperatures can be used for an assessment of existing structures, in the design of new structures with a high risk of fire loading or for numerical simulations of structures subjected to fire loading.

Fig. 13. Temperature dependences of the relative compressive strength of the investigated materials and their comparison with the data stated in EN 1992-1-2 [29].

Table 4
Summary of the results – temperatures (initial and final), values of the material property at the given temperature, relative values of the material property at the final temperature.

Material property	Lab. mark [method ref.]		Material RC		Material AC		Material PC		Material U		Material S	
Bulk density	MA [30]	[°C]	25	1000	25	1000	25	1000	25	1000	25	1000
		[kg/m³]	2306	1932	2277	2031	2306	1967	2570	2290	1543	1104
		[%]		83.80		89.22		85.29		89.12		71.57
	TZ [31,32]	[°C]	100	1000	100	1000	100	1000	100	1000	100	1000
		[kg/m³]	2339	2118	2322	2085	2344	2099	2626	2464	1630	1145
		[%]		90.57		89.79		89.53		93.83		70.27
Porosity	MA [30]	[°C]	25	1000	25	1000	25	1000	25	1000	25	1000
		[%]	11.57	28.48	11.95	25.39	10.86	27.62	12.25	28.53	39.68	63.03
		[%]		246.25		212.47		254.27		232.90		158.84
	TZ [32]	[°C]	100	1000	100	1000	100	1000	100	1000	100	600
		[%]	8.15	21.65	7.45	23.25	7.20	22.50	1.40	9.35	36.80	46.65
		[%]		265.64		312.08		312.50		667.86		126.77
Thermal conductivity	TZ [33]	[°C]	100	800	100	800	100	800	100	800	100	1000
		[W/(mK)]	2.68	1.21	2.61	1.26	2.60	1.23	2.21	1.30	0.73	0.66
		[%]		45.15		48.47		47.46		58.82		89.77
	MA [34]	[°C]	25	500	25	500	25	500	25	500	25	500
		[W/(mK)]	1.95	2.33	2.20	3.05	1.90	2.20	1.39	2.25	0.79	1.46
		[%]		119.18		138.61		115.93		160.81		182.32
Specific heat capacity	MA [14]	[°C]	25	1000	25	1000	25	1000	25	1000	25	1000
		[J/(kgK)]	898.78	977.58	825.87	1110.58	894.60	984.42	901.78	1049.87	979.29	975.45
		[%]		108.77		134.47		110.04		116.42		99.61
Permeability	TZ [35]	[°C]	20	1000	20	1000	20	1000	400	1000	20	600
		[m²]	1.15E−15	2.06E−13	1.17E−14	2.05E−13	5.88E−15	2.51E−13	2.95E−15	1.19E−13	4.65E−12	3.87E−12
		[%]		17825.51		1750.40		4264.19		4048.59		83.28
Compressive strength	KU [36]	[°C]	20	1000	20	1000	20	1000	20	800	20	800
		[MPa]	47.79	8.27	48.71	5.66	53.17	6.86	149.80	10.44	7.71	1.27
		[%]		17.30		11.62		12.91		6.97		16.43

5. Conclusions

This paper presented experimentally acquired material properties for various types of cementitious composites: reference concrete (RC), its derivatives air-entrained concrete (AC) and polypropylene fibre concrete (PC), ultra-high performance concrete with steel fibres (U) and innovative hybrid concrete with mineral insulation shreds (S).

The main aim of the paper was to compare the material properties development and simultaneously to compare the effect of the standardized or referenced testing approach on the resultant value of the tested material property. Therefore, some properties were measured by several methods or using varying specimen dimensions. All experimentally acquired results were presented in summary graphs and compared with values from the valid standards and referenced literature. The tests were performed in three accredited laboratories and one university research department. The outcome of the measurement was always dependent on the measurement method. Different laboratories use different test methods that produce contradictory results.

CRediT authorship contribution statement

Kateřina Horníková: Conceptualization, Formal analysis, Investigation, Writing - original draft, Writing - review & editing, Visualization. **Lenka Scheinherrová:** Formal analysis, Investigation, Writing - original draft, Writing - review & editing. **Radek Štefan:** Supervision, Formal analysis, Writing - review & editing, Methodology, Visualization. **Marek Foglar:** Supervision, Writing - review & editing, Methodology, Funding acquisition.

Declaration of Competing Interest

The authors declare that they have no known competing financial interests or personal relationships that could have appeared to influence the work reported in this paper.

Acknowledgement

References

[1] W. Sha, E.A. O'Neill, Z. Guo, Differential scanning calorimetry study of ordinary Portland cement, Cement Concr. Res. 29 (9) (1999) 1487–1489, https://doi.org/10.1016/S0008-8846(99), 00128-3s.

[2] J. Dweck, P.M. Buchler, A.C.V. Coelho, F.K. Cartledge, Hydration of a Portland cement blended with calcium carbonate, Thermochim. Acta 346 (1–2) (2000) 105–113, https://doi.org/10.1016/S0040-6031(99)00369-X.

[3] G. Dolino, The α-inc-β transitions of quartz: A century of research on displacive phase transitions, Phase Trans. 21 (1) (1990) 59–72, https://doi.org/10.1080/01411599008206882.

[4] A.M. Neville, Proparties of Concrete, 4th and final ed., Longman Group, Harlow, 1995. ISBN 0-582-23070-5.

[5] Z. Bažant, M.F. Kaplan, Concrete at High Temperatures: Material Properties and Mathematical Models. Concrete Design and Series Construction, Longman, Harlow, 1996. ISBN 0-582-08626-4.

[6] V. Kodur, Properties of concrete at elevated temperatures online, ISRN Civil Eng. 2014 (2014) 1–15, https://doi.org/10.1155/2014/468510.

[7] Fire Design of Concrete Structures: Materials, Structures And Modelling: State-Of-Art Report. (2007) Bulletin. Lausanne: International Federation for Structural Concrete. ISBN 978-2-88394-078-9

[8] Z. Guo, X. Shi, Experiment and Calculation of Reinforced Concrete At Elevated Temperatures, Butterworth-Heinemann, Waltham, MA, 2011.

[9] I. Asadi, P. Shafigh, Z.F.B. Abu Hassan, N.B. Mahyuddin, Thermal Conductivity of concrete – A review online, J. Build. Eng. 20 (2018) 81–93, https://doi.org/10.1016/j.jobe.2018.07.002.

[10] W.-C. Wang, Compressive strength and thermal conductivity of concrete with nanoclay under various high-temperatures online, Constr. Build. Mater. 147 (2017) 305–311, https://doi.org/10.1016/j.conbuildmat.2017.04.141.

[11] A.A. Sayadi, J.V. Tapia, T.R. Neitzert, G.C. Clifton, Effects of expanded polystyrene (Eps) particles on fire resistance, thermal conductivity and compressive strength of foamed concrete online, Constr. Build. Mater. 112 (2016) 716–724, https://doi.org/10.1016/j.conbuildmat.2016.02.218.

[12] M.A. Othuman, Y.C. Wang, Elevated-temperature thermal properties of lightweight foamed concrete online, Constr. Build. Mater. 25 (2) (2011) 705–716, https://doi.org/10.1016/j.conbuildmat.2010.07.016.

[13] M. Pomianowski, P. Heiselberg, R.L. Jensen, R. Cheng, Y. Zhang, A new experimental method to determine specific heat capacity of inhomogeneous concrete material with incorporated microencapsulated-PCM, Cement Concr. Res. 55 (2014) 22–34, https://doi.org/10.1016/j.cemconres.2013.09.012.

[14] J. Toman, R. Černy, Calorimetry of building materials online, J. Thermal Anal. 43 (2) (1995) 489–496, https://doi.org/10.1007/BF02546837.

[15] T. Ruuska, J. Vinha, H. Kivioja, Measuring thermal conductivity and specific heat capacity values of inhomogeneous materials with A Heat Flow Meter Apparatus Online, J. Build. Eng. 9 (2017) 135–141, https://doi.org/10.1016/j.jobe.2016.11.011.

[16] M.B. Ahlem Houaria, M. Abdelkader, C. Marta, K. Abdelhafid, Comparison between the permeability water and gas permeability of the concretes under the effect of temperature online, Energy Procedia 139 (2017) 725–730, https://doi.org/10.1016/j.egypro.2017.11.278.

[17] Z.A. Kameche, F. Ghomari, M. Choinska, A. Khelidj, Assessment of liquid water and gas permeabilities of partially saturated ordinary concrete Online, Constr. Build. Mater. 65 (2014) 551–565, https://doi.org/10.1016/j.conbuildmat.2014.04.137.

[18] M. Hoseini, V. Bindiganavile, N. Banthia, The effect of mechanical stress on permeability of concrete: a review online, Cement Concr. Compos. 31 (4) (2009) 213–220, https://doi.org/10.1016/j.cemconcomp.2009.02.003.

[19] J. Bošnjak, J. Ožbolt, R. Hahn, Permeability measurement on high strength concrete without and with polypropylene fibers at elevated temperatures using a new test setup online, Cement Concr. Res. 53 (2013) 104–111, https://doi.org/10.1016/j.cemconres.2013.06.005.

[20] A.N. Noumowe, R. Siddique, G. Debicki, Permeability of high-performance concrete subjected to elevated temperature (600°C), Constr. Build. Mater. 23 (5) (2009) 1855–1861, https://doi.org/10.1016/j.conbuildmat.2008.09.023.

[21] D. Gawin, C.E. Majorana, B.A. Schrefler, Numerical analysis of hygro-thermal behaviour and damage of concrete at high temperature, Mech. Cohes.-Frict. Mater. 4 (1999) 37–74, https://doi.org/10.1002/(SICI)1099-1484(199901)4:1<37::AID-CFM58>3.0.CO;2-S.

[22] Q. Ma, R. Guo, Z. Zhao, Z. Lin, K. He, Mechanical properties of concrete at high temperature—a review online, Constr. Build. Mater. 93 (2015) 371–383, https://doi.org/10.1016/j.conbuildmat.2015.05.131.

[23] O. Arioz, Effects of elevated temperatures on properties of concrete online, Fire Safety J. 42 (8) (2007) 516–522, https://doi.org/10.1016/j.firesaf.2007.01.003.

[24] L.T. Phan, N.J. Carino, Review of mechanical properties of HSC at elevated temperature, J. Mater. Civ. Eng. 10 (1) (1998) 58–65, https://doi.org/10.1061/(ASCE)0899-1561(1998)10:1(58).

[25] F.B. Varona, F.J. Baeza, D. Bru, S. Ivorra, Influence of high temperature on the mechanical properties of hybrid fibre reinforced normal and high strength concrete, Constr. Build. Mater. 159 (2018) 73–82, https://doi.org/10.1016/j.conbuildmat.2017.10.129.

[26] A. Baradaran-Nasiri, M. Nematzadeh, The effect of elevated temperatures on the mechanical properties of concrete with fine recycled refractory brick aggregate and aluminate cement, Constr. Build. Mater. 147 (2017) 865–875, https://doi.org/10.1016/j.conbuildmat.2017.04.138.

[27] E. Vejmelková, D. Koňáková, L. Scheinherrová, M. Doleželová, M. Keppert, R. Černý, High temperature durability of fiber reinforced high alumina cement composites online, Constr. Build. Mater. 162 (2018) 881–891, https://doi.org/10.1016/j.conbuildmat.2018.01.076.

[28] EN 206 (2013) + A1 (2016): Concrete – Part 1: Specification, performance, production and conformity.

[29] EN 1992-1-2 (2006): Eurocode 2: Design of concrete structures Part 1-2. General rules – Structural fire design

[30] M. Pavlíková, Z. Pavlík, M. Keppert, R. Černý, Salt transport and storage parameters of renovation plasters and their possible effects on restored buildings' walls, Constr. Build. Mater. 25 (3) (2011) 1205–1212, https://doi.org/10.1016/j.conbuildmat.2010.09.034.

[31] EN ISO 1927-6: Monolithic (unshaped) refractory products – Part 6: Measurement of physical properties.

[32] EN 993-1: Methods of test for dense shaped refractory products – Part 1: Determination of bulk density, apparent porosity and true porosity

[33] EN 993-15: (2005): Methods of test for dense shaped refractory products – Part 15: Determination of thermal conductivity by the hot-wire (Parallel) method

[34] R. Černý, E. Vejmelková, Apparent thermal conductivity approach at high-temperature measurements of porous materials, Measurement 44 (7) (2011) 1220–1228, https://doi.org/10.1016/j.measurement.2011.04.002.

[35] EN 993-4: (1996): Methods of test for dense shaped refractory products – Part 4: Determination of permeability gases

[36] EN 12390-3: Testing hardened concrete – Part 3: Compressive strength of test specimens

[37] P. Kalifa, M. Tsimbrovska, V. Baroghel-Bouny, High-performance concrete at elevated temperatures - an extensive experimental investigation of thermal and hygral properties and microstructure. International symposium on high-

performance and reactive powder concretes, Université de Sherbrooke, Sherbrooke, Canada, 1998, pp. 259–279.

[38] S.O. Osuji, U. Ukeme, Effects of elevated temperature on compressive strength of concrete: a case study of grade 40 concrete, Nigerian J. Technol. 34 (3) (2015) 472–477, https://doi.org/10.4314/njt.v34i3.7.

[39] P. Bamonte, P. Gambarova, Properties of Concrete Subjected to Extreme Thermal Conditions, J. Struct. Fire Eng. 5 (1) (2014) 47–62, https://doi.org/10.1260/2040-2317.5.1.47.

[40] R. Štefan, M. Foglar, J. Fládr, Experimental investigation of behaviour of various types of cementitious composites exposed to fire, Beton TKS 15 (6) (2015) 56–61 [in Czech].

[41] E. Vejmelková, D. Koňáková, M. Čáchová, M. Záleská, P. Svora, M. Keppert, P. Rovnaníková, R. Černý, High-strength concrete based on ternary binder with high pozzolan content, Struct. Concr. 19 (5) (2018) 1258–1267, https://doi.org/10.1002/suco.201700173.

[42] M. Keppert, E. Vejmelkova, R. Černý, S. Švarcová, P. Bezdička, Microstructural changes and residual properties of fiber reinforced cement composites exposed to elevated temperatures, Cement Wapno Beton 17 (2) (2012) 77–89.

[43] L. Scheinherrová, E. Vejmelková, M. Keppert, P. Bezdička, M. Doleželová, J. Krejsová, S. Grzeszczyk, A. Matuszek-Chmurowska, R. Černý, Effect of Cu-Zn coated steel fibers on high temperature resistance of reactive powder concrete, Cem. Concr. Res. 117 (2019) 45–57, https://doi.org/10.1016/j.cemconres.2018.12.008.

[44] L.C. Prinsloo, E.M. van der Merwe, L. Wadley, The thermal behaviour of silica varieties used for tool making in the Stone Age, J. Ther. Anal. Calor. 131 (2) (2018) 1135–1145, https://doi.org/10.1007/s10973-017-6602-z.

[45] Mindeguia, J.-C. (2009) Contribution expérimentale à la compréhension des risques d'instabilité thermique des bétons, PhD thesis, UPPA.

[46] Compressive Strength for Service and Accident Conditions. (1995) Online. Materials and Structures 28 (7): 410-414. https://10.1007/BF02473077.

[47] Pimienta, P., Mindeguia, J.-C., Simon, A. and Behloul, M. (2011) Behavior Of Uhpfrc At High Temperatures. In Designing and Building With UHPFRC, 579-600. Hoboken, NJ USA: John Wiley. https://10.1002/9781118557839.ch40

[48] Pliya, P., Beaucour, A.-L. and Noumowé, A. (2009) Strength and porosity of concrete incorporating polypropylene and steel fibres subjected to high temperature. Smirt 20 - Espoo (Helsinki), Finland., 10

[49] T. Drzymała, W. Jackiewicz-Rek, M. Tomaszewski, A. Kuś, J. Gałaj, R. Šukys, Effects of High Temperature on the Properties of High Performance Concrete (Hpc), Procedia Eng. 172 (2017) 256–263, https://doi.org/10.1016/j.proeng.2017.02.108.

[50] M. Abid, X. Hou, W. Zheng, R.R. Hussain, High temperature and residual properties of reactive powder concrete – a review, Constr. Build. Mater. 147 (2017) 339–351, https://doi.org/10.1016/j.conbuildmat.2017.04.083.

[51] G.F. Peng, S.Y.N. Chan, M. Anson, Chemical kinetics Of C-S-H decomposition in hardened cement paste subjected to elevated temperatures up To 800°C, Adv. Cem. Res. 13 (2) (2001) 47–52, https://doi.org/10.1680/adcr.13.2.47.39294.

Annex 2

Reprint of the Paper

ŠTEFAN, R. et al. Thermal, spalling, and mechanical behaviour of various types of cementitious composites exposed to fire: Experimental and numerical analysis. Construction and Building Materials. 2020, 262 ISSN 0950-0618. DOI 10.1016/j.conbuildmat.2020.119676

Contribution of the author of this thesis of the paper

The author of this thesis is contributed to the paper with evaluation of results of the experiment and collaborated on heat transfer analysis.

Radek Štefan: Conceptualization, Methodology, Software, Formal analysis, Investigation, Data curation, Writing – original draft, Writing – review & editing, Visualization, Supervision.

Marek Foglar: Conceptualization, Resources, Writing – review & editing, Supervision, Project administration, Funding acquisition.

Josef Fládr: Formal analysis, Investigation, Resources, Writing – review & editing.

Kateřina Horníková: Formal analysis, Writing – review & editing.

Jakub Holan: Formal analysis, Writing – original draft, Writing - review & editing.

Thermal, spalling, and mechanical behaviour of various types of cementitious composites exposed to fire: Experimental and numerical analysis

Radek Štefan [a,*], Marek Foglar [a], Josef Fládr [a], Kateřina Horníková [a], Jakub Holan [a]

[a] *Department of Concrete and Masonry Structures, Faculty of Civil Engineering, Czech Technical University in Prague, Thákurova 7, 166 29 Prague 6, Czech Republic*

HIGHLIGHTS

- High-temperature behaviour of various cementitious composites is described.
- Normal weight concrete has the highest residual compressive strength.
- The moisture content has a great effect on the temperature evolution.
- Addition of fibres affects the temperature evolutions in a material only very little.
- Simple models are suitable for simulations of thermal behaviour of various composites.

ARTICLE INFO

ABSTRACT

Nowadays, new types of cementitious composites are increasingly being used for the construction of structural members. This poses a problem regarding the structural fire safety design as the thermal behaviour and mechanical properties at high temperatures of these materials are usually not known. The main aim of this paper is to investigate and present the thermal behaviour, propensity to spalling, and residual strength of various types of cementitious composites exposed to fire. Namely, the following materials are investigated: ordinary normal-weight concrete with or without fibres, light-weight aggregate (LWA) concrete with or without fibres, recycled aggregate concrete with or without fibres, LWA concrete with open structure, and two novel cementitious composites – LWA concrete containing crushed textile and foam plastic, and concrete containing mineral wool insulation shreds. Additional aim of this investigation is to resolve whether widely-used simple transport and material models are suitable for numerical simulations of thermal behaviour of unusual cementitious composites. For the purposes of the investigation, experimental program was proposed and executed, and numerical simulations were performed. The experimental program consisted of fire test of wall-panel specimens and cube specimens in a vertical furnace and of measurement of physical and mechanical properties of the investigated materials. The numerical simulations consisted of finite element analysis of temperature evolutions in the wall-panel specimens. The paper summarizes the results and conclusions of the experimental and numerical investigations. Within the paper, compressive strengths and residual compressive strengths of the investigated materials are presented and discussed. Moreover, experimentally measured thermal behaviour is analysed and compared with the thermal behaviour predicted by numerical simulations. In addition to this, spalling behaviour and surface damage of the specimens made of the investigated materials are presented and discussed. The main conclusion of this paper is that widely-used simple heat transport and material models are suitable for numerical simulations of thermal behaviour of various cementitious composites. Additional important conclusion is that concrete containing mineral wool shreds performs very well when subjected to fire.

© 2020 Elsevier Ltd. All rights reserved.

---

* Corresponding author.
    E-mail address: radek.stefan@fsv.cvut.cz (R. Štefan).

1. Introduction

Fire behaviour of cementitious composites strongly depends on the specific type of material – see, e.g., [1]. For ordinary concretes (normal-weight concrete, normal-strength concrete, concrete with natural aggregate) and for some special concretes (high-strength concrete, light-weight concrete, refractory concrete), the material properties related to the fire behaviour (i.e. the mechanical properties, thermal properties, propensity to spalling, etc.) are generally known and well described in literature – see, e.g., [1–5]. However, for newly developed and non-traditional types of cementitious composites these properties can differ significantly in comparison with ordinary concrete and hence, they have to be studied in detail – see, e.g., [6–23], see also our previous work [24,25] and references therein.

As can be seen from recently published papers, analysis of various types of composite materials exposed to high temperatures are of considerable interest in the scientific community – see, e.g., the papers focused on the investigation of high-temperature properties and behaviour of: high-strength concrete [6–9]; light-weight concrete [10]; fibre-reinforced concrete [11–15]; concrete with recycled materials [16]; concrete with rubber aggregate [17–19]; concrete with recycled concrete aggregate [20]; concrete containing diabase, brick and tile waste, or steel slag [21]; concrete with hemp fibres [22]; geopolymer high-strength concrete [23], etc.

Within this paper, experimental and numerical analysis of fire-exposed specimens made of twelve different cementitious composites is presented in order to analyse their thermal, spalling, and mechanical behaviour. Namely, the following types of materials are investigated: ordinary normal-weight concrete with or without fibres, light-weight aggregate (LWA) concrete with or without fibres, recycled aggregate concrete with or without fibres, LWA concrete with open structure, and two novel cementitious composites – LWA concrete containing crushed textile and foam plastic, and concrete containing mineral wool insulation shreds.

The main aim of this paper is to investigate and present the thermal behaviour, propensity to spalling, and residual strength of the analysed materials exposed to fire. Additional aim of this investigation is to resolve whether widely-used simple transport and material models are suitable for numerical simulations of thermal behaviour of unusual cementitious composites.

A description of the experimental investigation and some preliminary results can also be found in our previous work [24,25].

The paper is organised as follows. In Section 2, the experimental part of the research is introduced – the investigated materials are described in detail, the layout of the experiment is presented, and the obtained data are summarized. In Section 3, a heat transfer model and its numerical implementation are described and applied for numerical simulations of the thermal behaviour of the analysed specimens during the conducted fire test. In Section 4, both the experimental and numerical results are presented and discussed in detail. In Section 5, summarizing conclusions are given.

2. Experimental investigation

In this section, the experimental part of the research is presented. The investigated materials and test specimens are described, and the data measured during the experiment are summarized.

2.1. Materials

Within the experiment, twelve different types of cementitious composites were analysed. These composites can be divided into five material groups.

- Group 1 consists of normal-weight concretes with natural aggregate. In this group, three variants of concrete are included: without fibres (material 1), with short polypropylene fibres (material 2), and with long polymer fibres (material 3). The fibres are of the following parameters (according to the fibre producers). The short polypropylene fibres: length of 16 mm, diameter of 18 μm, tensile strength of 300 MPa, modulus of elasticity of (1300–1800) MPa; these fibres are further denoted as PP 16/0.018 fibres. The long polymer fibres: length of 55 mm, diameter of 0.48 mm, tensile strength of 610 MPa, modulus of elasticity of 5170 MPa; these fibres are further denoted as PE/PP 55/0.48 fibres.
- Group 2 contains LWA (expanded clay) concrete in three variants: without fibres (material 4), with PP 16/0.018 fibres (material 5), and with PE/PP 55/0.48 fibres (material 6).
- In Group 3, recycled aggregate concretes are included, one without fibres (material 7), one with PE/PP 55/0.48 fibres (material 8).
- Group 4 contains LWA concretes with open structure and with the aggregate size of 1–4 mm (material 9) and 4–8 mm (material 10).
- Group 5 consists of two types of novel cementitious composites. The first composite (material 11) is a LWA concrete containing roughly crushed fragments of recycled automotive materials such as textile and foam plastic; the crushed fragments are of irregular shape with minimum size of 1–5 mm and maximum size of 10–30 mm, see [26,27]. The second composite in this group (material 12) is a concrete containing mineral wool insulation shreds (recycled glass and rock wool insulation) of irregular shape with maximum size of 50 mm, see [28].

The materials are summarized in Table 1. The compositions of the mixtures and selected material properties are given in Table 2.

2.2. Specimens

For each material, the following test specimens were manufactured:

- six cubes of the size of 150 mm × 150 mm × 150 mm;
- wall panel of the size of 300 mm × 300 mm × 30 mm;
- wall panel of the size of 300 mm × 300 mm × 60 mm;
- wall panel of the size of 300 mm × 300 mm × 120 mm.

During the casting of the wall-panel specimens, K-type thermo-couples (2 × ⌀ 0.5 mm wires) were placed in specified positions

Table 1
Investigated materials, see also [24].

Group	Material No.	Material description
1	1	Normal-weight concrete
	2	Normal-weight concrete with PP fibres 16/0.018
	3	Normal-weight concrete with PE/PP fibres 55/0.48
2	4	LWA concrete
	5	LWA concrete with PP fibres 16/0.01
	6	LWA concrete with PE/PP fibres 55/0.48
3	7	Recycled aggregate concrete
	8	Recycled aggregate concrete with PE/PP fibres 55/0.48
4	9	LWA concrete with open structure, aggregate size 1–4 mm
	10	LWA concrete with open structure, aggregate size 4–8 mm
5	11	LWA concrete with crushed textile and foam material
	12	Concrete containing mineral wool insulation shreds

Table 2
Mixtures compositions, measured material properties, see also [24].

Material No.	1	2	3	4	5	6	7	8	9	10	11	12
Component	Content [kg/m^3]											
Cement CEM I 42.5 R	520	520	520	490	490	490	260	260	420	420	590	875
Water	205	205	205	185	185	185	115	115	155	155	380	437
Natural siliceous aggr. 0/4	1070	1070	1070									
Natural siliceous aggr. 4/8	620	620	620									285
Expanded clay aggr. 1/4				180	180	180			480			
Expanded clay aggr. 4/8				170	170	170				420	170	
Recycled concrete aggr. 0/8							1600	1600				
Polycarboxylate superplasticizer	4.0	4.0	4.0									
PP fibres 16/0.018		2.5			3.1							
PE/PP fibres 55/0.48			4.5			5.7		9.1				
Crushed textile and foam											100	
Mineral wool shreds												190
Fibre volume fraction [%]		0.3	0.5		0.3	0.6		1.0				
Density [kg/m^3]	2322	2024	2299	953	975	962	1821	1849	914	898	1129	1645
Weight loss due to fire [%]	8	8	9	15	14	13	16	16	8	10	37	21
f_{cm} [MPa]	62.0	33.2	62.5	5.7	6.0	5.4	17.1	23.2	3.6	3.0	7.4	12.3
$f_{cm,res}$ [MPa]	13.8	5.0	10.9	1.3	1.9	1.8	2.4	3.3	0.7	0.9	0.8	3.9
$f_{cm,res}/f_{cm}$ [%]	22.2	15.2	17.5	23.3	32.4	33.1	13.9	14.2	18.4	31.5	11.4	31.5

within the panels, see Figs. 1 and 2. Throughout this paper, the panels are denoted by a number and a lower index, e.g. 2_{12}, where the number represents the number of a material (1–12, see Table 1) and the lower index (3, 6, or 12) indicates the thickness (in cm) of the wall panel, see Fig. 2.

After the casting, all specimens were air-cured at the ambient temperature of 25 °C and the relative humidity of 50 % for 2 months.

2.3. Test procedure

The cube specimens were used for the standardized measurements of the density and the compressive strength of the investigated materials. For each material, three cubes were measured, weighed, and tested in a hydraulic press at normal temperature. Two-pyramid failure mode was observed in the test specimens. The resulting mean values of the compressive strengths of the materials, f_{cm}, are presented in Table 2.

The cube specimens made of materials 11 and 12 were also used for indicative measurements of the thermal conductivities of these materials. The measurements were performed twice for each material using the ISOMET device as described, e.g., in [29]. The following results were obtained: 0.63 W m^{-1} K^{-1} and 0.49 W m^{-1} K^{-1} for material 11, and 0.38 W m^{-1} K^{-1} and 0.35 W m^{-1} K^{-1} for material 12.

The remaining three cubes of each material were measured and weighed immediately before the fire experiment. Afterwards, the cubes were placed in a test furnace and subjected to fire. The fire test was conducted in a vertical wall furnace, see Fig. 3.

After a cooling period of one day, the heated cubes were measured and weighed again and then tested in a hydraulic press. Two-pyramid failure mode was observed in the test specimens. The resulting mean values of the residual compressive strengths of the materials, both absolute $f_{cm,res}$ and relative $f_{cm,res}/f_{cm}$, are presented in Table 2.

Fig. 1. Moulds for the wall-panel specimens and positioning and fixing of thermocouples, see also [24].
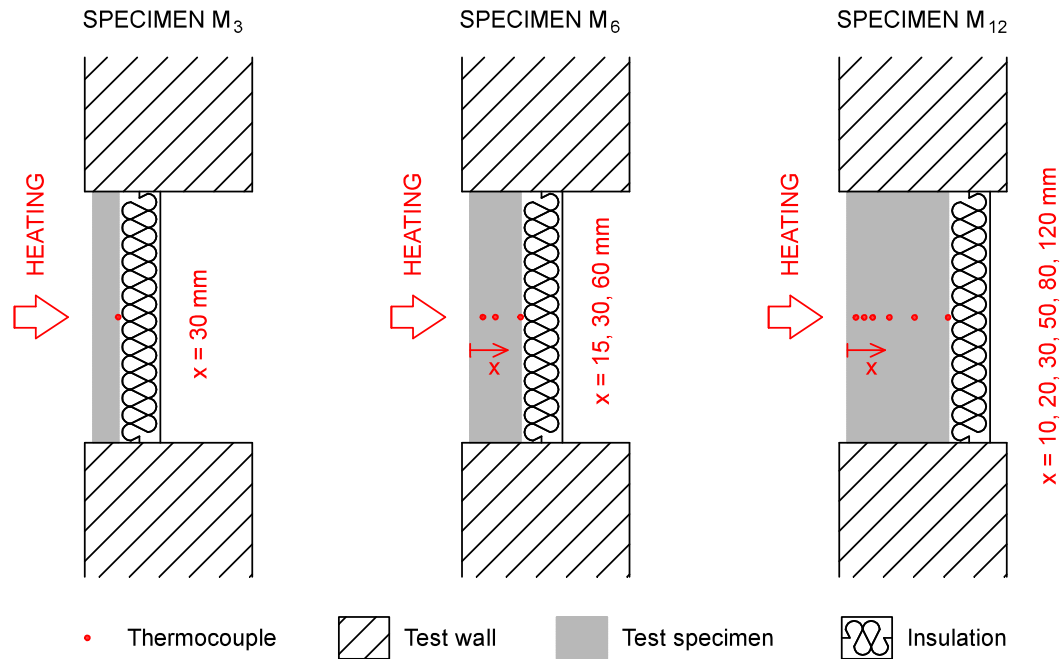
Fig. 2. Wall-panel specimens and positions of thermocouples. Notation: "M" represents the material number – see Table 1; the lower index: 3, 6, and 12, indicates the thickness (in cm) of the wall panel; "x" is the distance of a thermocouple from the heated surface.

Fig. 3. A vertical furnace used for the fire test: the furnace without the test wall (left); inside view of the furnace with the test wall and the test specimens set in place (right), see also [24].

The density of each material at normal temperature was determined from the weights and dimensions of all six cube samples at normal temperature (cf. [24]), see Table 2. By comparing the mean value of the residual density of a material after the fire test (measured on three cubes exposed to fire) and the mean value of its initial density (measures on all six cubes at normal temperature), the weight loss due to fire was determined, see Table 2. The value of the weight loss was further used for an approximate estimation of the initial moisture content in the material.

The wall panels, used for the determination of the thermal behaviour of the materials and their propensity to spalling, were arranged in a autoclaved aerated concrete masonry wall placed in a steel frame, as shown in Figs. 2–5. On the unheated side, the panels were insulated by a mineral wool insulation of the thickness of 50 mm – see Fig. 2.

The furnace temperature, controlled by 7 plate thermometers (see Figs. 3 and 5), followed the standard temperature–time curve (ISO 834 fire), e.g. [30, Eq. (3.4)]

$$\theta_g = 20 + 345 \log (8t/60 + 1), \tag{1}$$

where θ_g [°C] is the gas (fire) temperature, and t [s] is the time of heating, see Fig. 6.

The total time of heating was 120 minutes. The heating period was followed by a natural cooling for one day. After the cooling
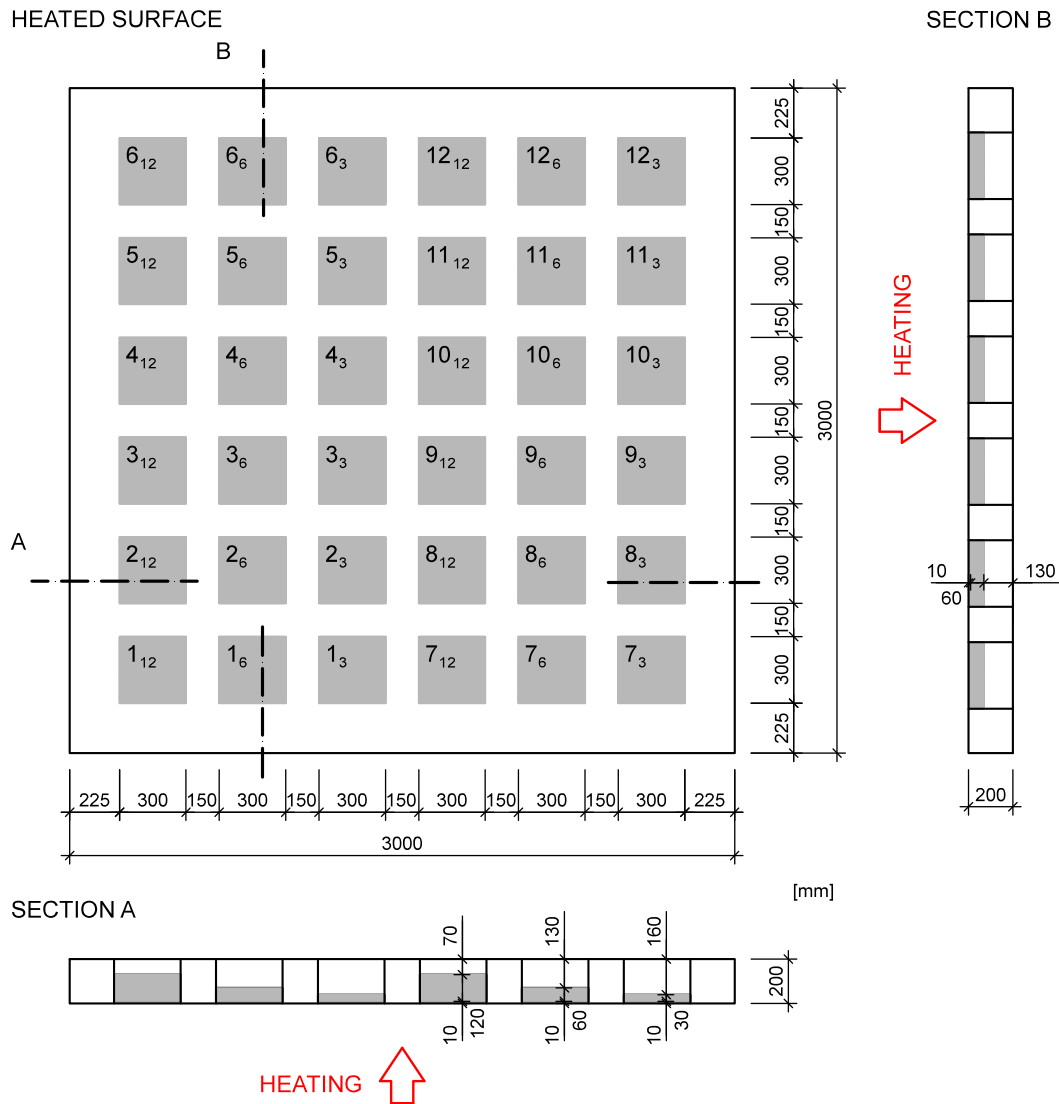
Fig. 4. Setup of the fire test, see also [24].

period, all specimens were closely analysed – i.e. measured, weighed, and photographed.

A total destruction of specimen 3_3 (wall-panel specimen of the thickness of 30 mm made of material 3 – normal-weight concrete with PE/PP 55/0.48 fibres) occurred after 10 minutes of fire exposure. This, however, did not affect any other specimen during the fire test. The opening in the test wall, incurred due to the 3_3 specimen destruction, was filled with a mineral wool insulation, which ensured the enclosure of the furnace for the rest of the test period.

2.4. Obtained data

The data obtained within the presented experimental investigation are summarized in the following list:

- compressive strengths of the investigated materials at normal temperature,
- residual compressive strengths of the investigated materials after the fire test,
- photographs of the heated surfaces of the wall-panel specimens after the fire test,
- spalling depths of the wall-panel specimens after the fire test,
- densities of the investigated materials at normal temperature,

- residual densities of the investigated materials after the fire test,
- thermal conductivities of materials 11 and 12 at normal temperature obtained using indicative measurements,
- temperature evolutions in the specimens during the fire test measured by the thermocouples placed in the wall-panel specimens,
- test conditions – temperature and pressure evolutions in the test furnace and the outside temperature.

The data, together with the results of numerical simulations described in Section 3, are closely analysed in Section 4.

3. Numerical modelling

In this section, numerical simulations of thermal behaviour of the investigated cementitious composites are presented. For the simulations, a common one-dimensional heat transfer model is employed in connection with widely-used simple material models describing the thermal properties of materials, see also our previous work [31–33] and refences therein. This approach is employed in order to determine whether the widely-used simple material models are generally applicable for the simulation of the heat

Fig. 5. Test wall with the wall-panel specimens: the outside view – the unheated surface (left); the inside view – the heated surface (right), see also [24].
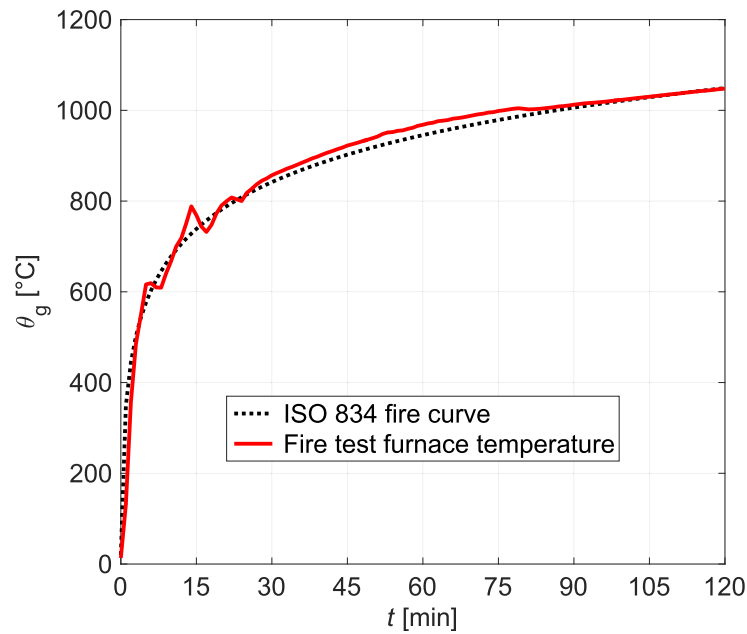

Fig. 6. Fire test furnace temperature evolution – mean values of the data obtained by 7 plate thermometers in the furnace, see also [24].

transfer in structures made of various cementitious composites. This will be resolved in Section 4 by a comparison of the results obtained using numerical simulations and the temperature evolutions measured in the wall-panel specimens during the fire test.

3.1. Heat transfer model

Assuming a one-dimensional heat transfer model with the temperature $\theta(x, t)$ [°C] as the primary unknown, we can write (e.g. [34–36], see also our previous work [31–33]):

for $t \in (0, T)$ and $x \in (0, L)$:

$$\rho(\theta) c_p(\theta) \frac{\partial \theta}{\partial t} = \frac{\partial}{\partial x} \left(\lambda(\theta) \frac{\partial \theta}{\partial x} \right), \qquad (2)$$

for $t \in (0, T)$ and $x = 0$ or $x = L$:

$$-\lambda(\theta) \frac{\partial \theta}{\partial x} n = \alpha_c (\theta - \theta_\infty) + \varepsilon \sigma \left[(\theta + 273.15)^4 - (\theta_\infty + 273.15)^4 \right], \qquad (3)$$

for $t = 0$ and $x \in (0, L)$:

$$\theta = \theta_0, \qquad (4)$$

where x [m] is the position coordinate, t [s] is the time, L [m] is the thickness of the analysed specimen, T [s] is the final time, ρ [kg m^{-3}], c_p [J kg^{-1} K^{-1}], and λ [W m^{-1} K^{-1}], respectively, are the density, the specific heat capacity, and the thermal conductivity of the analysed material, α_c [W m^{-2} K^{-1}] is the convective heat transfer coefficient, n is the unit normal, ε [–] is the surface emissivity,

$\sigma \left[\text{W}\,\text{m}^{-2}\,\text{K}^{-4}\right]$ is the Stefan–Boltzmann constant, θ_∞ [°C] is the ambient temperature, and θ_0 [°C] is the initial temperature.

3.2. Material properties

For the heat transfer model described in Section 3.1, it is necessary to define the density, the specific heat capacity, and the thermal conductivity of the analysed material. Moreover, due to the high temperature conditions reached during the presented experiment, the temperature dependencies of these material properties also need to be specified. As described in Section 2, only the compressive strength and the density of the investigated cementitious composites were measured within the experimental investigation. These material parameters were measured both at normal temperature and after the fire exposure. Therefore, the remaining material parameters and their temperature dependencies needed for the numerical simulation must be determined using another approach.

One possible approach to obtaining the required material properties (density, specific heat capacity, and thermal conductivity; or their combination in the form of the thermal diffusivity) is to utilize the measured temperature evolutions in the wall-panel specimens, and perform an inverse analysis, see e.g. [37–40]. However, the results and conclusions obtained using this approach would only be applicable to the specific analysed materials and cannot be generalized.

In the present paper, a different approach is employed. Despite the variety of the analysed materials, we decided to adopt widely-used simple material models given in fire design codes and literature. Using this approach, the general applicability of these material models for the heat transfer simulations in structures made of various cementitious composites will be investigated. In the following subsections, the employed material models are described.

3.2.1. Density

The density, ρ [kg m^{-3}], is described by the formula given in Eurocode 2 as [4, 3.3.2(3)]

$$\rho = \rho_0 \times \begin{cases} 1 & \text{for} \quad \theta \leqslant 115°\text{C}, \\ \left(1 - 0.02\frac{\theta-115}{85}\right) & \text{for} \quad 115°\text{C} < \theta \leqslant 200°\text{C}, \\ \left(0.98 - 0.03\frac{\theta-200}{200}\right) & \text{for} \quad 200°\text{C} < \theta \leqslant 400°\text{C}, \\ \left(0.95 - 0.07\frac{\theta-400}{800}\right) & \text{for} \quad 400°\text{C} < \theta \leqslant 1200°\text{C}, \end{cases} \tag{5}$$

where ρ_0 is the initial density at normal temperature.

3.2.2. Specific heat capacity

For the specific heat capacity, $c_p \left[\text{J}\,\text{kg}^{-1}\,\text{K}^{-1}\right]$, we adopt the formula given in Eurocode 2 [4, 3.3.2(1), (2)]

$$c_p = c_{p,0} + \begin{cases} 0 & \text{for} \quad \theta \leqslant 100°\text{C}, \\ c_{p,u} & \text{for} \quad 100°\text{C} < \theta \leqslant 115°\text{C}, \\ c_{p,u} - \left(c_{p,u} - 100\right)\frac{\theta-115}{85} & \text{for} \quad 115°\text{C} < \theta \leqslant 200°\text{C}, \\ 100 + \frac{\theta-200}{2} & \text{for} \quad 200°\text{C} < \theta \leqslant 400°\text{C}, \\ 200 & \text{for} \quad 400°\text{C} < \theta \leqslant 1200°\text{C}, \end{cases} \tag{6}$$

where $c_{p,0} \left[\text{J}\,\text{kg}^{-1}\,\text{K}^{-1}\right]$ is the initial specific heat capacity at normal temperature and $c_{p,u} \left[\text{J}\,\text{kg}^{-1}\,\text{K}^{-1}\right]$ is an additional capacity, which depends on the initial moisture content in the material as described below.

We have employed formula (6) in order to take into account the hygral effect of moisture content on the thermal behaviour implicitly as it is not explicitly expressed in the heat transfer model presented in Section 3.1 [4, Cl. 3.3.2(2)].

The hygral effect on the temperature distribution could be considered explicitly using a coupled heat and mass transport model, see e.g. [41,42] and our previous work [31,32] and references therein. Such approach is, however, beyond the scope of the present paper as one of the major goals of the paper is to evaluate the applicability of simple models (both transport and material) for the simulation of the heat transfer. Moreover, when applying a comprehensive coupled model, a detailed knowledge about the material properties and parameters (both thermal and hygral) is required. In the present work, the knowledge about the thermal and hygral properties of the analysed materials is limited. However, as the values of moisture content are considerably high (see the values of mass loss presented in Table 2), the hygral effect cannot be neglected. By employing formula (6), the effect of a moisture content is considered in a simplified way [34,41,42].

Formula (6) is given in Eurocode 2 [4, 3.3.2(1), (2)] only for normal-weight concrete. For light-weight concrete, only a constant value of the specific heat capacity is given in Eurocode 4 [5, 3.3.3 (2)]. However, the constant value cannot be used in the present work since the moisture content in the analysed light-weight materials was considerably high and hence it cannot be neglected. We have thus decided to use formula (6) not only for the normal-weight concrete but for all investigated materials regardless of their density, see also [43,44].

The value of the initial specific heat capacity at normal temperature $c_{p,0}$ depends on the type of concrete, and the additional capacity $c_{p,u}$ depends on the moisture content in the material.

For normal-weight concrete, the initial specific heat capacity is assumed as proposed in Eurocode 2 [4, 3.3.2], i.e. $c_{p,0} = 900$ J kg^{-1} K^{-1}. The additional capacity $c_{p,u}$ of normal-weight concrete is determined using the following values. In Eurocode 2 [4, 3.3.2], the following values are given: $c_{p,u} = 0$ J kg^{-1} K^{-1} for the moisture content $u = 0\%$ of concrete weight, $c_{p,u} = 570$ J kg^{-1} K^{-1} for $u = 1.5\%$ of concrete weight, and $c_{p,u} = 1120$ J kg^{-1} K^{-1} for $u = 3\%$ of concrete weight. These values are supplemented by $c_{p,u} = 4700$ J kg^{-1} K^{-1} for $u = 10\%$ of concrete weight, which is given in Eurocode 4 [5, 3.3.2]. For the values of moisture content between 0 and 10% of concrete weight, a linear interpolation is employed to obtain the appropriate value of $c_{p,u}$, see [4, 3.3.2(2)]. For the moisture content above the value of 10% of concrete weight, a linear extrapolation is used to determine $c_{p,u}$; this is not covered by Eurocodes 2 and 4, but it is not physically inaccurate, see e.g. [34].

For light-weight concrete, the parameters $c_{p,0}$ and $c_{p,u}$ are not specified in the Eurocodes. In the present investigation, the initial specific heat capacity is derived from the value for normal-weight concrete, i.e. $c_{p,0} = 900$ J kg^{-1} K^{-1}, by subtracting 160 J kg^{-1} K^{-1}. The value of 160 J kg^{-1} K^{-1} is the difference between the constant value of the specific heat capacity of normal-weight concrete, i.e. 1000 J kg^{-1} K^{-1}, and the constant value of the specific heat capacity of light-weight concrete, i.e. $c_p = 840$ J kg^{-1} K^{-1}, both given in Eurocode 4 [5, 3.3.3(2)] for simple calculations. The value of initial specific heat capacity of light-weight concrete is therefore $c_{p,0} = 900 - 160 = 740$ J kg^{-1} K^{-1}. For the additional capacity $c_{p,u}$, which depends on the initial moisture content in the material, the same values as for normal-weight concrete are assumed for the light-weight concrete.

3.2.3. Thermal conductivity

For normal-weight concrete, Eurocode 2 [4, Cl. 3.3.3(2)] provides two models of thermal conductivity, denoted as upper and lower limits. For concrete with siliceous aggregate, the upper limit is usually used, see e.g. [3,45,46], see also our previous work [47].

The upper limit is described by the following formula [4, Cl. 3.3.3 (2)]

$$\lambda = 2 - 0.2451\frac{\theta}{100} + 0.0107\left(\frac{\theta}{100}\right)^2. \tag{7}$$

For light-weight concrete, Eurocode 4 [5, Cl. 3.3.3(3)] defines the following model of thermal conductivity

$$\lambda = \lambda_0 \times \begin{cases} \left(1 - \frac{\theta}{1600}\right) & \text{for} \quad \theta \leqslant 800°\text{C}, \\ 0.5 & \text{for} \quad 800°\text{C} < \theta \leqslant 1200°\text{C}, \end{cases} \tag{8}$$

where λ_0 [W m^{-1} K^{-1}] is the initial conductivity at normal temperature, which is specified as $\lambda_0 = 1.0$ W m^{-1} K^{-1} for light-weight concrete in Eurocode 4 [5, Cl. 3.3.3(3)]. It should be pointed out that in Eurocode 4, the light-weight concrete is assumed of the density in the range from 1600 kg m^{-3} to 2000 kg m^{-3} [5, Cl. 3.4(3)].

For some of the light-weight composites investigated it the present paper, the density is considerably lower than 1600 kg m^{-3}. Moreover, these composites contain special aggregate (expanded clay) or other components (crushed textile and foam, mineral wool shreds) that significantly affect the thermal conductivity of the resulting composite material. Therefore, formula (8) may not be suitable for these materials.

Published data, see e.g. [3, Fig. 5–6], indicate that for some cementitious composites with low thermal conductivity, the conductivity can be assumed constant, without any significant temperature dependency, i.e.

$$\lambda = \lambda_0. \tag{9}$$

3.2.4. Material models and parameters used for the analysed materials

For the presented numerical simulations of thermal behaviour of the investigated materials, the material models and parameters for each specific material are chosen based on the measured initial density of the material and its composition (type of aggregate and other components). The material models and parameters are assumed as follows.

For all materials, the density is modelled using formula (5), where the initial density of each material ρ_0 is set to the value stated in Table 2. Each value was determined from measurements on six cube samples at normal temperature, see Section 2.

For the specific heat capacity c_p [J kg^{-1} K^{-1}] of all materials, formula (6) is used. Parameter $c_{p,0}$ is chosen based on the density of a material as described in Section 3.2.2, i.e., $c_{p,0} = 900$ J kg^{-1} K^{-1} for the normal-weight concretes (materials 1–3), and $c_{p,0} = 740$ J kg^{-1} K^{-1} for the light-weight composites (materials 4–12). Parameter $c_{p,u}$ is determined based on the initial moisture content in a material using linear interpolation or extrapolation of the data given in Eurocodes 2 and 4 [4,5], see Section 3.2.2.

The initial moisture content is set to the measured values stated in Table 2. For the materials with the measured moisture content above 20 % by weight (materials 11 and 12), a moisture content of 20 % by weight is assumed in the calculations. Moreover, in order to investigate the effect of moisture content on the resulting temperature distribution in normal-weight concretes in more detail, a half-value moisture content (in relation to the measured one) is also assumed for materials 1–3.

For the normal-weight concretes with siliceous aggregate investigated in this paper (materials 1–3), the thermal conductivity is determined by formula (7), which is the upper limit proposed by Eurocode 2 [4].

For the light-weight composites analysed in this paper (materials 4–12), formulae (8) and/or (9) are adopted, with parameter λ_0 determined from literature or using indicative measurements.

For the light-weight composites with recycled concrete aggregate (materials 7 and 8), the thermal conductivity is determined using formula (8) with $\lambda_0 = 1.0$ W m^{-1} K^{-1}, as recommended in Eurocode 4 [5] for light-weight concrete of the density in the range from 1600 kg m^{-3} to 2000 kg m^{-3}.

For the light-weight composites with expanded clay aggregate (materials 4–6, 9, and 10), formula (9) is used for the thermal conductivity, which means that the thermal conductivity is set to a constant value. The constant value is assumed as 0.4 W m^{-1} K^{-1}, which is in accordance with the data that can be found in literature for this specific material – see e.g. [3,43] and references therein.

As mentioned in Section 2.3, the thermal conductivity of the novel cementitious composites (materials 11 and 12) at normal temperature was determined by indicative measurements using the ISOMET device. The measurements were performed twice for each material and the following results were obtained: 0.63 W m^{-1} K^{-1} and 0.49 W m^{-1} K^{-1} for material 11, and 0.38 W m^{-1} K^{-1} and 0.35 W m^{-1} K^{-1} for material 12. These values are employed for the presented numerical simulations by two approaches. In the first approach, formula (8) is used with parameter λ_0 being set to the measured values. In the second approach, formula (9) is used, which means that the thermal conductivities of the materials are assumed as constants equal to the measured values.

All material models and parameters used for the investigated materials are summarized in Table 3.

3.3. Initial and boundary conditions

The initial temperature in Eq. (4) is taken as $\theta_0 = 13$ °C, which is the measured test furnace temperature at the beginning of the fire test.

The boundary conditions on both the heated and the unheated surfaces of the wall-panel specimens are determined by Eq. (3).

For the heated surface, the convective heat transfer coefficient is set to $\alpha_c = 25$ W m^{-2} K^{-1} [30, Cl. 3.2.1(2)], the surface emissivity is taken as $\varepsilon = 0.7$ [4, Cl. 2.2(2)], and the ambient temperature θ_∞ is set to the time dependent fire temperature measured in the test furnace during the experiment, see Fig. 6.

For the unexposed surface, the ambient temperature θ_∞ is assumed constant, equal to the initial temperature, i.e. $\theta_\infty = \theta_0 = 13$ °C, which is in accordance with the temperature measured outside the test furnace during the experiment. The heat flux on the unexposed boundary is modelled as a convective heat flux [30, 3.1(5)], and hence the surface emissivity is taken as $\varepsilon = 0$ in Eq. (3). The fact that the unexposed boundary was insulated by mineral wool insulation of the thickness $L_{ins} = 50$ mm, as shown in Figs. 2 and 5, has to be taken into account in the numerical simulations. The effect of the thermal insulation can be simulated by determining the convective heat transfer coefficient as described in [48, Ex. 13.1, fn. 3]: The convective heat transfer coefficient characterizing the environment (including the effect of radiation) is specified in [30, 3.1(5)] as $\alpha_{c,env} = 9$ W m^{-2} K^{-1}. The thermal conductivity of dry mineral wool insulation is usually taken as 0.04 W m^{-1} K^{-1}, e.g. [49]. However, with increasing humidity, the thermal conductivity of mineral wool increases up to 0.9 W m^{-1} K^{-1} in a saturated state [49, p. 42]. For partially saturated material of the moisture content in the range from 5% to 20% by volume, the thermal conductivity of the material reaches the values in the range from 0.1 W m^{-1} K^{-1} to 0.14 W m^{-1} K^{-1} [49, p. 42]. In the investigated fire test, the insulation was partially saturated by the water escaping from the heated specimens and hence, in our simulations, we assume the thermal conductivity of the insulation as $\lambda_{ins} = 0.13$ W m^{-1} K^{-1}. The convective heat trans-

Table 3
Material models and parameters employed for the numerical simulations.

Material	Density		Specific heat capacity			Thermal conductivity	
No.	Formula	$\rho_0 \; [\text{kg m}^{-3}]$	Formula	$c_{p,0} \; [\text{J kg}^{-1}\,\text{K}^{-1}]$	$u \; [\%$ by weight$]$	Formula	$\lambda_0 \; [\text{W m}^{-1}\,\text{K}^{-1}]$
1	(5)	2322	(6)	900	8; 4	(7)	–
2	(5)	2024	(6)	900	8; 4	(7)	–
3	(5)	2299	(6)	900	9; 4.5	(7)	–
4	(5)	953	(6)	740	15	(9)	0.4
5	(5)	975	(6)	740	14	(9)	0.4
6	(5)	962	(6)	740	13	(9)	0.4
7	(5)	1821	(6)	740	16	(8)	1.0
8	(5)	1849	(6)	740	16	(8)	1.0
9	(5)	914	(6)	740	8	(9)	0.4
10	(5)	898	(6)	740	10	(9)	0.4
11	(5)	1129	(6)	740	20	(8); (9)	0.63; 0.49
12	(5)	1645	(6)	740	20	(8); (9)	0.38; 0.35

fer coefficient representing the insulation can be expressed as [48, Ex. 13.1, fn. 3]

$$\alpha_{c,ins} = \frac{\lambda_{ins}}{L_{ins}} = \frac{0.13}{0.05} = 2.6 \; \text{W m}^{-2}\,\text{K}^{-1} \tag{10}$$

and, finally, the total convective heat transfer coefficient on the unexposed boundary can be determined as [48, Ex. 13.1, fn. 3]

$$\alpha_c = \frac{1}{\frac{1}{\alpha_{c,env}} + \frac{1}{\alpha_{c,ins}}} = \frac{1}{\frac{1}{9} + \frac{1}{2.6}} = 2 \; \text{W m}^{-2}\,\text{K}^{-1}. \tag{11}$$

The parameters of the boundary conditions employed in the numerical simulations are summarized in Table 4.

3.4. Numerical implementation

The heat transfer model presented in Section 3.1, with the material properties described in Section 3.2, and with the initial and boundary conditions specified in Section 3.3, has been implemented in MATLAB [50] environment, as described in detail, e.g., in our previous work [31], and utilized for the following numerical simulations.

The spatial discretization is conducted using one-dimensional linear finite elements of the size $\Delta x = 1$ mm. For the temporal discretization, a semi-implicit difference scheme is used. The time step is taken as $\Delta t = 10$ s.

The thickness of the analysed specimen, L, is set to 30 mm, 60 mm, or 120 mm. The final time is taken as $T = 120$ minutes.

3.5. Effect of spalling

As described in the following sections, during the fire test, significant spalling of concrete cover in the central part of the heated specimen surface, where the thermocouples were placed, occurred in specimen 1_{12} (wall-panel specimen of the thickness of 120 mm made of material 1 – normal-weight concrete without fibres). The spalling occured after 13 minutes of heating and the final spalling depth (measured after the test) was 10 mm. In order to capture this effect in the heat transfer simulation of specimen 1_{12}, the concrete spalling is taken into account by changing the position of the

Table 4
Parameters of boundary condition (3) employed for the numerical simulations.

	Exposed boundary	Unexposed boundary
$\theta_\infty \; [°\text{C}]$	$\theta_g(t)$, see Fig. 6	13
$\alpha_c \; [\text{W m}^{-2}\,\text{K}^{-1}]$	25	2
$\varepsilon \; [-]$	0.7	0

heated boundary, i.e. by assuming the 10 mm reduction of the specimen thickness at the time of heating $t = 13$ minutes. Such approach is widely used and well described in literature, e.g. [51–53].

Since significant concrete spalling occurred only in one specimen, the experimentally obtained data regarding the spalling are very limited. Thus, concrete spalling numerical simulations were not performed as the numerically obtained data could not be compared with the insufficient experimentally obtained data. Moreover, this paper is focused on the evaluation of the applicability of simple models (both transport and material) for the simulation of the heat transfer. As pointed out, e.g., in [51], the prediction of concrete spalling requires more sophisticated numerical approaches, such as coupled thermo-hygro-mechanical modelling – see, e.g., [31] and references therein.

4. Results and discussion

4.1. Compressive strength

The obtained values of compressive strengths of the investigated materials, both at normal temperature and after the fire exposure, are presented in Table 2 and Figs. 7–9. The obtained values of the relative residual compressive strength are presented in Table 2 and Fig. 10.

4.1.1. Compressive strength at normal temperature
Compressive strength of each material at normal temperature, f_{cm}, was determined as a mean value of the results obtained from compression tests performed on three cube specimens. The obtained mean values of compressive strengths range from 3 MPa to 62.5 MPa – see Table 2.

As can be readily seen in Fig. 7, the normal-weight concrete both with and without fibres (materials 1–3) had the highest compressive strength followed by the recycled aggregate concrete both with and without fibres (materials 7 and 8). This finding is not surprising as these are the only investigated materials which do not contain LWA nor any waste material.

For all of the investigated materials, a correlation between density and compressive strength exists. With decreasing density, the compressive strength at normal temperature also decreases. This can be seen in, e.g., a comparison between the novel materials (materials 11 and 12) and standard LWA materials (materials 4–6, 9, and 10). The novel materials have both higher density and higher compressive strength. Another example is the LWA concrete with open structure (materials 9 and 10), which has both lower density and lower compressive strength than LWA concrete with normal structure (materials 4–6).
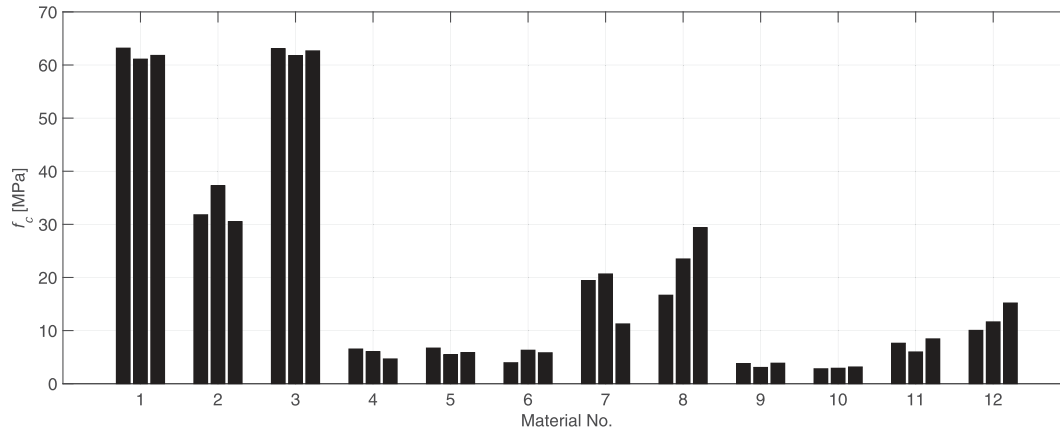
Fig. 7. Compressive strengths at normal temperature, f_c, of the investigated materials – individual measured values.
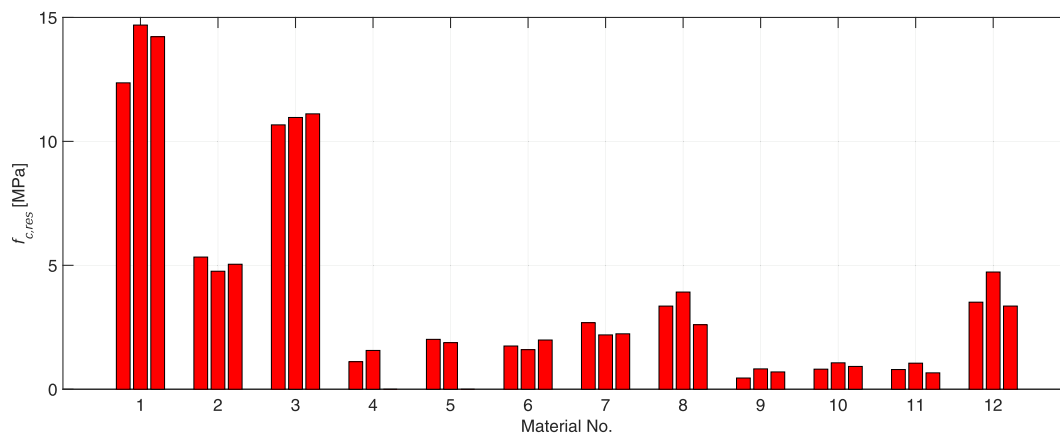

Fig. 8. Residual compressive strengths, $f_{c,res}$, of the investigated materials – individual measured values.
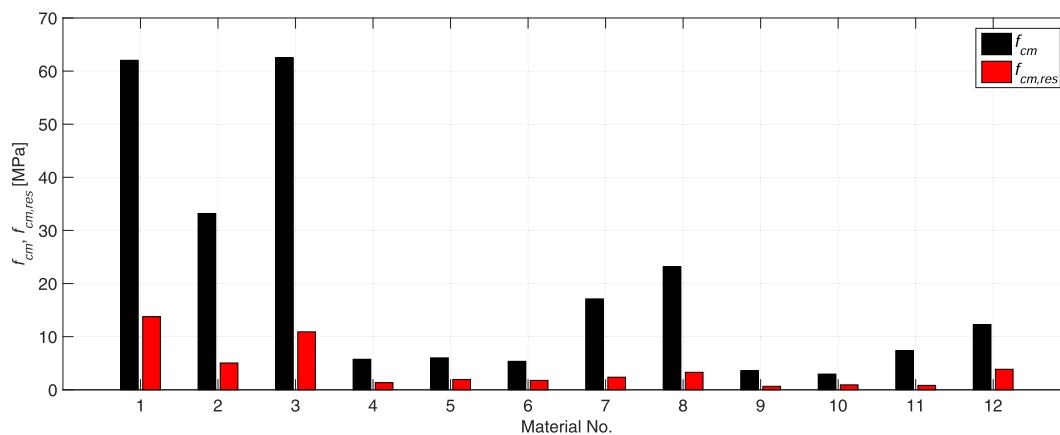

Fig. 9. Mean values of the compressive strength at normal temperature, f_{cm}, and mean values of the residual compressive strength, $f_{cm,res}$, of the investigated materials.

It is worth noting that significantly lower compressive strength was obtained for material 2 in comparison with materials 1 and 3 although all three materials are of similar compositions. This result is attributed to possible errors during mixing of the concrete mixture or during the compaction of the concrete in the moulds, which could have resulted in lower material density and lower compressive strength. The possibility of errors is supported by the fact that the measured values of strength of material 2 vary more than the measured values of strengths of materials 1 and 3.

4.1.2. Residual compressive strength

Compressive strength of each material after fire exposure, $f_{cm,res}$, was determined as a mean value of the results obtained from compression tests performed on three cube specimens previously subjected to fire during a fire test. The obtained mean values of residual compressive strength range from 0.7 MPa to 13.8 MPa – see Table 2.

The normal-weight concrete both with and without fibres (materials 1–3) has the highest residual compressive strength.
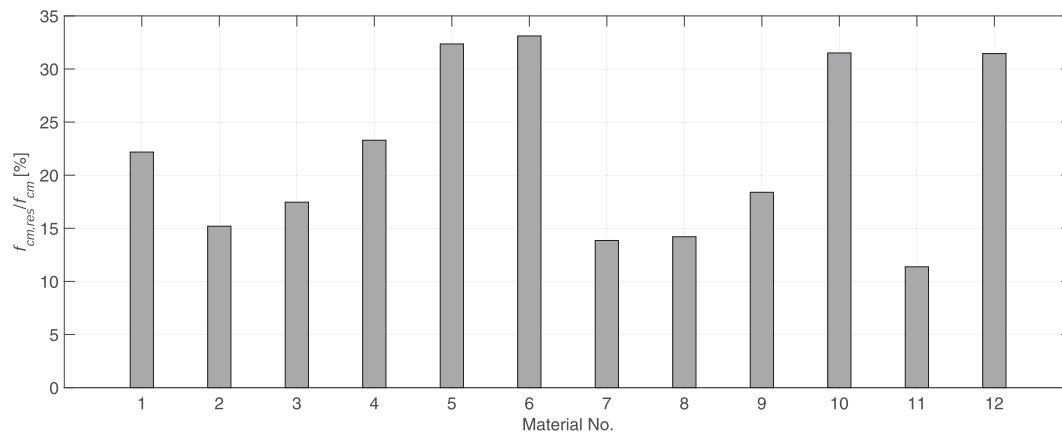
Fig. 10. Relative residual compressive strengths, i.e. $f_{cm,res}/f_{cm}$ ratio, of the investigated materials.

The second highest residual compressive strength was obtained for the novel concrete with mineral wool shreds (material 12). The lowest values of residual compressive strength were obtained for the LWA concrete with open structure (materials 9 and 10) and the LWA concrete with crushed textile and foam (material 11). In general, with decreasing initial density, the residual compressive strength also decreases. There are, however, some exceptions – e.g. materials 10 and 11.

4.1.3. Relative residual compressive strength

Relative residual compressive strength of each material, $f_{cm,res}/f_{cm}$, was determined as a ratio of the residual compressive strengths to the compressive strength at normal temperature. The obtained values of relative residual compressive strengths range from 11.4 % to 33.1 % – see Table 2 and Fig. 10.

Mostly, the highest relative residual compressive strengths were obtained for materials with low compressive strength at normal temperature, i.e. the LWA concrete with fibres and the open-structure LWA concrete with 4–8 aggregate size (materials 5, 6, and 10). The possible explanation for this is that the materials are so porous at normal temperature, which is indicated by the low compressive strengths at normal temperature, that the high temperature exposure does not affect the materials as much. This explanation is supported by the fact that the normal-weight concrete (materials 1–3) and the recycled aggregate concrete (materials 7 and 8), which have higher compressive strength at normal temperature and thus are possibly less porous, have lower relative residual compressive strength suggesting that they are more adversely affected by the high temperatures. An exception to this behaviour was observed in the concrete with mineral wool shreds (material 12), which has higher compressive strength at normal temperature than materials 5, 6, and 10 while having the same relative residual compressive strength.

The lowest relative residual strength was obtained for the LWA concrete with crushed textile and foam (material 11), which is one of the novel materials. This could be explained by the fact that crushed textile and foam are strongly adversely affected by the high temperatures, which in turn strongly adversely affects the relative residual compressive strength of the composite material.

4.1.4. General observations

It is worth pointing out that the concrete with mineral wool shreds (material 12), which is one of the novel materials, has performed quite well in the compression tests. The compressive strength at normal temperature and residual compressive strength were the second highest after the "conventional" concretes, i.e. the normal-weight concrete and the recycled aggregate concrete. The

relative residual strength was one of the highest obtained, exceeding the relative residual strengths of the "conventional" concretes.

As can be seen in Figs. 7 and 8, the least variation of strength can be observed in the normal-weight concrete both with and without fibres (materials 1–3) and both before and after the fire exposure. The materials containing LWA (materials 4–6, 9, and 10) and the novel materials (materials 11 and 12) show higher variation of strength. The highest variation of strength can be observed in the recycled aggregate concrete (materials 7 and 8); this could be explained by the fact that the concrete contains old crushed concrete which may be of highly various quality.

As can be seen in Fig. 10, the relative residual compressive strength of normal weigh concrete is adversely affected by the addition of fibres (compare material 1 with materials 2 and 3), and the relative residual compressive strength of LWA concrete is beneficially affected by the addition of fibres (compare material 4 with materials 5 and 6). Therefore, from the obtained result, a generally applicable conclusion regarding the effect of adding fibres on the compressive strength of a material cannot be made.

4.2. Spalling behaviour and surface damage

In this section, the spalling behaviour of the investigated materials and the surface damage of the investigated specimens are presented, see Figs. 11–15, and described.

The spalling behaviour of the normal-weight concrete without fibres (material 1) depended on the thickness of the specimen. With increasing thickness of the specimen, the spalling also increased – see Fig. 11. Spalling occurred in the 60 mm thick and 120 mm thick specimens, and the depth of the spalling was approximately 10 mm in both cases of spalling. The surfaces of the specimens were homogeneous without any visible cracks or pores, which corresponded with the spalling behaviour. The observed spalling behaviour validates a widely accepted fact that normal-weight concrete without fibres is prone to spalling, see e.g. [54].

The normal-weight concrete with short polypropylene fibres (material 2) exhibited no spalling. This validates a widely accepted fact that the addition of short polypropylene fibres reduces the risk of concrete spalling, see e.g. [54]. The surfaces of the specimens made of the normal-weight concrete with short fibres were more porous than the surfaces of the specimens made of the normal-weight concrete without fibres (material 1) and the normal-weight concrete with long fibres (material 3) – see Fig. 11; this corresponded with the fact that no spalling occurred.

The spalling behaviour of the normal-weight concrete with long polymer fibres (material 3) strongly depended on the
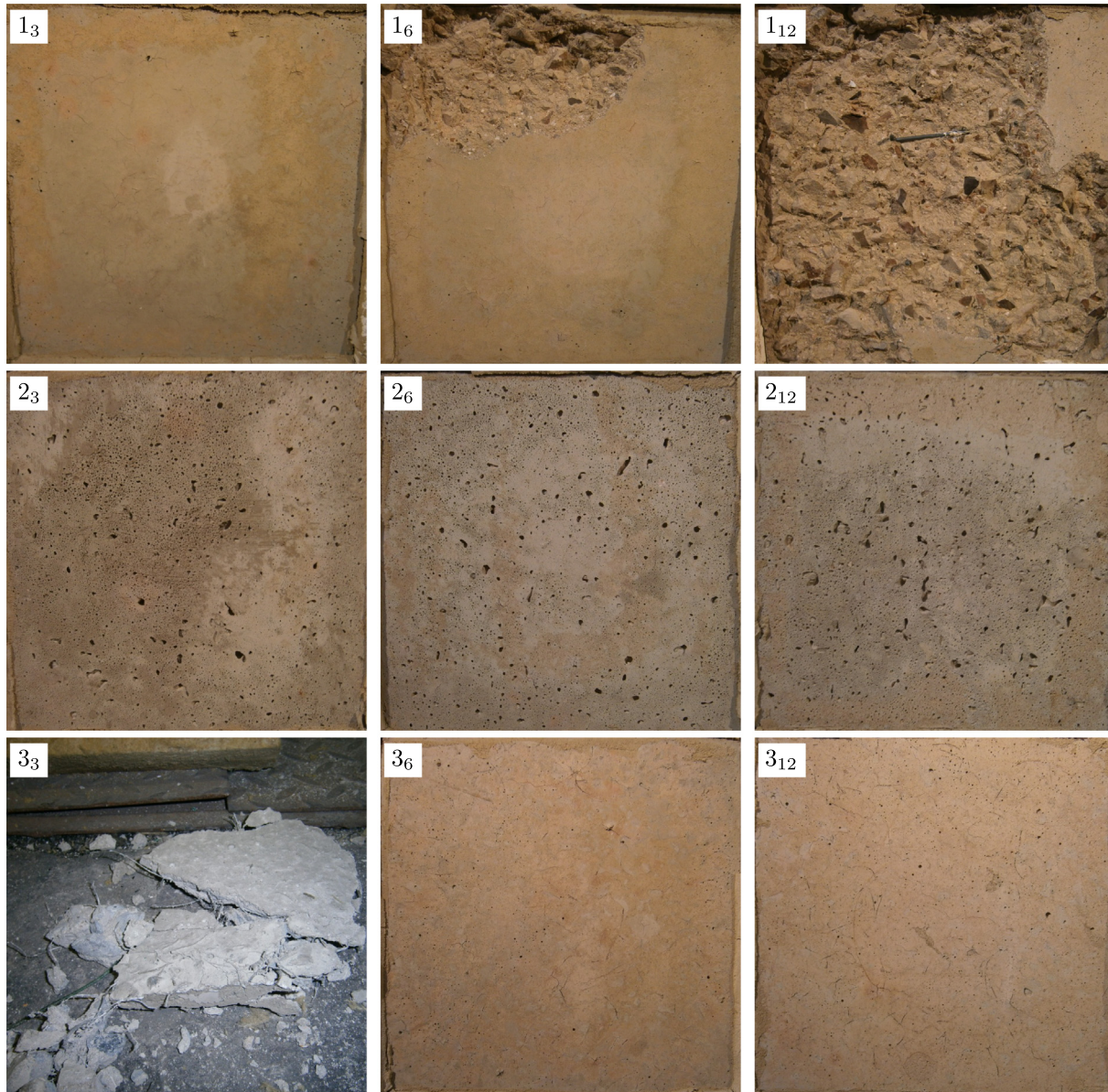
Fig. 11. Fire-exposed surfaces of the slab panel specimens made of normal-weight concrete (materials 1–3), see also [24].

thickness of the specimen – see Fig. 11. In the case of 30 mm thick specimen, an explosive spalling, which totally damaged the specimen, occurred after 10 minutes of fire exposure. The destruction of the specimen could be explained by the fact that the length of the fibres (55 mm) was higher than the thickness of the specimen (30 mm) and by the fact that the amount of fibres was quite high (4.5 kg per 1 cubic metre of the mixture). This means that many fibres could have spanned over the entire thickness of the specimen. At the time of the specimen destruction, the temperature on its unexposed surface was around 120 °C, see Section 4.3. Although on the heated surface and in the inner parts of the specimen the temperatures were higher (see the temperature evolutions in the 10 mm and 15 mm positions for the thicker specimens in Section 4.3), it is evident from Fig. 11 that the fibres in the specimen did not melt and hence the pore pressure in the material was not reduced. It seems that in the case of thin specimen with high amount of long fibres, the fibres could weaken the integrity of the composite material which resulted in the destruction of the specimen. No spalling

was observed in the case of thicker specimens which suggests that the long fibres reduce the risk of concrete spalling in thick specimens. In comparison to normal-weight concrete with short fibres (material 2), the surfaces were less porous. On the surfaces of the specimens, lines resembling micro-cracks could be observed. These lines were not micro-cracks but small cavities created by the burn-out of the long fibres.

The LWA concrete specimens both with and without fibres (materials 4–6) withstood the fire exposure very well. No spalling nor cracking was observed – see Fig. 12. This behaviour is not surprising as the LWA concrete has high porosity and permeability even without the addition of fibres. The effect of porosity and permeability on concrete spalling is described in detail, e.g., in [54]. When compared with the normal-weight concrete (materials 1–3), higher surface porosity could be observed on the surfaces of the LWA concrete (material 4–6) specimens. Quite surprisingly, the specimens made of the LWA concrete with fibres (materials 4 and 5) seemed to have slightly less porous surfaces than the specimens made of the LWA without fibres (material 4).
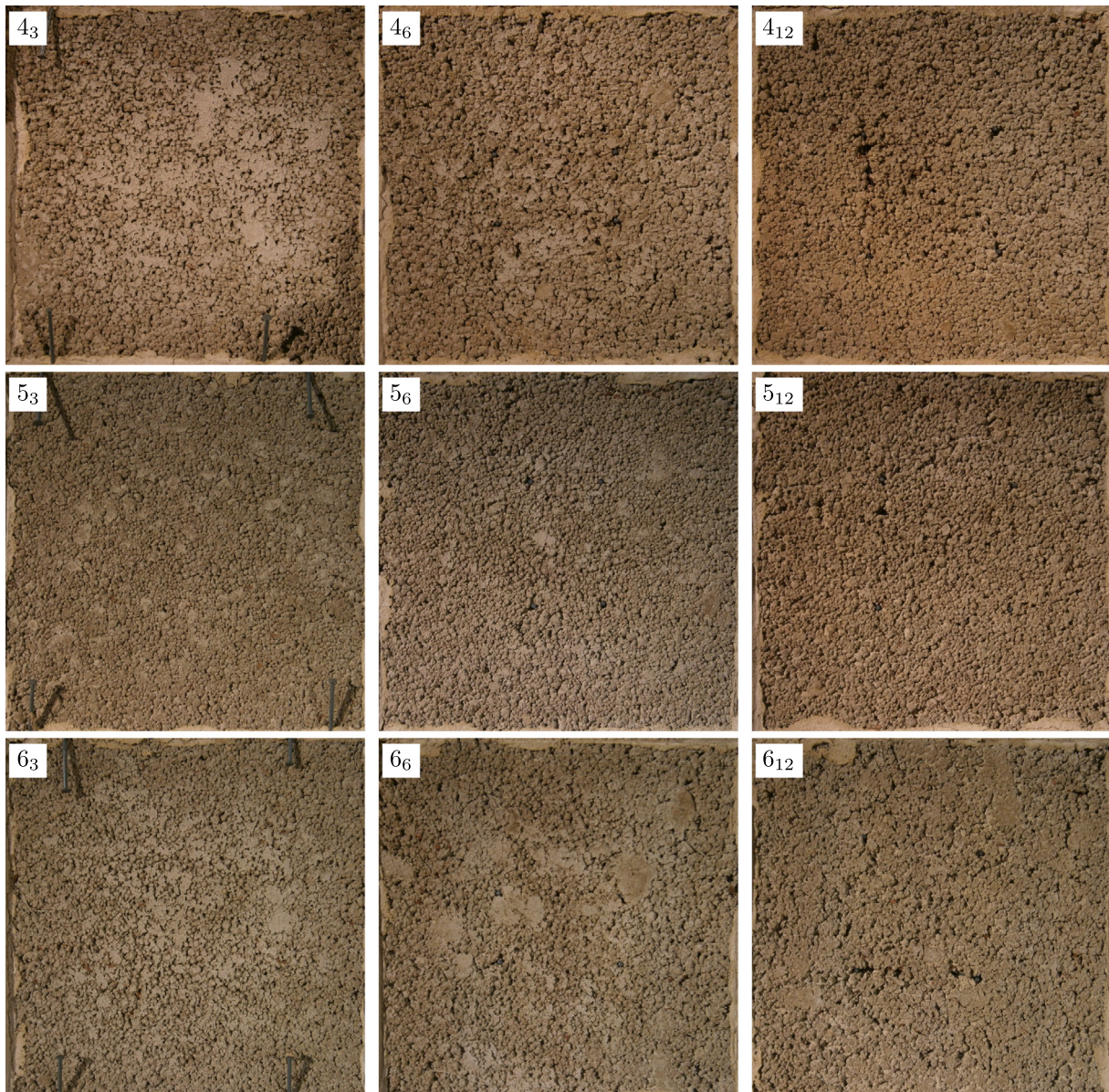
Fig. 12. Fire-exposed surfaces of the slab panel specimens made of LWA concrete (materials 4–6), see also [24].

The recycled aggregate concrete specimens both with and without fibres (materials 7 and 8) also withstood the fire exposure very well. No spalling nor cracking was observed – see Fig. 13. The surface porosity of the recycled aggregate concrete (materials 7 and 8) was higher than the surface porosity of the normal-weight concrete (materials 1–3) but lower than the surface porosity of the LWA concrete (material 4–6).

The LWA concrete with open structure (materials 9 and 10) had the highest surface porosity of all investigated materials, where the concrete with bigger aggregate size (material 10) has higher porosity than the concrete with smaller aggregate size (material 9). Due to the high porosity, no spalling nor cracking was observed – see Fig. 14.

The LWA concrete with crushed textile and foam (material 11) was severely adversely affected by the fire exposure. Although no spalling was observed, long and thick cracks could be seen in all three specimens of varying thicknesses – see Fig. 15. In some places, the aggregate has crumbled out of the specimen. The severity of the damage seems to have increased with the thickness of the specimen.

The concrete containing mineral wool shreds (material 12) withstood the fire exposure very well. No spalling was observed in any of the specimens – see Fig. 15. Some minimal micro-cracking was observed but only in the thickest specimen. The surface porosity of the material was quite low – lower surface porosity was observed only in the normal-weight concrete specimens (materials 1–3).

4.3. Thermal behaviour

4.3.1. Comparison of measured and numerically obtained data

In this section, the data measured during the experiment described in Section 2 are compared with the data obtained by numerical simulations described in Section 3. The comparison is done in order to determine whether accurate prediction of real thermal behaviour can be obtained using the simple heat transport and material models which were employed for the numerical simulations.
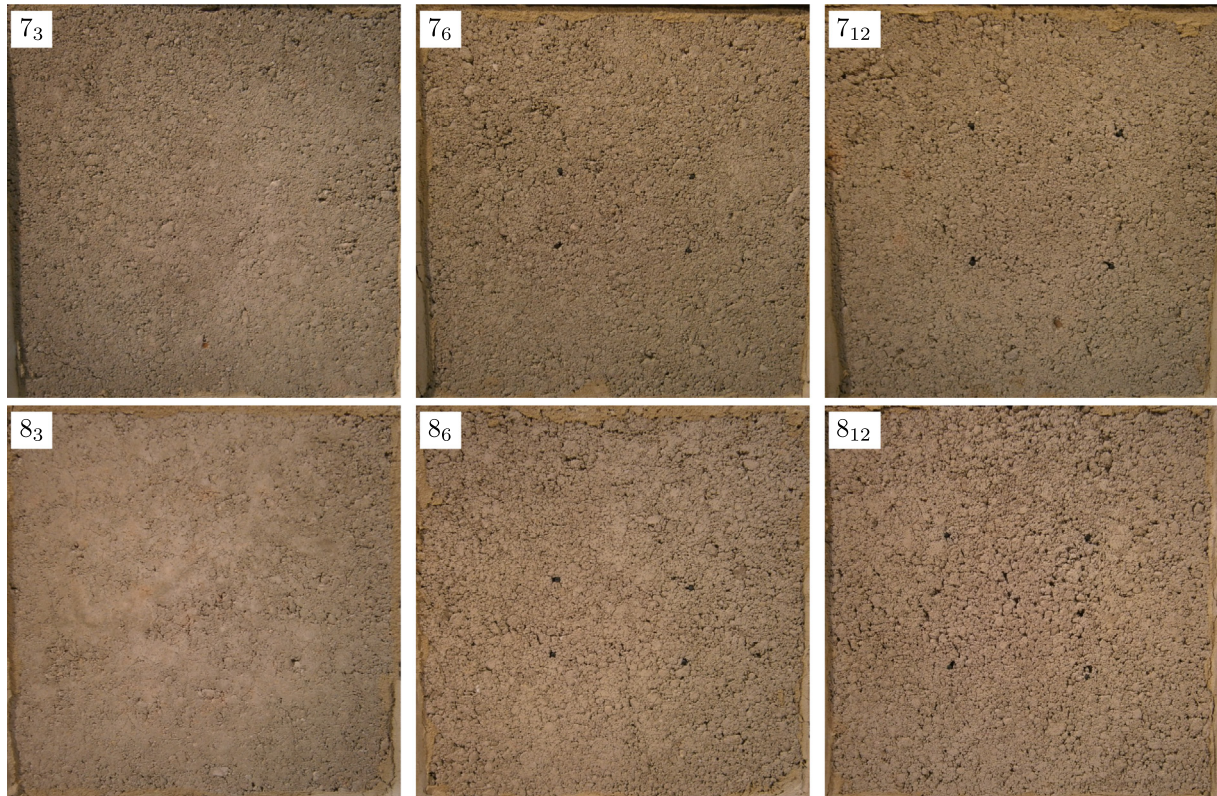
Fig. 13. Fire-exposed surfaces of the slab panel specimens made of recycled aggregate concrete (materials 7 and 8), see also [24].
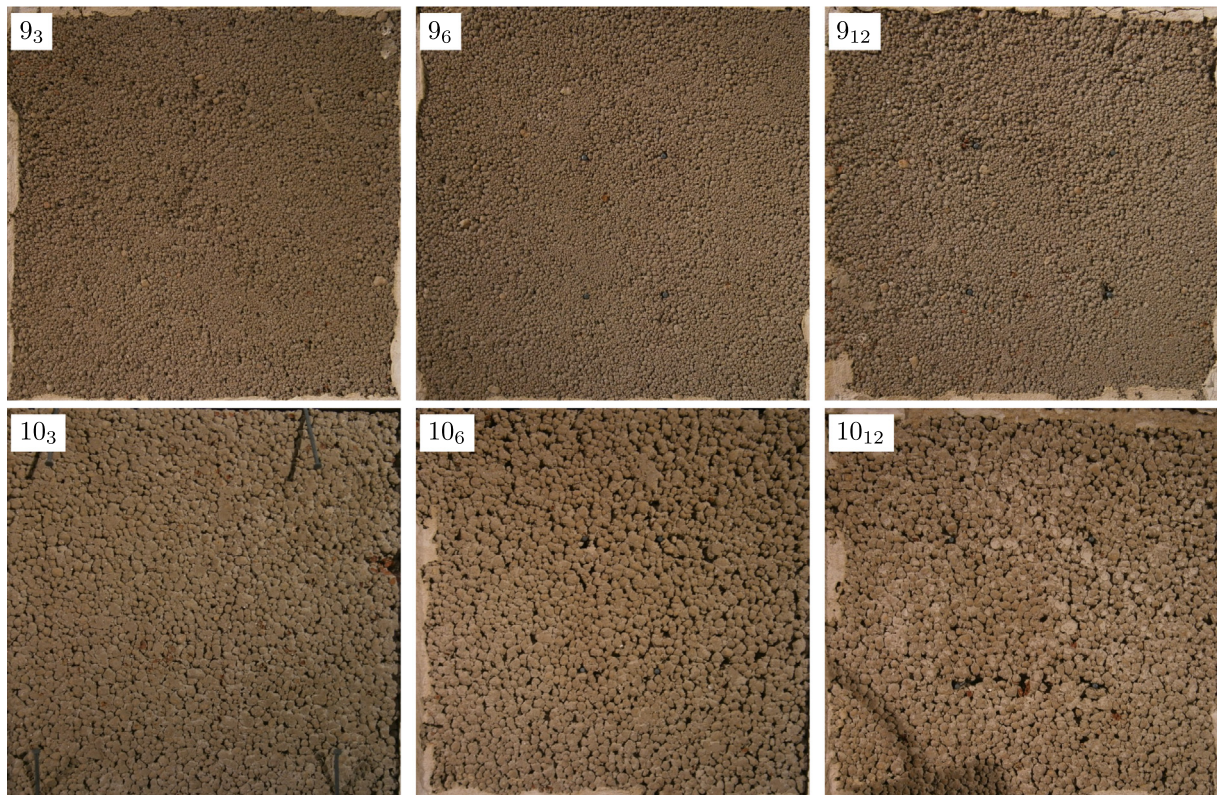

Fig. 14. Fire-exposed surfaces of the slab panel specimens made of open-strucutre LWA concrete (materials 9 and 10), see also [24].
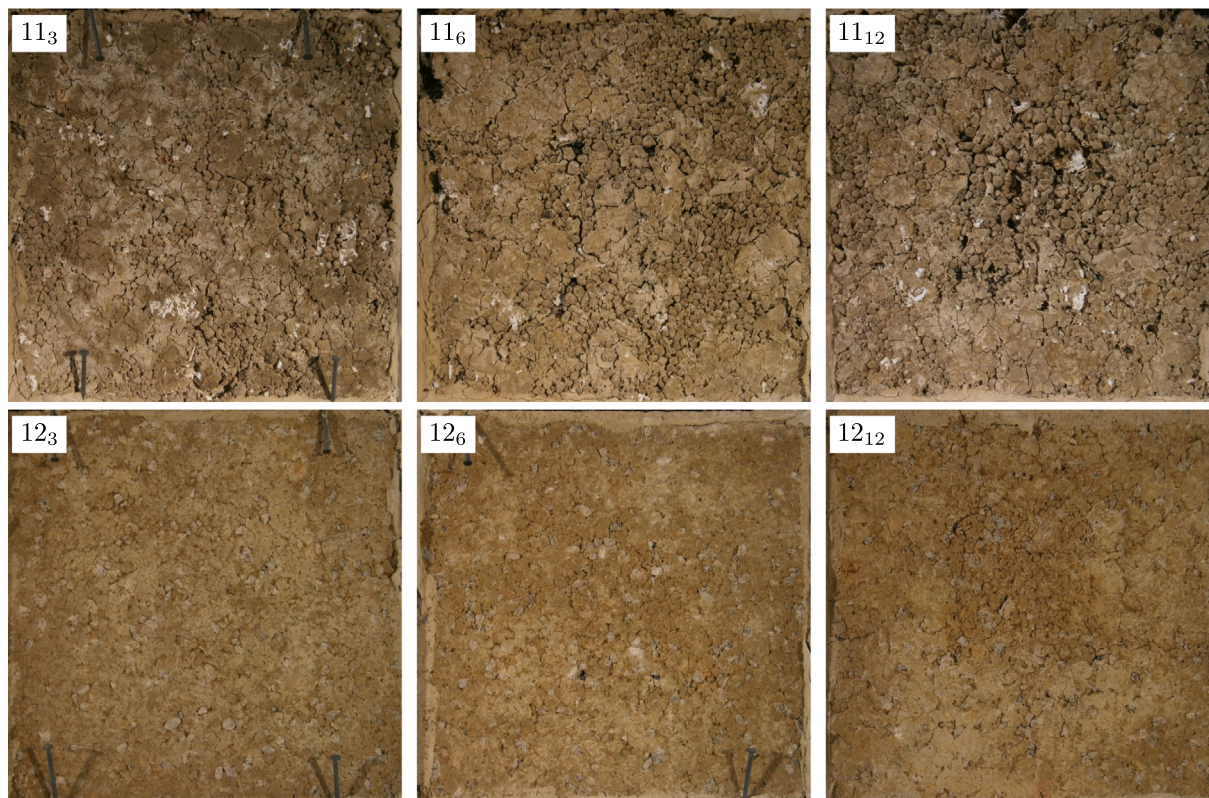
Fig. 15. Fire-exposed surfaces of the slab panel specimens made of the novel materials (materials 11 and 12), see also [24].

For the normal-weight concrete without fibres (material 1), the temperature evolutions obtained by numerical simulations are very close to the evolutions obtained during the experiment – see Fig. 16. This is valid for all thicknesses of the wall-panel specimens and for all thermocouple positions. The agreement between the data can be expected as the simple material models used for the numerical simulations are proposed in [4] for normal-weight concrete without fibres. Regarding the moisture content, better agreement between the data can be seen when the moisture content is assumed as a half of the weight loss during the fire exposure. An anomaly caused by concrete spalling can be seen in the figure presenting the measured temperature evolution in the 120 mm thick specimen. In the numerical simulation, the effect of concrete spalling was captured quite well using the approach described in Section 3.5, i.e. the spalling was modelled by changing the position of the heated boundary.

For the normal-weight concrete with short polypropylene fibres (material 2), the agreement between the temperature evolutions obtained by numerical simulations and measured during the experiment is lower than in the case of normal-weight concrete without fibres (material 1) but is still very good. In the case of 30 mm thick specimen, the spread between the measured and calculated values is quite high; however, the computed values are higher, and thus it is safe to use these values in the fire design of structures. Regarding the moisture content, better agreement between the measured and computed values can be seen when the moisture content is assumed as the full weight loss during the fire exposure.

For the normal-weight concrete with long polymer fibres (material 3), the agreement between the temperature evolutions obtained by numerical simulations and during the experiment are still very good; however, the calculated values are lower than the measured values. This should be taken into account during

the fire design of structures. Regarding the moisture content, better agreement between the measured and calculated values can be seen when the moisture content is assumed as a half of the weight loss during the fire exposure.

For the LWA concrete both with and without fibres (materials 4–6), mostly a good agreement between the experimentally and numerically obtained temperature evolutions can be seen in Fig. 17. A significant difference between the evolutions can be observed in the layers close to the surface exposed to fire. This could be explained by the fact that low compaction and high amount and volume of voids, which can be assumed in the LWA concrete, allow for the heat transfer due to fluid flow (i.e. liquid water flow, water vapour flow, and air flow, see, e.g., our previous work [55] and references therein) to occur in the layers close to the exposed surface. As only conductive heat transfer through the specimens is modelled in the numerical simulations, lower temperatures are obtained using the simulations.

For the recycled aggregate concrete (materials 7 and 8), the experimentally and numerically obtained temperature evolutions in 30 mm and 60 mm thick specimens are in a very good agreement – see Fig. 18. For the 120 mm thick specimen, the numerically obtained values are higher, and thus the agreement is lower; however, as the calculated values are higher, it is safe to use these values in the fire design of structures.

In the case of the open-structure LWA concrete with the aggregate size 1–4 mm (material 9), a good agreement between the experimentally and numerically obtained data can be observed – see Fig. 19. Although in some layers a difference between the measured and calculated values can be seen, the calculated values are higher and thus are safe to use in the fire design of structures.

In the case of the open-structure LWA concrete with the aggregate size 4–8 mm (material 10), a good agreement between the
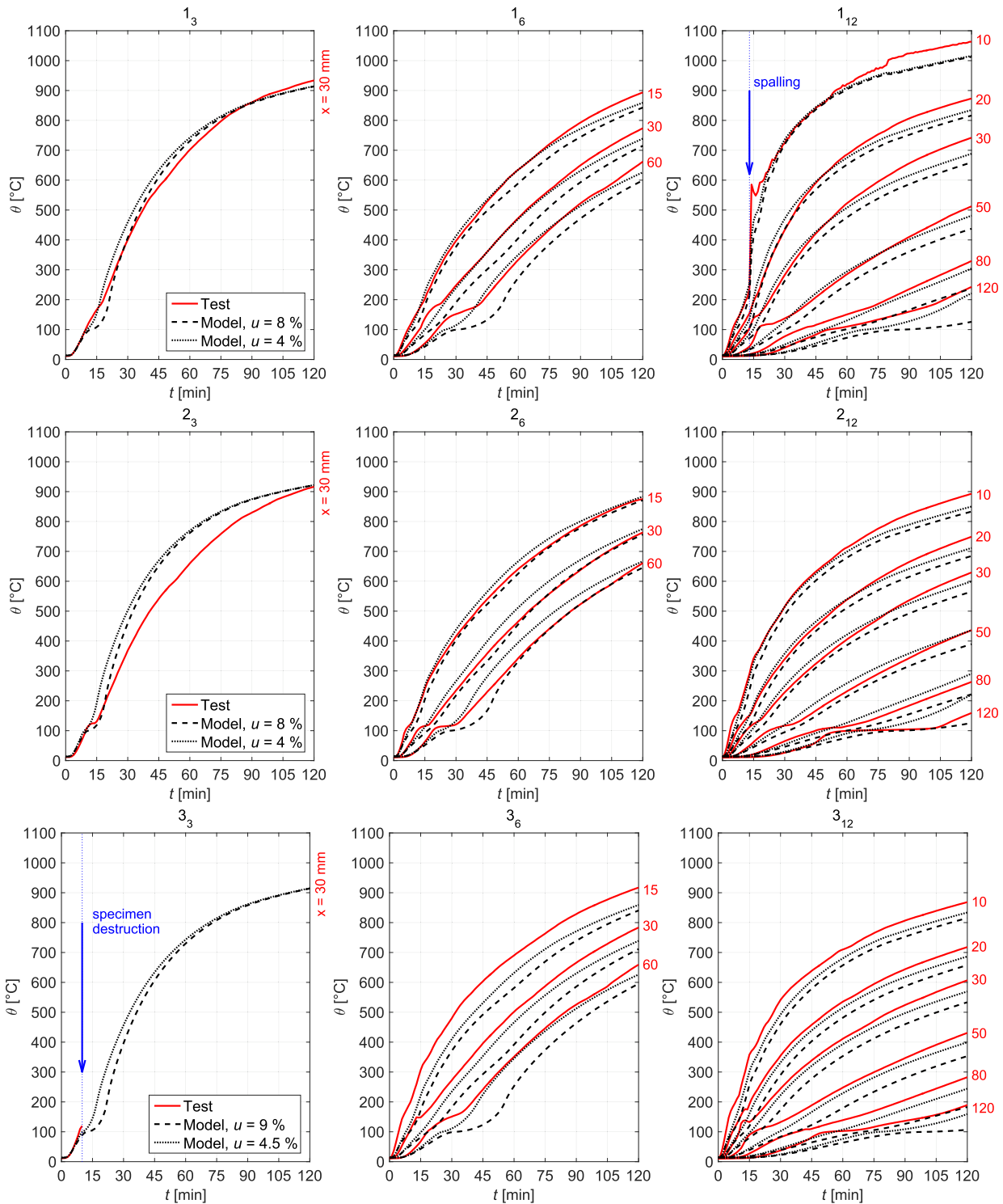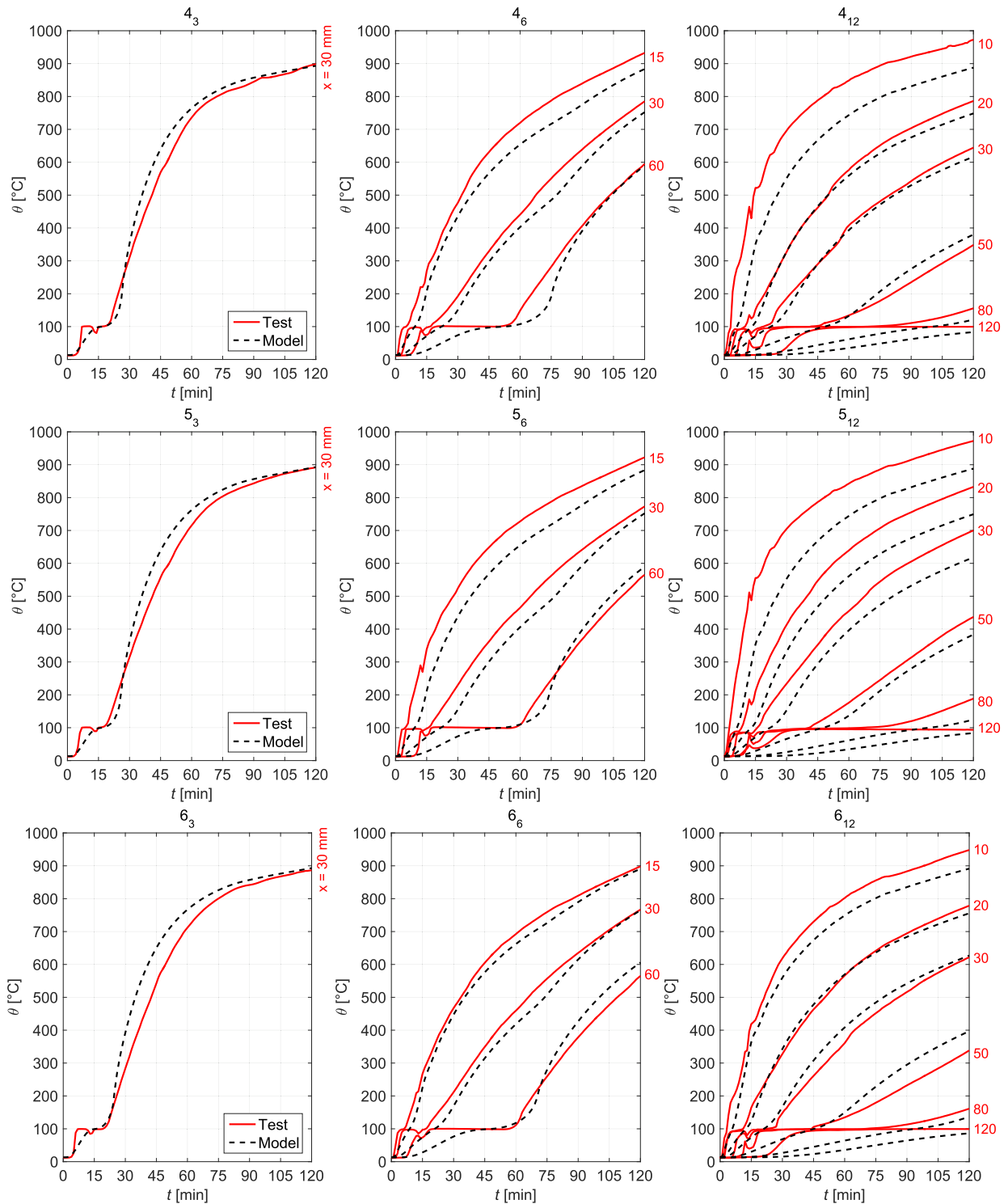
Fig. 16. Temperature evolutions in the analysed wall-panel specimens made of the normal-weight concrete (materials 1–3) measured by the thermocouples (see Fig. 2) during the fire test and calculated using the heat transfer model described in Section 3.

experimentally and numerically obtained data has been obtained in the inner layers of the specimens and on the unexposed surface – see Fig. 19. On the exposed surface, a high difference between the measured and calculated values can be observed. This could again be explained by the fact that low compaction and high amount and volume of voids, which can be assumed in the open-structure LWA concrete, allow for the heat transfer due to fluid flow to occur in the layers closer to surface. As only conductive heat transfer

through the specimens is modelled in the numerical simulations, lower temperatures are obtained using the simulations.

For the LWA concrete with crushed textile and foam (material 11), higher agreement between the experimentally and numerically obtained temperature evolutions on the unexposed surfaces of the specimens is achieved when a temperature-dependent thermal conductivity (Eq. (8)) is assumed – see Fig. 20. As for the temperature evolutions inside the specimens, higher agreement is

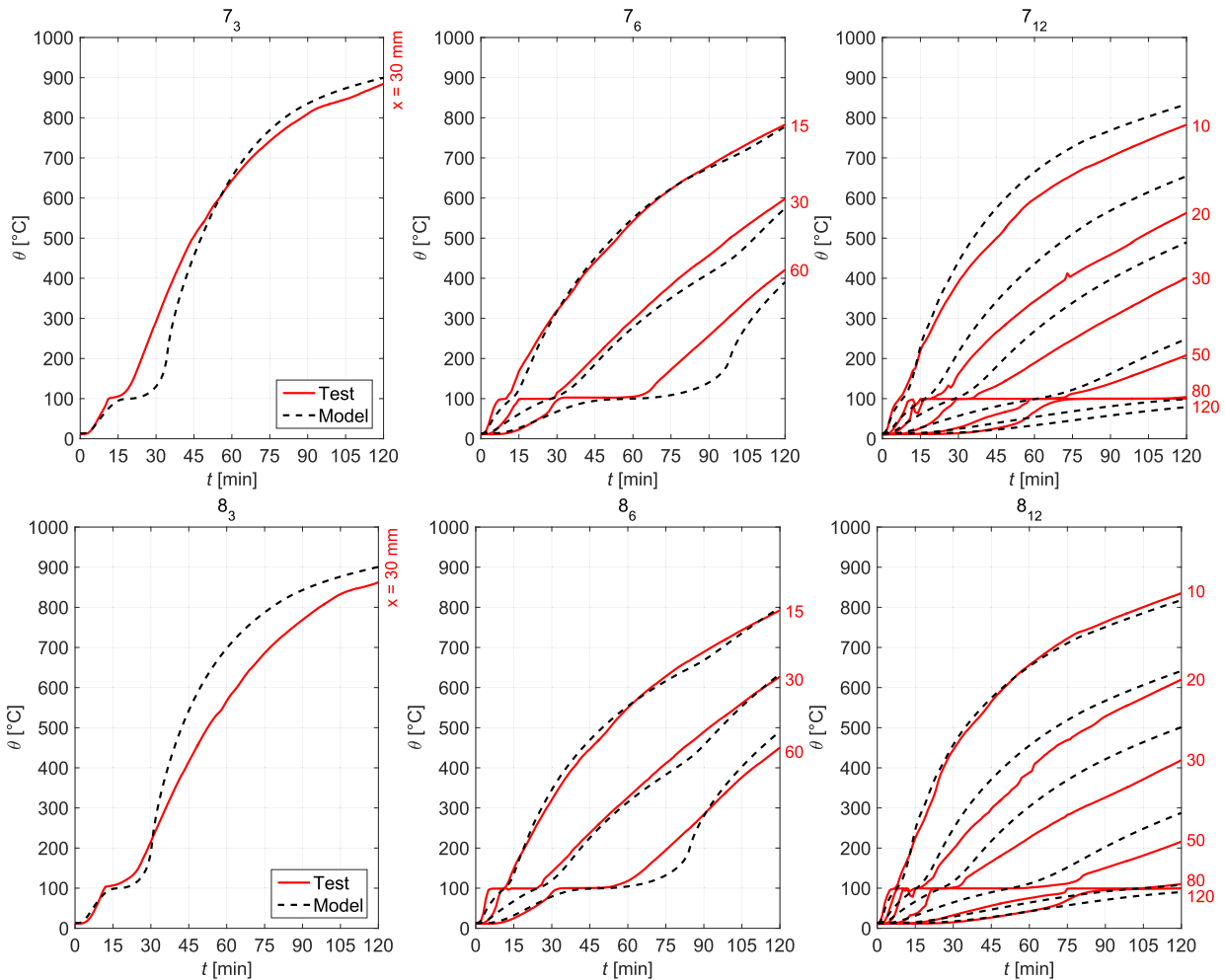**Fig. 17.** Temperature evolutions in the analysed wall-panel specimens made of the LWA concrete (materials 4–6) measured by the thermocouples (see Fig. 2) during the fire test and calculated using the heat transfer model described in Section 3.

achieved when a constant thermal conductivity (Eq. (9)) is assumed. It is advised by the authors of this paper that a constant thermal conductivity be used for the numerical simulations. By assuming the constant value, good agreement between the measured and calculated values is mostly achieved, and in the cases when the agreement is lower, the calculated values are higher, and thus it is safe to use those values for the fire design of structures.

In the case of the concrete containing mineral wool shreds (material 12), higher agreement between the experimentally and numerically obtained temperature evolutions in a 120 mm thick specimen is achieved when a temperature-dependent thermal conductivity (Eq. (8)) is assumed – see Fig. 21. In a 30 mm thick specimen and 60 mm thick specimen, higher agreement between the temperature evolutions is achieved when a constant thermal conductivity (Eq. (9)) is assumed. It is advised by the authors of this

Fig. 18. Temperature evolutions in the analysed wall-panel specimens made of the recycled aggregate concrete (materials 7 and 8) measured by the thermocouples (see Fig. 2) during the fire test and calculated using the heat transfer model described in Section 3.

paper that a constant thermal conductivity should be used for the numerical simulations as by assuming the constant value either good agreement is achieved or the calculated values are higher. Thus, it is safe to use the calculated values for the fire design of structures.

In many of the measured temperature evolutions, a sharp increase to the temperature of 100 °C followed by a constant hold of the temperature can be observed. The sharp increase was most probably caused by moisture transport and heat transfer due to fluid flow through the specimen. The constant hold of temperature was caused by the evaporation of water escaping from the heated specimen and concentrating near its unexposed surface, i.e. the heat was being consumed by the phase change and hence the temperature did not increase. In the case of numerical simulation, the temperature on the unexposed side increased more slowly and steadily. This is due to the fact that the moisture transport in the specimen was not modelled.

In some of the materials, a high difference between the experimentally and numerically obtained data can be observed. Generally, the difference can be attributed to the following.

- In the numerical modelling of thermal behaviour of the wall-panel specimens, initial moisture content was taken into account. This moisture content was determined by weight measurements on cube specimens made of the same materials. However, the moisture content in the cube specimens may have

been different than in the wall-panel specimens. Thus, the value of initial moisture content used for the numerical modelling might have been different than the actual value of initial moisture content in the wall panel. This would cause a difference between the experimentally and numerically obtained data.

- In the numerical modelling of the thermal behaviour of the analysed specimens, the presence of initial moisture content was taken into account only by its effect on the specific heat capacity. The transport of moisture was not taken into account. The moisture transport affected the temperature evolutions measured during the fire test; this effect was, however, not modelled in the numerical simulations.
- For the numerical modelling of thermal behaviour of the analysed specimens, simple transport and material models were assumed. The real behaviour of the investigated materials is much more complex. The difference between the real complex and assumed simple behaviour can cause the difference between the experimentally and numerically obtained data.

4.3.2. Thermal behaviour observed during the experimental investigation

In this section, the data measured during the experiment described in Section 2 and presented in Section 4.3.1 are discussed. The following observations are made from the temperature evolutions in the specimens of all thicknesses (30 mm, 60 mm, and 120 mm) and hold true for all of the thicknesses.
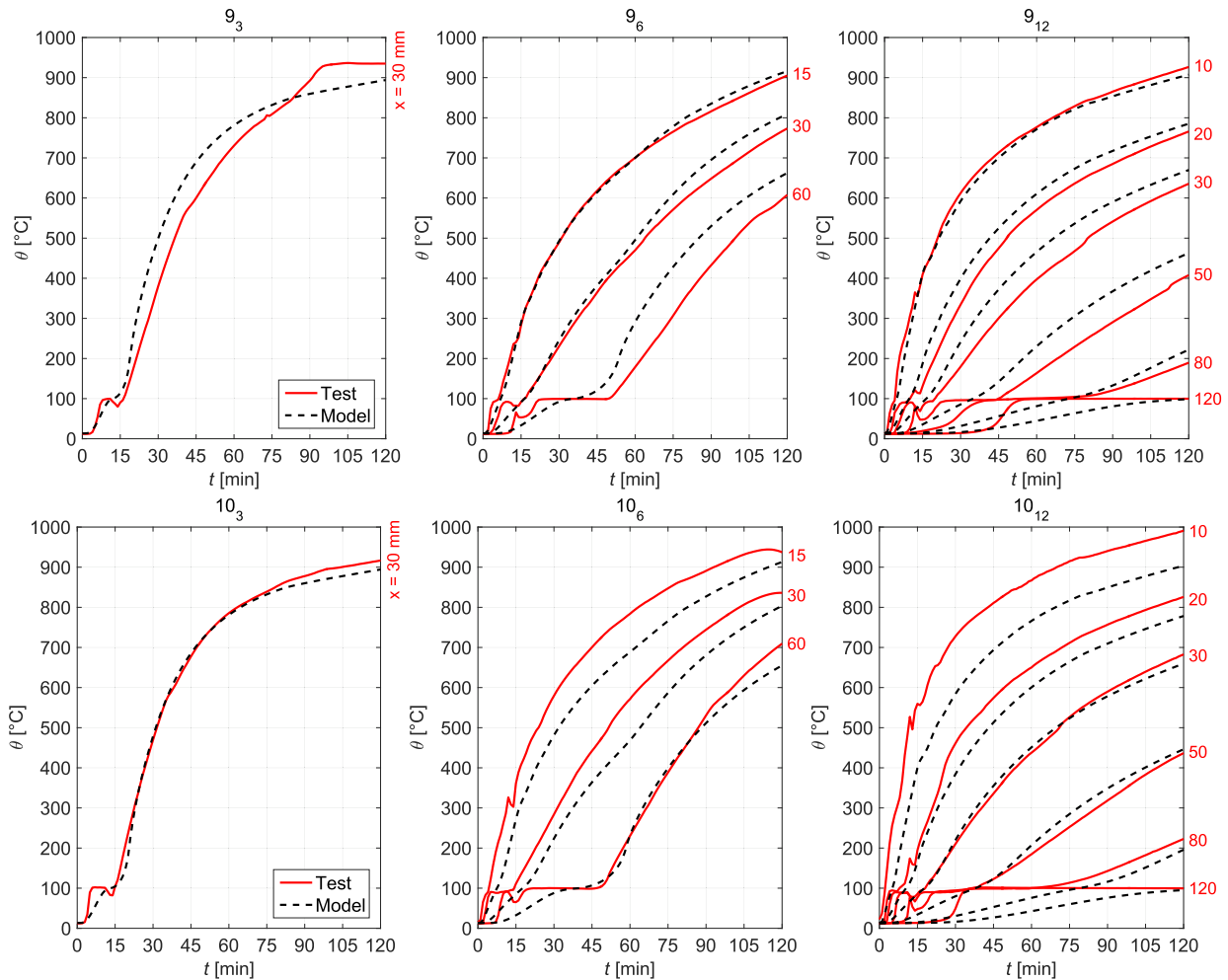
Fig. 19. Temperature evolutions in the analysed wall-panel specimens made of the LWA concrete with open-structure (materials 9 and 10) measured by the thermocouples (see Fig. 2) during the fire test and calculated using the heat transfer model described in Section 3.

The fastest temperature rise and the highest temperatures reached were observed in open-structure LWA concrete with 4–8 mm aggregate (material 10). This is not surprising as the material has high amount and volume of voids, which allowed for the heat transfer due to fluid flow to occur in addition to the conductive heat transfer. One could argue that an exception can be observed in the 120 mm thick specimens where in the specimen made of normal-weight concrete without fibres (material 1) higher temperatures were reached than in the specimen made of open-structure LWA concrete with 4–8 mm aggregates (material 10). However, this was not caused by the material properties of the materials but by the fact that spalling occurred in the specimen made of material 1, which decreased the thickness of the specimen by 10 mm thus decreasing the distance of the thermocouples from the exposed surface.

The slowest temperature rise and lowest reached temperatures were observed in one of the novel materials, i.e. concrete containing mineral wool shreds (material 12). This is also not surprising as the mineral wool acts as a thermal insulator lowering the thermal conductivity of the material.

In all of the fibre-reinforced investigated materials, it was observed that the addition of fibres to a material has little effect on the temperature evolutions in the material.

In many of the temperature evolutions, a sharp increase to the temperature of 100 °C followed by a constant hold of the temperature can be observed. The sharp increase was most probably caused by moisture transport and heat transfer due to fluid flow through the specimen. The constant hold of temperature was caused by the evaporation of water escaping from the heated specimen and concentrating near its unexposed surface, i.e. the heat was being consumed by the phase change and hence the temperature did not increase. This suggests that the moisture content has significant effect on the temperature evolution.

5. Conclusions

The normal-weight concrete (materials 1–3) had the highest residual compressive strength. In general, with decreasing initial density, the residual compressive strength also decreased. Mostly, the highest relative residual compressive strengths was obtained for materials with low compressive strength at normal temperature, i.e. the LWA concrete with fibres and the open-structure LWA concrete 4–8 mm aggregate size (materials 5, 6, and 10).

The least thick specimen made of the normal-weight concrete with long polymer fibres (material 3) performed the worst during the fire exposure as this specimen was completely destroyed. The thickest specimen made of normal-weight concrete without fibres (material 1) was severely damaged by spalling on nearly all of its surface. Spalling risk in normal-weight concrete was strongly
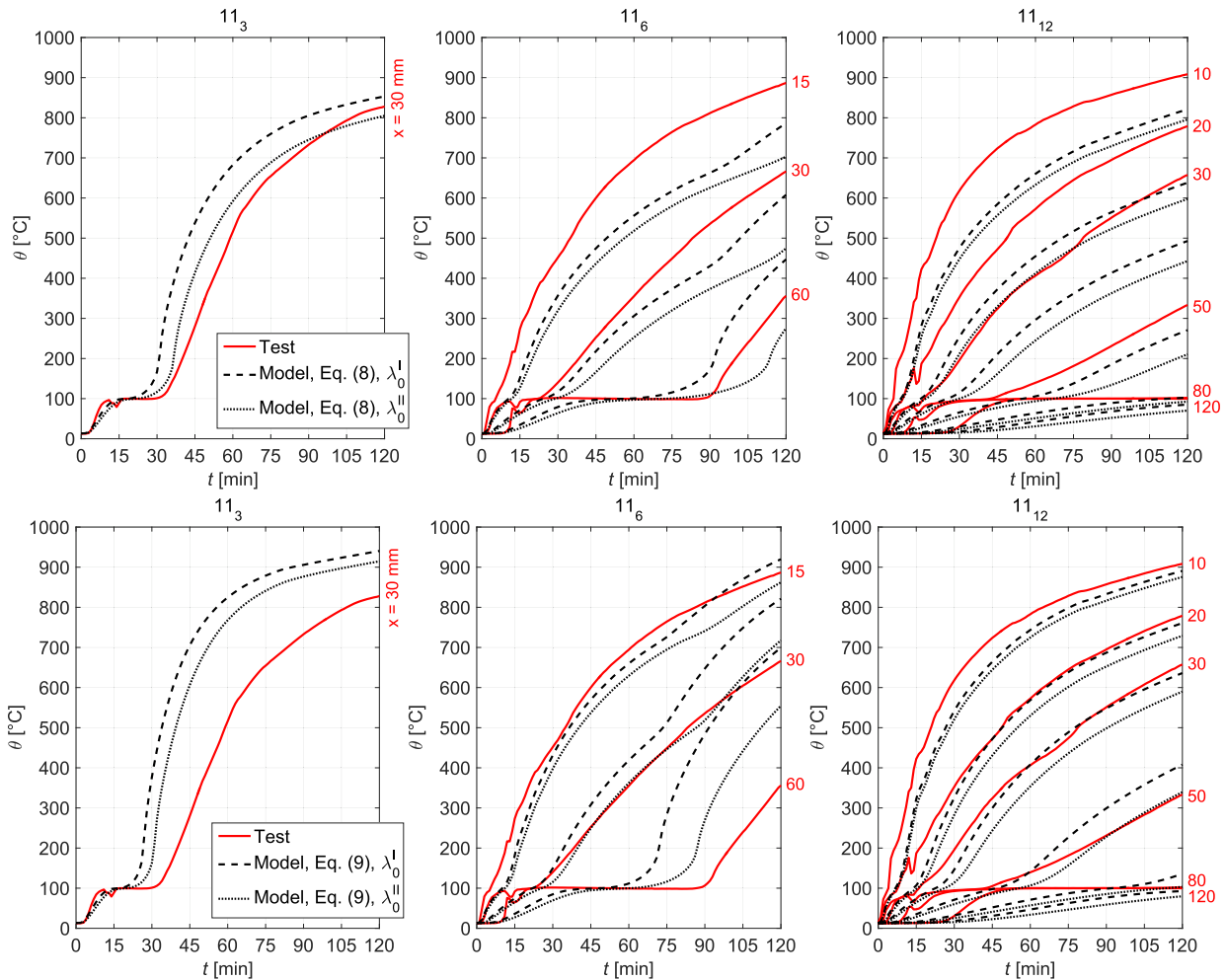
Fig. 20. Temperature evolutions in the analysed wall-panel specimens made of the LWA concrete with crushed textile and foam (material 11) measured by the thermocouples (see Fig. 2) during the fire test and calculated using the heat transfer model described in Section 3 by assuming temperature dependent thermal conductivity (Eq. (8), upper figures) or constant thermal conductivity (Eq. (9), lower figures); in both cases, the initial thermal conductivity was set to $\lambda_0^I = 0.63 \, \mathrm{W \, m^{-1} \, K^{-1}}$ or $\lambda_0^{II} = 0.49 \, \mathrm{W \, m^{-1} \, K^{-1}}$, see Section 2.3 and Table 3.

reduced when fibres whose length is smaller than the thickness of the specimen are used in the concrete. In the case of the LWA concrete with crushed textile and foam (material 11), long and thick cracks developed in the material as a result of the fire exposure.

For the ordinary materials, such as normal-weight concrete both with and without fibres and recycled aggregate concrete, the experimentally and numerically obtained temperature evolutions in the specimens are very similar. For the unusual materials, such as LWA concrete with crushed textile and foam and open-structure LWA concrete, the agreement between experimentally and numerically obtained temperatures evolutions is lower than in the case of ordinary materials. For all the investigated materials, the numerically obtained temperatures are either very close to the measured temperatures or higher than the measured temperatures. Thus, it can be concluded that from the point of the fire design of structures, simple material models can be used for the numerical prediction of temperature evolution in specimens made of various cementitious composites.

The moisture content had a great effect on the temperature evolution. The addition of fibres to a material affected the temperature evolutions in the material only very little.

The LWA concrete with crushed textile and foam (material 11) performed quite poorly. Both the residual compressive strength and the relative residual compressive strength were among the lowest measured values. Long and thick cracks were observed in the wall-panel specimens. The calculated temperature evolutions are only partially in agreement with the measured temperature evolutions.

The concrete containing mineral wool shreds (material 12) performed very well. Compressive strength at normal temperature, residual compressive strength, and the relative residual compressive strength were among the highest measured values. No spalling and only minimal micro-cracking was observed. The calculated temperature evolutions are in good agreement with the measured temperature evolutions. Out of the all investigated materials, lowest temperatures were observed in this material suggesting that the material has low thermal conductivity.

CRediT authorship contribution statement

Radek Štefan: Conceptualization, Methodology, Software, Formal analysis, Investigation, Data curation, Writing - original draft,
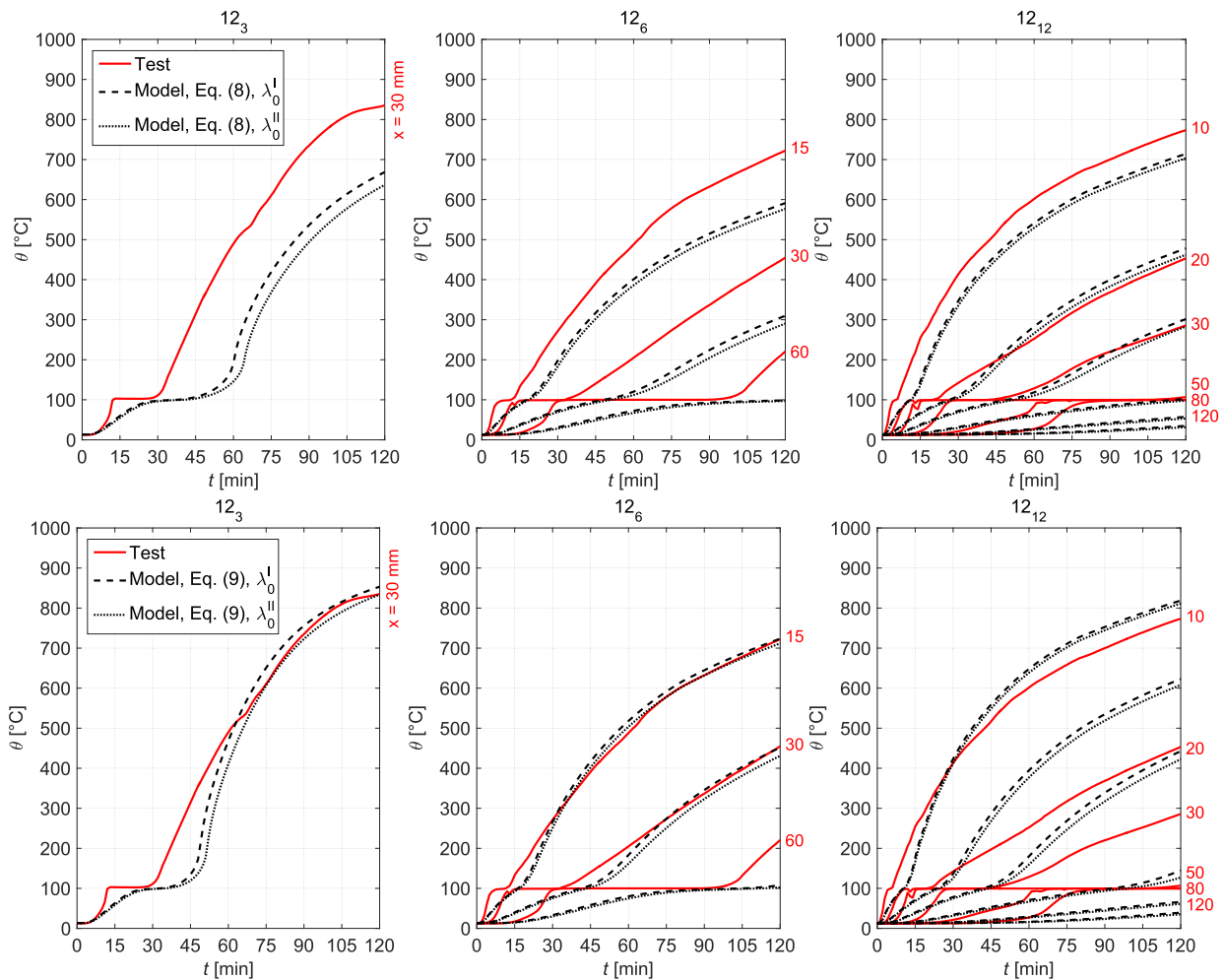
Fig. 21. Temperature evolutions in the analysed wall-panel specimens made of the concrete containing mineral wool shreds (material 12) measured by the thermocouples (see Fig. 2) during the fire test and calculated using the heat transfer model described in Section 3 by assuming temperature dependent thermal conductivity (Eq. (8), upper figures) or constant thermal conductivity (Eq. (9), lower figures); in both cases, the initial thermal conductivity was set to $\lambda_0^I = 0.38\,\mathrm{W\,m^{-1}\,K^{-1}}$ or $\lambda_0^{II} = 0.35\,\mathrm{W\,m^{-1}\,K^{-1}}$, see Section 2.3 and Table 3.

Writing - review & editing, Visualization, Supervision. **Marek Foglar:** Conceptualization, Resources, Writing - review & editing, Supervision, Project administration, Funding acquisition. **Josef Fládr:** Formal analysis, Investigation, Resources, Writing - review & editing. **Kateřina Horníková:** Formal analysis, Writing - review & editing. **Jakub Holan:** Formal analysis, Writing - original draft, Writing - review & editing.

Declaration of Competing Interest

The authors declare that they have no known competing financial interests or personal relationships that could have appeared to influence the work reported in this paper.

Acknowledgement

References

[1] fib Bulletin 38. Fire design of concrete structures – materials, structures and modelling, fib, 2007.

[2] Z.P. Bažant, M.F. Kaplan, Concrete at High Temperatures. Material Properties and Mathematical Models, Concrete Design and Construction Series, Longman, 1996.

[3] Z. Guo, X. Shi, Experiment and Calculation of Reinforced Concrete at Eleveted Temperatures, Elsevier, 2011.

[4] EN 1992-1-2, Eurocode 2: Design of concrete structures – Part 1–2: General rules – Structural fire design, CEN, 2004.

[5] EN 1994-1-2, Eurocode 4: Design of composite steel and concrete structures – Part 1–2: General rules – Structural fire design, CEN, 2005.

[6] A.Z. Mohd Ali, J. Sanjayan, M. Guerrieri, Effect of aggregate size on the spalling of high-strength wall panels exposed to hydrocarbon fire, J. Mater. Civ. Eng. 29 (12) (2017), 04017237. https://doi.org/10.1061/(ASCE)MT.1943-5533.0002087.

[7] M. Guerrieri, S. Fragomeni, An experimental investigation into the influence of specimen size, in-situ pore pressures and temperatures on the spalling of difference size concrete panels when exposed to a hydrocarbon fire, MATEC Web Conf. 6 (2013) 01002, https://doi.org/10.1051/matecconf/20130601002.

[8] M. Guerrieri, S. Fragomeni, Mechanisms of spalling of concrete panels of different geometry in hydrocarbon fire, J. Mater. Civ. Eng. 28 (12) (2016) 04016164, https://doi.org/10.1061/(ASCE)MT.1943-5533.0001680.

[9] I. Hager, K. Mróz, T. Tracz, Concrete propensity to fire spalling: testing and observations, MATEC Web Conf. 163 (2018) 02004, https://doi.org/10.1051/matecconf/201816302004.

[10] A. Al-Sibahy, R. Edwards, Thermal behaviour of novel lightweight concrete at ambient and elevated temperatures: Experimental, modelling and parametric studies, Constr. Build. Mater. 31 (2012) 174–187, https://doi.org/10.1016/j.conbuildmat.2011.12.096.

[11] J.-C. Mindeguia, Contribution expérimentale a la compréhension des risques d'instabilité thermique des bétons Ph.D. thesis, UPPA (2009).

[12] J.-C. Mindeguia, P. Pimienta, H. Carré, C.L. Borderie, Experimental analysis of concrete spalling due to fire exposure, Eur. J. Environ. Civil Eng. 17 (6) (2013) 453–466, https://doi.org/10.1080/19648189.2013.786245.

[13] R. Jansson, Fire Spalling of Concrete. Theoretical and Experimental Studies, Ph. D. thesis, KTH Royal Institute of Technology, Stockholm, Sweden, 2013.

[14] Z.-G. Yan, Y. Shen, H.-H. Zhu, X.-J. Li, Y. Lu, Experimental investigation of reinforced concrete and hybrid fibre reinforced concrete shield tunnel segments subjected to elevated temperature, Fire Saf. J. 71 (2015) 86–99, https://doi.org/10.1016/j.firesaf.2014.11.009.

[15] J. Novák, A. Kohoutková, Mechanical properties of concrete composites subject to elevated temperature, Fire Saf. J. 95 (2018) 66–76, https://doi.org/10.1016/j.firesaf.2017.10.010.

[16] D. Cree, M. Green, A. Noumowé, Residual strength of concrete containing recycled materials after exposure to fire: A review, Constr. Build. Mater. 45 (2013) 208–223, https://doi.org/10.1016/j.conbuildmat.2013.04.005.

[17] A.M. Marques, J.R. Correia, J. de Brito, Post-fire residual mechanical properties of concrete made with recycled rubber aggregate, Fire Saf. J. 58 (2013) 49–57, https://doi.org/10.1016/j.firesaf.2013.02.002.

[18] M. Mousavimehr, M. Nematzadeh, Predicting post-fire behavior of crumb rubber aggregate concrete, Constr. Build. Mater. 229 (2019), 116834. https://doi.org/10.1016/j.conbuildmat.2019.116834.

[19] H. Akbarzadeh Bengar, A.A. Shahmansouri, N. Akkas Zangebari Sabet, K. Kabirifar, V.W.Y. Tam, Impact of elevated temperatures on the structural performance of recycled rubber concrete: Experimental and mathematical modeling, Constr. Build. Mater. 255 (2020), 119374. https://doi.org/10.1016/j.conbuildmat.2020.119374.

[20] J.P.B. Vieira, J.R. Correia, J. de Brito, Post-fire residual mechanical properties of concrete made with recycled concrete coarse aggregates, Cem. Concr. Res. 41 (5) (2011) 533–541, https://doi.org/10.1016/j.cemconres.2011.02.002.

[21] I. Netinger, I. Kesegic, I. Guljas, The effect of high temperatures on the mechanical properties of concrete made with different types of aggregates, Fire Saf. J. 46 (7) (2011) 425–430, https://doi.org/10.1016/j.firesaf.2011.07.002.

[22] I. Netinger Grubeša, B. Marković, A. Gojević, J. Brdarić, Effect of hemp fibers on fire resistance of concrete, Constr. Build. Mater. 184 (2018) 473–484, https://doi.org/10.1016/j.conbuildmat.2018.07.014.

[23] A.Z. Mohd Ali, J. Sanjayan, The spalling of geopolymer high strength concrete wall panels and cylinders under hydrocarbon fire, MATEC Web Conf. 47 (2016) 02005, https://doi.org/10.1051/matecconf/20164702005.

[24] R. Štefan, M. Foglar, J. Fládr, Experimental investigation of behaviour of various types of cementitious composites exposed to fire, Beton TKS 15 (6) (2015) 56–61 [in Czech]. URL:http://www.betontks.cz/sites/default/files/2015-6-56.pdf.

[25] M. Foglar, R. Hájek, R. Štefan, J. Stöhr, Performance Investigation of Cementitious Composites Subjected to Extreme Loading. Experiments, Modelling, Technology, CTU in Prague, Prague, Czech Republic, 2016 [in Czech].

[26] M. Foglar, J. Fládr, Cement Composite with Increased Ability to Absorb Mechanical Energy, Czech Republic Patent CZ 305495, Industrial Property Office, Sept. 16 2015 (2015).

[27] M. Foglar, J. Fládr, Cement Composite with Enhanced Ability to Absorb Mechanical Energy, United States Patent US 9,249,051 B2, United States Patent and Trademark Office, Feb. 2 2016 (2016).

[28] M. Foglar, J. Fládr, Cement Composite Exhibiting Increased Ability of Absorption of Mechanical, Acoustic and Thermal Energies, Czech Republic Patent CZ 305906, Industrial Property Office, Mar. 16 2016 (2016).

[29] Z. Pavlík, M. Záleská, M. Pavlíková, R. Černý, The thermal and mechanical performance of cement-based composites with enhanced thermal insulation properties, in: Advanced Computational Methods and Experiments in Heat Transfer XIII, 2014, pp. 251–260. https://doi.org/10.2495/HT140231.

[30] EN 1991-1-2, Eurocode 1: Actions on structures – Part 1–2: General actions – Actions on structures exposed to fire, CEN, 2002.

[31] R. Štefan, Transport Processes in Concrete at High Temperatures. Mathematical Modelling and Engineering Applications with Focus on Concrete Spalling, PhD thesis, CTU in Prague (2015).

[32] R. Štefan, J. Procházka, Modelling of hygro-thermal processes in steel-concrete composite columns exposed to high temperatures, in: Proceedings from 22nd Czech Concrete Day 2015, Vol. 249 of Solid State Phenomena, Trans Tech Publications, 2016, pp. 246–252. https://doi.org/10.4028/www.scientific.net/SSP.249.246.

[33] R. Štefan, J. Procházka, J. Novák, J. Fládr, F. Wald, A. Kohoutková, L. Scheinherrová, M. Čáchová, Heat transfer in hybrid fibre reinforced concrete-steel composite column exposed to a gas-fired radiant heater, IOP Conf.Series:

[34] H.-B. Wang, Heat Transfer Analysis of Components of Construction Exposed to Fire. A Theoretical, Numerical and Experimental Approach, PhD thesis, University of Salford (1995).

[35] J.A. Purkiss, Fire safety engineering, Design of structures, 2nd ed., Elsevier, 2007.

[36] J.M. Bergheau, R. Fortunier, Finite Element Simulation of Heat Transfer, Wiley, 2008.

[37] A.M. Mohaghegh, J. Silfwerbrand, V. Arskog, R. Jansson McNamee, Fire spalling of high-performance basalt fibre concrete, Nordic Concrete Res. 57 (2) (2017) 89–102.

[38] R. Felicetti, Assessment of the equivalent thermal diffusivity for fire analysis of concrete structures, in: J.P. Rodriguez, G.A. Khoury, N.P. Hoj (Eds.), Proc. Fib Task Group 4.3 Workshop Fire Design of Concrete Structures, 2007, pp. 149–158.

[39] N. Ukrainczyk, Thermal diffusivity estimation using numerical inverse solution for 1D heat conduction, Int. J. Heat Mass Transf. 52 (25) (2009) 5675–5681, https://doi.org/10.1016/j.ijheatmasstransfer.2009.07.029.

[40] J.J. Kim, K.-S. Youm, M.M. Reda Taha, Extracting concrete thermal characteristics from temperature time history of RC column exposed to standard fire, Sci. World J. (2014), 242806. https://doi.org/10.1155/2014/242806.

[41] C.N. Ang, Y.C. Wang, The effect of water movement on specific heat of gypsum plasterboard in heat transfer analysis under natural fire exposure, Constr. Build. Mater. 18 (7) (2004) 505–515, https://doi.org/10.1016/j.conbuildmat.2004.04.003.

[42] C.N. Ang, Y.C. Wang, Effect of moisture transfer on specific heat of gypsum plasterboard at high temperatures, Constr. Build. Mater. 23 (2) (2009) 675–686, https://doi.org/10.1016/j.conbuildmat.2008.02.016.

[43] M. Hora, The fire resistance of lightweight concrete elements, Master's thesis, CTU in Prague, [in Czech] (2012).

[44] M. Hora, R. Štefan, J. Procházka, Temperature analysis of lightweight aggregate concrete slab members at elevated temperatures for predicting fire resistance, in: F. Wald, I. Burgess, K. Horová, T. Jána, J. Jirku (Eds.), Applications of Structural Fire Engineering, CTU in Prague, Prague, Czech Republic, 2013.

[45] K. Hertz, Users Guide for the program ConFire.exe. 2. Edition [online], URL: http://www.byg.dtu.dk/english/-/media/Institutter/Byg/publikationer/software/confire_users_guide_ver_2.ashx?la=da, (2012).

[46] Z. Tao, M. Ghannam, Heat transfer in concrete-filled carbon and stainless steel tubes exposed to fire, Fire Safety J. 61 (Supplement C) (2013) 1–11, https://doi.org/10.1016/j.firesaf.2013.07.004.

[47] R. Štefan, J. Sura, J. Procházka, A. Kohoutková, F. Wald, Numerical investigation of slender reinforced concrete and steel-concrete composite columns at normal and high temperatures using sectional analysis and moment-curvature approach, Eng. Struct. 190 (2019) 285–305, https://doi.org/10.1016/j.engstruct.2019.03.071.

[48] Z.P. Bažant, M. Jirásek, Creep and Hygrothermal Effects in Concrete Structures, Springer, 2018.

[49] M. Jerman, R. Černý, Effect of moisture content on heat and moisture transport and storage properties of thermal insulation materials, Energy Build. 53 (2012) 39–46, https://doi.org/10.1016/j.enbuild.2012.07.002.

[50] MATLAB, Version 8.6.0 (R2015b), The MathWorks Inc, Natick, Massachusetts, United States (2015).

[51] S. Deeny, T. Stratford, R. Dhakal, P.J. Moss, A.H. Buchanan, Spalling of concrete: Implications for structural performance in fire, in: Australasian Conference on Mechanics of Structure and Materials (ACMSM20), 2008.

[52] M. Zeiml, R. Lackner, F. Pesavento, B.A. Schrefler, Thermo-hydro-chemical couplings considered in safety assessment of shallow tunnels subjected to fire load, Fire Saf. J. 43 (2) (2008) 83–95, https://doi.org/10.1016/j.firesaf.2007.05.006.

[53] S. Bo, Finite Element Simulation of Fire Induced Spalling in High Strength Concrete Slabs Master's thesis, Lehigh University, 2011.

[54] A. Khoury, Y. Anderberg, Fire safety design – Concrete spalling review, Swedish National Road Administration (2000).

[55] M. Beneš, R. Štefan, Hygro-thermo-mechanical analysis of spalling in concrete walls at high temperatures as a moving boundary problem, Int. J. Heat Mass Tran. 85 (2015) 110–134, https://doi.org/10.1016/j.ijheatmasstransfer.2015.01.050.

Annex 3

Reprint of the Paper

HÁJEK, R., K. HORNÍKOVÁ a M. FOGLAR. Numerical assessment of the response of a heterogeneous concrete-based composite bridge deck to a near field explosion. Engineering Structures. 2020, 225 ISSN 1873-7323. DOI 10.1016/j.engstruct.2020.111206

Contribution of the author of this thesis of the paper

The author of this thesis is contributed to the paper with evaluation of results of the numerical simulations and collaborated on development of numerical models of blast events in LS-DYNA software.

Radek Hájek: Conceptualization, Software, Formal analysis, Investigation, Writing – original draft, Writing – review & editing, Visualization,

Kateřina Horníková: Software, Formal analysis, Investigation, Writing – original draft, Writing – review & editing, Visualization.

Marek Foglar: Supervision, Conceptualization, Writing – review & editing, Methodology, Funding acquisition
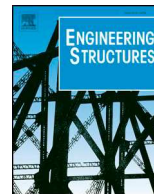
Numerical assessment of the response of a heterogeneous concrete-based composite bridge deck to a near field explosion

Radek Hájek, Kateřina Horníková, Marek Foglar*

Czech Technical University in Prague, Faculty of Civil Engineering, Department of Concrete and Masonry Structures, Prague, Czech Republic

ARTICLE INFO

ABSTRACT

This paper reports on numerical assessment of the blast response of a heterogeneous composite structure using LS-DYNA solver. There experimentally observed effect of heterogeneity on the overall response of the structure is numerically assessed. Multiple approaches to the introduction of material heterogeneity are proposed, modelled and tested.

The numerical results are confronted with the authors' original experimental program on a full-scale concrete structure subjected to a near field explosion. Tests were carried out on a total of three specimens. All the specimens were subjected to the same close-in blast loading from 25 kg TNT charges placed on steel chairs in the middle of each slab. The chairs provided 450 mm standoff from the top surface of the slab. Two of the analyzed specimens were reinforced concrete slabs 6 m in length, 1.5 m in width and 0.3 m in thickness. The first specimen contained basalt fiber meshes in multiple layers along the depth of the specimen. The second specimen contained two layers of recycled textile sheets 100 mm in total thickness. The third specimen was a commercial hollow-core precast prestressed panel 6 m in length, 1.2 m in width and 0.32 m in thickness.

The paper aims to verify and explain the experimental findings. It was numerically proved that the highly heterogeneous concrete-based composite bridge decks consume the blast energy by layer delamination in the pre-determined damage zones. The findings are supported by PDV measurements.

1. Introduction

The need to improve the resistance of the civil and transport infrastructure to blasts or impacts caused by terrorist events in recent years has led to raised interest in research and development of various materials and their resistance to high-rate loading.

This paper deals with numerical modelling of the response of building structures to such loading, focusing on the effect of the material heterogeneity of concrete-based composites on the blast response of the structure. The research is based on the authors' long-term experimental program focused on the blast resistance of hybrid concrete specimens subjected to close-in blast loading, and its dependence on the composition and the material properties of the specimen. Since 2010, the authors have been conducting experiments with basically the same arrangement, using various types and compositions of concrete, ranging from normal strength steel bar reinforced concrete (NSC) to ultrahigh-performance fiber-reinforced concrete (UHPFRC) [1–4]. In addition to the blast tests, the authors have also studied the materials in quasi-static and slow-strain-rate experiments [5].

To achieve the goal of developing a blast-resistant structure, the authors originally progressed from standard reinforced concrete to fiber-reinforced concrete and then to ultra-high-performance fiber reinforced concrete while trying to introduce more ductile concrete behavior. The use of heterogeneous composites was the next logical step. Composite materials were chosen as the next logical step to further increase the blast resistance of concrete structures with additional materials embedded inside the concrete matrix.

Full-scale testing is the most accurate method for determining the blast resistance of a complex heterogeneous material such as concrete or other cementitious composites. The current state-of-the-art methods for numerical modelling can provide reliable data on blast loading, but it is always challenging to produce accurately calibrated material models. The response of a structure to blast loading calculated by the model is highly sensitive even to a slight variation in material definitions and properties. The authors therefore consider that modelling must always be supplemented by a suitable experiment to verify the results of the computational analysis. The authors perform numerical modelling mainly as a tool for identifying and visualizing non-measurable processes occurring inside the specimen during the experiment.

During the experimental program, a complex structural behavior

* Corresponding author at: ČVUT v Praze, Thákurova 7, 166 29 Praha 6, Czech Republic.
E-mail address: marek.foglar@fsv.cvut.cz (M. Foglar).

was observed. It was assumed that the highly heterogeneous concrete-based composite bridge decks consume the blast energy by layer delamination in the pre-determined damage zones. The paper aims to verify and explain the experimental findings with the use of numerical simulations. The use of full-scale experiments on one hand provides complex results that can be applied in protective engineering structures design, on the other hand it complicates the detailed evaluation of the findings.

1.1. The use of heterogeneity to improve blast resistance

The concept of using a combination of materials to obtain a more resistant structure is well-established throughout all engineering disciplines. It is based on the principle that specific parts of a structure require corresponding properties of the structural material. In many cases, no single material can encompass all the requirements, or would do so only at great cost. A much more effective solution is to combine multiple materials to obtain suitable overall behavior of the structure. A typical example of this principle is the use of reinforced concrete in building structures. Concrete is a material with significant compressive strength. Its tensile strength is governed by the strength of the bond of the cementitious matrix with the aggregates and it is much lower than the compressive strength. To prevent concrete failing in tension, steel reinforcement is introduced in the parts of the structure that are subjected to tension, and, as a result, the overall resistance of the structure is improved.

A similar principle can be applied in blast-protection structures. For example, a concrete wall can be reinforced with a steel plate on the soffit opposed to the loading. If properly bonded, the plate carries the tensile stresses that would otherwise concentrate on the concrete surface and cause cracking and spalling. In this arrangement, a composite structure can exhibit more ductile behavior in comparison to plain concrete. Another effect of heterogeneity can be observed when studying a shock wave passing through the heterogeneous environment. During the transfer of energy between domains with differing bulk densities, some energy gets reflected from the interface, which causes stress concentration at the interface and reduces the amount of energy that passes through the structure.

In the presented paper, the authors decided to study ways to utilize this phenomenon to positively influence the structural blast response. Instead of introducing more high-strength and expensive materials to the structure, the authors used non-conventional materials and methods to increase the heterogeneity of the internal composition of the structure, rather than increase its mechanical strength.

1.2. State-of-the-art on concrete-based composites and computer modeling of their blast response

Although the most accurate results are always obtained from experiments (if possible, performed in full scale), many authors use computer modeling to supplement their experimental results and to identify and quantify various physical phenomena that cannot be measured directly during the experiment.

The authors' use of finite element (FE) modeling to study the formation and the behavior of the air shock waves caused by an explosion is presented in [6] and [7]. In both papers, the LS-DYNA commercial hydrocode [8,9] was used for numerical modeling. The software is based on the finite element method (FEM), either in implicit form or in explicit form. This allows the creation of finite element meshes of elements defined by various mathematical formulations, and their combinations, to create mathematical models for various types of materials and loadings.

The resistance of structures subjected to impact or blast loads is very difficult to determine empirically, so an experiment on a prototype is usually used. A computer simulation can substitute for many experiments to reduce the costs. Kong et al. [10] studied the resistance of non-composite steel–concrete-steel sandwich panels to high-speed impact. FE modeling in LS-DYNA was included. The FE model was validated against experimental results. Their numerical models were able to predict the initial flexural response of the specimen, followed by the resistance of the tensile membrane at large deformation. However, the authors have pointed out the difficulties of accurate numerical modeling. The strain rate effects of the materials and the choice of the concrete material model has a significant effect on the numerically predicted response.

Hao & Hao [11] conducted a study on the dynamic increase factor (DIF) for concrete. Several empirical DIF relations have been proposed for modeling the concrete material strength increment at high strain rates. A numerical study was conducted using various DIF values, and the results were compared.

Tai et al. [12] studied the dynamic response of a reinforced concrete slab loaded by an air blast. The LS-DYNA numerical model was used in a parametric study on the effect of the reinforcement ratio on the behavior of a reinforced concrete structure.

Matsagar [13] compared the performance of composite and non-composite panels under blast loading. A thorough parametric study was conducted. A finite element model was created in ABAQUS software. Before it was used, the model results were validated against experimental data obtained from the literature. The study included specimens prepared using steel plates, reinforced and non-reinforced concrete slabs and composite sandwich panels with foam and sand cores. It was possible to perform this kind of extensive parametric study with the use of numerical analysis. It would have been much more expensive and much more time-consuming to have obtained comparable results from an experimental program.

Li et al. [14] investigated the resistance of a normal concrete slab and an ultrahigh-performance concrete slab to contact explosion. A detailed numerical model, including all the essential details of the specimen, was created in LS-DYNA. A thorough study of material models was also presented in the paper. The authors used a novel approach to model the UHPC, based on experimental data. The feasibility and the accuracy of the optimized FE model were discussed in detail.

FE modeling was also used by Stohr et al. [15] to supplement an experimental program to evaluate the use of scaling in blast testing of concrete. The authors created reduced-scale specimens based on the full-scale experimental program presented in [1]. Issues concerning the use of computer modeling on a reduced scale, and on interpreting the results, are also discussed in the paper.

There are various ways to introduce heterogeneity into a structure. Liu et al. [16] increased the heterogeneity of their geopolymer-based high performance concrete material by adding a steel wire mesh reinforcement and an aluminum foam material. Christian & Ong Khim Chye [17] embedded a steel sandwich composite system in their concrete specimens to increase their survivability as blast mitigation panels. Additional steel parts increased the ductility of the specimen as well as the ability to dissipate energy through plastic deformation.

Fallon & McShane [18] studied the response of elastomer-coated concrete subjected to air blast loading. The authors used FE analysis in ABAQUS with a coupled Eulerian-Lagrangian model to accurately portray the air and the structure. This kind of coating is a typical example of a protective measure that can be applied to an existing structure during a retrofit. A similar polyurea elastomeric protective coating was studied by Iqbal et al. [19]. Coatings with suitable material properties can greatly reduce the fragmentation of the tested concrete tiles by dissipating the shock wave energy at the surface of the structure.

A more conventional approach to retrofitting existing structures was studied by Maazoun et al. [20], who tested RC hollow-core slabs retrofitted with a concrete topping combined with CFRP strips. They compared the behavior of the original slabs and the retrofitted slabs based on the experimental results, and also based on explicit FE modelling, using LS-DYNA solver.

1.3. Original experimental program

The results of blast experiments on hybrid concrete specimens made of concrete-based composite materials conducted in 2015 were used as a basis for developing and calibrating the numerical models. For a full description of the original experimental program, see [4].

Tests were carried out on a total of three specimens, named no. 18, no. 19 and no. 20 with respect to the history of the experimental program. All the specimens were subjected to close-in blast loading from 25 kg TNT charges placed on steel chairs in the middle of each slab. The chairs provided 450 mm standoff from the top surface of the slab. The charge was composed of solid TNT molded blocks supplied by the Czech Army tied together to form a coherent block with dimensions ca. $0.32 \times 0.32 \times 0.15$ m. Detonator was placed in 30 g of Semtex A1 plastic explosive in the middle point of the TNT block.

The main motivation for the experimental program was to determine the effect of heterogeneity of the material on the blast performance of the specimen. The composition of each specimen was therefore unique, allowing multiple types of heterogeneity to be studied and compared with previous results. Specimens no. 18 and 19 were concrete slabs 6 m in length, 1.5 m in width and 0.3 m in thickness. Specimen no. 18 contained basalt fiber meshes in multiple layers along the depth of the specimen. Specimen no. 19 contained two layers of recycled textile sheets 100 mm in total thickness. Specimen no. 20 was a commercial hollow-core precast prestressed panel 6 m in length, 1.2 m in width and 0.32 m in thickness, as defined by the manufacturer's program. The panel was reinforced only with 6 prestressing strands placed in the ribs.

Specimen no. 18 contained basalt fiber meshes in multiple layers along the depth of the specimen about 50 mm apart. The basalt fibers have a melting point of 1350 °C. The tensile strength of the basalt fabric was about 4200 MPa, with a tensile modulus of elasticity of about 85 GPa. The unit weight of the mesh was 250 g/m^2 with a weight density of 2.67 g/cm^3. Each string of the mesh consists of multiple fibers, so the diameter of each string cannot be accurately defined. From the parameters presented above, the effective area of each string was calculated to be 1.4 mm^2. Specimen no. 19 contained two layers of recycled textile sheets 100 mm in total thickness. The textile sheets were made of pieces of fire-resistant textile used in the automotive industry, bonded together with polyurethane. This material is patented for use for acoustic, thermal and vibration insulation. Hollow-core specimen no. 20 had internal voids filled only with air. The artificial materials embedded into concrete to increase structure heterogeneity are shown in Fig. 1. For detailed description of material properties refer the description of material models below.

Specimens no. 18 and no. 19 were reinforced with standard steel bars with a characteristic yield stress of 500 MPa. The reinforcement was kept the same in order to provide continuity with the previous research and to represent realistic structure, i.e. a pre-cast bridge deck between main girders. The amount of reinforcement was designed accordingly. There were 11 pcs $\varnothing$ 16 mm reinforcing bars every 140 mm on both surfaces, $\varnothing$ 10 mm every 150 mm as an outer transverse reinforcement, and shear reinforcement was provided by $\varnothing$ 8 mm links (9 pcs/m^2). The concrete cover is 50 mm to the surface of the transverse reinforcement. Because of the different structural type, the specimen No. 20 was reinforced only with 6 prestressing strands with a characteristic yield stress of 1860 MPa and a nominal diameter of 12.5 mm. No other reinforcement was present in the specimen. Specimen No. 20 serves as an example of typical pre-cast voided prestressed panels used in housing projects. The arrangement of the experiment is shown in Fig. 2. The cross sections of all the specimens are shown in Fig. 3.

The compressive and tensile strength of the concrete, the type of fiber and the fiber dosage for each specimen are summarized in Table 1. The strength of the concrete used in specimens no. 18 and 19 was measured in a laboratory on small test specimens cast during the casting of the full-scale panels. Specimen no. 20 was a commercially produced panel, and the material properties were obtained from the information given by the manufacturer, mainly the particular concrete strength class guaranteed by the manufacturer for the panel.

Since the experiment was focused on the material heterogeneity induced by the additional materials introduced into the specimen, the type of concrete used in specimens no 18 and 19 should ideally be the same. The use of a basalt mesh in specimen no. 18, however, limited the maximum length of the steel fibers to 13 mm. Although the maximum compressive stress of the two materials is very similar, their tensile stress and their fracture energy differ, and this had to be taken into consideration in the evaluation of the experimental results; see [4].

2. Modelling the heterogeneity of the structure

A numerical model of the experiment, mainly focused on the effect of material heterogeneity on the propagation of a blast wave, was developed to evaluate the experimental results. The model set-up process is described in the following text. The numerical model and the material models of the concrete were calibrated according to the outcomes of the experiments. The LS-DYNA explicit finite element (FE) solver was used for a non-linear analysis of the experiment.

2.1. Basic description of the FE models

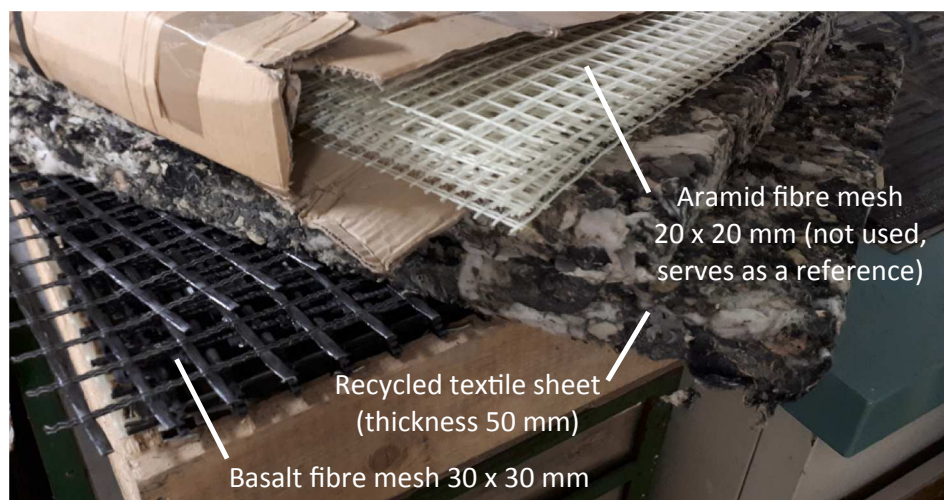The parameters of the numerical models were adopted from

Fig. 1. Materials embedded to concrete specimens.
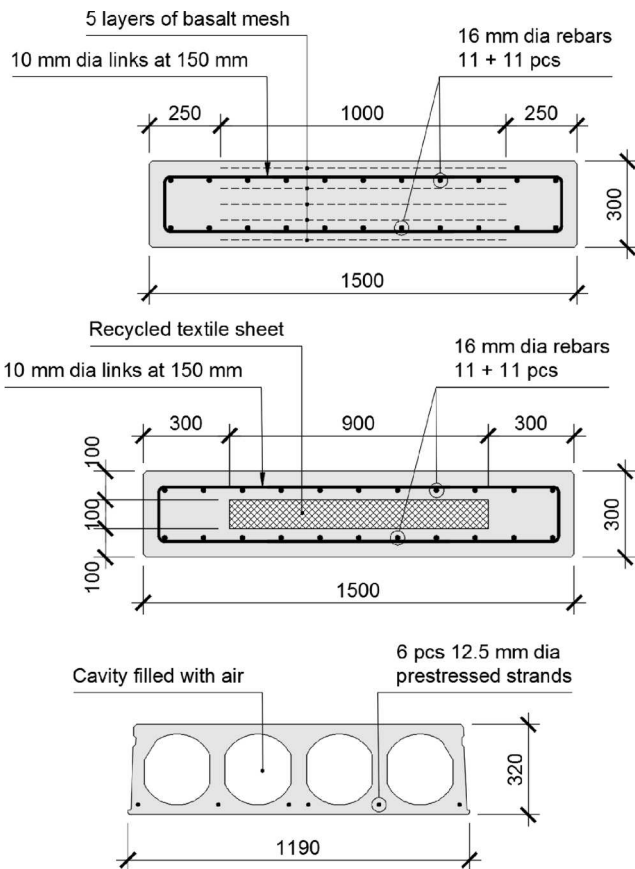
Fig. 2. Arrangement of the experiment.

Fig. 3. Arrangement of the specimens (from top to bottom Specimen no. 18, 19, 20).

Table 1
Concrete properties of the specimens.

Specimen No.	18	19	20
Compressive strength (cube) [MPa]	77.9	78.3	63*
Flexural tensile strength [MPa]	8.2	10.7	3.8*
35 mm fibers [kg/m^3]	–	80	–
13 mm fibers [kg/m^3]	120	80	–

*Note: * minimum strength according to the manufacturer's certification.*

materials present in the tested specimens are shown in Table 2.

The heterogeneity of the concrete itself – the fact that the concrete matrix consists of aggregate, cement mortar, water and air – is neglected. For the purposes of the model, concrete is treated as an isotropic material. It was modelled with the LS-DYNA native MAT_CSCM material model, i.e. the continuous surface cap model (a brittle material model with damage and loading rate sensitivity). The widely-used MAT_PLASTIC_KINEMATIC material model with appropriate yield strength and density parameters was used to model the steel and the basalt reinforcement. The textile sheets made of recycled textile from the automotive industry were modelled with the MAT_LOW_DENSITY_FOAM material model.

The mesh size varied from 1 mm to 12 mm according to the amount of fine detail within the concrete specimen that needed to be modelled. The details of the finite element mesh of all three computational models representing each of the experimental specimens (nos. 18, 19 and 20) are shown in Figs. 4 to 6. The same mesh was used on the first two models to exclude the effect of element size on the results. The only difference between the models is the material of particular elements.

To reduce the computational time and to improve the readability of the results, use was made of the symmetry of the specimen and of the entire experimental setup; only one quarter of the specimen was modeled. The boundary conditions were defined to restrain movement of the nodes in planes of symmetry perpendicular to the planes of symmetry. A timber cylinder was modelled to represent the actual on-site supports. The fact that the reduction in the size of the model and the boundary conditions do not influence the results was verified against a full model.

previous research by the authors [1,2,3]. Each FE model contains the concrete specimen, including the reinforcement and other relevant details. The heterogeneity of the specimen is taken into consideration by introducing more materials for particular finite elements of the element mesh. For the material properties of the concrete used in the experiments, see Table 1. The material properties of all additional

Table 2
Properties of the other materials present in the specimens.

Material	Specimen No.	Characteristic properties
Steel (reinforcement)	18, 19, 20	E = 200 GPa; σ_y = 0.500 GPa; ν = 0.2; ρ = 7850 kg/m^3
Steel (prestressing)	20	E = 195 GPa; σ_y = 1.860 GPa; ν = 0.2; ρ = 7850 kg/m^3
Basalt fibers	18	E = 85 GPa; σ_y = 4.000 GPa; ν = 0.2; ρ = 3000 kg/m^3
Textile sheet*	19	E = 210 kPa; σ_y = 0.033 MPa; ν = 0.1; ρ = 300 kg/m^3

Legend: E … Young's Modulus, ν … Poisson's ratio, σ_y … yield strength; ρ … weight density.
Note: * The material properties of the textile sheet were derived from information obtained from the manufacturer.

2.2. Modelling the blast loading

An adjacent detonation of 25 kg with 450 mm standoff above the top surface of the specimen was modeled. A block-shaped TNT charge with dimensions ca. 0.32 × 0.32 × 0.15 m was used in the experiments. Detonator was placed in ca. 30 g of Semtex A1 plastic explosive in the middle point of the TNT block to ensure complete detonation of the charge composed of multiple molded blocks of TNT. A different approach to detonation modeling was used from that in the authors' previous models [1–2]. Previously, a fluid dynamics model of air and explosive using arbitrary Lagrangian-Eulerian (ALE) elements was used. The blast load was hence determined from the equations of state of air and explosive. Although this is a correct approach, it results in a complex model with a long computational time. In the models presented in this paper, the native LS-DYNA function LOAD_BLAST_ENHANCED (LBE) was used instead. This function is derived from U.S. Department of Defense Conventional Weapons Effects Calculation Software (ConWep). The function is set up with the position and the weight of the charge and the TNT equivalent of the explosive material. For each selected face, the function calculates the dynamic loading based on the relative standoff distance and the angle of impact.

It should be noted that this approach to modelling of the explosion presumes a spherical explosive charge, as opposed to the block shaped TNT charge used in the experiment. LBE approach is also calibrated only for a limited range of standoff distances and charge weights. Although the generation of blast load using LBE function was already successfully used in authors' previous work [3] it was decided to numerically check the usability of this modelling approach for close-in blast modelling against the complex ALE approach again. A simplified FE computational model was developed for the purpose. The layout of the model is shown in Fig. 7. The pressure load generated on the top surface of the specimen by the LBE function was compared with the pressure generated by the complex ALE model in three monitored positions (Fig. 8). The pressure–time history was very similar in each instance (Figs. 9 to 11).

Based on the results, it was decided that the simplified approach to blast modelling is sufficient for the purposes of the calculations presented in this paper, and that it can be used without compromising the outcome of the discussion in this paper.

2.3. Fiber-reinforced concrete material model

Specimens no. 18 and 19 are made of fiber reinforced concrete (FRC). Although FRC is a type of concrete with the same production process and similar material properties, there are some key differences in comparison with plain unreinforced concrete. A plain concrete specimen fails in tension after reaching its tensile strength. When FRC is used, the stiffness of the specimen decreases after the tensile strength is reached (strain softening), the fibers take over the tensile stress during strain softening, and the material performs with the residual tensile strength without critical failure. The MAT_CSCM (MAT_159) material model of plain concrete (a material model with damage and plasticity)
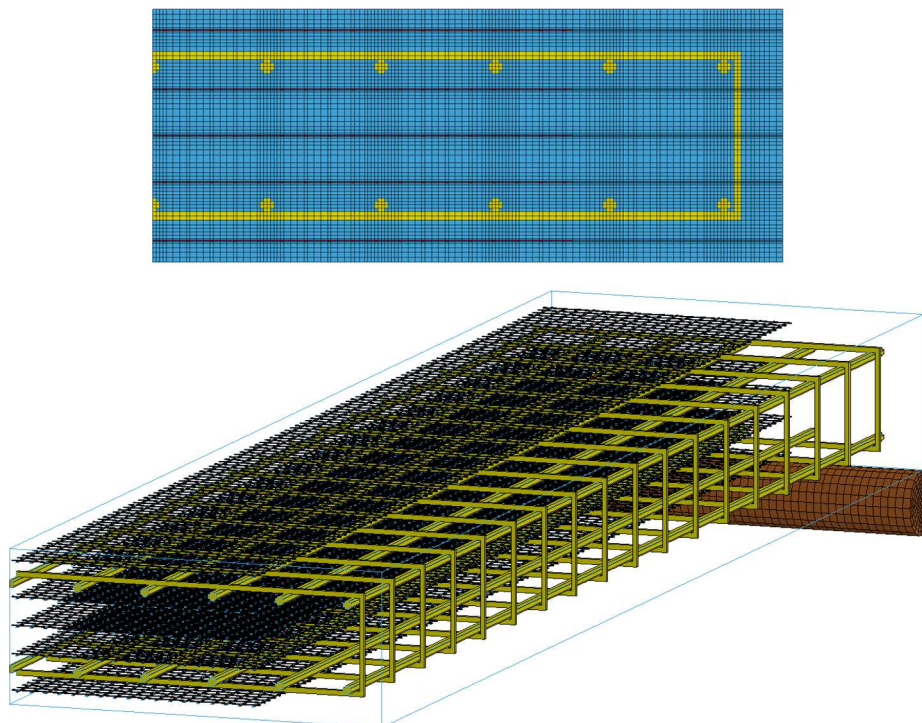

Fig. 4. FE model of Specimen no. 18: Cross section with a visible mesh (above); axonometric view with transparent concrete (below).
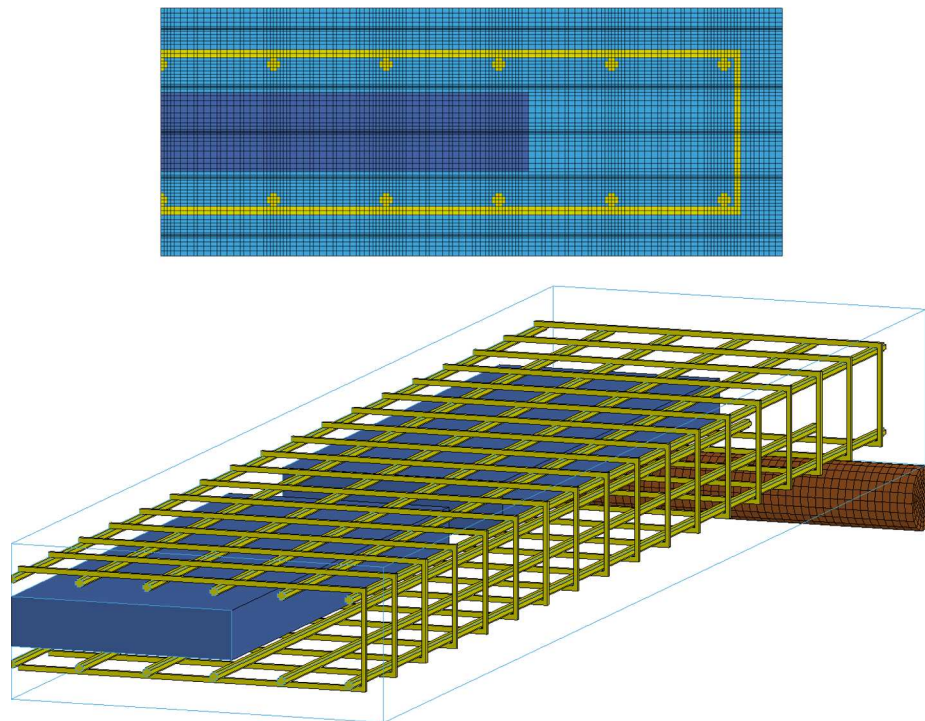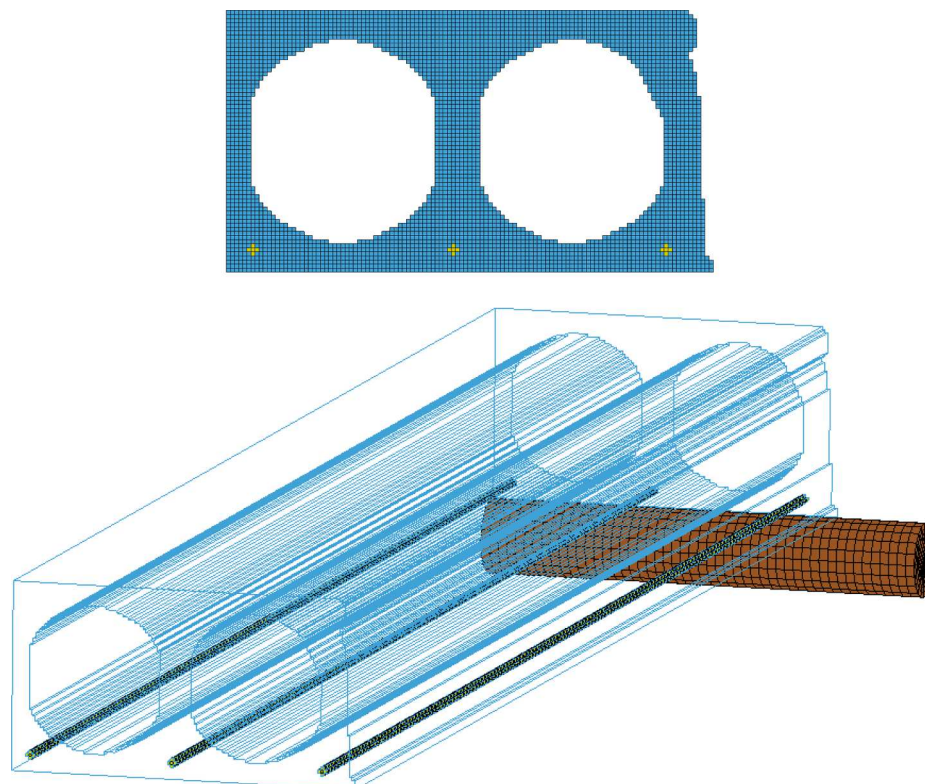
**Fig. 5.** FE model of Specimen no. 19: Cross section with a visible mesh (top); axonometric view with transparent concrete (bottom).

used in the LS-DYNA solver had to be recalibrated to provide ductile behavior typical for FRC. The key to the calibration of the material model lies in tuning the softening part of the stress–strain diagram to describe the behavior of FRC while the loading part of the stress–strain diagram can remain unchanged.

Four-point bending tests of concrete beam specimens were performed to characterize the behavior of the concrete mixture used in specimens 18 and 19. The arrangement of the four-point bending test is shown in Fig. 12. The results of the calibration experiments in the form of force–deflection diagrams are presented in Fig. 13.

The results clearly show some key differences in the response of the two types of concrete, mainly in the post-crack zone. The residual

Fig. 6. FE model of Specimen no. 20: Cross section with a visible mesh (above); axonometric view with transparent concrete (below).
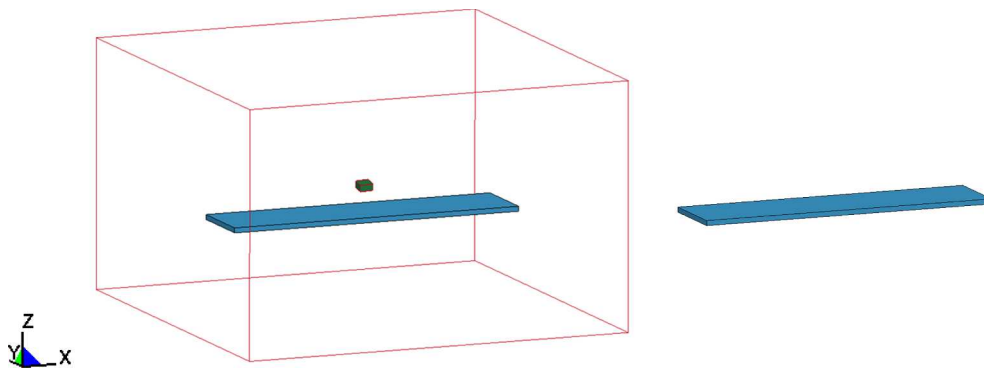
Fig. 7. Layout of the FEM model: ALE approach (left) and LBE approach (right).
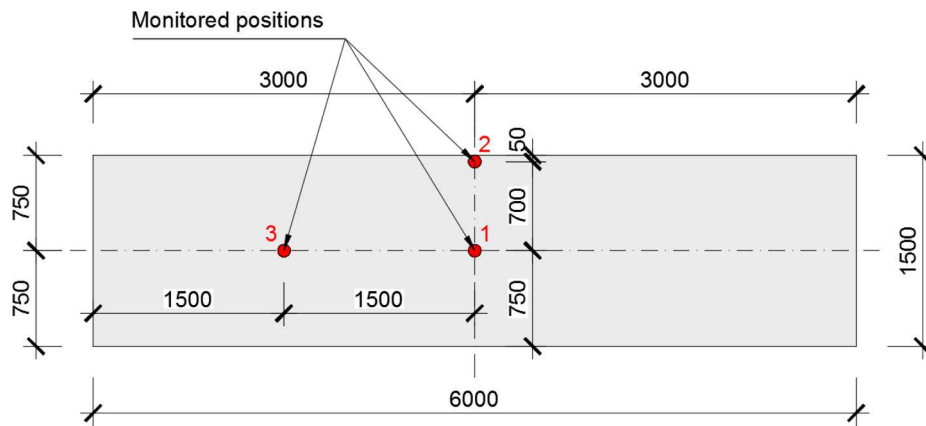
Fig. 8. Layout of the specimen with monitored positions marked.
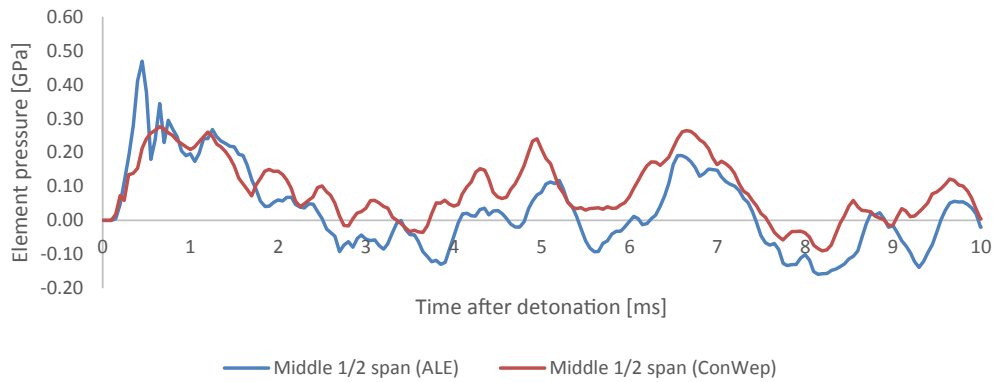
Fig. 9. Element Von Mises stress at position no. 1 as shown in Fig. 8.
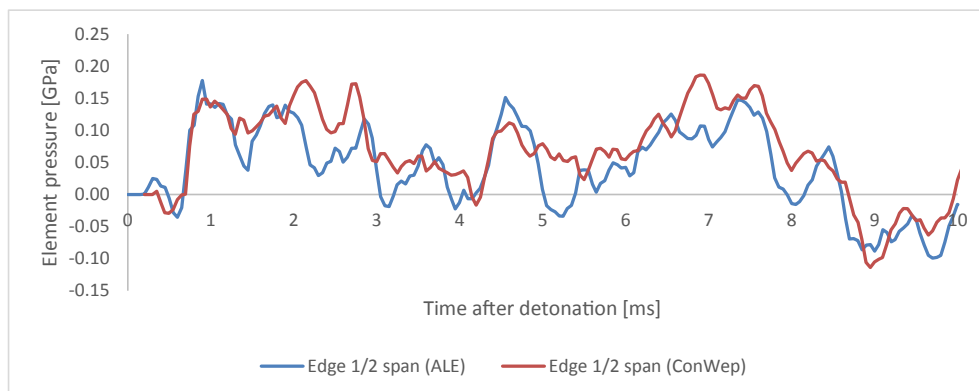
Fig. 10. Element Von Mises stress at position no. 2 as shown in Fig. 8.
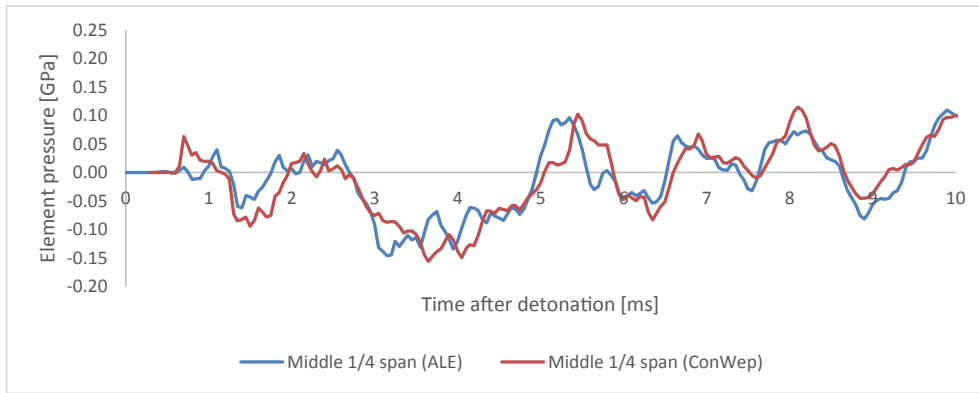
Fig. 11. Element Von Mises stress at position no. 3 as shown in Fig. 8.
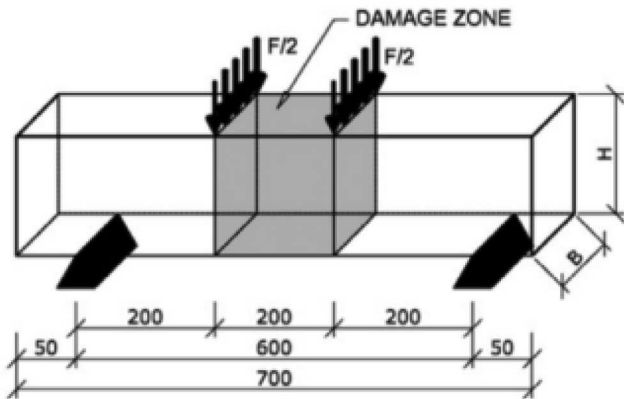
Fig. 12. Arrangement of the four-point bending experiment.

tensile strength of the material for specimen no. 19 with longer steel fibers is considerably greater than for material specimen no. 18, and the same is true for the fracture energy of the two materials.

At this time, a decision was made by the authors to diverge from the experimental program and to focus on the effect of the additional materials introduced into the specimens, and to neglect the differences in

the material properties of concrete and FRC.

Considering the constraints of mathematical definitions of the CSCM material model, it proved to be challenging to obtain FE model results comparable with the measured data from the experiment. Although an exact match could not be achieved, a good representation of concrete was found for the purposes of the FE model as described above.

The substitute CSCM model was used first in a computational representation of the four-point bending test and compared with the experimental results. The comparison is shown in Fig. 6. Table 3 presents the values obtained for the fracture energy from the four-point bending experiment for both materials, in comparison with the substitute CSCM material model. The fracture energy in this case is determined from integration of the force – deflection diagram. (i.e. the area below the curve shown in Fig. 13).

The extent of breach, spall and crack propagation is a typical indicator of the damage to concrete subjected to blast loading. It is therefore usually used for evaluating the accuracy of the modeling approach. The material model (MAT_CSCM) of the concrete elements offers another indicator for the damage to the element: the plastic strain value. The elements erode if the plastic strain indicator exceeds the set-up value; this corresponds to the breach, spall and crack propagation observed in the experiments. The shape and the size of the plastic strain pattern is therefore the decisive quantity for the accuracy of the numerical evaluation.
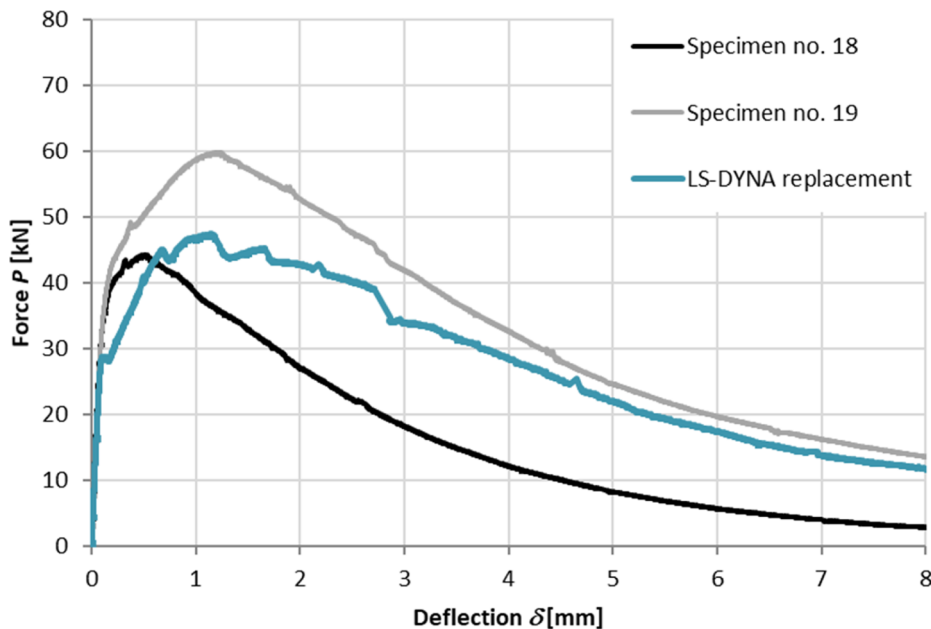

Fig. 13. Force-deflection diagrams of the concrete mixtures from the experimental program and from the numerical simulation.

Table 3
Fracture energy of the concrete and of the calibrated numerical model.

Specimen	Fracture energy [N/m]
Bending test for specimen no. 18	6493.9
Bending test for specimen no. 19	14227.7
Substitute MAT_159 model	11293.8

The results obtained from numerical modeling of FRC subjected to blast loading, the method for incorporating the effect of the fibers on the blast performance of the concrete based on increasing the fracture energy, was compared with the experimental results.

2.4. Modeling the reinforcement details and bond

The reinforcement was modeled with 3D finite elements to provide realistic behavior of the model. To achieve a perfect connection, a single fine mesh was created for the panel. Materials were introduced by specifying the material properties of the corresponding elements. No further definition of the contact between the materials is required when this approach is used. Failure of the connection between materials is determined by the resistance of the materials to concentrated loads, very similarly to the behavior of a real RC structure.

2.5. Modeling the basalt mesh

Specimen no. 18 was reinforced with multiple layers of basalt mesh. Basalt or aramid fabrics are commonly used in constructing or retrofitting concrete structures, and they can provide additional blast resistance [21,22]. The basalt mesh had a strong influence on the experimental results, as discussed above. The mesh was modeled in the same way as the reinforcement. Corresponding FE mesh elements were attributed to a material representing the basalt fabric. The MAT_PLASTIC_KINEMATIC (MAT_003) LS-DYNA native material model with the material parameters shown in Table 2 was used to model the basalt mesh. Erosion criterion was set up to limit the plastic deformation as the failure mode of the material is brittle soon after the limit yield stress (Table 2) is reached.

2.6. Modeling the recycled textile sheet

The sheets embedded in the middle of specimen no. 19 are made from a much softer material than concrete. The sheet consists of a mixture of strips of various materials recycled from mixed technical synthetic textiles bonded with polyurethane (PUR) binder and pressed into the shape. The resultant material shown in Fig. 1 has an open porous structure and sponge-like mechanical properties. The presence of such a different material in the composite structure of the specimen should have significant effect on the behavior of the specimen when subjected to blast loading. Special attention was paid to a proper material description of the textile sheet in order to set up the FE computational model of composite specimen no. 19.

A deflection-driven experiment was performed to assess the response of the sheet material to compressive loading. A block of the material 50 × 50 × 50 mm in dimensions was subjected to one-directional compression. The arrangement of the experiment is shown in Fig. 14. The results of the experiment are presented in Fig. 15.

An FE computational model of the experiment was created to calibrate a material model suitable for the recycled textile sheet. The material model must be able to describe the elastic behavior of the sheet and the non-linearity of the modulus of elasticity when the porous structure of the material is being crushed. Based on comparative studies, the MAT_LOW_DENSITY_FOAM (MAT_057) material model was selected as the most suitable for this case. It is widely used to model low-density recoverable polyurethane foams utilized for various
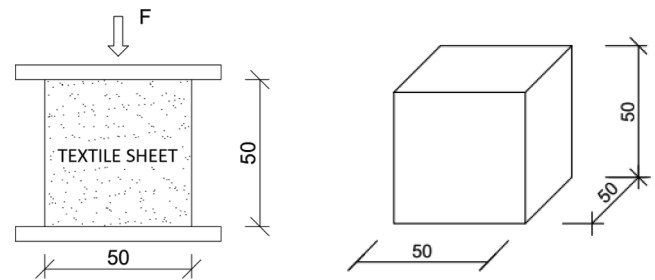

Fig. 14. Arrangement of the compressive test of the textile sheet and the shape of the test specimen.

purposes and applications, e.g. for padding seat cushions in the automotive industry, for insulation layers in construction, etc.

The MAT_LOW_DENSITY_FOAM (MAT_057) material model is defined by a relatively small number of parameters, which must either be obtained from the material manufacturer or be measured in a laboratory. To set up the model, the following data is needed: Young's modulus, density, the nominal stress–strain curve and the tensile cut-off stress. The nominal stress–strain curve was defined from the experiment described above. The other parameters were obtained from the manufacturer of the material and are summarized in Table 2. Through multiple iterations, an optimal definition of the material model was found and was tested on the FE model representing the calibration experiment. A comparison between the numerical results and the experimental results is shown in Fig. 15.

3. FE modelling results vs. Experiments

This section contains the results of the numerical assessment of the specimens subjected to close-in blast. A comparison between FE calculations and experimental results is presented for each of the specimens tested in the experiment discussed here. Although the FE models have the same arrangement as the experiments described in previous sections, and were calibrated according to experimental results, the main goal of the modelling is not to recreate the experiment with absolute accuracy, but to support the evaluation of the experimental results by providing time-dependent data on the behavior of the specimens which cannot be measured during the experiment. It is the authors' opinion that due to the severe effects of blast loading, mainly on civil infrastructure, experiments, preferably in full scale, should always play the main role in examining the behavior of a structure, while FE modelling should serve as a support for an evaluation of the behavior of the specimen during the experiment.

The shock wave passing through the specimen rebounds off any interface between various materials (concrete/reinforcement, concrete/air, etc.) The rebound generally results in locally increased stress around the rebound surface. The results of the experiment presented above cannot properly illustrate this effect. It can be only postulated from the experimental results. However, it can be clearly observed in the results of FE modeling. The results of computer modelling have provided the authors with data in any position within the specimen during the entire examined time interval. It is then easy to show the propagation of the shock wave after the detonation and the resulting distribution of pressure in the specimen.

3.1. FE model of the specimen with the basalt mesh

The arrangement of the FE model of specimen no. 18 is shown in Fig. 4. The definition of the material model and geometry corresponds with the information given in previous sections. The main goal of this numerical model was to illustrate the influence of multiple layers of basalt mesh on the propagation of the blast-induced shock wave throughout the specimen.
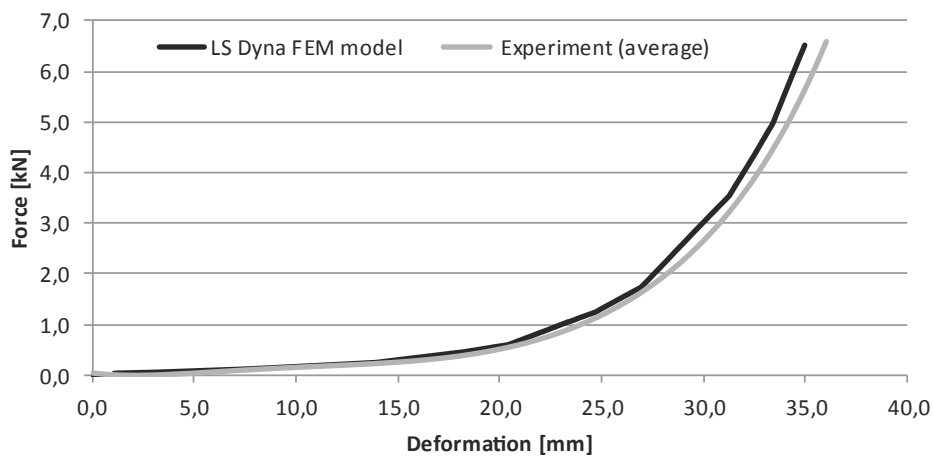
Fig. 15. . Force-deformation diagram of the textile sheet (experiment vs. FE model).
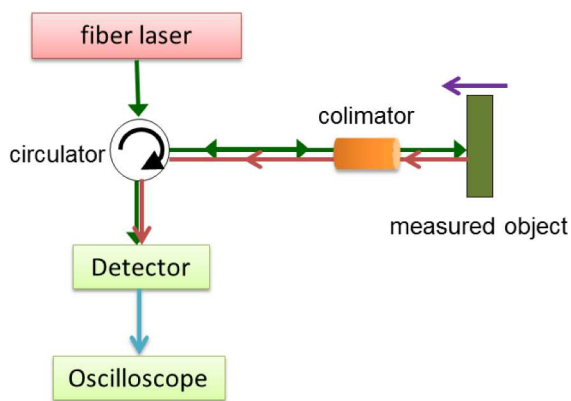

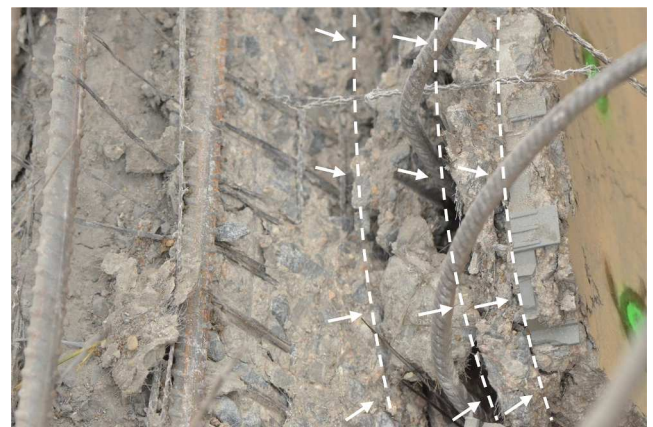**Fig. 16.** Basic principle diagram of the Photonic-Doppler Velocimetry measuring device.

Fig. 18. Multi-layer longitudinal cracking of specimen No. 18 along the basalt mesh and steel reinforcement.

This specimen is a direct follow-up to the authors' previous research, where a panel with a single layer of basalt mesh was used and caused delamination of the specimen along the plane of the basalt mesh. The philosophy of this specimen was to try to utilize the effect to increase the blast energy dissipation inside the specimen and to prevent spalling.

The results of the experiment – thoroughly described in [4] and

Fig. 17. Damage to specimen No. 18 after the blast. Overall view (top image), top view (bottom left image), bottom view (bottom right image).

Fig. 19. Damage to reference specimen No. 1 after the blast. Top view (left image), bottom view (right image).
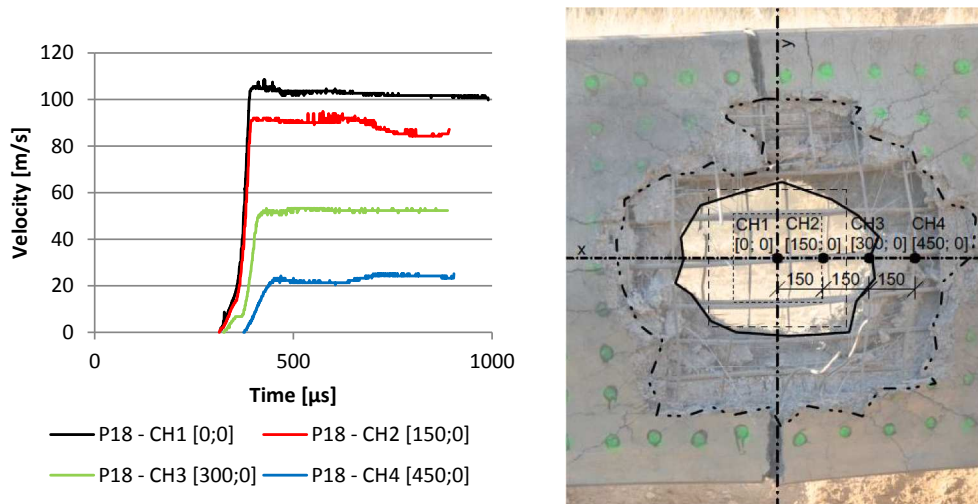
Fig. 20. PDV measurements – Specimen no. 18.
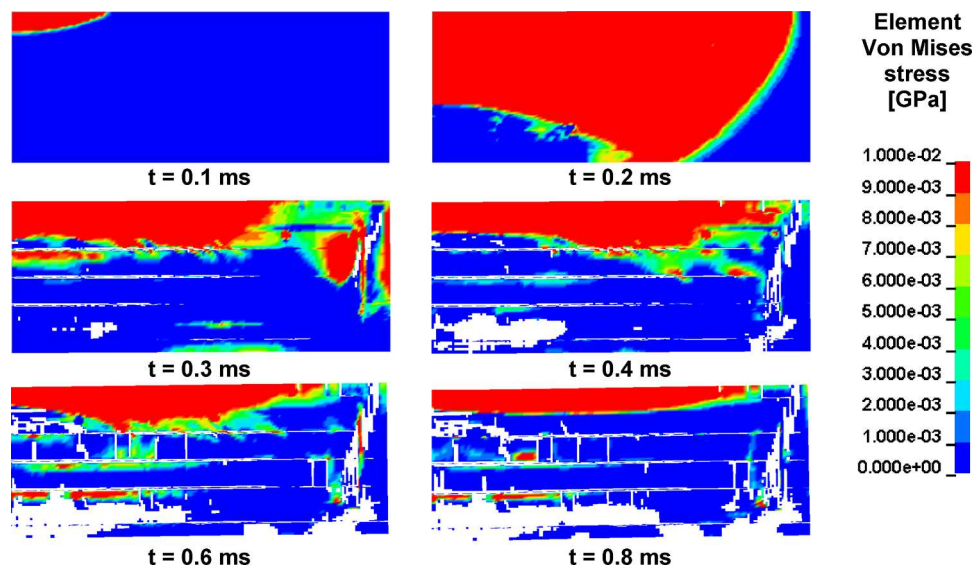
Fig. 21. FE calculation results for specimen no. 18. Fringe of pressure in various times after detonation (cross section in the center of the specimen).

presented in Fig. 17 – clearly show that the spall area is greatly reduced on the soffit of the specimen in comparison with reference standard RC specimen no. 1 (Fig. 19), and that the formation of a typical blast-related cone-shaped hole in the specimen was prevented altogether. Multiple layers of basalt fibers instead concentrated the damage on the middle section of the specimen, while reducing the spalling of the concrete cover. The amount of concrete ejected from the specimen was

limited, as was the velocity of the fragments obtained from high-speed camera recordings and Photonic Doppler Velocimetry (PDV) measurements. The velocity development of the specimen soffit measured during the experiment is presented in Fig. 20, together with the position of the measurement points on the soffit of the specimen. Instruments utilizing the PDV method were used to obtain the measurements.

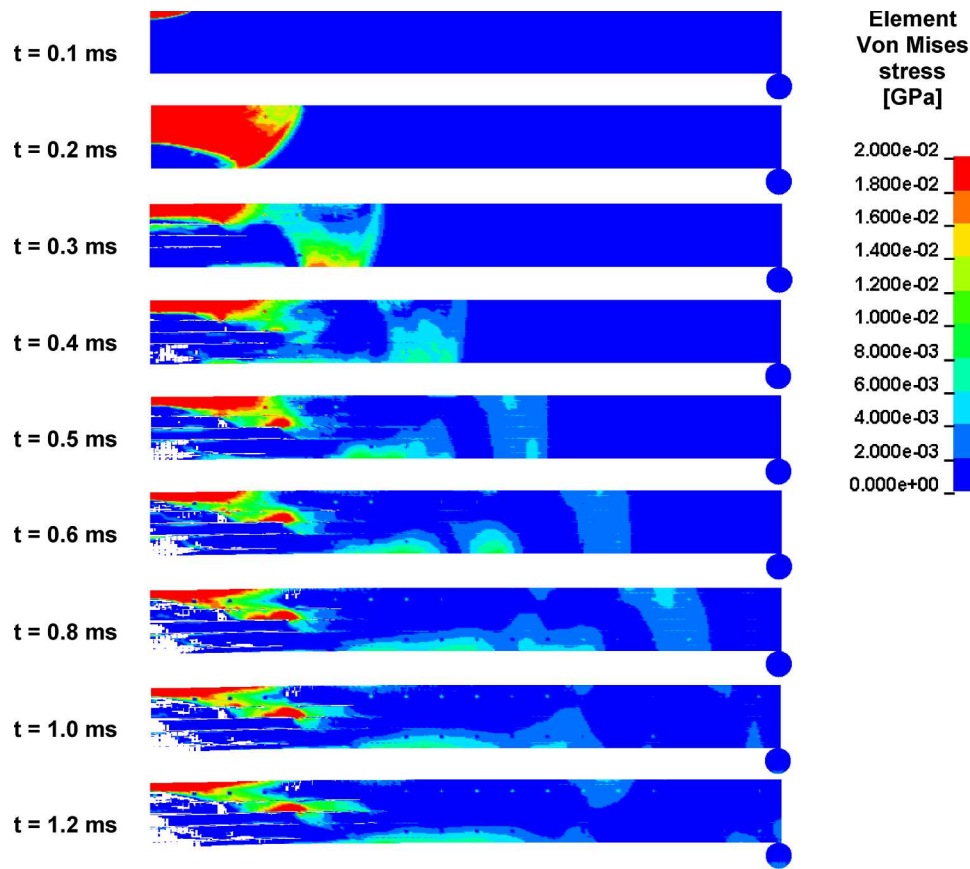The measuring device uses Doppler shift of the reflected light and

Fig. 22. FE calculation results for specimen no. 18: Fringe of pressure in various times after detonation (longitudinal section in the middle of the specimen) FE model of a specimen with a textile sheet.

Fig. 23. Damage to specimen No. 19 after the blast. Overall view (top image), top view (bottom left image), bottom view (bottom right image).

heterodyning to enable measurement of rapidly accelerating surface. The Doppler shifted light reflected from the target is coupled with the incident light (either reflected from the end of the fiber or collimator or from reference arm of the system) generating beats due to superposition of the shifted and unshifted waves. Based on the bandwidth of the recording oscilloscope velocities in the range of km/s are routinely measurable with sub-nanosecond resolution. The basic principle of the

measurement is shown in Fig. 16.

The results of numerical modelling shown in Fig. 21 and Fig. 22 demonstrate the process of pressure concentration and the formation of longitudinal cracks along the material interface between the basalt mesh and the concrete rather than shear cracking, which would have formed a cone-shaped hole in a standard concrete specimen without the layers of basalt mesh. The damage caused by the phenomenon

Fig. 24. A comparison of the amount and the size of the fragments after the blast for specimen no. 18 (left image) and for specimen no. 19 (right image).
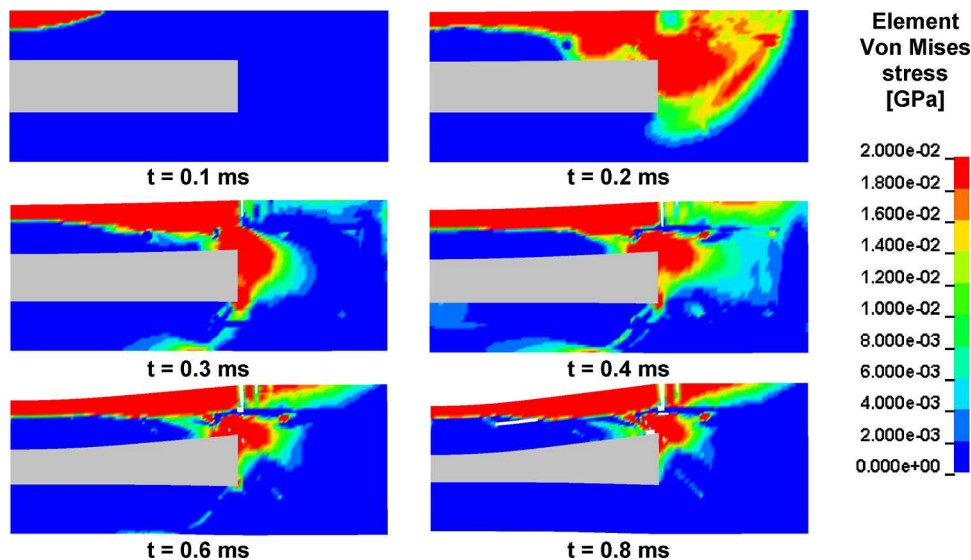

Fig. 25. FE calculation results for specimen no. 19. Fringe of pressure in various times after detonation (cross section in the center of the specimen, the textile sheets are shown in grey for clarity).

described above can be clearly identified in the experimental results, and the longitudinal cracking is shown in Fig. 18.

The concentration of damage on the inside of the specimen also ensures some degree of residual load-bearing capacity. Even though the specimen is cracked, as shown in Fig. 17, the structure is still compact and can carry at least its self-weight. This residual capacity can for example allow the evacuation of occupants of a building after an explosive event, etc.

3.2. FE model of the specimen with the textile sheet

The arrangement of the FE model of specimen no. 19 is shown in Fig. 5. The definitions of the material model and the geometry correspond with the information given in previous sections. The main goal of this numerical model was to illustrate the influence of a thick layer of soft material embedded in the concrete on the propagation of the blast-induced shock wave throughout the specimen.

The results of the experiment – thoroughly described in [4] and presented in Fig. 23 – clearly show that both the spall area and the formation of the typical blast-related cone-shaped hole were also reduced in comparison with reference standard RC specimen no. 1

(Fig. 19), to a very similar extent as for specimen no. 18 (Fig. 17). However, the amount of material ejected by the blast (the extent of the puncture) is considerably greater. The research in this case focuses on the behavior of soft material subjected to the shock wave from the explosion, and the behavior of the shockwave at the interface between the concrete and the soft material.

Due to the extreme differences in the stiffness and the density of the two neighboring materials, a significant reflection was expected at the interface, coupled with large deformation of the soft sheets embedded in the specimen. The results of numerical modelling confirmed these expectations. Almost all the shock wave energy is reflected off the interface back to the concrete. The blast damage to the specimen is more visibly shown in Fig. 24. PDV measurement results are shown in Fig. 27.

The results of the FE modelling shown in Fig. 25 and Fig. 26 demonstrate the passage of the shock wave through the specimen. Because there was only a negligible change in the pressure state, the soft sheet material is shown in constant grey for greater clarity. It is clearly shown that the initial shock wave is constrained in the concrete layer above the textile sheet, and that it does not reach the specimen soffit immediately. Unlike for specimen no. 18, therefore, the damage and spalling at the soffit is not caused by the reflection of the initial shock
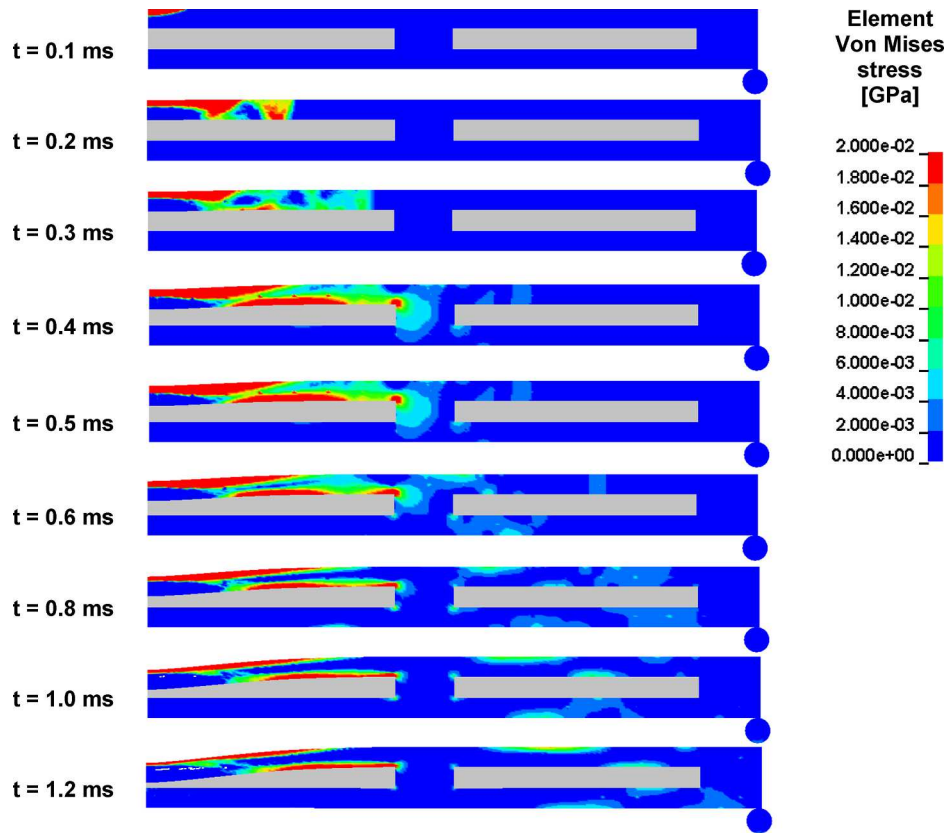
Fig. 26. FE calculation results for specimen no. 19: Fringe of pressure in various times after detonation (longitudinal section in the middle of the specimen, the textile sheets are shown in grey for clarity).
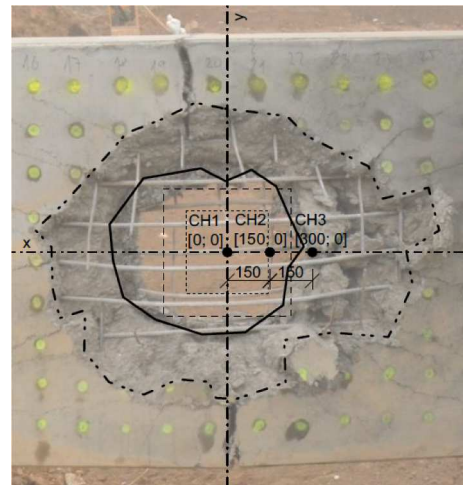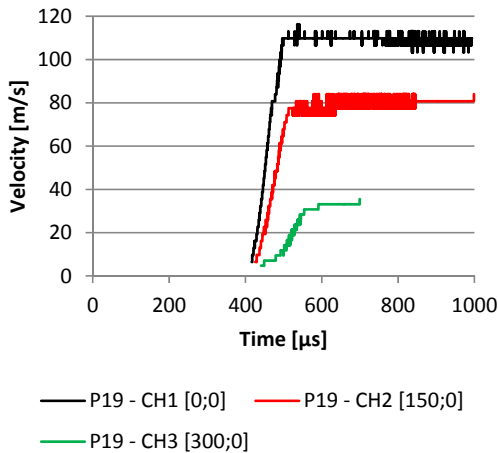

Fig. 27. PDV measurements – Specimen no. 19.

wave, but rather by the impact of the debris of the top concrete layer that passes through the soft textile layer that is deteriorated by the effect of the fireball. The response of the specimen soffit to the blast is significantly slower in this case, as can be seen from a comparison between Fig. 21 and Fig. 25, or between Fig. 22 and Fig. 26.

At the time of 1.2 ms after the blast, it is clearly shown that specimen no. 18 was already cracked, and that spalling had occurred. However, at the same time there is still no visible damage to the soffit of specimen no. 19. Even though the damage eventually reaches a similar extent, the recording of the time response obtained from high-speed cameras and laser measurements suggests that the fragments were ejected from the soffit of the specimen at slower velocities. This can be

attributed to differences in the passing of the blast energy to the particular part of the structure. While in the case of specimen no. 18 the energy is passed directly through the material in the form of a shock wave, in the case of specimen no. 19 the blast has to break the top surface and transfer the blast energy to kinetic energy of the broken concrete top layer. The impact of the fragments of the top concrete layer on the bottom concrete layer then finally causes the damage to the soffit of the specimen.

The soffit velocity of specimen no. 19 measured during the experiment is shown in Fig. 27, together with the positions of the sensors on the soffit of the specimen. A comparison of the results for specimens no. 18 and 19 for the corresponding soffit locations is shown in Fig. 28.
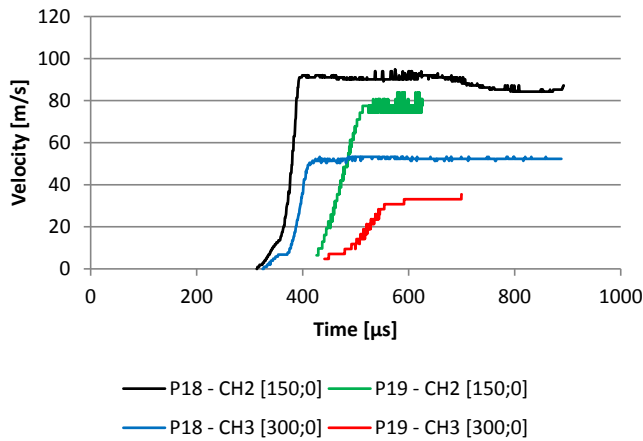
Fig. 28. PDV measurements – Comparison of specimen no. 18 and no. 19.
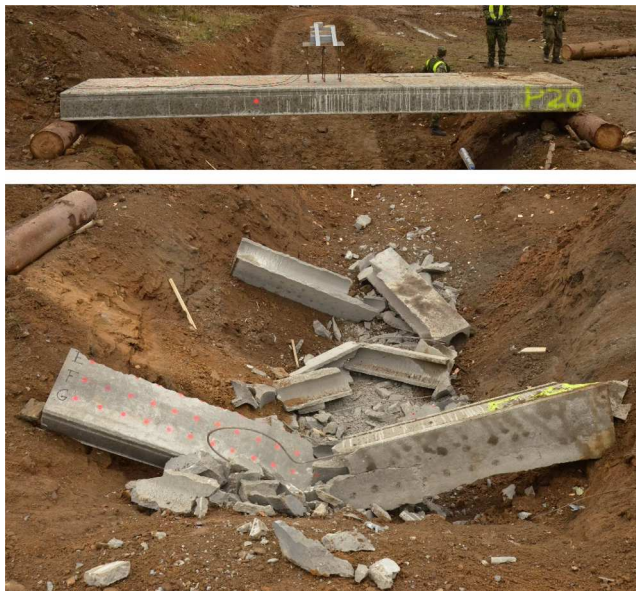

Fig. 29. Specimen No. 20 before the blast (above) and after the blast (below).

There is a clear difference in the final velocity of the soffit, except at the dead center of the specimen, where the difference in velocity between the two experiments is marginal.

Fig. 30. PDV measurements – Specimen no. 20.

The overall damage is still comparable in the two specimens, no. 18 and no. 19. There is decreased fragment velocity in both specimens despite the absence of any additional reinforcement in the cover layer. However, the size of the fragments is comparable, so it can be assumed that the extent of the additional damage caused by fragmentation in a real structure would be reduced by the insertion of a soft sheet in the center of the specimen.

3.3. FE model of a hollow-core specimen

Hollow-core specimen no. 20 differed from all other specimens in many ways. It was made of plain concrete with no distributed reinforcement or reinforcing bars. It was reinforced only with prestressed high-strength steel strands. The specimen also contained internal voids. The cross section of the specimen is shown in Fig. 6.

Prior to the experiment, it was estimated that the specimen should have significantly lower overall blast resistance than the other specimens due to the differences mentioned above, mainly due to the smaller cross-sectional area and the lower robustness of the specimen, and due to the lack of reinforcement. With no reinforcement to provide tensile strength for the concrete composite material, brittle behavior was predicted.

The smaller volume of concrete inevitably results in an increase in the pressure inside the specimen in comparison with a cross section without holes. Shock waves passing through the specimen reflect off any surface of the specimen and gradually create a significant concentration of pressure in the concrete ribs between the holes, resulting in brittle failure of the material in the critical areas.

The results of the experiment – thoroughly described in [4] and presented in Fig. 29 – clearly show that the predominant mode of failure of the specimen is the formation of longitudinal cracks along the specimen in areas where the concrete is thinner, i.e. the ribs, and in the areas below and above the center of the circular holes.

Similar PDV measurements as described earlier in this text for other specimens were made during the experiment. The results of the measurements are presented in Fig. 30. The output is significantly 'stepped', because the measuring oscilloscope was set to the same range and sampling frequency as for the other experiments. However, in this case the measured values were smaller than expected. A comparison with the response of specimens no. 18 (Fig. 20) and no. 19 (Fig. 27) shows clearly that the soffit of specimen no. 20 accelerates significantly more slowly and to a much lower final velocity, indicating a completely different mode of blast damage. Because the structure fails during the first passage of the shock wave through the specimen, large amounts of blast energy are dissipated by the cracking and crushing of the concrete
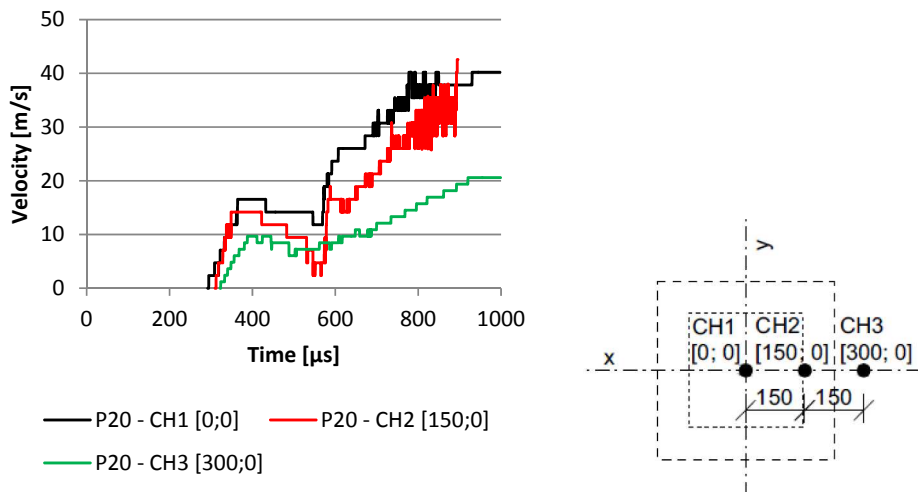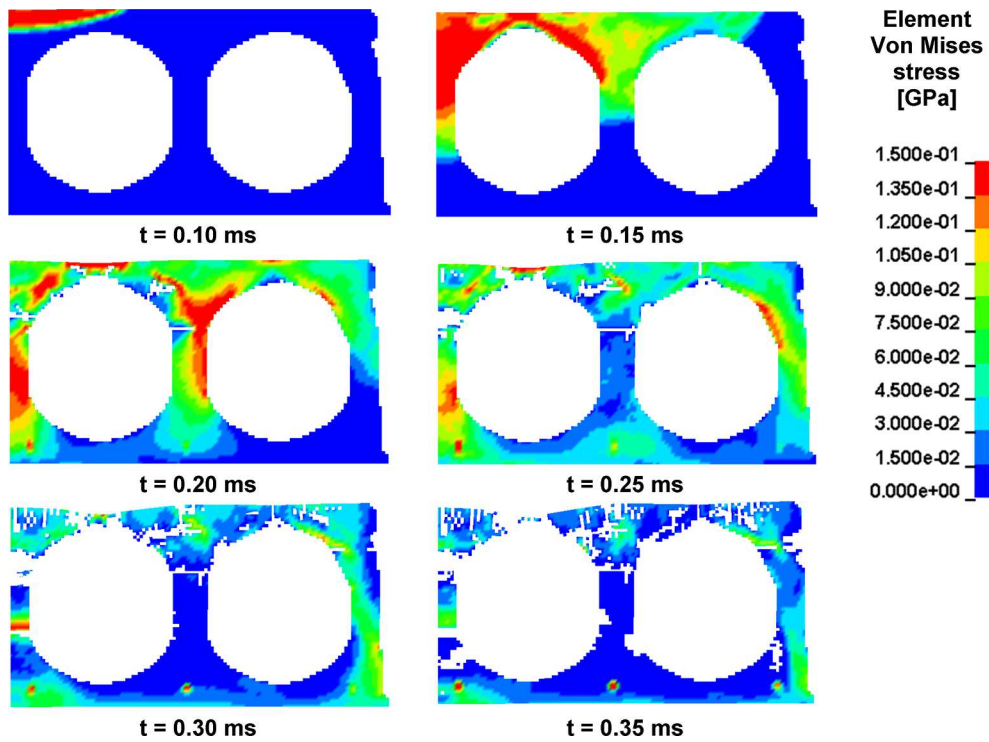
Fig. 31. FE calculation results. Specimen no. 20. Fringe of the pressure at various times after the detonation. Cross section in the center of the specimen.
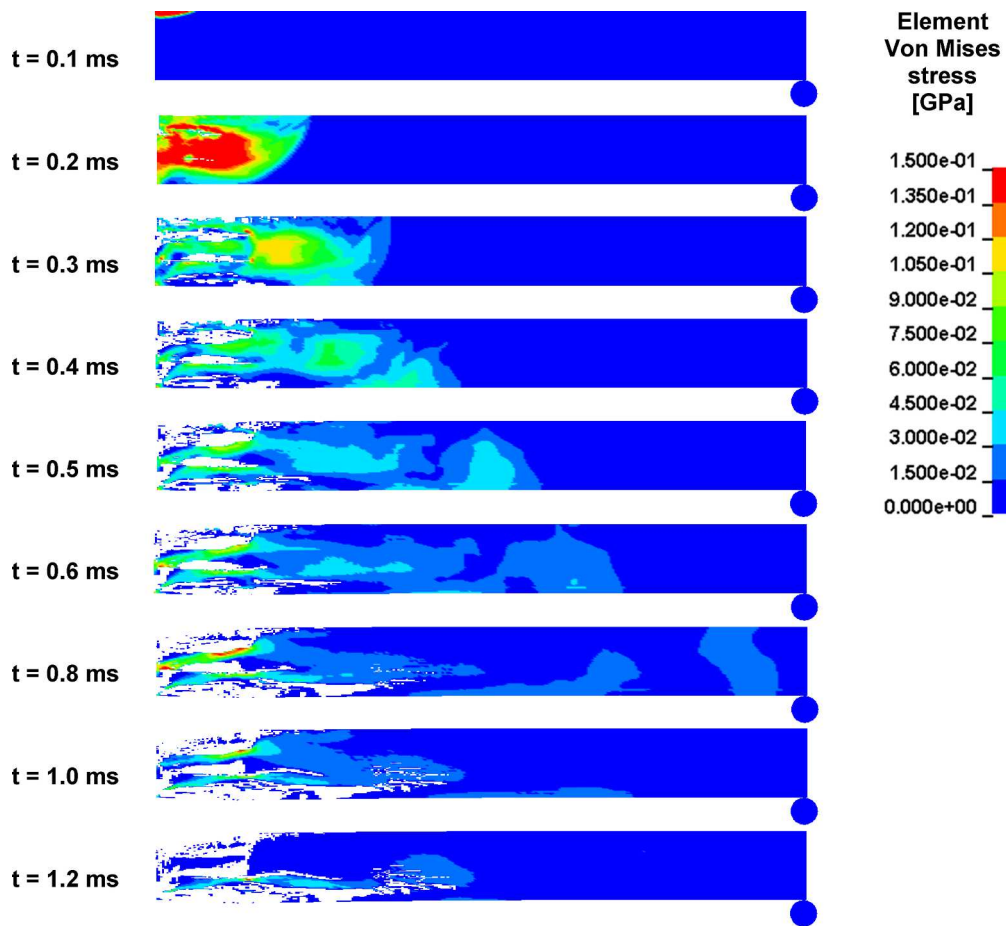

Fig. 32. FE calculation results. Specimen no. 20. Fringe of the pressure at various times after the detonation (longitudinal section in the central rib of the specimen).

inside the specimen. The other notable difference that slows the specimen soffit down is the greater size of the fragments than for the other specimens. The greater fragment mass increases the inertia of the fragments, hence limiting their acceleration.

The process of pressure concentration formation, resulting in the development of cracks, is clearly visible from results of numerical modelling. Fig. 31 shows the propagation of a pressure wave in the middle of the specimen (directly under the explosive). The pressure concentrations in the areas described above are clearly visible. The erosion of elements represents the formation of cracks. A longitudinal section through the rib in the middle of the specimen is shown in Fig. 32. The figure shows the formation and the propagation of the longitudinal crack through the rib. The area below the explosive (left side of the figure) is crushed due to the extreme pressure that the specimen is subjected to. The shock wave propagates further along the rib at a velocity in excess of 3 km/s, followed by the formation of a longitudinal crack. The longitudinal cracks in effect delaminate the specimen, causing total loss of its integrity and load-bearing capacity, just as is shown by the experimental results (Fig. 29).

4. Conclusions

This paper has presented numerical assessment of the response of heterogeneous concrete-based composite bridge decks subjected to near field blast loading.

The paper aimed to verify and explain the experimental findings that showed consumption of the blast energy by layer delamination in the pre-determined damage zones. The internal heterogeneity can be to some degree neglected in numerical modelling without compromising the results (i.e. concrete can be modelled as an isotropic material with the proper material model). However, when using composites consisting of various significantly different materials, it is necessary to include the heterogeneity in the model. In the case of the presented specimens, the basalt mesh or recycled textile sheet respectively had to be modelled. Material heterogeneity has great influence on the behavior of a structure subjected to blast loading. The shockwave passing through the structure rebounds off any interface between domains with varying densities. Due to the rebound, an area of stress concentration is created at the interface In these areas, the structure is more susceptible to localized failure (cracking of concrete, loss of the reinforcement bond, delamination of sandwich composites, etc.).

This effect usually reduces the blast resistance of the structure. In the case of a standard bar reinforcement, the stress concentration around the steel reinforcing bars weakens the bond between the concrete and the reinforcement, especially in areas where the reinforcing bars are overlapped. Loss of the bond seriously affect the overall behavior and above all the residual load-bearing capacity of a structure. In the case of delamination, however, the structure can be designed in such a way that the delamination does not cause a significant decrease in the post-event residual loadbearing capacity. The overall resistance of the structure to blast can even be increased by this effect, because delamination of the composite material can be very effective in dissipating the energy of the blast wave. This was observed experimentally, and the behavior was observed in the numerical assessment.

The results of the experimental program have shown, and numerical modelling has confirmed, that the differences in the properties of various materials coexisting within a heterogeneous structure have significant influence on its overall behavior under high strain-rate loading. These differences must not be dismissed in the numerical investigation. Without making a thorough investigation, it is hard to estimate whether the effect of heterogeneity will reduce or increase the blast resistance of a structure.

References

[1] Foglar M, Kovar M. Conclusions from experimental testing of blast resistance of FRC and RC bridge decks. Int J Impact Eng 2013;59:18–28. https://doi.org/10.1016/j.ijimpeng.2013.03.008.

[2] Foglar M, Hajek R, Kovar M, Štoller J. Blast performance of RC panels with waste steel fibers. Constr Build Mater 2015;94:536–46. https://doi.org/10.1016/j.conbuildmat.2015.07.082.

[3] Foglar M, Hajek R, Fladr J, Pachman J, Stoller J. Full-scale experimental testing of the blast resistance of HPFRC and UHPFRC bridge decks. Constr Build Mater 2017;145:588–601. https://doi.org/10.1016/j.conbuildmat.2017.04.054.

[4] Hajek R, Fladr J, Pachman J, Stoller J, Foglar M. An experimental evaluation of the blast resistance of heterogeneous concrete-based composite bridge decks. Eng Struct 2019;179:204–10. https://doi.org/10.1016/j.engstruct.2018.10.070.

[5] Kovar M, Foglar M. An analytical description of the force-deflection diagram of FRC. Compos B 2015;69:550–61. https://doi.org/10.1016/j.compositesb.2014.10.021.

[6] Hajek R, Foglar M. Numerical and experimental analysis of the effect of rigid barriers on blast wave propagation. ASCE J Struct Eng 2015. https://doi.org/10.1061/(ASCE)ST.1943-541X.0001308, 04015061.

[7] Hajek R, Foglar M, Fladr J. Influence of barrier material and barrier shape on blast wave mitigation. Constr Build Mater 2016;120:54–64. https://doi.org/10.1016/j.conbuildmat.2016.05.078.

[8] LS-DYNA (2006). Theory Manual. Livermore Software Technology Corp. (LSTC).

[9] LS-DYNA (2007). Keyword User's Manual, Version 971. LSTC.

[10] Kong SY, Remennikov AM, Uy B. Numerical simulation of the response of non-composite steel-concrete-steel sandwich panels to impact loading. AJSE 2012;12(3). https://doi.org/10.7158/S11-098.2012.12.3.

[11] Hao Y, Hao H. Influence of the concrete DIF model on the numerical predictions of RC wall responses to blast loadings. Eng Struct 2014;73:24–38. https://doi.org/10.1016/j.engstruct.2014.04.042.

[12] Tai YS, Chu TL, Hu HT, Wu JY. Dynamic response of a reinforced concrete slab subjected to air blast load. Theor Appl Fract Mech 2011;56(3):140–7. https://doi.org/10.1016/j.tafmec.2011.11.002.

[13] Matsagar VA. Comparative performance of composite sandwich panels and non-composite panels under blast loading. Mater Struct 2016;49:611–29. https://doi.org/10.1617/s11527-015-0523-8.

[14] Li J, Wu C, Hao H, Wang Z, Su Y. Experimental investigation of ultra-high performance concrete slabs under contact explosions. Int J Impact Eng 2016;93:62–75. https://doi.org/10.1016/j.ijimpeng.2016.02.007.

[15] Stöhr J, Hájek R, Foglar M. Blast performance of reduced scale reinforced concrete specimens (2015). Stirling: Civil-Comp Press Ltd; 2015.

[16] Liu J, Wu C, Li C, Dong W, Su Y, Li J, et al. Blast testing of high performance geopolymer composite walls reinforced with steel wire mesh and aluminium foam. Constr Build Mater 2019;197:533–47. https://doi.org/10.1016/j.conbuildmat.2018.11.207.

[17] Christian Abraham, Chye Gary Ong Khim. Performance of Fiber Reinforced High-strength concrete with steel sandwich composite system as blast mitigation panel. Procedia Eng 2014;95:150–7. https://doi.org/10.1016/j.proeng.2014.12.174.

[18] Fallon C, McShane GJ. Fluid-structure interactions for the air blast loading of elastomer-coated concrete. Int J Solids Struct 2019;168:138–52. https://doi.org/10.1016/j.ijsolstr.2019.03.017.

[19] Iqbal N, Sharma PK, Kumar D, Roy PK. Protective polyurea coatings for enhanced blast survivability of concrete. Constr Build Mater 2018;175:682–90. https://doi.org/10.1016/j.conbuildmat.2018.04.204.

[20] Maazoun A, Matthys S, Belkassem B, Lecompte D, Vantomme J. Blast response of retrofitted reinforced concrete hollow core slabs under a close distance explosion. Eng Struct 2019;191:447–59. https://doi.org/10.1016/j.engstruct.2019.04.068.

[21] Draganic H, Gazic G, Varevac D. Experimental investigation of design and retrofit methods for blast load mitigation – A state-of-the-art review. Eng Struct 2019;190:189–209. https://doi.org/10.1016/j.engstruct.2019.03.088.

[22] Goswami A, Das Adhikary S. Retrofitting materials for enhanced blast performance of structures: recent advancement and challenges ahead. Constr Build Mater 2019;204:224–43. https://doi.org/10.1016/j.conbuildmat.2019.01.188.